Title

Discovery and characterization of protein-protein interaction stabilizers

Author

Vickery, Holly Renee

Publication Date

2024

Peer reviewed|Thesis/dissertation

Discovery and Characterization of Protein-Protein Interaction Stabilizers

by
Holly Vickery

DISSERTATION
Submitted in partial satisfaction of the requirements for degree of
DOCTOR OF PHILOSOPHY

in

Chemistry and Chemical Biology

in the

GRADUATE DIVISION
of the
UNIVERSITY OF CALIFORNIA, SAN FRANCISCO

Approved:

DocuSigned by:
Michelle Arkin
992885B79658434...

Michelle Arkin
Chair

DocuSigned by:
Jason Gestwicki
DocuSigned by:
Frank Mccormick
094D275D833840E...

Jason Gestwicki

Frank Mccormick

Committee Members

Acknowledgments

I first would like to thank members of the UCSF scientific community who have shaped my experience in graduate school. I first thank my Ph.D. advisor, Michelle Arkin, for her unwavering support and mentorship. You have guided me through multiple projects, successful collaborations, and many, many new techniques and concepts in PPI stabilization and drug discovery. I also would like to thank you for the environment you instill in your lab. The welcoming, enthusiastic, collaborative, and driven culture of the Arkin Lab greatly contributed to my success and how much I enjoyed my time during graduate school. I thank everyone who has cycled through the Arkin Lab during my time at UCSF, but especially Johanna Virta, Markella Konstantinidou, and Dyana Kenanova (AKA Team 14-3-3). Johanna, my experience in the Arkin Lab would not have been the same without you. It has been so rewarding to watch you grow as a scientist and have your support on our many projects together. I'm not sure I will ever have another coworker who I will want to share a TC hood with to do transfections, arrive at the same time as every single day, or spend every waking moment with on a 6-week trip to Europe. Working with you has truly been one of the highlights of my PhD, and I'm so glad we were able to convince you to join the Arkin Lab. All I ask is that you don't move too far away from California when you complete your PhD! Markella, my thesis project would be absolutely nothing without you. I thank you for being such a brilliant chemist, enthusiastic scientist, and kind person. It has been a pleasure to work together on the CRAF project over the years. Dyana, we had so much fun together from our first day in the Arkin Lab. Thank you for being a constant source of smiles and laughter. I will never forget when you lost the cells on the centrifuge. I have made so many amazing memories with you in and out of lab that I will forever cherish. I am also very grateful for Ziwen Jiang and Andy Ambrose for helping me every step of the way with any questions I had. I also would like to thank Jez Revalde and Zain Alam for instrument training. I thank Kayque Silva for his enthusiasm and willingness to help with my assays and keeping care of my cells. I also

thank Amanda Paulson for quickly uploading lots of screening data. I thank Maryam Pearson for expressing and purifying protein whenever I needed it. I thank Kazuko Olson for handling numerous reimbursements, scheduling many meetings, and lots of fun times. I still can't believe we got to meet Cody Rigsby together! I also thank Ninwe Maraha for keeping our lab running smoothly. I would like to thank the whole Arkin Lab for the many fun hikes, lunches, and happy hours that kept me smiling over the past five years.

I would also like to thank the members of my qualifying examination and thesis committees, Jason Gestwicki (both), Frank McCormick (thesis), Adam Renslo, Natalia Jura, and Andrei Goga (qualifying), for their time, advice, and support on my various projects throughout graduate school. I would also like to thank Lucy Young for training and providing instrumental input on my project throughout the years.

Next, I would like to thank my collaborators at Eindhoven University of Technology. I would like to thank Luc Brunsveld for welcoming me to his lab for a month and supporting my research and the 14-3-3 collaboration. I thank Christian Ottmann for his enthusiasm and amazing scientific advice over the years. I would like to thank Eline Sijbesma, Emira Visser, and Bente Somsen for advice and collaboration. I thank Maxime van den Oetelaar, Marloes Pennings, and Guido Oerlemans for teaching me crystallography during my time in Eindhoven and continued collaboration. Dank je wel!

I would also like to thank my collaborators and friends at UCSF. First, I would like to thank Julian Braxton for being such an amazing friend and roommate. Thanks for being my adventure buddy and letting me and my parents show you all around California and Utah. Most importantly, thank you for being such an amazing friend to Mr. Puppy. I would also like to thank Elissa Fink for being a wonderful and supportive friend and fellow Beyoncé lover. You have been the best concert buddy, and I can't wait to hang out in Greece again someday soon. I also thank Paul Burroughs, Tia Tummino, and Izzy Glenn for friendship and support.

Next, I would like to thank my friends outside of UCSF. First, Zoe Feldman has been my best friend for 17 years and I would like to thank her for continuous support, daily texts, and constantly making fun of my middle school outfits. I cannot wait for you to move slightly closer to me in the near future! I also thank Keila Wedow for many fun years of friendship and for letting me into the Genentech store to buy many shirts.

Next, I would like to thank everyone who influenced my scientific path before graduate school. I would like to thank Sheila David and Chandrima Majumdar for their mentorship and support throughout my undergraduate research and through graduate school. I also thank Perry Gee for being a fantastic advisor and friend throughout my time at UC Davis and beyond. I thank Sarah Potter for being an incredible friend and coworker during our time at UC Davis and her continued support throughout graduate school. Please come back to California! I also thank Adam Lancaster for his mentorship and continued support throughout graduate school.

Lastly, I would like to thank my family. I would like to thank my mom and dad, Jill and Larry Vickery, for their continuous support. It has been exciting to follow in your field and be able to discuss details of projects and experiments with you. From helping me optimize protein purifications to analyzing electron density in crystal structures, it has been a joy to be able to share so much of this experience with both of you. I would also like to thank my other family members including Grandma Imo, Jack, Vicky, Tasha, Tonya, Maddie, Connor, Julie, Aaron, Kacie, Trenton, Ryan, Brian, and Forrest. Finally, I would like to thank all the dogs in my life for the emotional support they have provided me. I love you Ernie Poo, Oscar Man, Callie Girl, Daisy Poo, Ella, WtP, Percy, Rocket, Thunder, and Huckleberry.

Contributions

Chapter 2 is a published manuscript:

Kenanova, D. N.[+], Visser, E. J.[+], Virta, J. M., Sijbesma, E., Centorrino, F., Vickery, H. R., Zhong, M., Neitz, R. J., Brunsveld, L., Ottmann, C., and Arkin, M. R. A Systematic Approach to the Discovery of Protein–Protein Interaction Stabilizers. *ACS Cent. Sci.* **9**, 937–946 (2023).

Chapter 3 is a manuscript in review:

Vickery, H. R.[+], Virta, J. M.[+], Konstantinidou, M., and Arkin, M. R. (2024) Development of a NanoBRET assay for evaluation of 14-3-3σ molecular glues.

Chapter 4 is a manuscript in preparation:

Vickery, H. R.[+], Konstantinidou, M.[+], Virta, J. M., Pennings, M., van den Oetelaar, M. C. M., Neitz, R. J., Ottmann, C., Brunsveld, L., and Arkin, M. R. (2024) Small molecule stabilization of the 14-3-3σ/CRAF complex inhibits the MAPK pathway.

Discovery and characterization of protein-protein interaction stabilizers

Holly Renee Vickery

Abstract

Protein-protein interactions (PPIs) are vital for biology as they govern numerous essential biological processes, including signal transduction, enzymatic activity regulation, protein localization, and complex formation, collectively orchestrating cellular functions and maintaining homeostasis. The hub protein 14-3-3 interacts with hundreds of client proteins, including key signaling proteins CRAF and SOS1 and transcription factors Estrogen Receptor α (ERα), FOXO1, and TAZ. These 14-3-3/client interactions can be altered in disease, leading to undesirable activity and signaling. The Arkin Lab has pioneered a mass spectrometry-based site-directed disulfide tethering screen to identify PPI stabilizers and inhibitors. We have used this screen to discover stabilizers of various 14-3-3σ/client interactions including, CRAF, FOXO1, ERα, SOS1, and USP8. Disulfide fragment stabilizers lead to a 4 – 250-fold stabilization of 14-3-3σ/client complexes. To further characterize the effects of these stabilizers, we have developed Nanoluciferase bioluminescence resonance energy transfer (NanoBRET) assays to measure 14-3-3σ/CRAF, TAZ, and ERα interactions, where we have measured stabilizer EC_{50} values between 100 nM – 1 μM. We have optimized 14-3-3σ/CRAF stabilizers for selectivity and potency and measured increased PPI formation in cells, decreased CRAF kinase activity, and decreased signaling through the mitogen-activated protein kinase (MAPK) pathway. Finally, we have expanded the disulfide tethering technology to a new class of hub proteins to discover stabilizers of additional PPIs to modulate their interaction in disease.

The first chapter of this dissertation provides a brief introduction to protein-protein interactions, their role in disease, and how they can be modulated. Moreover, it introduces the hub protein 14-3-3 and the critical roles it plays in regulating client protein biology.

The second chapter describes a mass spectrometry-based site-directed disulfide tethering screen and how it has been applied to identify 14-3-3σ/client stabilizers for five different 14-3-3 client proteins. We have identified general stabilizers, which stabilize multiple 14-3-3σ/client interactions, as well as selective stabilizers. These stabilizers were analyzed by mass spectrometry, fluorescence anisotropy, and X-ray crystallography to assess their binding, potency, and interactions at the PPI interface, respectively. This work identified stabilizers that were further optimized to selectively stabilize the 14-3-3σ/FOXO1, 14-3-3σ/ERα, and 14-3-3σ/CRAF interactions.

The third chapter reports the development of a NanoBRET assay to characterize 14-3-3σ/client molecular glues. We developed this NanoBRET assay for three 14-3-3σ/client interactions: CRAF, TAZ, and ERα. Developing this cellular NanoBRET system for the hub protein 14-3-3σ allows for a streamlined approach in the assay development process for other 14-3-3σ clients, bypassing multiple optimization steps. These results offer a robust platform for library exploration to identify and evaluate PPI stabilizers and inhibitors.

The fourth chapter describes the optimization and evaluation of 14-3-3σ/CRAF stabilizers to inhibit the MAPK pathway in cancer. We show that compounds designed through a fragment merging approach have been optimized for potency and selectivity for CRAF over ARAF and BRAF. X-ray crystallography uncovers interactions between 14-3-3σ, RAF peptides, and stabilizers to reveal mechanisms of compound selectivity. Optimized compounds glue the 14-3-3σ/CRAF PPI in cells and inhibit signaling through the MAPK pathway in cancer cells.

The fifth chapter builds upon the hub protein stabilization technology developed in the Arkin Lab with the hub protein 14-3-3 and expands this technology to a new hub protein/client system. The tethering screen identified stabilizers and inhibitors of the hub protein/client interaction, suggesting that this technology can be extended to identify modulators of many PPIs implicated in various diseases.

Table of Contents

List of Figures

List of Tables

Chapter 1

Modulating protein-protein interactions in disease

Contributing Authors:

Holly R. Vickery[1]

[1]Department of Pharmaceutical Chemistry and Small Molecule Discovery Center (SMDC); University of California, San Francisco; San Francisco, CA 94158, USA

Abstract

Protein-protein interactions (PPIs) play a pivotal role in the pathogenesis of various diseases, serving as crucial determinants of cellular signaling, function, and dysregulation in conditions such as cancer, neurodegenerative disorders, and infectious diseases. Modulating PPIs with small molecules offers a promising therapeutic strategy, enabling precise control over complex biological processes implicated in disease progression and providing avenues for the development of novel therapeutic interventions. 14-3-3 proteins are a family of highly conserved hub proteins which play key roles in diverse cellular processes by binding to numerous partner proteins, therefore influencing their cellular localization, stability, and activity in various cellular pathways. Stabilizing PPIs involving 14-3-3 proteins with molecular glues represents a promising therapeutic approach and selective method to study the role of a single PPI. Stabilizers of 14-3-3/client interactions have been identified through a disulfide tethering screen, which measures the covalent binding of disulfide-containing fragments to 14-3-3/client complexes. Discovering PPI stabilizers can lead to a deeper understanding of the role of proteins in complex pathways, single PPIs within PPI networks, and PPIs and pathways in disease.

Main Text

PPIs are central to biology and serve as the foundation of virtually every cellular process, playing pivotal roles in signal transduction, gene regulation, enzymatic activity, and various other biological functions.[1–3] These interactions occur when two or more proteins come into physical contact to form complexes, which can have profound implications for the structure, function, and regulations of proteins within cells (Figure 1.1A). Understanding the intricate networks of PPIs is essential for deciphering the complexity of cellular pathways and for elucidating the molecular mechanisms underlying physiological and pathological processes. Hub proteins are proteins that interact with many other proteins within a biological network.[2] These proteins have complex interactomes and exceptionally high degrees of connectivity (Figure 1.1B). In recent years, advancements in experimental techniques and computational methods have significantly improved our ability to study and characterize new PPIs, opening new opportunities for drug discovery and the development of targeted therapeutics.[1–7]

When targeting a protein interactome with small molecules, one can either directly target proteins themselves or target PPIs. PPIs were once considered undruggable due to their lack of well-defined binding pockets on protein surfaces and their dynamics and flexibility. Advancements in structural biology, computational modeling, and screening technologies have led to the discovery of new approaches and strategies for targeting PPIs.[1–3,6–8] Targeting PPIs offers several advantages over directly targeting individual proteins. Firstly, directly targeting a single protein may inadvertently impact other proteins it interacts with, along with the signaling pathways in which it participates. Conversely, selectively modulating a PPI ensures that only the targeted interaction is influenced, leaving the remaining PPIs intact. Additionally, many biological processes are regulated by complex networks of protein interactions rather than single proteins alone. By disrupting specific PPIs, small molecules can modulate entire pathways or signaling cascades, leading to more profound and targeted therapeutic effects. Moreover, since PPIs

typically involve interactions between structurally conserved domains or motifs across different proteins, small molecules targeting PPIs may exhibit broader specificity and applicability across various disease states. Overall, targeting PPIs presents a promising approach for developing innovative and effective therapies for a wide range of diseases, including cancer, neurodegenerative disorders, and infectious diseases.[1–3,7]

PPIs can be modulated in two primary ways: inhibition and stabilization. PPI inhibition involves disrupting or preventing the interaction between two proteins.[1,9] This can be achieved by designing molecules that bind to the interface of the interacting proteins, thereby blocking their interaction. By inhibiting crucial PPIs involved in disease pathways, such as those related to cancer or inflammation, it is possible to intervene and potentially halt disease progression. Conversely, PPI stabilization involves enhancing or promoting the interaction between two proteins.[2,3,6,7] This can be desirable when the natural interaction between two proteins is weak or transient but plays a critical role in cellular function. Stabilizing PPIs can be therapeutically beneficial in cases where enhancing specific interactions can restore normal cellular function or promote beneficial signaling pathways. PPI stabilization could be just as important for drug discovery as inhibition and may be a more selective approach to study the role of a single PPI in a hub protein's network. However, approaches to identify stabilizers of PPIs are have only recently been developed.[2,3,7]

14-3-3 is a hub protein that interacts with hundreds of client proteins and therefore regulates many cellular pathways. The 14-3-3 family plays essential roles in diverse cellular processes such as signal transduction, cell cycle control, apoptosis, and protein trafficking.[10–14] 14-3-3 proteins bind to phosphorylated (phospho-Serine or phospho-Threonine), unstructured regions on client proteins, thereby modulating the activity, stability, and subcellular localization of the client protein (Figure 1.2).[10] Dysregulation of 14-3-3-mediated signaling has been implicated in numerous diseases, including cancer, neurodegenerative disorders, and metabolic syndromes,

highlighting the importance of this protein family as potential therapeutic targets.[15] Noteworthy among its numerous clients are key proteins such as the kinase CRAF and the transcription factor ERα, both intricately linked to various cancers.[16–23] Consequently, targeting the protein-protein interaction between 14-3-3 and its clients presents a compelling avenue for the development of innovative therapeutic strategies aimed at combatting these diseases.

Site-directed tethering is an approach developed to identify disulfide-containing fragments that covalently bind to a protein of interest by formation of a disulfide bond.[2,3,7,24,25] This high-throughput screen can be used to identify fragments that bind to a protein of interest or to a PPI. To identify stabilizers of 14-3-3/client interactions, we have pioneered a mass spectrometry-based site-directed disulfide tethering screen. This screen has been used to identify stabilizers and inhibitors of various 14-3-3σ/client interactions by tethering from the native C38 in 14-3-3σ, or engineering cysteine residues in 14-3-3σ or other isoforms.[2,3]

Figures

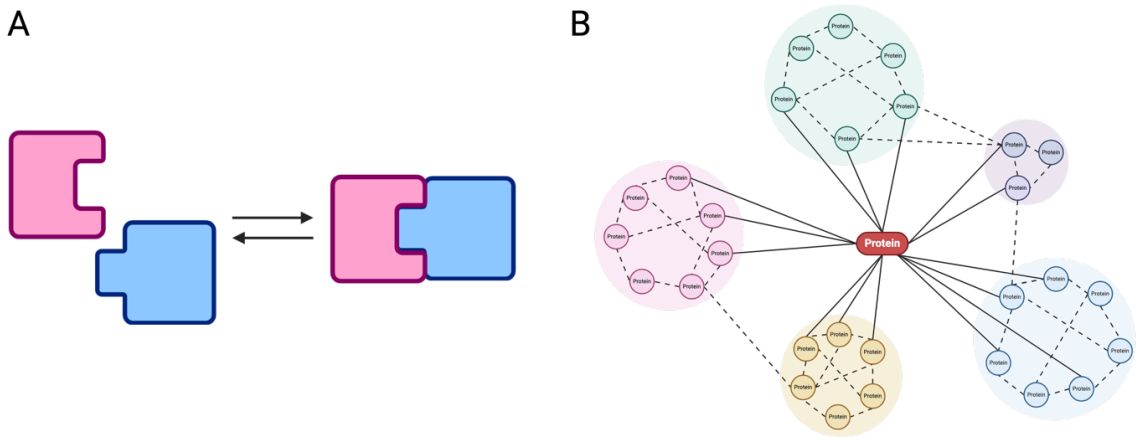

Figure 1.1: Protein-protein interactions
A) PPIs occur upon physical contact between two or more proteins. **B)** Example of a hub protein interactome. Hub proteins interact with many other proteins which may also interact with each other.

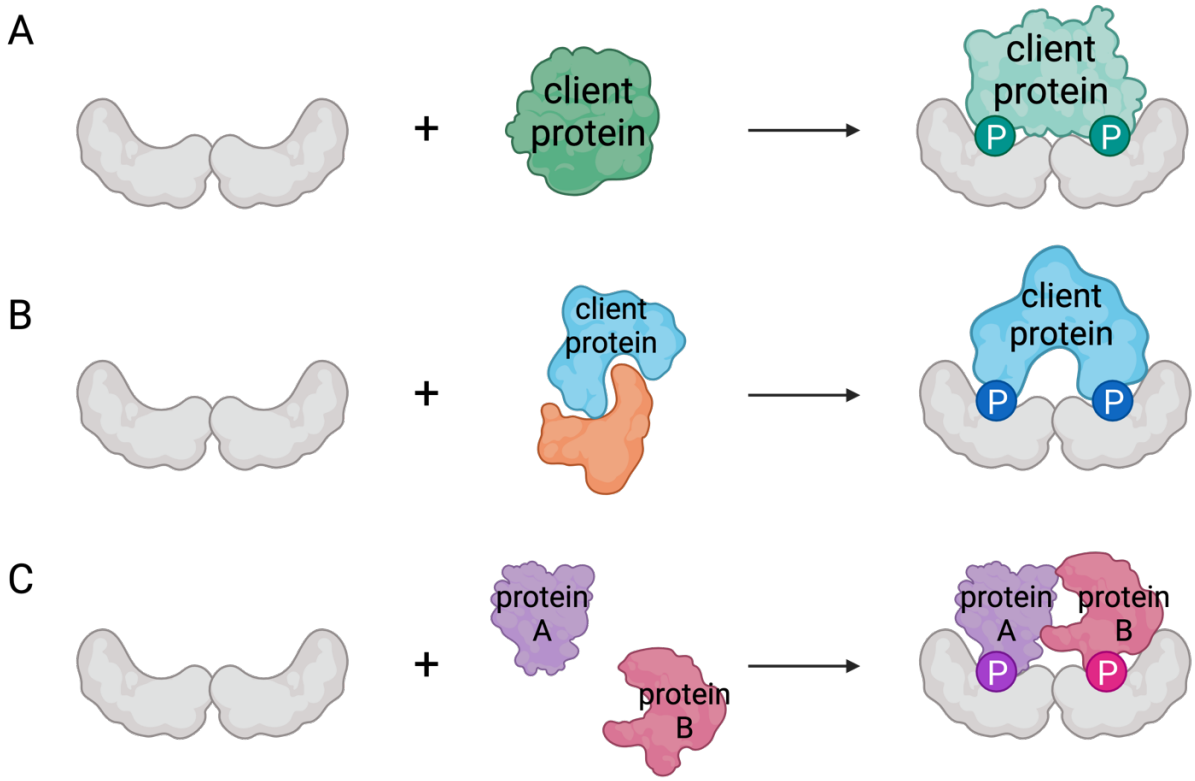

Figure 1.2: Functions of the hub protein 14-3-3
Upon binding to a client protein, 14-3-3 can have various functions. **A)** 14-3-3 can structurally change its client protein. This can have effects such as regulating client protein enzyme activity. **B)** 14-3-3 can physically occlude structural features on its client protein, having effects such as inhibiting the formation of other PPIs, protecting residues from dephosphorylation, and regulating the client protein subcellular localization. **C)** 14-3-3 can scaffold other PPIs, stabilizing multiprotein complexes.

References

1. Arkin, M. R., Tang, Y. & Wells, J. A. Small-Molecule Inhibitors of Protein-Protein Interactions: Progressing toward the Reality. *Chem. Biol.* **21**, 1102–1114 (2014).

2. Kenanova, D. N. *et al.* A Systematic Approach to the Discovery of Protein–Protein Interaction Stabilizers. *ACS Cent. Sci.* (2023) doi:10.1021/acscentsci.2c01449.

3. Sijbesma, E. *et al.* Site-Directed Fragment-Based Screening for the Discovery of Protein-Protein Interaction Stabilizers. *J. Am. Chem. Soc.* **141**, 3524–3531 (2019).

4. Ding, Z. & Kihara, D. Computational identification of protein-protein interactions in model plant proteomes. *Sci. Rep.* **9**, 8740 (2019).

5. Rao, V. S., Srinivas, K., Sujini, G. N. & Kumar, G. N. S. Protein-Protein Interaction Detection: Methods and Analysis. *Int. J. Proteomics* **2014**, 147648 (2014).

6. Konstantinidou, M. *et al.* Structure-Based Optimization of Covalent, Small-Molecule Stabilizers of the 14-3-3σ/ERα Protein–Protein Interaction from Nonselective Fragments. *J. Am. Chem. Soc.* **145**, 20328–20343 (2023).

7. Hallenbeck, K. K. *et al.* A Liquid Chromatography/Mass Spectrometry Method for Screening Disulfide Tethering Fragments. *SLAS Discov. Adv. Sci. Drug Discov.* **23**, 183–192 (2018).

8. Dong, G., Ding, Y., He, S. & Sheng, C. Molecular Glues for Targeted Protein Degradation: From Serendipity to Rational Discovery. *J. Med. Chem.* **64**, 10606–10620 (2021).

9. Ran, X. & Gestwicki, J. E. Inhibitors of Protein-Protein Interactions (PPIs): An Analysis of Scaffold Choices and Buried Surface Area. *Curr. Opin. Chem. Biol.* **44**, 75–86 (2018).

10. Obsil, T. & Obsilova, V. Structural basis of 14-3-3 protein functions. *Semin. Cell Dev. Biol.* **22**, 663–672 (2011).

11. Stevers, L. M. *et al.* Modulators of 14-3-3 Protein–Protein Interactions. *J. Med. Chem.* **61**, 3755–3778 (2018).

12. Obsilova, V. & Obsil, T. The 14-3-3 Proteins as Important Allosteric Regulators of Protein Kinases. *Int. J. Mol. Sci.* **21**, 8824 (2020).

13. Pennington, K. L., Chan, T. Y., Torres, M. P. & Andersen, J. L. The dynamic and stress-adaptive signaling hub of 14-3-3: emerging mechanisms of regulation and context-dependent protein-protein interactions. *Oncogene* **37**, 5587–5604 (2018).

14. Ballone, A., Centorrino, F. & Ottmann, C. 14-3-3: A Case Study in PPI Modulation. *Mol. Basel Switz.* **23**, (2018).

15. Freeman, A. K. & Morrison, D. K. 14-3-3 Proteins: Diverse Functions in Cell Proliferation and Cancer Progression. *Semin. Cell Dev. Biol.* **22**, 681–687 (2011).

16. Molzan, M. *et al.* Impaired Binding of 14-3-3 to CRAF in Noonan Syndrome Suggests New Approaches in Diseases with Increased Ras Signaling. *Mol. Cell. Biol.* **30**, 4698–4711 (2010).

17. De Vries-van Leeuwen, I. J. *et al.* Interaction of 14-3-3 proteins with the estrogen receptor alpha F domain provides a drug target interface. *Proc. Natl. Acad. Sci. U. S. A.* **110**, 8894–8899 (2013).

18. Lavoie, H. & Therrien, M. Regulation of RAF protein kinases in ERK signalling. *Nat. Rev. Mol. Cell Biol.* **16**, 281–298 (2015).

19. Park, E. *et al.* Architecture of autoinhibited and active BRAF–MEK1–14-3-3 complexes. *Nature* **575**, 545–550 (2019).

20. Kondo, Y. *et al.* Cryo-EM structure of a dimeric B-Raf:14-3-3 complex reveals asymmetry in the active sites of B-Raf kinases. *Science* **366**, 109–115 (2019).

21. Martinez Fiesco, J. A., Durrant, D. E., Morrison, D. K. & Zhang, P. Structural insights into the BRAF monomer-to-dimer transition mediated by RAS binding. *Nat. Commun.* **13**, 486 (2022).

22. Sun, Q. & Wang, W. Structures of BRAF-MEK1-14-3-3 sheds light on drug discovery. *Signal Transduct. Target. Ther.* **4**, 59 (2019).

23. Park, E. *et al.* Cryo-EM structure of a RAS/RAF recruitment complex. *Nat. Commun.* **14**, 4580 (2023).

24. Burlingame, M. A., Tom, C. T. M. B. & Renslo, A. R. Simple One-Pot Synthesis of Disulfide Fragments for Use in Disulfide-Exchange Screening. *ACS Comb. Sci.* **13**, 205–208 (2011).

25. Erlanson, D. A. *et al.* Site-directed ligand discovery. *Proc. Natl. Acad. Sci.* **97**, 9367–9372 (2000).

Chapter 2

A systematic approach to the discovery of protein-protein interaction stabilizers

Contributing Authors:

Dyana N. Kenanova[1,‡], Emira J. Visser[2,‡], Johanna M. Virta[1], Eline Sijbesma[2], Frederica Centorrino[2], Holly R. Vickery[1], Menqi Zhong[1], R. Jeffrey Neitz[1], Luc Brunsveld[2], Christian Ottmann[2], and Michelle R. Arkin[1].

[1]Department of Pharmaceutical Chemistry and Small Molecule Discovery Center (SMDC); University of California, San Francisco; San Francisco, CA 94158, USA

[2]Laboratory of Chemical Biology, Department of Biomedical Engineering and Institute for Complex Molecular Systems (ICMS), Eindhoven University of Technology, 5600 MB Eindhoven, The Netherlands

[‡]D.N.K. and E.J.V. contributed equally to this work.

Abstract

Protein-protein interactions (PPIs) are responsible for the proper function of biological processes and, when dysregulated, commonly lead to disease. PPI stabilization has only recently been systematically explored for drug discovery despite being a powerful approach to selectively target intrinsically disordered proteins and hub proteins, like 14-3-3, with multiple interaction partners. Disulfide tethering is a site-directed fragment-based drug discovery (FBDD) methodology for screening small molecules in a quantitative, high-throughput manner. We explore the scope of the disulfide tethering technology for the discovery of selective fragments as starting points for the development of potent small molecule PPI stabilizers and molecular glues using the hub protein 14-3-3σ. The complexes with 5 biologically and structurally diverse phospho-peptides, derived from the 14-3-3 client proteins ERα, FOXO1, CRAF, USP8, and SOS1, were screened for hit identification. Stabilizing fragments could be found for 4/5 client complexes with a diversified hit-rate and stabilizing efficacy for the different 14-3-3/client phospho-peptides. Extensive structural elucidation revealed the ability and adaptivity of the peptide to make productive interactions with the tethered fragments as key criterion for cooperative complex formation. We validated eight fragment stabilizers, six of which showed selectivity for one phospho-peptide client, and structurally characterized two nonselective hits and four fragments that selectively stabilized CRAF or FOXO1. The most efficacious of these fragments increased 14-3-3σ/CRAF phospho-peptide affinity by 430-fold. Disulfide tethering to the wildtype C38 in 14-3-3σprovided diverse structures for future optimization of 14-3-3/client stabilizers and highlighted a systematic method to discover molecular glues.

Introduction

Protein-protein interactions (PPIs) are essential to biology and their dysregulation is central to many diseases including cancer and neurodegeneration.[1–4] Many of these important PPIs include “hub proteins” that interact with a large number of protein partners, ranging from a few dozen to a few thousand.[5] Small molecules that inhibit or stabilize individual PPIs within these networks would be powerful tools to understand the effect of a single PPI on cellular function. Although PPIs were historically considered “undruggable”, there has been much progress in developing small molecule PPI inhibitors as biological probes and therapeutics.[6–10] By contrast, PPI stabilization has remained largely underexplored, despite its potential to be a selective method for the manipulation of a single interaction within a protein network.[11,12] Stabilization also has the potential to target unstructured, difficult to drug proteins via composite PPI binding pockets.[13,14] Molecular glue degraders and natural products have demonstrated the therapeutic value of stabilizing native or non-native (neomorphic) PPIs.[15–17] However, there are few robust, generalizable strategies to discover PPI stabilizers prospectively.[11,18] Here, we describe a robust and instructive approach, using site-directed fragment based drug discovery (FBDD) to systematically discover molecular glues.

FBDD is a well-established method for the discovery of small molecules towards challenging targets.[19,20] Fragments are simple chemical building blocks that – owing to their small number of atoms – sample chemical space efficiently. FBDD involves screening for weakly binding fragments that target subsites within a binding site, followed by fragment optimization via linking two fragments or elaborating a fragment-sized core. Disulfide tethering is a method of FBDD that capitalizes on a native or engineered cysteine residue proximal to an envisaged ligand binding site.[21–24] In the context of orthosteric PPI stabilization, this binding site is composed of both members of the protein complex (the composite PPI interface). Fragments that bind to this site with the correct positioning to form a protein-fragment disulfide bond are detected by intact

protein mass spectrometry (MS) in a high-throughput screen.[25] We utilize a library of approximately 1600 disulfide molecules with diverse fragments and linkers between the fragment and the disulfide.[26] To test the efficacy of this technology to discover PPI stabilizers, we have selected the hub protein 14-3-3 and a set of its diverse partner proteins.

14-3-3 is ubiquitously expressed in mammals and plays multiple roles within the cell, including phosphorylation protection, conformational changes, subcellular trafficking, and induction or disruption of other PPIs.[13,27–29] 14-3-3 typically binds to a phosphorylated serine/threonine of intrinsically disordered regions of its clients.30 With several hundred known interacting partners, the 14-3-3-binding proteome pro-vides diverse PPI interfaces with which to test the scope and limitations of our screening technology. Furthermore, 14-3-3/client stabilization could lead to therapeutics in a variety of disease fields including oncology, neurodegeneration, inflammation, and metabolic disease.[29,31] Previous studies using natural products such as Fusicoccin (FC-A) and Cotylenin-A (CN-A) have shown that stabilizing 14-3-3/client interactions regulates the activity of important cell signaling pathways including estrogen receptor α (ERα) and CRAF, respectively.[14,32]

We recently demonstrated the utility of disulfide tethering to identify molecular glues of the 14-3-3/ERα PPI. We dis-covered a series of disulfide fragments that stabilized the complex when bound to an engineered cysteine residue in the binding groove of 14-3-3, enhancing binding of the ERα C-terminal phosphopeptide up to 40-fold.[25] We now focus on targeting the native cysteine found in the 14-3-3 sigma isoform (14-3-3σ), which offers greater translatability for covalent molecules. Of the 7 isoforms found in mammalian cells, 14-3-3σ is the only one that harbors a cysteine residue proximal to the client binding groove, providing an additional degree of isoform specificity (Figure 2.1A).[30] The Protein Data Bank contains dozens of crystallographic structures of 14-3-3 with bound phospho-peptides derived from many of its binding partners, as well as a few examples of cryo-EM structures of full length proteins.[13,33–35] This wealth of structural

information allows for direct visualization of the various 14-3-3/client binding interfaces which could be capitalized on for the discovery of selective fragment stabilizers and the development of potent lead compounds through structure-guided chemical optimization. For our screens, we utilized the phospho-peptide mimetics of 14-3-3 PPI partners which bind 14-3-3 in a similar fashion to the unstructured regions of the full-length proteins but offer greater synthetic flexibility and simplified crystallography.[13,34]

Here, we used the disulfide tethering technology to systematically achieve selective PPI stabilization of 14-3-3 client phospho-peptides with diverse sequences and structures. The selected clients are also modulated by 14-3-3 in a way that could be therapeutically useful in cancer, metabolic disease, and/or rare disease.[14,36–39] For four of the five targets, effective PPI stabilizers were identified. Crystallographic and functional data highlight the molecular recognition of fragments for the distinctive composite PPI interfaces formed by 14-3-3 bound to client phospho-peptides. In particular, the CRAF- and FOXO1-based peptide-protein interactions with 14-3-3 yielded fragments with high selectivity and/or stabilization factors. The diversity of sequences and conformations found in 14 3 3/client complexes make the 14-3-3 interactome particularly promising for small-molecule PPI stabilization; furthermore, the disulfide tethering approach is remarkably effective at selecting chemical starting points for further design of potent and selective PPI stabilizers.

Results and Discussion

Primary Screen for 14-3-3/Client Stabilizers

The disulfide tethering screen targeted C38, a native cysteine on 14-3-3σ located proximal to the natural product binding pocket within the phospho-peptide recognition groove (Figure 2.1A, Figure S2.1). The cysteine forms a reversible covalent bond with the fragment thiol through disulfide exchange; the amount of bound fragment is measured by MS. A fragment stabilizer is

expected to show a higher "% tethering" in the presence of the 14-3-3σ/client phospho-peptide complex than 14-3-3σ alone due to cooperativity between the fragment and the peptide (Figure 2.1B). The screening was performed on five different peptide targets displaying three conceptually distinct 14-3-3 interaction motifs (Figure 2.1C): truncated (ERα),[14,40] turned (FOXO1),[37] and linear (CRAF, USP8, SOS1).[32,35,38,41]

14-3-3σ (100 nM) was screened in complex with the 5 client phospho-peptides at a concentration twice their respective K_D values (Figure S2.2). This condition provided a consistent presence of the 14-3-3σ/phospho-peptide composite interface that the fragments would engage. The 14-3-3σ/phospho-peptide complex was incubated with a single concentration of fragment (200 μM) under reducing conditions (250 μM β-mercaptoethanol) for 3 hours before samples were measured by intact-protein LC/MS. The % tethering threshold for hit selection was three standard deviations (3*SD) above the average % tethering for that condition (Figure 2.2A). In the quadrant of highest interest, potential stabilizing fragments showed % tethering above the tethering threshold in the peptide screen and % tethering below the tethering threshold in the *apo* screen (Figure 2.2B, green quadrant). Neutral compounds showed significant % tethering for both 14-3-3σ/phospho-peptide and *apo* (Figure 2.2B, yellow quadrant). Potential inhibitory fragments showed significant % tethering above the tethering threshold in the *apo* screen but not in the presence of peptide (Figure 2.2B, red quadrant). Compounds were clustered in a heat map based on % tethering in each of the five peptide screens and *apo* 14-3-3 screen (Figure 2.2C). An overlapping fragment hit cluster was identified for ERα, USP8, and SOS1 (Figure 2.2C, green box), whereas a cluster of unique hit fragments was identified for both CRAF and FOXO1 (Figure 2.2C, yellow boxes), indicating a difference in the abundance of selective stabilizers from the primary screens.

Each 14-3-3σ/phospho-peptide screen yielded potential stabilizing fragments, but the number and binding efficiency varied (Figure 2.2A, 2.2C, 2.2D, and Tables S2.1-S2.5). The initial

screen for ERα yielded 15 hit fragments including 7 unique stabilizers and a 33% tethering threshold. The FOXO1 screen yielded 23 hit fragments including 21 unique stabilizers and a 28% tethering threshold. The CRAF screen yielded 21 fragments including 16 unique stabilizers and a 35% tethering threshold. The USP8 screen yielded 10 hit fragments including 5 unique stabilizers and a 29% tethering threshold. The SOS1 screen yielded 8 hit fragments including 4 unique stabilizers and a 22% tethering threshold (Figures 2.2A and 2.2D). Figure 2.2E depicts representative chemical structures for each target.

Non-Selective Stabilizing Compound 1

In the initial screen, compound **1** was identified as top hit for ERα, CRAF and USP8 (Figure 2.2). **1** was further characterized by three dose-response experiments. Mass spectrometry (MSDR, analyzing fragment binding to protein, quantified by DR_{50} values) and fluorescent anisotropy (FADR, analyzing peptide binding to protein in the presence of compound, quantified by EC_{50} values) defined the binding affinity for the fragment and its effective concentration, respectively (Figure 2.3B). The compound's effect on the 14-3-3/client PPI was then determined by titrating 14-3-3 in a fluorescence anisotropy assay at constant peptide and compound concentrations (quantified by *app*K_D). In all three validation assays, **1** displayed a strong preference for CRAF, followed by ERα and USP8, and had no activity with FOXO1 or SOS1. Compound **1** showed DR_{50} values of 7 nM for CRAF, 18.1 μM for ERα, and 24 nM for USP8 (Figure 2.3C) as well as EC_{50} values of 922 nM for CRAF, 1.31 μM for ERα, and 3.38μM for USP8 (Figure S2.3). In the protein titrations, **1** increased peptide affinity for 14-3-3σ by 81-fold in the CRAF complex, 19-fold for 14-3-3σ/ERα, and 4-fold for 14-3-3σ/USP8 (Figure 2.3D and Table 2.1).

Crystal structures for compound **1** were obtained by co-crystallizing with ERα, CRAF, or USP8 bound to 14-3-3σ (Figure 2.3E), with clear density for both **1** and the peptides (Figure S2.4). Comparing the three co-crystal structures, the strongest electron density and ligand occupancy

for **1** was observed in the co-crystal structure with ERα. For ERα, the phenyl ring of **1** stacked against the +1 Val with a distance of ~4 Å (Figure 2.3E). Compound **1** showed an identical binding mode in the presence of CRAF (Figure 2.3F), for which the +1 Thr was 3.5 Å from the phenyl ring, while the remainder of the CRAF peptide wrapped around the fragment. These additional hydrophobic interactions could explain the higher fold stabilization with the CRAF peptide compared to ERα (Figure 2.3D, 2.3F). Interestingly, **1** shared the binding moiety with N42C-tethered stabilizers that were discovered previously for ERα (Figure 2.3G).25 Whereas compound **1**'s chloro-group was not positioned identically, the longer linker of **1** bridged the larger distance from C38 compared to N42C. In the presence of the USP8 peptide, the phenyl ring of **1** was turned, thereby shifting the fragment up and back into the 14-3-3σ pocket (Figure 2.3E). This conformational change seemed necessary because the USP8 peptide allowed for less space (Figure 2.3H). While the +1 Ser of UPS8 did not show any specific interaction with **1**, its +4 Ile pushed the fragment towards 14-3-3σ, which was not an ideal position for this fragment as was reflected by the weak electron density and the minimal stabilization for USP8. By contrast, the +4 Val of CRAF allowed for more space, thereby positioning **1** in a preferred conformation. It is noteworthy that **1** did not stabilize FOXO1 or SOS1 to 14-3-3σ. A crystallographic overlay of **1** with the FOXO1 peptide showed a steric clash with the +1 Trp of FOXO1, explaining its lack of stabilization (Figure S2.5A). In contrast, the +1 Ala residue of SOS1 would not contact the phenyl ring of **1**, perhaps explaining why no stabilization was observed (Figure S2.5B).

FOXO1 Selective Stabilizers

The FOXO1 peptide showed the highest number of stabilizing hits in our initial screen. For FOXO1, of the 23 initial stabilizers, 21 showed selectivity for the 14-3-3σ/FOXO1 phospho-peptide complex over *apo* 14-3-3σ and the other phospho-peptide clients in the initial screen (Figure 3.2D). Interestingly, the unique 21 FOXO-stabilizers had a highly conserved scaffold, with the phenyl ring engaging FOXO1 often decorated with halogens or a triazole moiety (Figure S3.6).

Eight of these compounds were validated in the MSDR (Figure S3.7). Of the eight compounds, five compounds had enough material to retest and were active in the FADR assays (Figure 3.4A, Figure S3.8, and Table S3.2). The binding affinity of compound **2** to 14-3-3σ was >10,000-fold better in the presence of the FOXO1 phospho-peptide than *apo* 14-3-3σ and all other phospho-peptide clients (DR_{50} = 360 nM vs. >2 mM; Figure 3.4B and Table 3.2). Compounds **3** and **4** had DR_{50} values >450-fold and >2,000-fold better, respectively (Table 3.2 and Figure S3.7). Compounds **2**, **3**, and **4** showed the greatest fold-stabilization in the protein titrations decreasing 14-3-3σ/FOXO1 K_D values 5-fold, 4-fold, and 12-fold (Figure 3.4C, Table 3.2, and Figure S3.9). It should be noted that while a high % tethering was observed for the FOXO1 stabilizers, the protein titrations only showed a modest shift in stabilization. This is likely due to the tight binding of the FOXO1 phospho-peptide, with a K_D value of 50 nM, already close to the limit of detection of this assay. A co-crystal structure for FOXO1/**2**/14-3-3σ was obtained, with clear density for both **2** and the FOXO1 peptide (Figure S3.10A). The phenyl ring of **2** stacked against the front of the FOXO1 peptide consisting of the +1 Trp and the +2 Pro residues (Figure 3.4D). Strikingly, in the presence of **2**, the Trp of FOXO1 underwent a conformational change to form a hydrogen bond with its NH and the amide carbonyl of **2** (Figure 3.4E). Moreover, the hydroxyl on the phenyl ring of **2** made a hydrogen bond with the S45 of 14-3-3σ, explaining the benefit of a hydrogen donor or, potentially, acceptor at that position. Compound **3** was also co-crystallized with FOXO1 (Figure S3.10B), showing a highly similar binding mode, but a lack of the hydrogen bonding with S45 of 14-3-3σ (Figure S3.10C). An overlay of **2** with the other peptides revealed that **2** could not reach the smaller +1 residues in the other client peptides or that the peptides sterically clashed (Figure S3.11), potentially explaining its selectivity for FOXO1 over the other peptides. Previous work discovered imine-based stabilizers for the 14-3-3/Pin-1 complex which, similar to FOXO1, has a +1 Trp.[42] In that work, the Trp engaged in π-π stacking interactions with an aromatic ring of the stabilizers. By contrast, the +2 Pro of FOXO1 locked the conformation of the +1 Trp and thereby prevented such a π-π stacking interaction with **2**, while the +2 Arg of Pin-1 allowed π-π stacking

to take place. Thus, while the compound **2**/**3** scaffold emphasized the chemical moieties necessary for stabilizing FOXO1, crystal structures also expose a lack of flexibility of the FOXO1 peptide.

CRAF Selective Stabilizers

Following FOXO1, CRAF had the highest number of stabilizers. Of the 21 initial CRAF stabilizers, 16 compounds showed selectivity for the 14 3 3σ/CRAF phospho-peptide complex over *apo* 14-3-3σ and the other phospho-peptide clients in the primary screen (Figure 3.2D). Eleven compounds showed a similar scaffold which was remarkably analogous to the conserved scaffold for the FOXO1 stabilizers (Figure S3.12). However, the linker element of these compounds was often longer in the case for CRAF, and the phenyl ring was decorated with large cyclic groups while for FOXO1 only smaller halogen groups were tolerated. This is likely due to the smaller +1 residue of CRAF (Thr for CRAF, Trp for FOXO1), thereby leaving more space for the compound. Furthermore, two CRAF stabilizers were shared with ERα, both of which have a similar size in +1 residue (Val for ERα, Thr for CRAF). Nine of the 16 selective compounds were validated for potency and selectivity in the MSDR (Figure S3.13). Four of the nine compounds (compounds **5**-**8**; Figure 3.5A) showed activity in FADR (Figure S14 and Table S3) and stabilization in the protein titrations (Table 3.3 and Figure S3.15).

Compounds **5** and **6** were the most effective stabilizers. Compound **5** had a DR_{50} value >3,000-fold lower in the presence of the CRAF peptide compared to 14-3-3σ alone (Figure 3.5B) and showed a 246-fold stabilization of the 14-3-3σ/CRAF phospho-peptide complex (K_D = 23 μM to 92 nM; Figure 3.5C). Compound 6 had a DR_{50} value 230-fold lower in the presence of CRAF compared to *apo* 14-3-3σ and a 426-fold stabilization of the 14-3-3σ/CRAF complex (Table 3.3, Figure S3.13 and S3.15).

The crystal structure of **5** with CRAF and 14-3-3σ revealed a contact between the naphthalene ring of **5** and the +1 Thr residue of CRAF. The methyl group of **5** also seems

important for hydrophobic interactions with the +1 Thr residue of CRAF, at a distance of 3.8 Å (Figure 3.5D, Figure S3.16A). An overlay of the CRAF peptide in the presence of **5** with the *apo* CRAF peptide showed no change in conformation of the +1 Thr residue. In contrast, the +4 Val residue of the CRAF peptide changed conformation to make space for **5** (Figure 3.5E).

We also crystallized compound **7** as a representative of the other structural class of the selective CRAF stabilizers (Figure S3.16B). Compound **7** had a DR_{50} value >228-fold lower in the presence of the CRAF peptide than *apo* 14-3-3σ (Figure 3.5F) and was less selective for CRAF compared to **5** in the MSDR (Figure S3.13). However, compound **7** showed no stabilization of any of the peptides other than CRAF in the FADR (Figure S3.14C), reflecting the selectivity shown in the primary screen. The weaker 14-3-3σ binding of **7** (12.2 μM DR_{50}) was reflected in a somewhat lower stabilization of the 14-3-3σ/CRAF complex compared to the other chemotype of **5** and **6** (77-fold vs 246- and 426-fold, respectively; Figure 3.5G, Figure S3.15). Co-crystallization of **7** with CRAF and 14-3-3σ revealed a novel orientation of its phenyl ring towards the roof of 14-3-3σ, positioning its trifluoromethyl group above the CRAF peptide (Figure 3.5H). While the conformations of **5** and **7** were quite different, an overlay of the two structures shows that the trifluoromethyl group of **7** occupied the same cavity as the naphthalene ring of **5** (Figure S3.16C). Furthermore, an overlay of the CRAF peptide in the presence of **7** with the *apo* CRAF peptide revealed a conformational change of the +4 Val of CRAF, which stacked against the compound, pushing it towards 14-3-3σ. Additionally, a water-mediated hydrogen bond was formed between **7** and the backbone of CRAF peptide (Figure 3.5I). The lower specificity for CRAF of **7** in the MSDR could be due to its small size, leaving room for alternative +1 residues to have a cooperative effect on 14-3-3σ engagement. Stabilizer 8 had an almost identical structure to **7**, differing only in a chloro-group in the para-position of the phenyl ring, and showed similar binding modes to **7** in its structure with CRAF (Figure S3.16D and E).

Next to these CRAF selective stabilizers, the non-selective stabilizer compound **1** also showed a large fold-stabilization towards the CRAF peptide (Figure 3.3). A crystallographic overlay of these three scaffolds revealed remarkable differences in conformation of the CRAF/compound interactions (Figure S3.16F). These changes highlight the flexibility of the CRAF peptide, perhaps leading to its facility for stabilization, especially in the case of the stabilizers' phenyl ring, which can occupy a wide range of positions and conformations in combination with the CRAF client phospho-peptide.

Conclusions

Systematic methods to discover small-molecule stabilizers of PPI would enable chemical biologists to probe challenging biological systems with potency and precision. By trapping proteins in complexes, stabilization can target proteins with intrinsically disordered regions and allow manipulation of a specific PPI from among related hub protein complexes within a network. Disulfide tethering, a powerful FBDD technique, is readily tunable to a specific site on a protein of interest, amenable to HTS, and provides a direct quantitative measurement of fragment binding.

Here, we explored the scope of the disulfide tethering technology using the hub protein 14-3-3σ and 5 biologically and structurally diverse phospho-peptides derived from the 14-3-3 client proteins ERα, FOXO1, CRAF, USP8, and SOS1. Of the 1600 fragments in the disulfide library, 62 showed activity as stabilizers for one or more phospho-peptides and were assessed by MSDR. 36 of the 62 compounds were taken forward into the FADR assays to determine stabilization of a 14-3-3 client phospho-peptide. Finally, eight compounds showed cooperativity with the 14-3-3σ/phospho-peptide complex via 14-3-3σ protein titrations, and six were structurally characterized for their contacts with 14-3-3σ and the client phospho-peptide via x-ray crystallography (Figure S3.17A). Thus, the disulfide tethering strategy systematically discovered stabilizers for a range of peptide sequences, conformations, and affinities.

Of the 5 peptide targets selected, we discovered stabilizers for four clients, two of which also had selective stabilizers. Fragments increased binding affinity of the 14-3-3σ/phospho-peptide complex as much as 430-fold in the case of **6** and 250-fold for our best structurally characterized hit, **5**. Selective stabilizers distinguished between phospho-peptide clients due to the unique composite binding surface created by the phospho-peptide/14-3-3σ interface (Figures 3.4 and 3.5). The non-selective stabilizers also showed varying degrees of efficacy in stabilizing different clients. Compound **1** facilitated a greater than 80-fold shift in affinity for CRAF, a 19-fold shift for ERα, a more modest 4-fold shift for USP8, but had no effect on SOS1 and FOXO1 (Figure 3.3).

The individual phospho-peptide binding motifs and C-terminal residues following the phosphorylation site create a distinct environment around the 14-3-3σ C38 fragment binding pocket, dictating what chemical moieties effectively facilitated cooperativity between 14-3-3σ, the phospho-peptide client, and the fragments. The stabilizers for FOXO1 had a highly conserved scaffold, consistent with the rigidity of this peptide (Figure S3.17B). In contrast, the stabilizers of CRAF were larger and showed more chemical diversity in their scaffold, emphasizing the flexibility of the CRAF peptide. The short ERα peptide resulted in limited selectivity, sharing many stabilizers with CRAF. Lastly, USP8 and SOS1 were the hardest to target, likely due to the proximity of the peptide C-terminus to C38 of 14-3-3σ, which was also reflected in the small scaffold of the discovered stabilizers from the primary screen (Figure S3.17B). Alternative cysteine tethering mutations could sample different sub-pockets to stabilize peptides which occupy more of the 14-3-3 binding groove. Taken together, the intrinsic diversity of the 14 3 3/phospho-peptide composite binding interface allowed for selectivity and precision when targeting a specific 14-3-3/client PPI.

While the focus of the screen was the discovery of fragment stabilizers, the screen also identified selective inhibitors, non-selective inhibitors, and neutral compounds for each client

peptide and 14-3-3 (Figure S3.18). Therefore, disulfide tethering is a versatile tool that can be expanded to meet a wide range of conditions and results in hits that disrupt or stabilize PPIs. 14-3-3 provides an exciting proof of concept due to its large roster of clients, involvement in many biological processes, therapeutic potential, and extensive structural data, but the applicability of FBDD reaches beyond targeting a singular protein. It is due to this ease of access and applicability that disulfide tethering lends itself to the discovery of biological probes for PPIs and novel therapeutics for previously inaccessible biological challenges and diseases related to intrinsically disordered proteins.

Figures

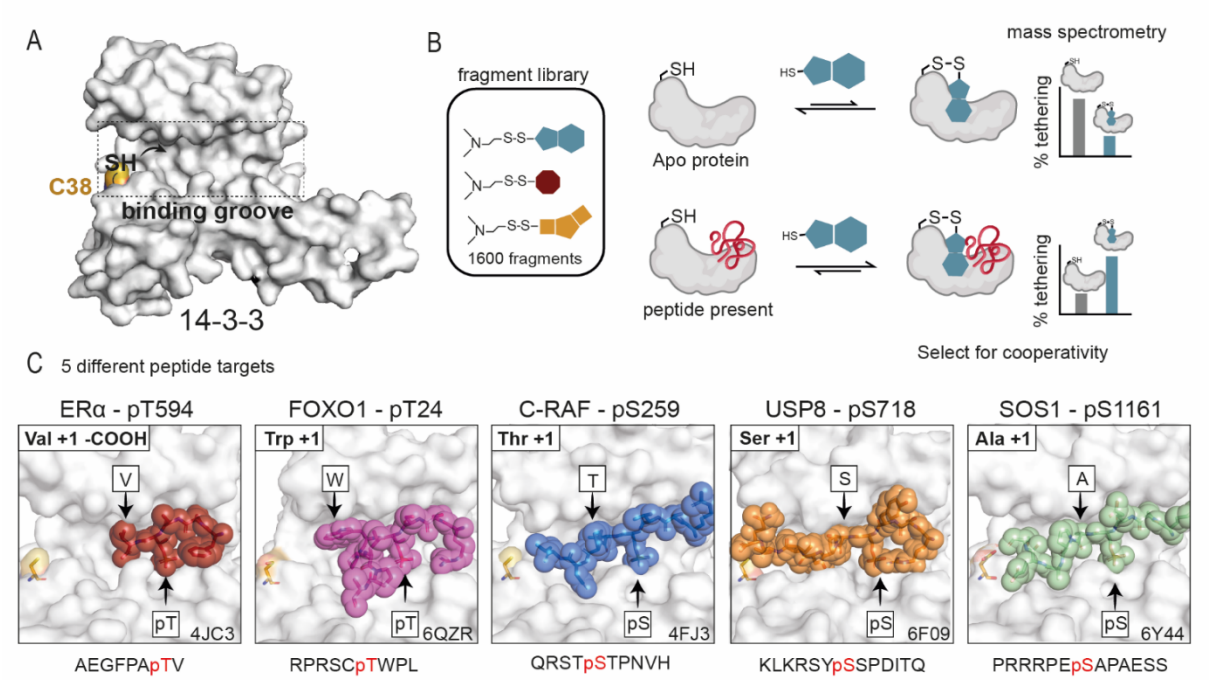

Figure 2.1: 14-3-3/client stabilizer approach
A) The client protein binding groove of a 14-3-3σ monomer (white surface) highlighting the native cysteine (C38; yellow surface) and target thiol. **B)** General schematic of the primary disulfide tethering screen. Fragments were incubated with *apo* 14-3-3σ (white) without any phospho-peptide (top) and 14-3-3σ with the phospho-peptide client present (bottom). Fragments were assessed for their covalent engagement of C38 via mass spectrometry, termed "% tethering". Fragments that bind 14-3-3σ with a higher % tethering in the presence of phospho-peptide than in the *apo* screen are selected for further analysis of cooperativity. **C)** Crystallographic structures of the 5 phospho-peptide clients bound in the 14-3-3σ (white surface) binding pocket showing proximity to C38 (yellow surface). ERα (red sticks) has a C-terminal motif with phospho-threonine (pT) in the penultimate position and C-terminal valine (V) in the +1 position. FOXO1 (pink sticks) has a curved motif with tryptophan (W) in +1 position. CRAF (blue sticks), USP8 (orange sticks), and SOS1 (green sticks) extend to various degrees into the 14-3-3 binding groove, with threonine (T), serine (S), and alanine (A) residues in the +1 position, respectively. PDB left to right: 4JC3, 6QZR, 4FJ3, 6F09, 6Y44.

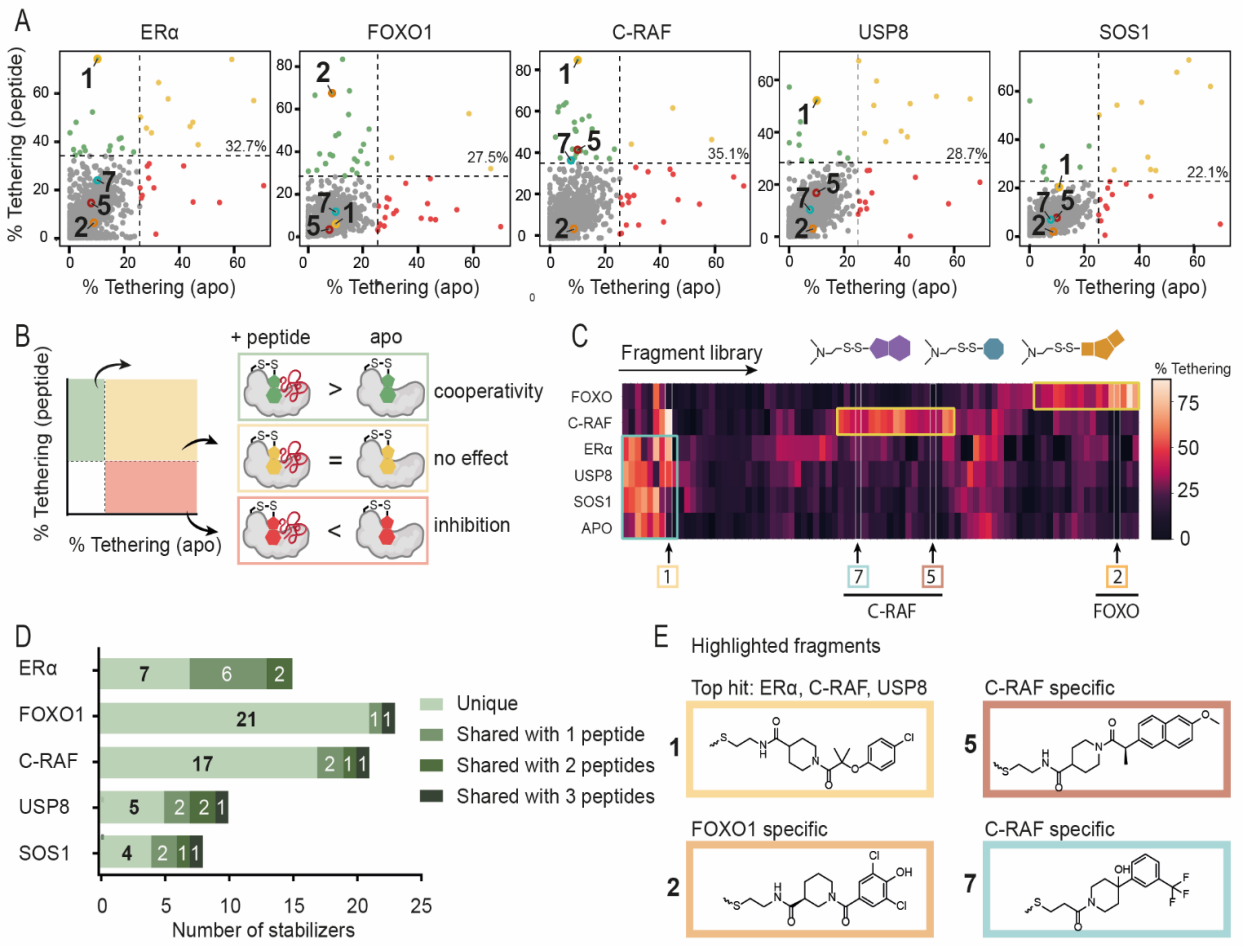

Figure 2.2: Primary tethering screen results

A) Scatterplot data illustrating the correlation of % tethering of fragments to 14-3-3σ in the presence of the phospho-peptide (y-axis) as compared to *apo* 14-3-3σ (x-axis). Hit selection threshold (mean + 3*SD) in each screen is indicated by a black dashed line. Compounds **1**, **2**, **5** and **7** are indicated as yellow, orange, red and cyan circles, respectively. **B)** Schematic of compound scatterplots. Quadrants are outlined by dotted lines signifying 3*SD above average % tethering for compounds in the presence of phospho-peptide (horizontal line) and *apo* 14-3-3σ (vertical line). Compounds in green quadrant showed increased binding to 14-3-3σ in the presence of phospho-peptide, yellow quadrant showed neutral binding to 14-3-3σ, and red quadrant showed a reduced binding in presence of phospho-peptide. **C)** Heat map of hit fragments across all 5 phospho-peptide screens and *apo* 14-3-3σ screen. Compounds clustered based on % tethering in each screen. Compounds **1**, **2**, **5** and **7** were of primary interest as non-selective and selective stabilizers. (D) Number of stabilizers of each peptide that were: unique, shared with one other peptide, shared with two other peptides, or shared with three other peptides (green bars with the darker color shared with more peptides). (E) Chemical structures of highlighted fragment hits **1**, **2**, **5**, and **7**.

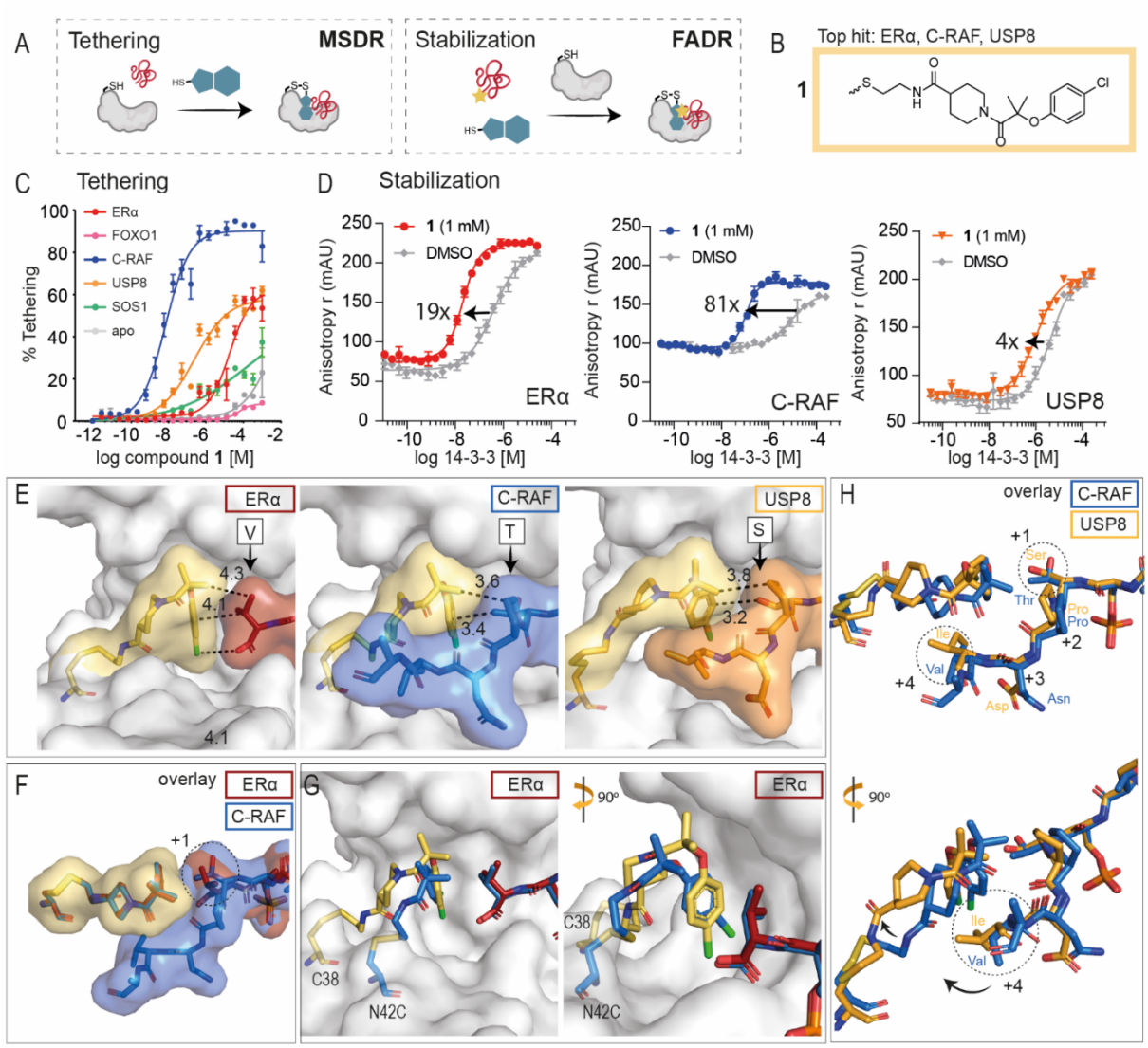

Figure 2.3: Overview of biochemical and structural properties of non-selective stabilizer 1
A) In mass spec dose response (MSDR), the focus was on compound binding to 14-3-3σ, measured by % tethering; fluorescence anisotropy dose response (FADR) experiments determined degree of stabilization, measured by phospho-peptide binding to 14-3-3σ in presence of compound. **B)** Chemical structure of stabilizer **1**. **C)** MSDR curves for **1** showing percentage of fragment/protein conjugate formation with 14-3-3σ *apo,* or in the presence of ERα, FOXO1, CRAF, USP8 or SOS1 peptide. **D)** 14-3-3σ titrations to fluorescein-labeled ERα, CRAF or USP8 in the presence of DMSO or **1** (1 mM), reporting a 19-, 81-, and 4-fold increase of the 14-3-3σ/peptide binding interface, respectively. **E)** Crystal structure of **1** bound to 14-3-3σ C38 in complex with (from left to right) ERα peptide, CRAF peptide, and USP8 peptide. Distances are indicated (Å, black dashes). **F)** Overlay of **1's** conformations when interacting with ERα and CRAF. **G)** Overlay of **1** (yellow) bound to 14-3-3σ C38 and previously reported stabilizer (blue) bound to 14-3-3σ mutant N42C (PDB ID: 6HMT) interacting with ERα phospho-peptides. **H)** Overlay of **1** bound to 14-3-3σ C38 interacting with CRAF and USP8.

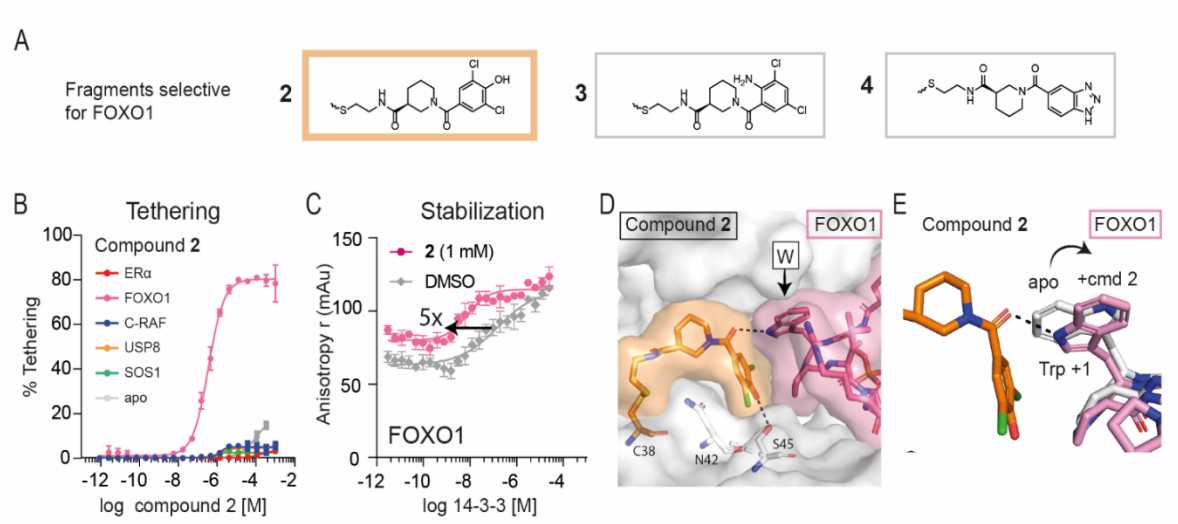

Figure 2.4: Overview of selective stabilizers for FOXO1
A) Chemical structures of highlighted FOXO1 selective stabilizers **2**-**4**. **B)** MSDR curves for **2** showing percentage of fragment/protein conjugate formation with 14-3-3σ *apo*, or in the presence of ERα, FOXO1, CRAF, USP8 or SOS1 peptide. **C)** 14-3-3σ titrations to fluorescein-labeled FOXO1 in the presence of DMSO or **2** (1 mM), reporting a 5-fold increase in 14-3-3σ/FOXO1 binding. **D)** Crystal structure of **2** (orange) bound to 14-3-3σ (white) C38 in complex with FOXO1 phospho-peptide (pink). **E)** Overlay of FOXO1 peptide in the apo-structure (white) with the FOXO peptide (pink) in presence of **2** (orange).

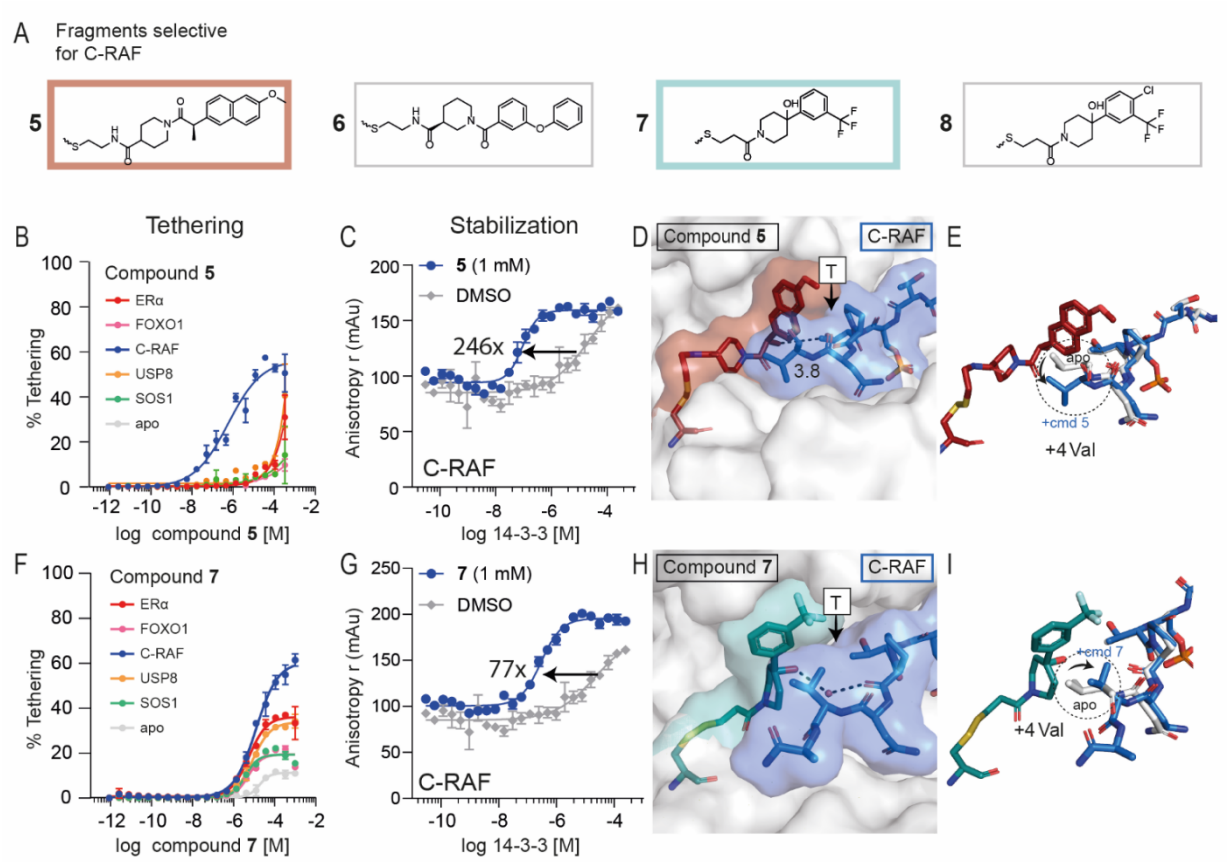

Figure 2.5: Overview of selective stabilizers for CRAF

A) Chemical structures of highlighted CRAF selective stabilizers **5-8. B)** MSDR curves for **5** showing percentage of fragment/protein conjugate formation with 14-3-3σ apo, or in the presence of ERα, FOXO1, CRAF, USP8 or SOS1 peptide. **C)** 14-3-3σ titration to fluorescein-labeled CRAF in the presence of DMSO or **5** (1 mM), reporting a 246-fold increase of 14-3-3σ/CRAF binding. **D)** Crystal structure of **5** (red) bound to 14-3-3σ (white) in complex with CRAF phospho-peptide (blue). **E)** Overlay of CRAF peptide in the apo-structure (white) with the CRAF peptide (blue) in presence of **5** (red). **F)** MSDR curves for **7** showing percentage of fragment/protein conjugate formation with 14-3-3σ apo, or in the presence of ERα, FOXO1, CRAF, USP8 or SOS1 peptide. **G)** 14-3-3σ titration to fluorescein-labeled CRAF in the presence of DMSO or **7** (1 mM), reporting a 77-fold increase of 14-3-3σ/CRAF binding **H)** Crystal structure of **7** (teal) bound to 14-3-3σ (white) in complex with CRAF phospho-peptide (blue). **I)** Overlay of CRAF peptide in the apo-structure (white) with the CRAF peptide (blue) in presence of **7** (teal).

Tables

Table 2.1: Tethering and stabilization of 14-3-3σ/clients by compound 1

	MSDR (250 μM BME)	FADR (50 μM BME)	Protein Titrations (50 μM BME)		
Peptide	**DR_{50} (μM)**	**EC_{50} (μM)**	**K_{D_app}**	**K_{D_DMSO}**	**Fold Stab.**
CRAF	0.007	0.922	106 nM	8.5 μM	81
ERα	18.1	1.31	21 nM	360 nM	19
USP8	0.024	3.38	1.1 μM	4.5 μM	4
SOS1	>2 mM	>2 mM	N/A	N/A	N/A
FOXO1	>2 mM	>2 mM	N/A	N/A	N/A
apo	>2 mM	>2 mM	N/A	N/A	N/A

Table 2.2: Properties of selective FOXO1 stabilizers

	MSDR (250 μM BME)	FADR (50 μM BME)	Protein Titrations (50 μM BME)		
Cmpnd	**DR_{50} (μM)**	**EC_{50} (μM)**	**K_{D_app}**	**K_{D_DMSO}***	**Fold Stab.**
2	0.36	5.10	7.7 nM	39 nM	5
3	2.2	N/A	10.6 nM	42 nM	4
4	143	N/A	9.7 nM	111 nM	12

*K_D for peptide is accurate within 3-fold range. These values are shown on the same plate as protein titrations with compound.

Table 2.3: Properties of selective CRAF stabilizers

	MSDR (250 μM BME)	FADR (50 μM BME)	Protein Titrations (50 μM BME)		
Cmpnd	**DR_{50} (μM)**	**EC_{50} (μM)**	**K_{D_app}**	**K_{D_DMSO}***	**Fold Stab.**
5	0.58	0.22	92 nM	23 μM	246
6	8.78	1.33	100 nM	42 μM	426
7	12.2	3.18	294 nM	23 μM	77
8	3.71	13.5	207 nM	23 μM	110

*K_D for peptide is accurate within 3-fold range. These values are shown on the same plate as protein titrations with compound.

Supplementary Figures

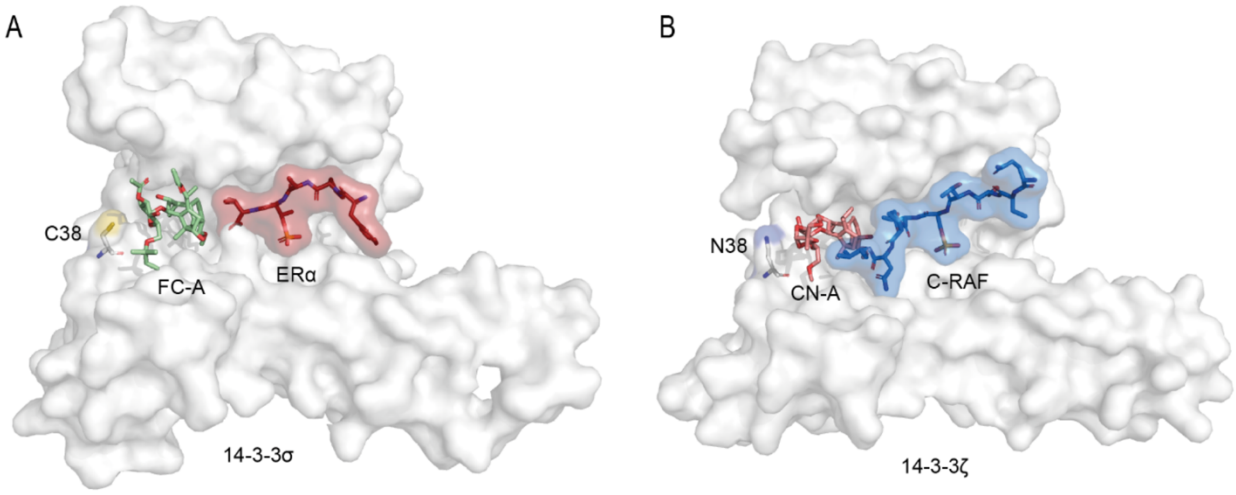

Figure S2.1: Crystal structures of natural product stabilizers
A) Fusicoccin-A (green sticks) and **B)** Cotylenin-A (pink sticks) bound to 14-3-3 (white surface) and clients ERα (red sticks) and CRAF (blue sticks), respectively. Cysteine 38 depicted as white sticks. PDB ID: 4JDD and 4IHL.

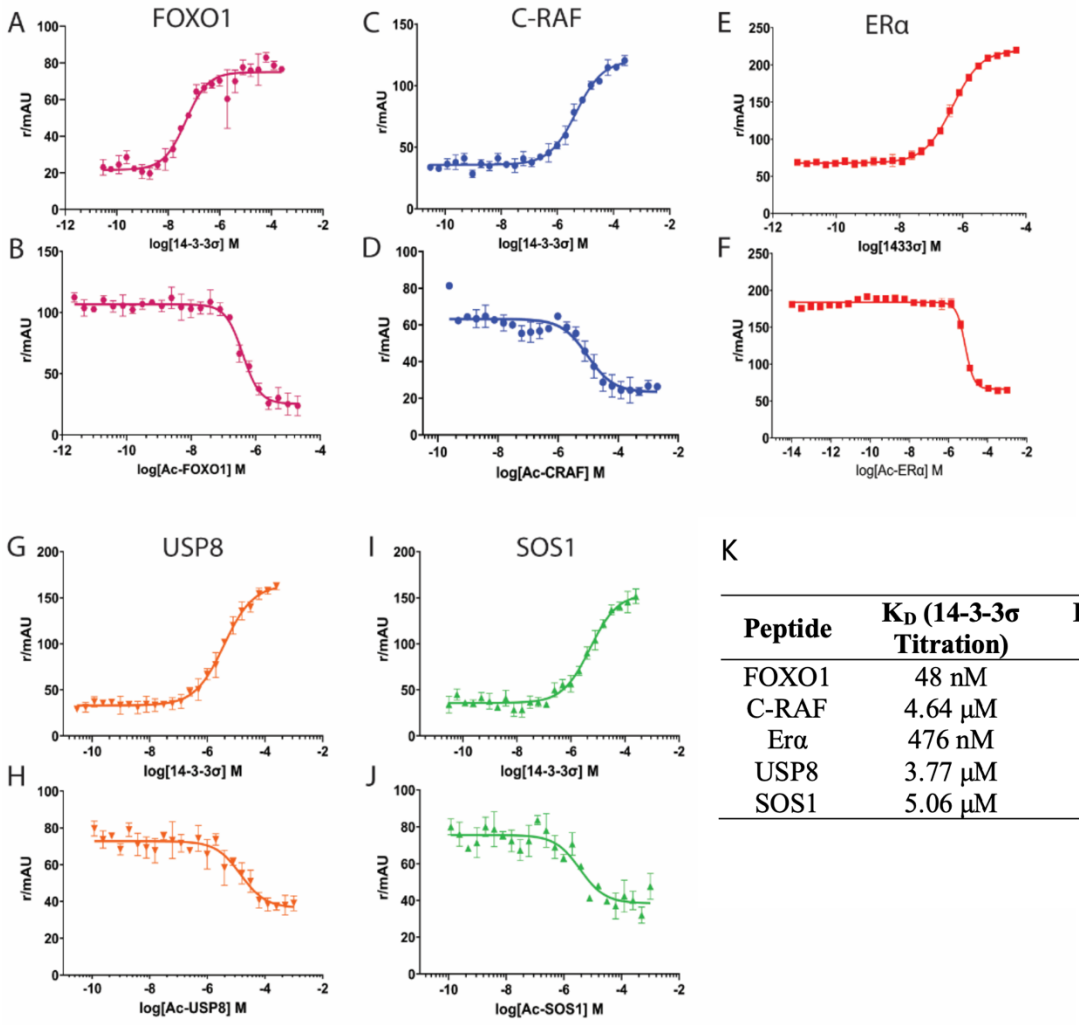

K

Peptide	K_D (14-3-3σ Titration)	K_i (Ac-peptide competition)
FOXO1	48 nM	396 nM
C-RAF	4.64 μM	9.50 μM
Erα	476 nM	7.10 μM
USP8	3.77 μM	14.3 μM
SOS1	5.06 μM	3.66 μM

Figure S2.2: 14-3-3σ/phosphopeptide binding curves

A) Protein titration with 14-3-3σ in presence of 100 nM FITC-labeled FOXO1 11-mer peptide determined K_D. **B)** Competition assay used to determine K_i of acetylated FOXO1 11-mer peptide (Ac-FOXO1) for mass spectrometry experiments. Ac-FOXO1 was titrated from high to low concentration in presence of 100 nM FITC-FOXO1 peptide and 14-3-3σ at 3/2 K_D value determined in (A). **C)** Protein titration with 14-3-3σ in presence of 100 nM FITC-labeled CRAF 36-mer peptide determined K_D. **D)** Competition assay used to determine K_i of acetylated CRAF 11-mer peptide (Ac-CRAF). **E)** Protein titration with 14-3-3σ in presence of 100 nM FITC-labeled ERα 15-mer peptide determined K_D. **F)** Competition assay used to determine K_i of acetylated ERα 15-mer peptide (Ac-ERα). **G)** Protein titration with 14-3-3σ in presence of 100 nM FITC-labeled USP8 13-mer peptide determined K_D. **H)** Competition assay used to determine K_i of acetylated USP8 13-mer peptide (Ac-USP8). **I)** Protein titration with 14- 3-3σ in presence of 100 nM FITC-labeled SOS1 13-mer peptide determined K_D. **J)** Competition assay used to determine K_i of acetylated SOS1 13-mer peptide (Ac-SOS1). **K)** Table of peptide affinities to 14-3-3σ based on data from A-J.

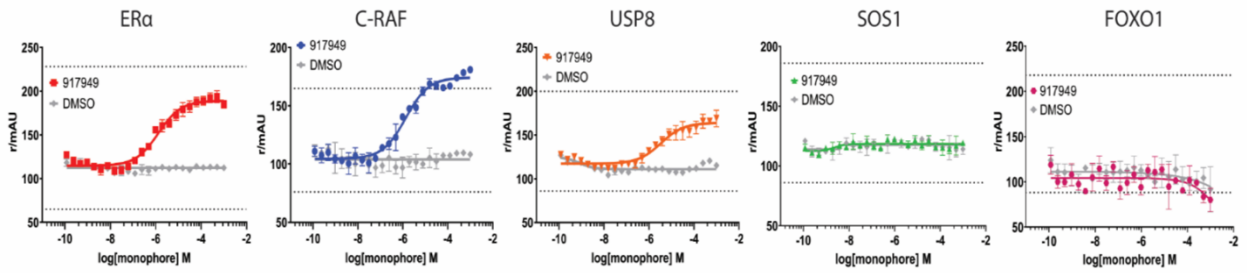

Figure S2.3: FADR curves for non-selective stabilizer 1
Top black dashed line signifies maximum anisotropy control, the value of which was determined by peptide bound to 250 μM 14-3-3σ (at least 50-fold excess of peptide K_D). Bottom dashed line signifies minimum anisotropy control, value determined by peptide only and no 14-3-3σ. From left to right: 917949 dose-dependent stabilization of ERα phospho-peptide (red) binding to 14-3-3σ; 917949 stabilization of CRAF (blue) binding to 14-3-3σ; 917949 stabilization of USP8 (orange) binding to 14-3-3σ. SOS1 (green) and FOXO1 (pink) showed no stabilization as compared to DMSO control (grey). From left to right EC_{50} values: 1.31 μM (ERα); 922 nM (CRAF); 3.38 μM (USP8); >2000 μM (SOS1); >2000 μM (FOXO1).

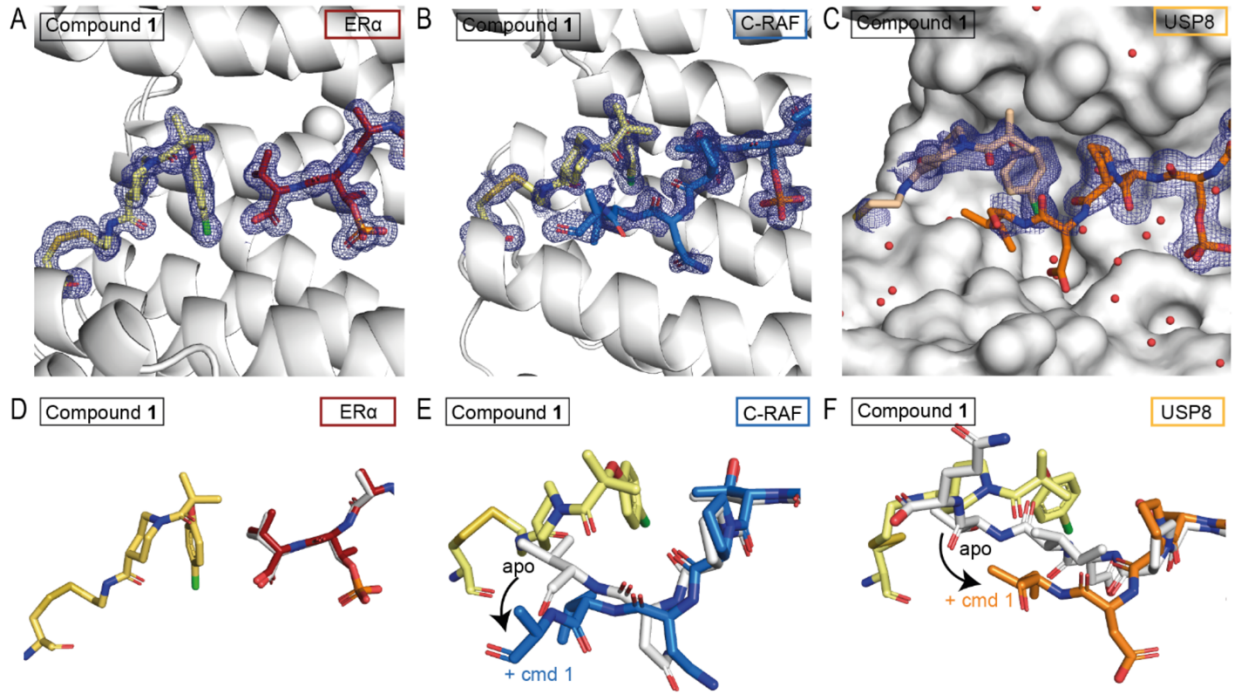

Figure S2.4: Crystal structures of Compound 1 bound to 14-3-3σ/client complexes
A-C) Crystal structures of Compound **1** (yellow sticks) with **(A)** ERα (red sticks) **(B)** CRAF (blue sticks) and **(C)** USP8 (orange sticks) complexed with 14-3-3σ (white cartoon and surface). **D-F)** Overlay of crystal structures of compound **1** (yellow sticks) – peptide complex with **(D)** ERα (red sticks when complexed with compound **1**, white sticks as apo), **(E)** C- RAF (blue sticks when complex with compound **1**, white sticks as apo), **(F)** USP8 (orange sticks when complexed with compound **1**, white sticks as apo). PDB ID apo structures: 4JC3, 4FJ3, 6F09. 2Fo-Fc electron density maps are contoured at 1σ.

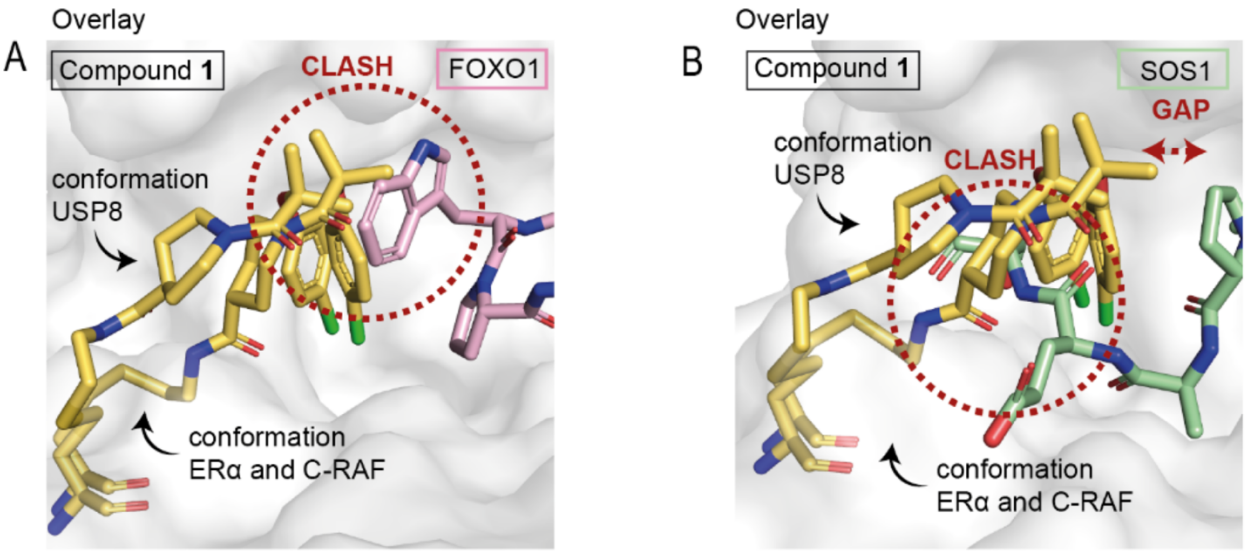

Figure S2.5: Overlays of compound 1 bound with different 14-3-3σ client peptides
Crystallographic overlay of compound **1** (yellow sticks) with **A)** FOXO1 (pink sticks) and **B)** SOS1 (green sticks) in 14-3-3 (white surface), highlighting the clash of compound **1** with these peptides. PDB ID apo structures: 6QZR and 6Y44.

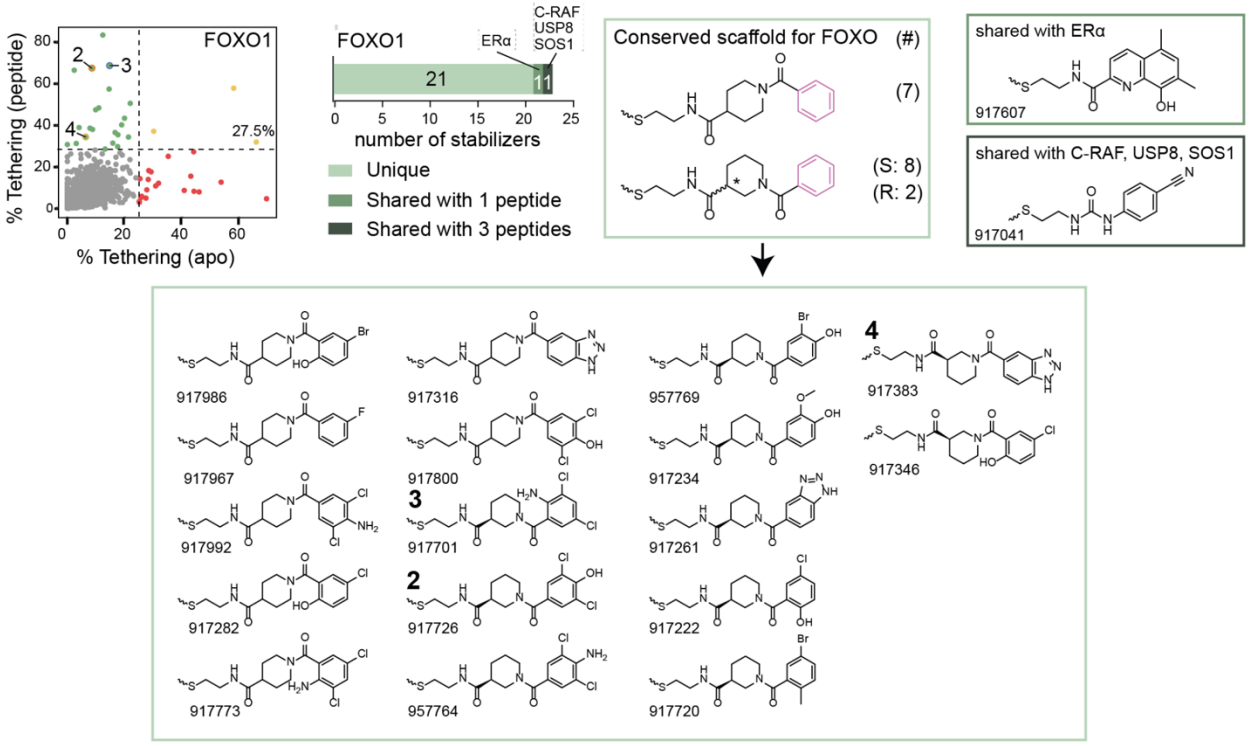

Figure S2.6: FOXO1 stabilizer structures
Scatter plot and chemical structures of the discovered stabilizers for FOXO1 from the primary screen, with in the light green box the unique stabilizers, the darker green box stabilizer shared with ERα and in the darkest green box the stabilizer shared with CRAF, USP8 and SOS1.

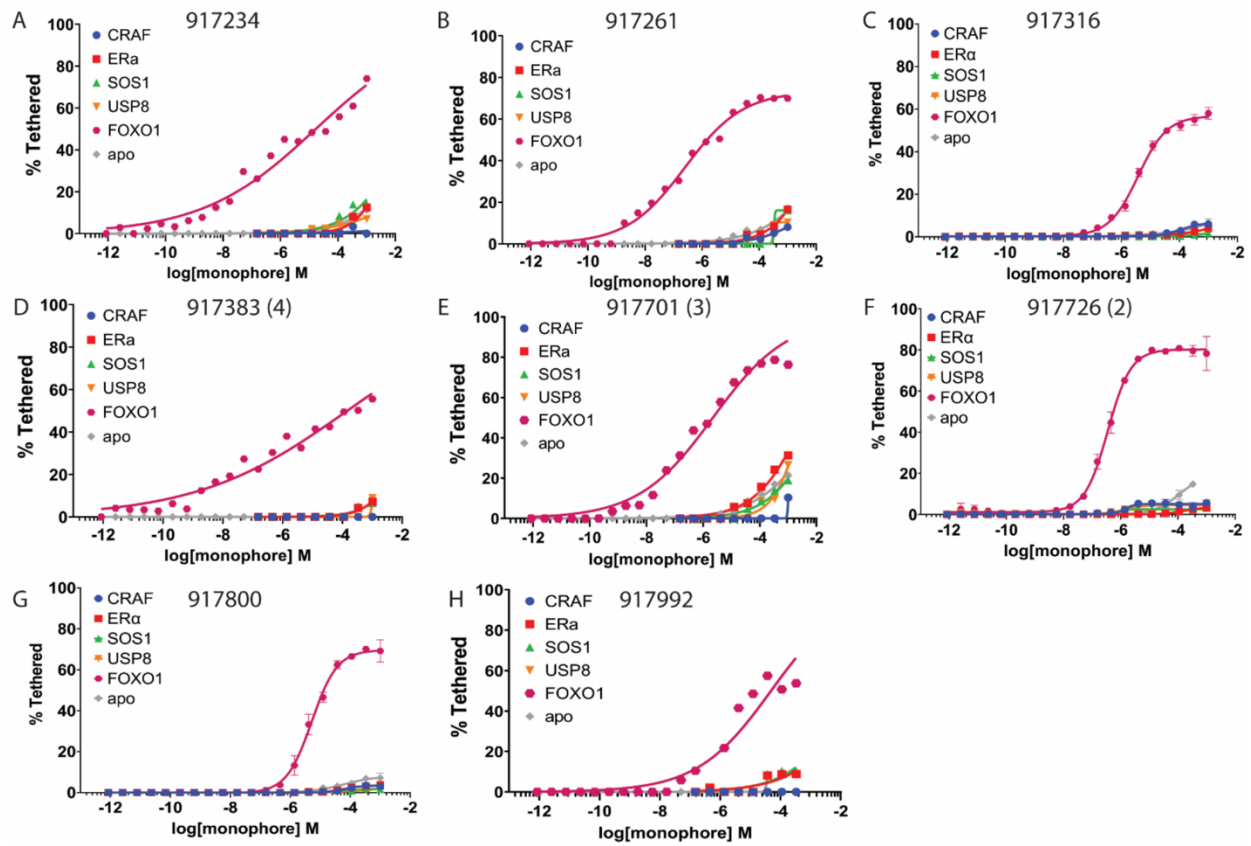

Figure S2.7: MSDR results for top FOXO1 selective stabilizers
A) MSDR for FOXO1 hit compound 917234 showing selectivity for FOXO1 over other four 14-3-3σ client phospho-peptides and *apo*. DR_{50}: 16.9 μM. **B)** MSDR for FOXO1 selective hit compound 917261. DR_{50}: 3.61 μM. **C)** MSDR for FOXO1 selective hit compound 917316. DR_{50}: 42 nM. **D)** MSDR for FOXO1 selective hit compound 917383 (compound **4** in main text). DR_{50}: 143.4 μM. **E)** MSDR for FOXO1 selective hit compound 917701 (compound **3** in main text). DR_{50}: 2.2 μM. **F)** MSDR for FOXO1 selective hit compound 917726 (compound **2** in main text). DR_{50}: 360 nM. **G)** MSDR for FOXO1 selective hit compound 917800. **H)** MSDR for FOXO1 selective compound 917992. DR_{50}: 48.7 μM.

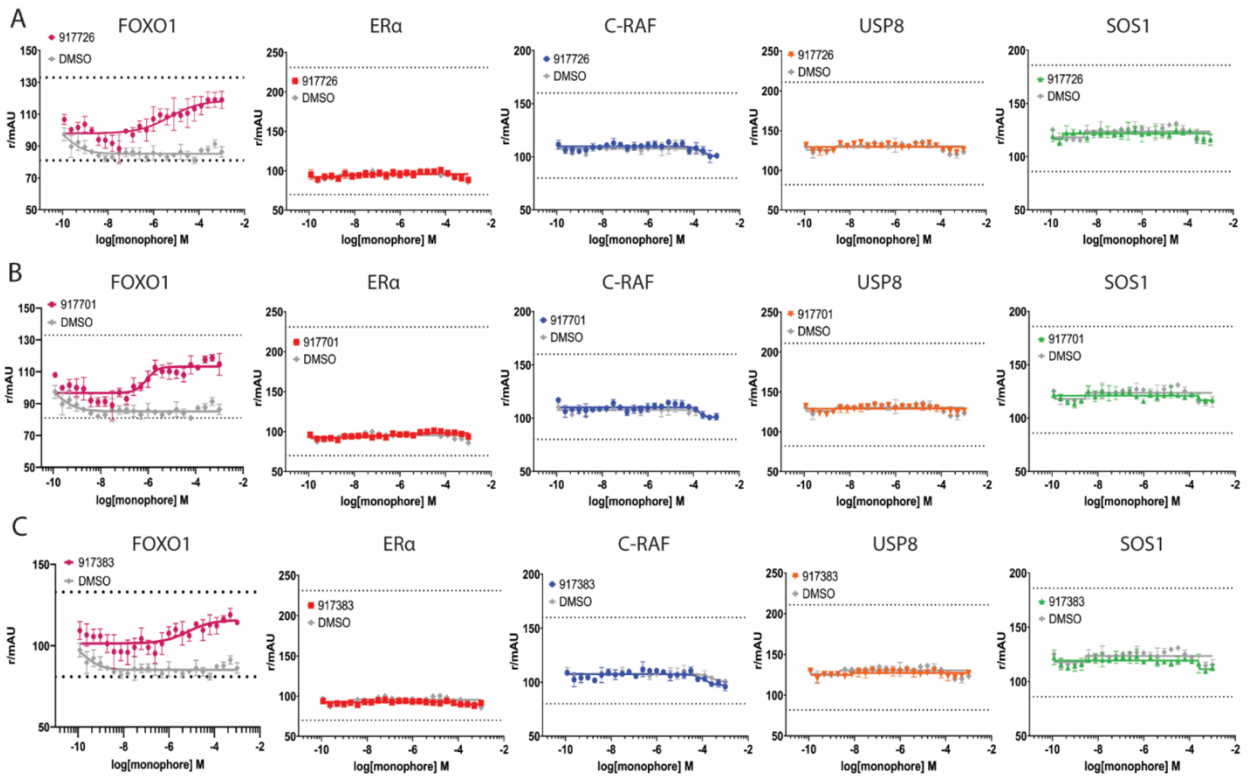

Figure S2.8: FADR for FOXO1 selective stabilizers
Fluorescence anisotropy dose response (FADR) curves for FOXO1 selective stabilizers 917726, 917701, and 917383 (compounds **2**-**4** in main text, respectively). Top black dashed line signifies maximum anisotropy control, the value of which was determined by peptide bound to 250 μM 14-3-3σ (at least 50-fold excess of peptide K_D). Bottom dashed line signifies minimum anisotropy control, value determined by peptide only and no 14-3-3σ. Controls were measured per plate. **A)** 917726 dose-dependent stabilization of FOXO1 phospho-peptide (pink) binding to 14-3-3σ. EC_{50} value with FOXO1: 5.1 μM. ERα (red), CRAF (blue), USP8 (orange), and SOS1 (green) showed no increase in anisotropy over DMSO control (grey) indicating no stabilization. **B)** 917701 stabilization of FOXO1 (pink) binding to 14-3-3σ. EC_{50} value with FOXO1: 850 nM. No increase stabilization over DMSO control (grey) observed for ERα (red), CRAF (blue), USP8 (orange), or SOS1 (green). **C)** 917383 stabilization of FOXO1 (pink) binding to 14-3-3σ. EC_{50} value with FOXO1: 6.69μM. No increase stabilization over DMSO control (grey) observed for ERα (red), CRAF (blue), USP8 (orange), or SOS1 (green).

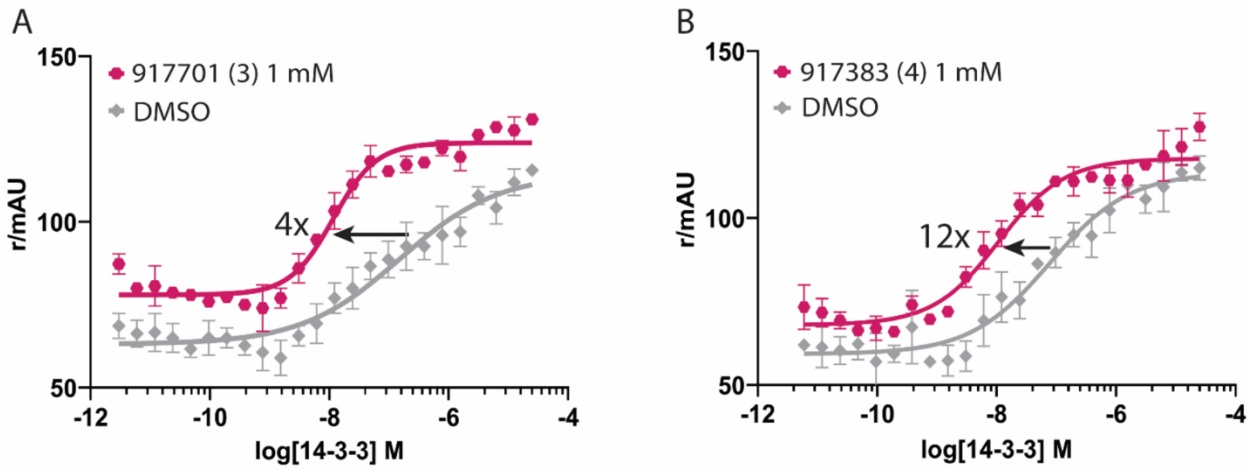

Figure S2.9: Fluorescence anisotropy protein titrations with selective compounds 2 and 3
Fluorescence anisotropy protein titrations for FOXO1 and CRAF selective stabilizers 917701 and 917383 (compounds **2** and **3** in main text, respectively. **A)** Addition of 1 mM 917701 (compound **3**; pink curve) resulted in 4-fold decrease in 14-3-3σ/FOXO1 K_D (10.6 nM vs. 42 nM) compared to DMSO control (grey curve). **B)** Addition of 1 mM 917383 (compound **4**; pink curve) resulted in 12-fold decrease in 14-3-3σ/FOXO1 K_D (9.7 nM vs. 111 nM) compared to DMSO control (grey curve).

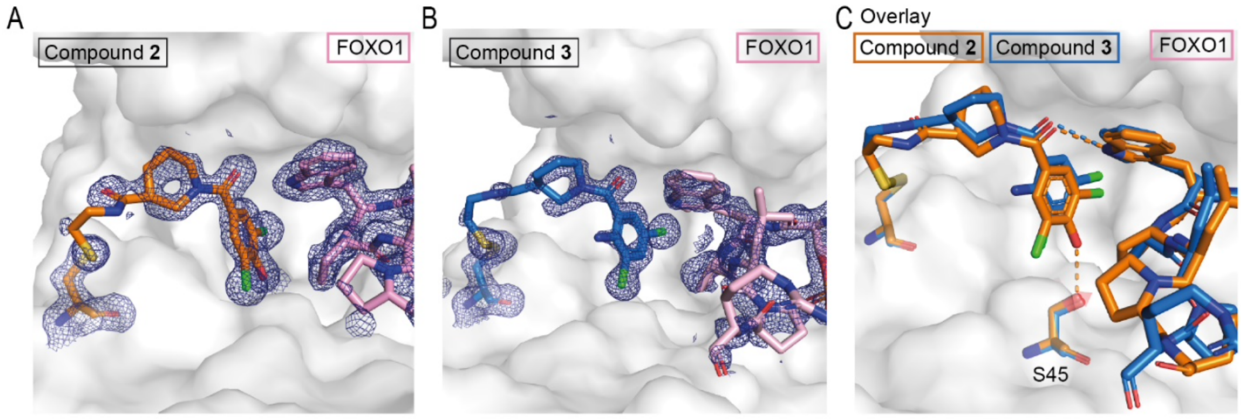

Figure S2.10: Comparison of compounds 1 and 2 binding to the 14-3-3σ/FOXO1 complex
Crystal structures of **A)** compound **2** (orange sticks) in complex with FOXO1 (pink sticks) and 14-3-3 (white surface) and **B)** compound **3** (blue sticks) with FOXO1 (pink sticks) and 14-3-3 (white surface). **C)** Crystallographic overlay of compound **2** (orange sticks) and compound **3** (blue sticks) with the FOXO1 peptide (peptide color matching compound complexed with) in 14-3-3 (white surface). Hydrogen interactions are depicted as orange dashed lines for compound **2** and blue dashed lines for compound **3**. 2Fo-Fc electron density maps are contoured at 1σ.

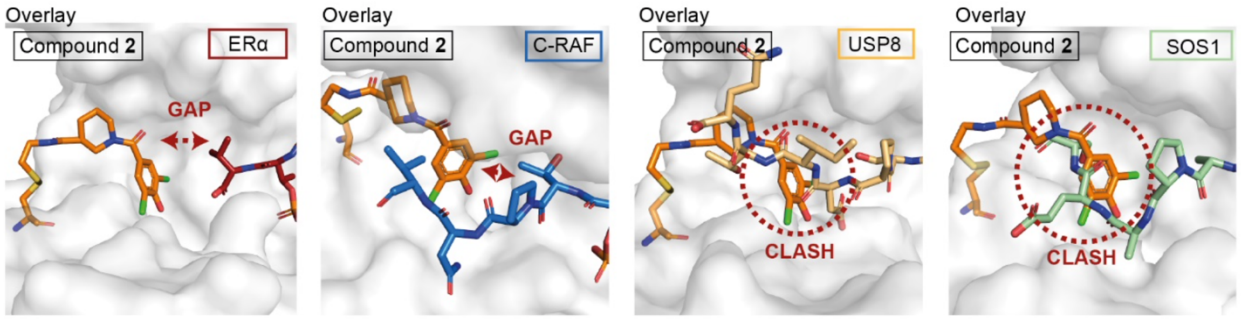

Figure S2.11: Crystallographic overlay of compound 2 with various 14-3-3σ clients
Crystallographic overlay of compound **2** (orange sticks) with ERα (red sticks), CRAF (blue sticks), USP8 (light orange sticks) and SOS1 (green sticks) in 14-3-3 (white surface). (PDB ID: 4JC3 (ERα), 4FJ3 (CRAF), 6F09 (USP8), 6Y44 (SOS1).

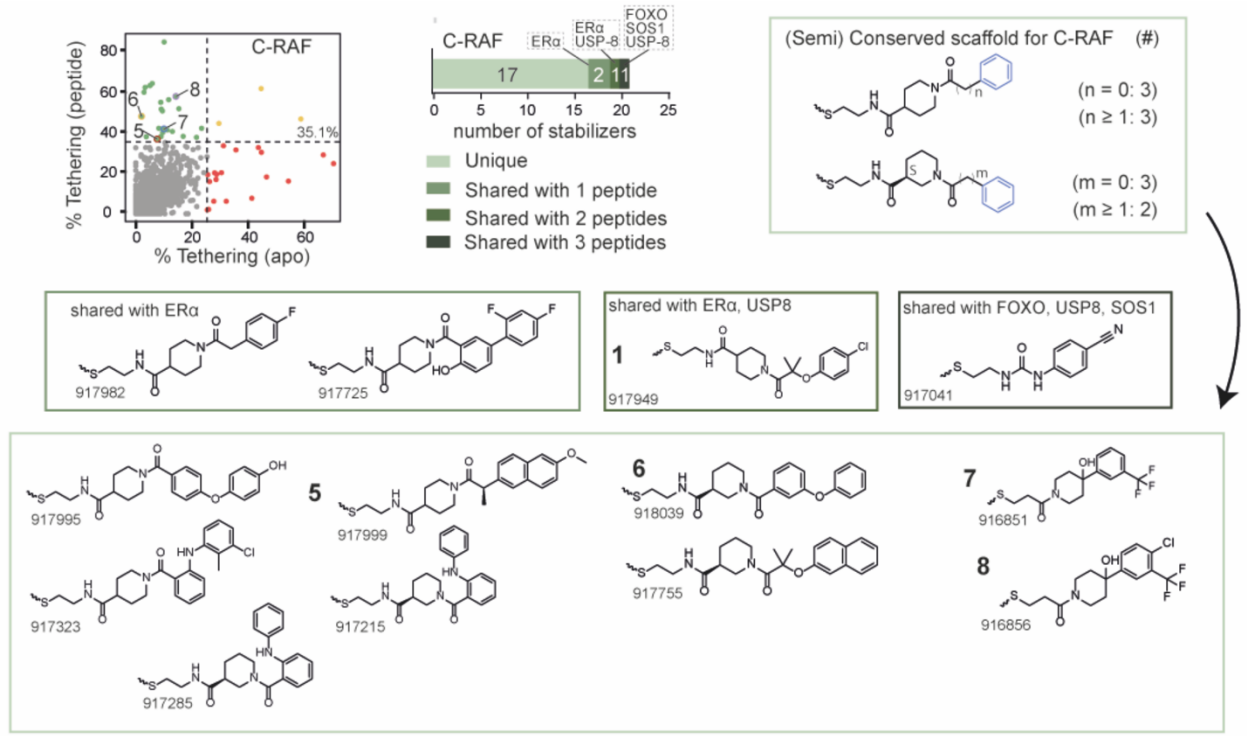

Figure S2.12: CRAF stabilizer structures
Scatter plot and chemical structures of the discovered stabilizers for CRAF from the primary screen, with in the light green box the unique stabilizers, in darker green box the stabilizers shared with ERα, in the darker green box shared with ERα and USP8 (= compound **1**) and in the darkest green box shared with FOXO1, USP8 and SOS1.

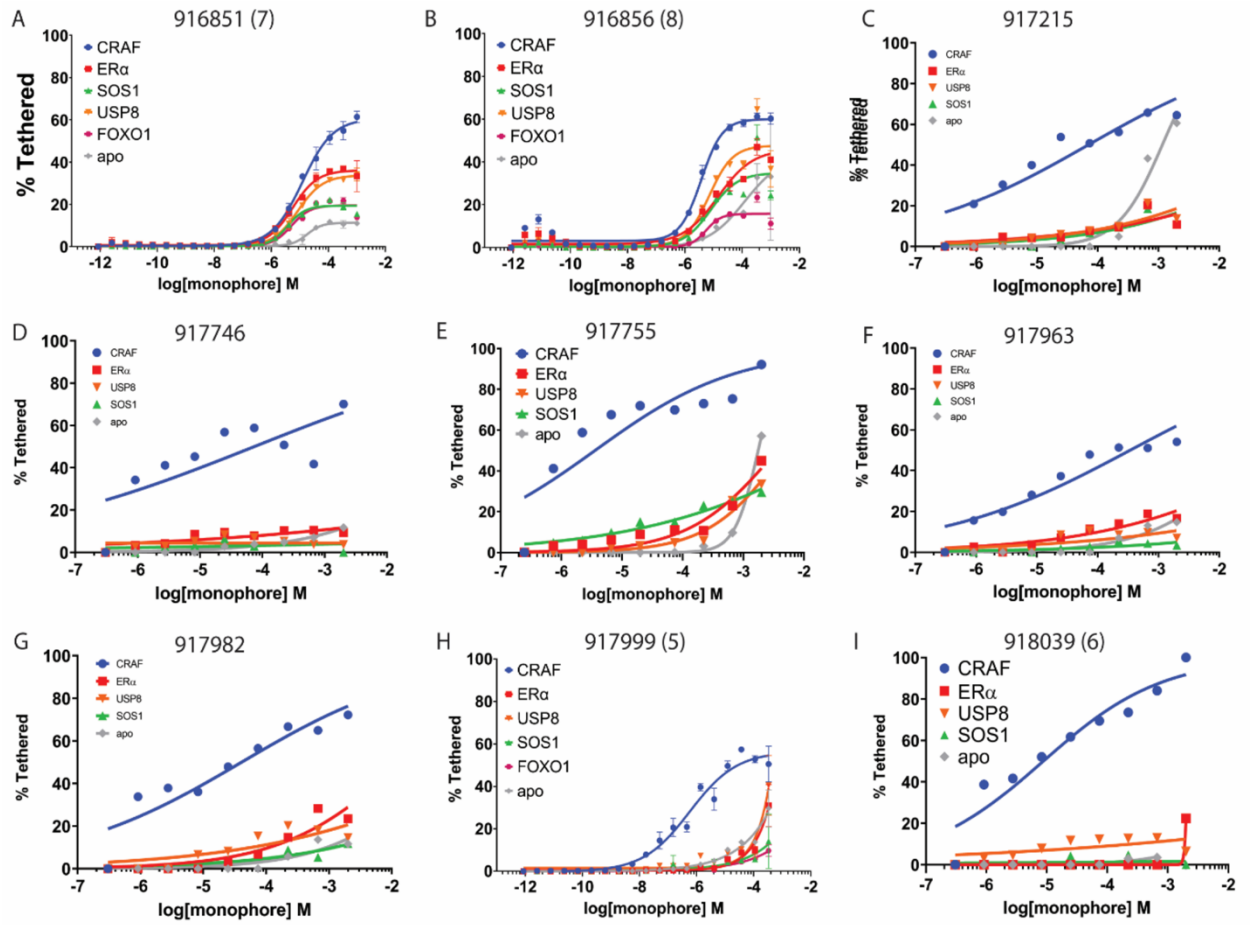

Figure S2.13: MSDR for CRAF selective stabilizers
Mass spectrometry dose response (MSDR) curves (blue) for top CRAF selective stabilizers. **A)** MSDR for CRAF hit compound 916851 (compound **7** in main text) showing preferential binding in presence of CRAF phospho-peptide over other four 14-3-3σ client phospho-peptides and *apo*. DR_{50} values: 12.2 μM (CRAF), 5.62 μM (ERα), 8.54 μM (USP8), >2000 μM (SOS1), >2000 μM (SOS1), >2000 μM (apo). **B)** MSDR for CRAF hit compound 916856 (compound **8** in main text). 916856 was also a hit stabilizer in ERα primary screen and shows dose dependent engagement of 14-3-3σ in MSDR. DR_{50} values: 4.96 μM (CRAF), 14.5 μM (ERα), 7.05 μM (USP8), >2000 μM (SOS1), >2000 μM (FOXO1), >2000 μM (apo). **C)** MSDR for CRAF selective hit compound 917215. DR_{50}: 5.1 μM. **D)** MSDR for CRAF selective compound 917746. DR_{50}: 910 nM. **E)** MSDR for CRAF selective compound 917755. DR_{50}: 5.82 μM. **F)** MSDR for CRAF selective compound 917963. DR_{50}: 5.29 μM. **G)** MSDR for CRAF selective compound 917982. DR_{50}: 5.45 μM. **H)** MSDR for CRAF selective hit compound 917999 (compound **5** in main text). DR_{50}: 580 nM. **I)** MSDR for CRAF selective hit compound 918039 (compound **6** in main text). DR_{50}: 8.78 μM.

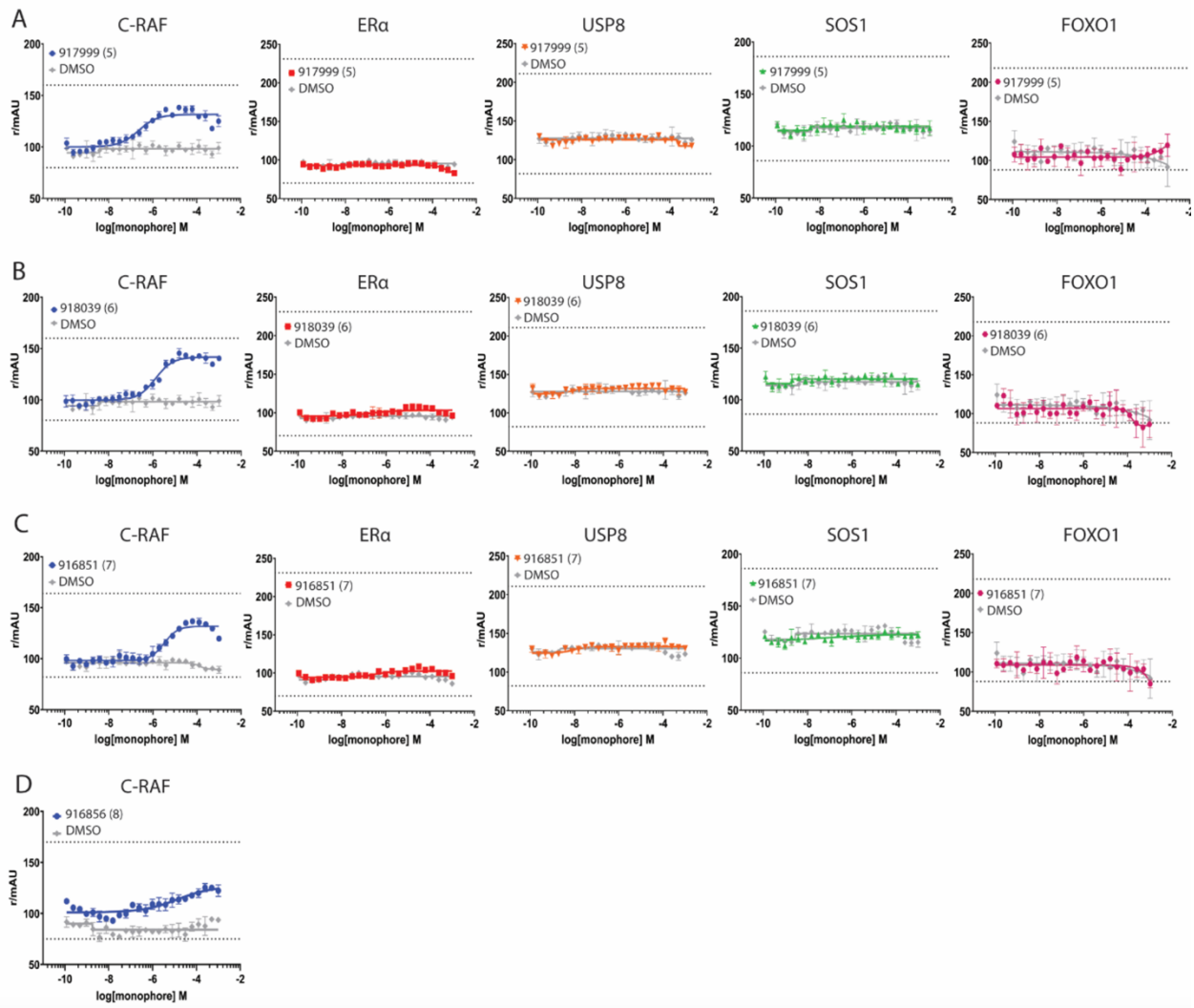

Figure S2.14: FADR for FOXO1 selective stabilizers

Fluorescence anisotropy dose response (FADR) curves for CRAF selective stabilizers 917999, 918039, 916851, and 916856 (compounds **5-8** in main text, respectively). Top black dashed line signifies maximum anisotropy control, the value of which was determined by peptide bound to 250 μM 14-3-3σ (at least 50-fold excess of peptide K_D). Bottom dashed line signifies minimum anisotropy control, value determined by peptide only and no 14-3-3σ. Controls were measured per plate. **A)** 917999 dose-dependent stabilization of CRAF phospho-peptide (blue) binding to 14-3-3σ. EC_{50} values with CRAF: 220 nM. ERα (red), USP8 (orange), SOS1 (green), and FOXO1 (pink) showed no increase in anisotropy over DMSO control (grey) indicating no stabilization. **B)** 918039 stabilization of CRAF (blue) binding to 14-3-3σ. EC_{50} value with CRAF: 1.33 μM. No increased stabilization over DMSO control (grey) observed for ERα (red), USP8 (orange), SOS1 (green), or FOXO1 (pink). **C)** 916851 stabilization of CRAF (blue) binding to 14-3-3σ. EC_{50} value with CRAF: 3.18 μM. No increased stabilization over DMSO control (grey) observed for ERα (red), USP8 (orange), SOS1 (green), or FOXO1 (pink). **D)** 916856 stabilization of CRAF (blue) binding to 14-3-3σ. EC_{50} value: 13.5 μM. Not sufficient compound for FADR with other peptides.

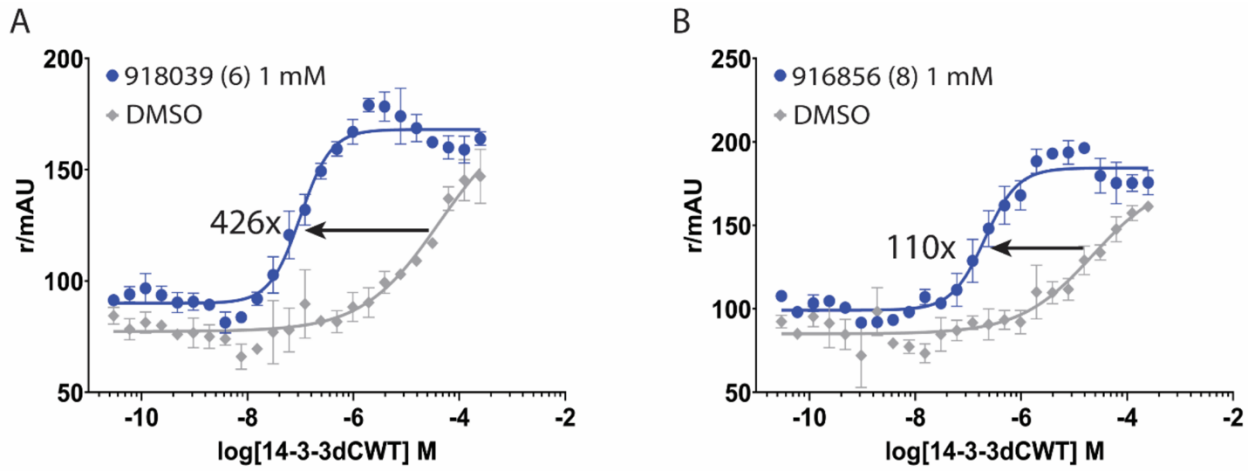

Figure S2.15: FA protein titrations with selective compounds 6 and 8
Fluorescence anisotropy protein titrations for FOXO1 and CRAF selective stabilizers 918039 and 916856 (compounds **6** and **8** in main text, respectively. **A)** Addition of 1 mM 918039 (compound **6**; blue curve) resulted in 426-fold decrease in 14-3-3σ/CRAF K_D (100 nM vs. 42 μM) compared to DMSO control (grey curve). **B)** Addition of 1 mM 916856 (compound **8**; blue curve) resulted in 110-fold decrease in 14-3-3σ/CRAF K_D (207 nM vs. 23 μM) compared to DMSO control (grey).

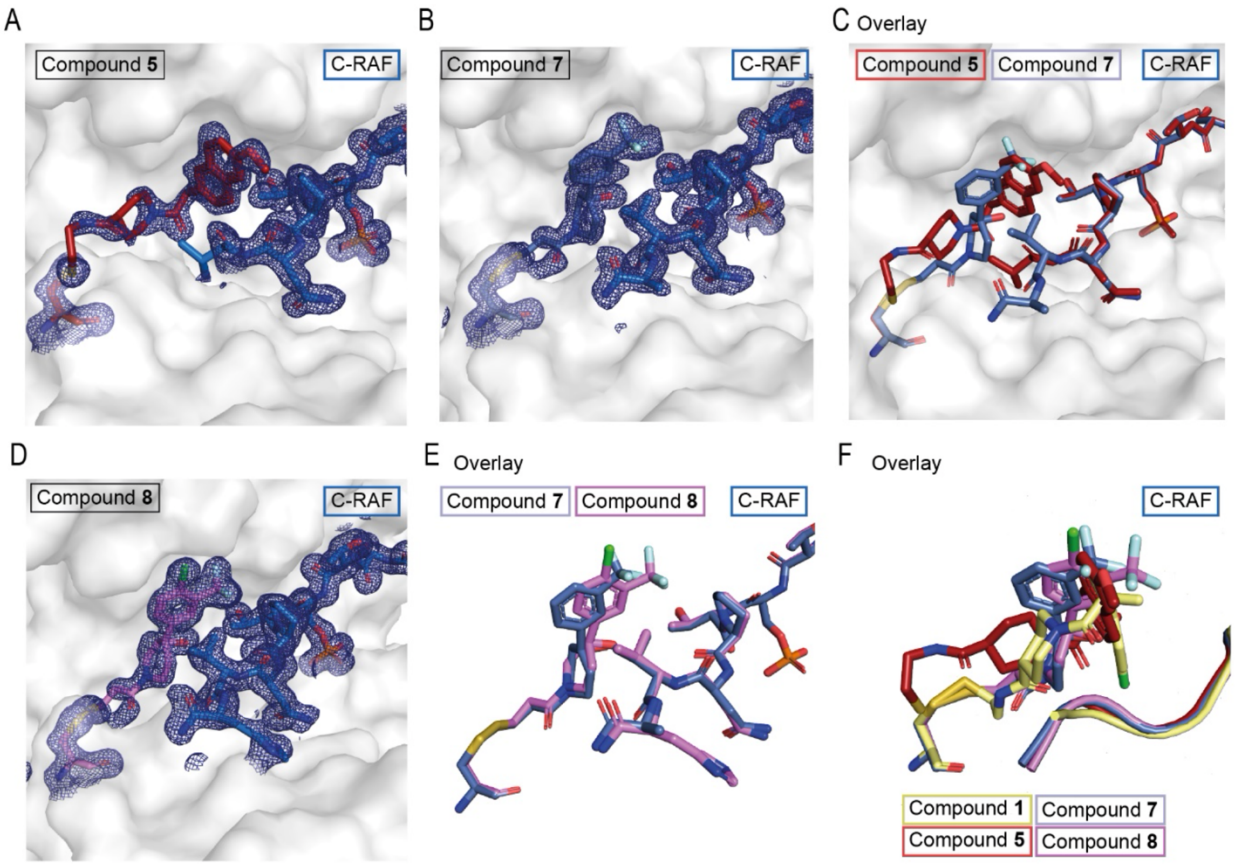

Figure S2.16: Crystal structures of CRAF stabilizers
A) Electron density of compound **5** (red sticks) complexed with C- RAF (blue sticks) in 14-3-3 (white surface). **B)** Electron density of compound **7** (light blue sticks) complexed with CRAF (blue sticks) in 14-3-3 (white surface). **C)** Crystallographic overlay of compound **5** (red sticks) and compound **7** (light blue sticks) with CRAF (color peptide matching the compound complexed with) in 14-3-3 (white surface). **D)** Electron density of compound **8** (violet sticks) with CRAF (blue sticks) in 14-3-3 (white surface). **E)** Crystallographic overlay of compound **7** (light blue sticks) and compound **8** (violet sticks) with CRAF (color peptide matching the compound. **F)** Crystallographic overlay of all crystallized stabilizers with CRAF with compound **1** (yellow sticks), compound **5** (red sticks), compound **7** (light blue sticks) and compound **8** (violet sticks) with CRAF represented as cartoon (color matching the compound complexed with) in 14-3-3 (white surface). 2Fo-Fc electron density maps are contoured at 1σ.

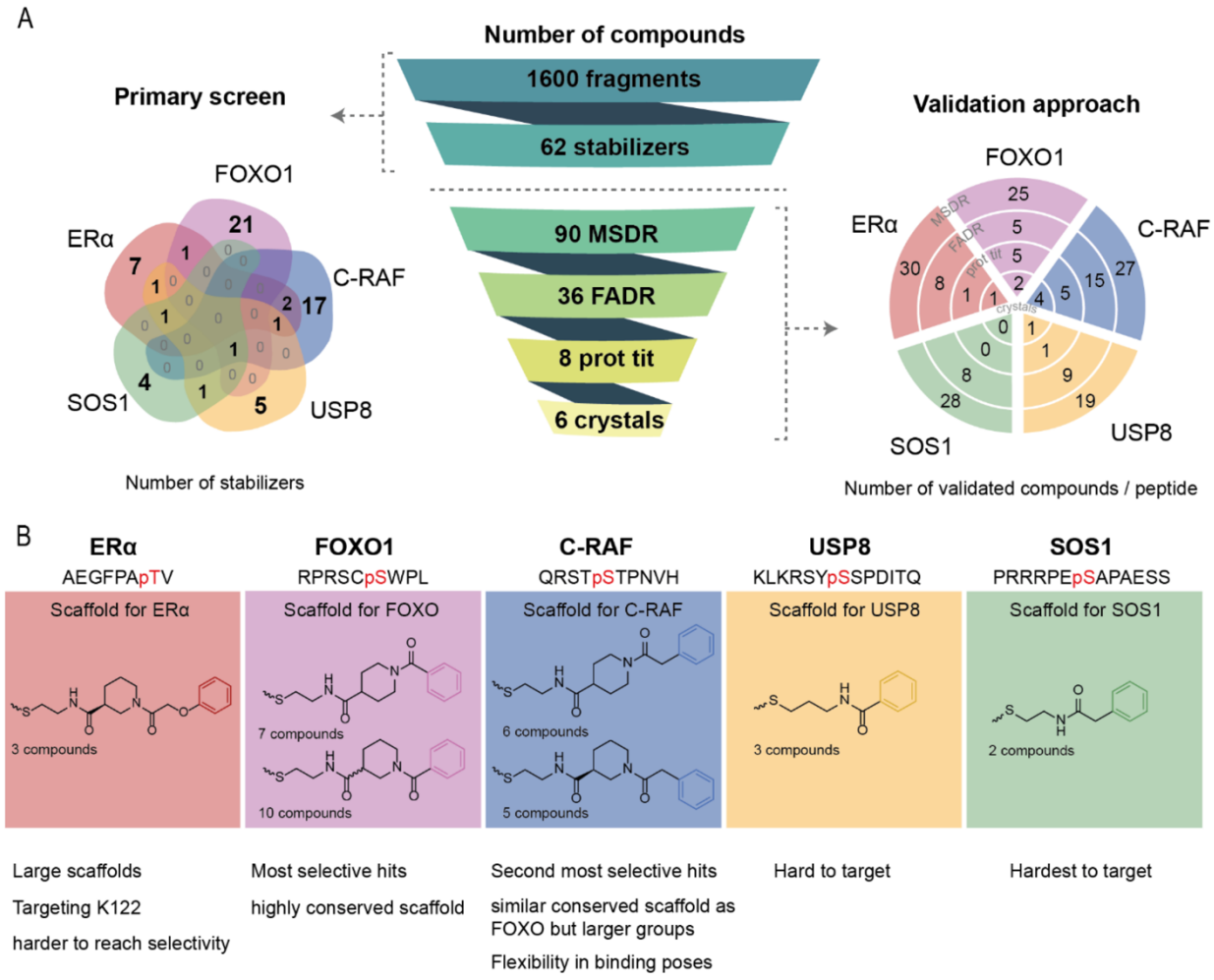

Figure S2.17: Overview of the screens performed
A) The screening funnel starting with the primary screen at the left depicted as a Venn diagram with the number of stabilizers discovered for each peptide and at the right the validation approach taken after the primary screen with the number of validated compounds per peptide per assay. **B)** Conserved scaffold needed for stabilization of each peptide discovered from the primary screen.

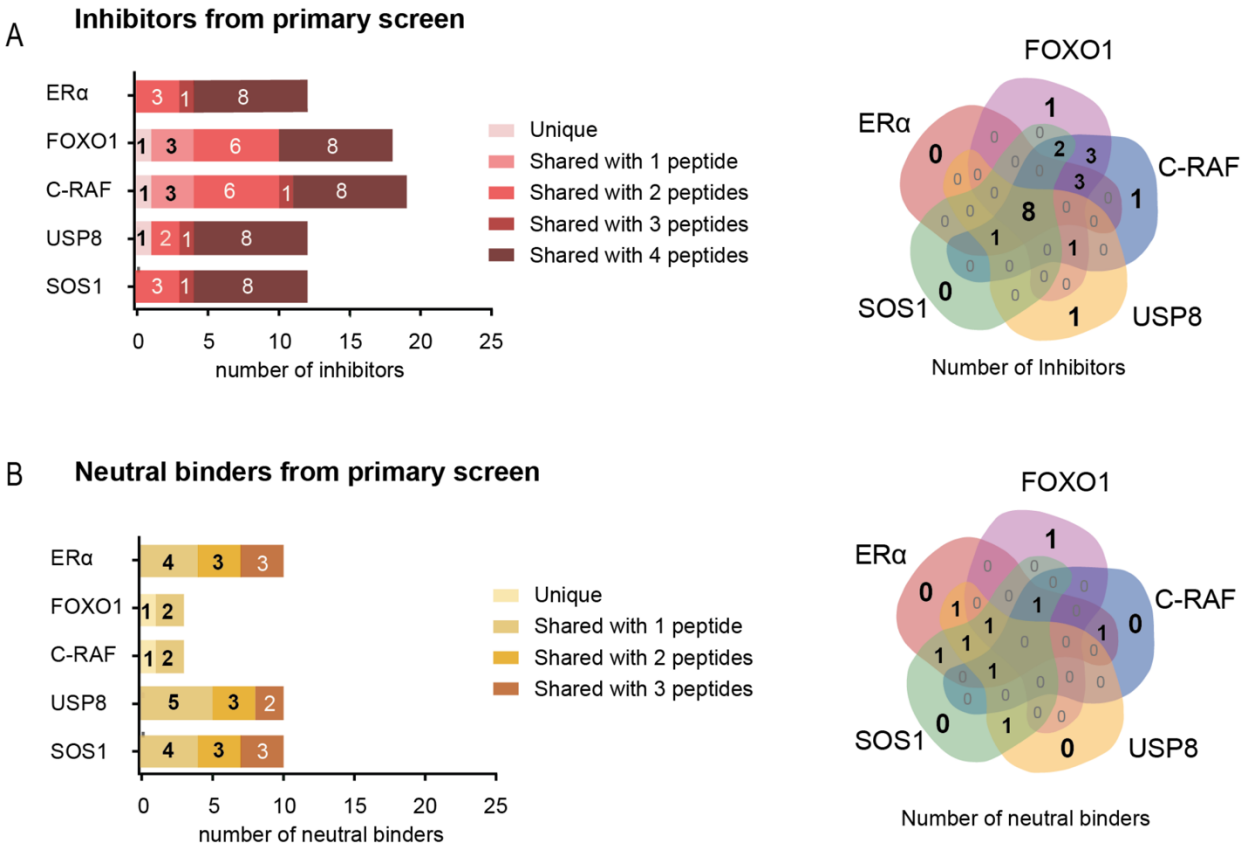

Figure S2.18: Overview of the number of inhibitors and neutral binders discovered
A) Number of discovered inhibitors for each peptide depicted as (left) bar plots and (right) as a Venn diagram. **B)** Number of discovered neutral binders for each peptide depicted as (left) bar plots and (right) as a Venn diagram.

Supplementary Tables

Table S2.1: Tethering and stabilization of 14-3-3σ/CRAF primary screen hit compounds

	Primary Screen (250 µM BME)	MSDR (250 µM BME)	FADR (50 µM BME)	Protein Titrations (50 µM BME)		
SMDC ID	**% Tethering**	**DR_{50} (µM)**	**EC_{50} (µM)**	**K_{D_app}**	**K_{D_DMSO}**	**Fold Stabilization**
916851 (**7**)	42.4	12.2	3.18	294 nM	23 µM	77
916856 (**8**)	58.3	4.96	13.5	207 nM	23 µM	110
916935	44.9	>2000	—	—	—	—
917041	38	>2000	—	—	—	—
917072	62.8	465	>2000	—	—	—
917215	40.4	5.01	>2000	—	—	—
917215	38.3	5.01	>2000	—	—	—
917285	56.7	5.61	—	—	—	—
917285	38.4	5.61	—	—	—	—
917323	42.5	>2000	—	—	—	—
917426	40.9	5.76	—	—	—	—
917692	62.2	>2000	>2000	—	—	—
917725	42.5	—	—	—	—	—
917729	38.5	5.24	—	—	—	—
917746	35.4	<0.91	19.4	—	—	—
917748	15.8+/-17	>2000	—	—	—	—
917755	51.1	5.82	>2000	—	—	—
917845	13.9+/-16	—	—	—	—	—
917866	52.2	>2000	>2000	—	—	—
917908	64.7	>2000	—	—	—	—
917922	47.1	>2000	>2000	—	—	—
917949 (**1**)	85.3	0.007	0.922	106 nM	8.5 µM	81
917963	52	5.29	>2000	—	—	—
917982	63.7	5.45	0.58	—	—	—
917988	55.4	>2000	—	—	—	—
917995	41.7	>2000	—	—	—	—
917999 (**5**)	37.1	0.58	0.22	92	23 µM	246
918000	60.4	3.95	—	—	—	—
918039 (**6**)	48.3	8.78	1.33	100 nM	42 µM	426

Table S2.2: Tethering and stabilization of 14-3-3σ/FOXO1 primary screen hit compounds

	Primary Screen (250 μM BME)	MSDR (250 μM BME)	FADR (50 μM BME)	Protein Titrations (50 μM BME)		
SMDC ID	**% Tethering**	**DR_{50} (μM)**	**EC_{50} (μM)**	**K_{D_app}**	**K_{D_DMSO}**	**Fold Stabilization**
917034	29.7	>2000	—	—	—	—
917041	34.3	>2000	—	—	—	—
917222	50.6	—	—	—	—	—
917234	34.3	16.9	—	—	—	—
917261	57.5	3.61	—	—	—	—
917282	48.4	—	—	—	—	—
917316	83.6	0.042	—	117 nM	87 nM	—
917346	36.5	>2000	—	—	—	—
917383 (**4**)	34.3	143.4	6.69	9.7 nM	111 nM	12
917429	28.5	>2000	—	—	—	—
917607	35.4	—	—	—	—	—
917701 (**3**)	68.7	2.2	0.85	10.6 nM	42 nM	4
917720	31.4	>2000	—	—	—	—
917726 (**2**)	67.6	0.36	5.1	7.7 nM	39 nM	5
917748	14.8+/-14	>2000	—	—	—	—
917773	47.5	>2000	—	—	—	—
917800	66.6	4.78	2.41	69 nM	66 nM	—
917845	13.8+/-14	—	—	—	—	—
917848	10.4+/-13	>2000	—	—	—	—
917922	57.9	>2000	—	—	—	—
917967	31.2	>2000	—	—	—	—
917986	38	>2000	—	—	—	—
917992	38.9	48.7	—	—	—	—
957764	30.7	>2000	—	—	—	—
957769	38.6	>2000	—	—	—	—
960037	31.9	—	—	—	—	—
966848	28	>2000	—	—	—	—
966851	37.1	>2000	—	—	—	—
966864	43.4	>2000	—	—	—	—
966943	40.2	>2000	—	—	—	—

Table S2.3: Tethering and stabilization of 14-3-3σ/ERα primary screen hit compounds

	Primary Screen (250 μM BME)	MSDR (250 μM BME)	FADR (50 μM BME)	Protien Titrations (50 μM BME)		
SMDC ID	**% Tethering**	**DR_{50} (μM)**	**EC_{50} (μM)**	**K_{D_app}**	**K_{D_DMSO}**	**Fold Stabilization**
916848	40.9	>2000	>2000	—	—	—
916854	35.1	786	—	—	—	—
916856 (**8**)	35.7	14.5	—	—	—	—
916874	47.3	>2000	—	—	—	—
916933	45.6	>2000	—	—	—	—
916935	43	>2000	—	—	—	—
916936	33.3	>2000	—	—	—	—
916945	56.9	>2000	—	—	—	—
916974	34.9	133	—	—	—	—
917101	38.1	74.1	—	—	—	—
917607	40.5	1900	>2000	—	—	—
917692	47.3	>2000	—	—	—	—
917717	36.7	>2000	>2000	—	—	—
917725	51.5	>2000	—	—	—	—
917730	37.6	>2000	1.51	—	—	—
917748	20.8+/-17	18.5	129	—	—	—
917750	18.3+/-14	>2000	>2000	—	—	—
917770	17.3+/-13	>2000	—	—	—	—
917848	17.2+/-13	>2000	>2000	—	—	—
917878	36.1	>2000	—	—	—	—
917922	73.1	3.67	—	—	—	—
917949 (**1**)	73.1	18.1	1.31	21 nM	360 nM	19
917952	33.4	>2000	—	—	—	—
917982	37.1	>2000	—	—	—	—
918016	35.7	4.47	—	—	—	—
957766	44.9	459	—	—	—	—
957779	63.6	>2000	—	—	—	—
960009	49.4	—	—	—	—	—
960037	56.2	8.31	—	—	—	—
966784	33.8	>2000	—	—	—	—
966840	43	>2000	—	—	—	—
993941	34.2	—	—	—	—	—
994336	38.2	—	—	—	—	—
994825	39.8	—	—	—	—	—

Table S2.4: Tethering and stabilization of 14-3-3σ/USP8 primary screen hit compounds

	Primary Screen (250 μM BME)	MSDR (250 μM BME)	FADR (50 μM BME)	Protein Titrations (50 μM BME)		
SMDC ID	**% Tethering**	**DR_{50} (μM)**	**EC_{50} (μM)**	**K_{D_app}**	**K_{D_DMSO}**	**Fold Stabilization**
916848	0	>2000	4.21	—	—	—
916933	38.3	>2000	—	—	—	—
916945	36.5	>2000	—	—	—	—
916974	39.4	>2000	—	—	—	—
917041	30.1	>2000	>2000	—	—	—
917252	44.1	>2000		—	—	—
917340	50.4	648	1140	—	—	—
917644	18.7+/-23	—		—	—	—
917659	28.9	>2000	>2000	—	—	—
917692	51.1	240	—	—	—	—
917748	19.5+/-19	—	—	—	—	—
917848	15.5+/-13	>2000	—	—	—	—
917949 (**1**)	52.3	0.024	3.38	1.1	4.5	4
957766	39.7	1636	>2000	—	—	—
957779	59.8	>2000	>2000	—	—	—
957817	35.1	>2000	—	—	—	—
957821	57.5	—	—	—	—	—
957824	36	>2000	—	—	—	—
957999	29.4	>2000	—	—	—	—
958001	53.9	>2000	>2000	—	—	—
960009	67.6	—	—	—	—	—
960031	12.8+/-13	>2000	—	—	—	—
960037	52.9	1749	>2000	—	—	—
967287	35.8	—	—	—	—	—
967289	30.4	—	—	—	—	—
994439	36.1	—	—	—	—	—
994487	41.1	—	—	—	—	—
994782	31	—	—	—	—	—
994821	48.2	—	—	—	—	—

Table S2.5: Tethering and stabilization of 14-3-3σ/SOS1 primary screen hit compounds

	Primary Screen (250 μM BME)	MSDR (250 μM BME)	FADR (50 μM BME)	Prot Titrations (50 μM BME)		
SMDC ID	**% Tethering**	**DR_{50} (μM)**	**EC_{50} (μM)**	**K_{D_app}**	**K_{D_DMSO}**	**Fold Stabilization**
916848	28.3	>2000	1598	—	—	—
916933	32.5	>2000	297	—	—	—
916935	22.3	—	—	—	—	—
916992	28.4	>2000	>2000	—	—	—
917041	23	>2000	—	—	—	—
917101	26.9	>2000	—	—	—	—
917340	27.2	>2000	55.1	—	—	—
917447	37.1	>2000	148	—	—	—
917602	9.33+/-12	>2000	—	—	—	—
917609	11.3+/-14	>2000	—	—	—	—
917611	9.73+/-12	>2000	—	—	—	—
917621	10.7+/-13	>2000	—	—	—	—
917692	27.3	325	>2000	—	—	—
917748	15.1+/-16	4.26	—	—	—	—
917845	9.67+/-12	266	—	—	—	—
917848	14.1+/-15	>2000	—	—	—	—
917879	10.4+/-12	>2000	—	—	—	—
917922	72.9	1912	—	—	—	—
917941	23.2	>2000	>2000	—	—	—
957779	54.1	>2000	—	—	—	—
957795	55.3	>2000	—	—	—	—
957999	37.1	>2000	—	—	—	—
958001	67.8	>2000	—	—	—	—
960009	50	28.2	—	—	—	—
960031	15.2+/-15	>2000	—	—	—	—
960037	61.9	562	241	—	—	—
960039	7.73+/-10	>2000	—	—	—	—
966837	26.3	>2000	—	—	—	—
966840	55.9	>2000	—	—	—	—

Materials and Methods

Protein Expression and Purification

The 14-3-3 σ isoform with a truncated C-terminus after T231 (ΔC; to enhance crystallization) and an N-terminal His6 tag was expressed in RosettaTM 2(DE3)pLysS competent E. coli (Novagen) from a pPROEX HTb expression vector. After transformation following manufacturer's instructions, single colonies were picked to inoculate 30 mL precultures (LB), which were added to 1.5 L terrific broth (TB) medium after overnight growth at 37 °C, 250 rpm. Expression was induced upon reaching OD600 1.9−2.1 by adding 400 μM IPTG. After overnight expression at 30°C, 150 rpm, cells were harvested by centrifugation at 6,500 rpm, resuspended in lysis buffer (50 mM HEPES pH 7.5, 500 mM NaCl, 20 mM imidazole, 10% glycerol, 1 mM TCEP), and lysed by sonication. The His6-tagged protein was first purified by Ni-affinity chromatography (Ni-NTA Agarose, Invitrogen) (Wash buffer 50 mM HEPES pH 7.5, 500 mM NaCl, 20 mM imidazole, 1 mM TCEP; Elution buffer 50 mM HEPES pH 7.5, 500 mM NaCl, 500 mM imidazole, 1 mM TCEP) followed by His-tag cleavage by TEV protease during dialysis (50 mM HEPES pH 7.5, 150 mM NaCl, 1 mM TCEP) overnight at 4 °C. The flowthrough of a second Ni-affinity column was collected and analyzed for purity by SDS-PAGE and Q-Tof LC/MS. The protein was buffer exchanged (Storage buffer 25 mM HEPES pH 7.5, 150 mM NaCl, 1 mM TCEP) and concentrated to ~13 mg/mL and aliquots flash-frozen for storage at −80°C. 14-3-3σΔC used for crystallography was concentrated to ~70 mg/mL and aliquots were flash-frozen for storage at -80 °C.

Peptide Sequences

Peptides for disulfide trapping were ordered from ScenicBio (Houston, Texas) as lyophilized solids. Sequences were as follows: ERα-pp (Ac-KYYITGEAEGF-PA{pT}V-COOH);

SOS1-pp (Ac-PRRRPE{pS}APAESS-CONH2); USP8-pp (Ac- KLKRSY{pS}SPDITQ-CONH2); CRAF-pp (Ac-RQRST{pS}TPNVH-CONH2); FOXO1-pp (Ac-RPRSC{pT}WPLPR-CONH2.

2 mM peptide stocks were suspended in water. Fluorescein-labeled peptides were ordered from ScenicBio and Elim Biopharmaceuticals, Inc. (Hayward, CA) as lyophilized solids. Sequences were as written above with N-terminal 5-FAM-label for ERα-pp, SOS1-pp, USP8-pp, and FOXO1-pp. CRAF-pp sequence was as follows: (5-FAM-QHRYSTPHAFTFNTSSPSSEGSLSQRQRST{pS}TPNVH-CONH2). 20 μM stocks were suspended in water. Peptides for crystallography were ordered from Genscript Biotech Corp. Sequences were as follows: ERα-pp (Ac-AEGFPA{pT}V-COOH); USP8-pp (Ac-KLKRSY{pS}SPDITQ-CONH2); CRAF-pp (QRST{pS}TPNVHH-CONH2); FOXO1-pp (Ac-RPR{pS}C{pT}WPLPR-CONH2). 5 mM stocks were suspended in Complexation Buffer (25 mM HEPES pH 7.5, 2 mM $MgCl_2$ and 2 mM βME).

Disulfide Tethering Screen and Data Processing

The primary disulfide tethering screen was performed by incubating target 14-3-3σ protein/phospho-peptide complex with small molecule in a 384-well plate format. The UCSF Small Molecule Discovery Center (SMDC) custom 1600 disulfide-containing fragment library was available as 50 mM stock solutions in DMSO. The screen was performed using 100 nM 14-3-3σ ΔC protein diluted in buffer (10 mM Tris, 250 μM β-mercaptoethanol (βME), pH 8.0) and plated in 384-well plates (25 μL/well). 100 nL of each fragment was pinned from library master plates using non-sterile disposable 384 polypropylene pin tools (V & P Scientific) to give a final concentration of 200 μM. The peptide screens additionally contained a concentration of peptide equivalent to twice the K_D as established by fluorescence anisotropy and competition experiments: (2 μM ERα-pp, 10 μM SOS1-pp, 10 μM USP8-pp, 18 μM CRAF-pp, and 750 nM FOXO1-pp). The reactions were incubated at room temperature for 3 hours before being measured by LC/MS (I-class Acquity

UPLC/ Xevo G2-XS Quadrupole Time of Flight mass spectrometer, Waters). Data collection and automated processing followed a custom workflow, as previously described. Compound resynthesis was done following the published procedures.

Dose Response LC/MS Experiments

The initial mass spectrometry dose response follow-up experiments were performed under the same conditions as the primary screen with the exception that the compounds were titrated from 50 mM to 23 µM in a 3-fold dilution series in DMSO. Then 1 µL of the compound was transferred into 24 µL of protein-peptide solution for final concentrations of 2 mM – 914 nM and 4% DMSO. A final well of DMSO without compound was used as a control at the end of every dilution series. Compounds which displayed dose dependent activity in the presence of phospho-peptide were taken forward into more extensive dose responses in order to determine DR_{50} values. Fragments were titrated from 50 mM to 0.129 nM in a 3-fold dilution series in DMSO. Then 1 µL of the compound was transferred into 24 µL of protein-peptide solution for final concentrations of 2 mM – 5.16 pM and 4% DMSO. A final well of DMSO without compound was used as a control at the end of every dilution series. Initial validation was done in single replicate. Hits were taken forward to fluorescence anisotropy experiments. DR_{50} curves were graphed and calculated using log(agonist) vs. response – Variable slope (four parameters) from GraphPad Prism version 9.0 for Mac, GraphPad Software, San Diego, California USA, www.graphpad.com.

Dose Response Fluorescence Anisotropy Experiments

The fluorescence anisotropy compound dose responses were performed using 100 nM fluorescein-labeled peptides (with the exception of FOXO1-pp which was 10 nM) and 14-3-3σ protein diluted in buffer (10 mM HEPES pH 8.0, 150 mM NaCl, 0.01% TWEEN-20). 14-3-3σ protein concentration was equivalent to approximately half of the K_D determined by fluorescence

anisotropy and competition experiments (CRAF: 1 μM 14-3-3σ; ERα: 250 nM 14-3-3σ; FOXO1: 25 nM 14-3-3σ; USP8: 2.5 μM 14-3-3σ). Fragments were titrated from 50 mM to 11.9 nM in a 2-fold dilution series in DMSO. 1 μL of compound was transferred in triplicates into 24 μL of protein-peptide solution for final concentrations of 2 mM – 0.477 nM and 4% DMSO. A final well of DMSO without compound was used as a control at the end of the dilution series. A row of 5-FAM-labeled peptide alone was used as a lower limit and a row of 5-FAM-labeled peptide with 14-3-3 excess of the K_D was used as an upper limit when calculating the EC_{50} of the fragments. EC_{50} measurements were graphed and calculated using log(agonist) vs. response – Variable slope (four parameters) from GraphPad Prism version 9.0 for Mac, GraphPad Software, San Diego, California USA, www.graphpad.com. 14-3-3σ protein titrations were performed using 2-fold dilution of 14-3-3σ in buffer from starting concentration of 250 μM to 59.6 pM for CRAF and USP8 and 25 μM starting concentration to 5.96 pM for FOXO1 and ERα. Final well contained only 5-FAM-labeled peptide and compound as a control. 5-FAM-peptides were used at 100 nM except FOXO1 which was at 10 nM. Fragments were added at a single concentration of 1 mM in order to maximize 14-3-3σ engagement. Apparent K_D values of 14-3-3σ/phospho- peptide in presence of compounds were compared to K_D values of DMSO control. Fold stabilization (ΔK_D) was determined as the quotient of the apparent K_D of the DMSO control over the apparent K_D with compound. EC_{50} and apparent K_D measurements were graphed and calculated using log(agonist) vs. response – Variable slope (four parameters) from GraphPad Prism version 9.0 for Mac, GraphPad Software, San Diego, California USA, www.graphpad.com.

X-ray Crystallography

The 14-3-3σΔC protein, acetylated ERα, CRAF and FOXO1 peptides and fragments (stock solution of 50mM in DMSO) were dissolved in complexation buffer (25 mM HEPES pH 7.5, 2 mM $MgCl_2$ and 2 mM βME) and mixed in a 1:2:2 molar stoichiometry (protein:peptide:fragment)

at a final protein concentration of 12 mg/mL. The complex was set up for sitting-drop crystallization after overnight incubation at 4 °C, in a custom crystallization liquor (0.095 M HEPES (pH 7.1, 7.3, 7.5, 7.7), 0.19 M $CaCl_2$, 24-29 % PEG 400 and 5% (v/v) glycerol). Crystals grew within 10 – 14 days at 4 °C. Crystals were fished and flash-cooled in liquid nitrogen. X-ray diffraction (XRD) data were either collected at the Deutsche Elektronen-Synchrotron (DESY) PETRA III beamline P11, Hamburg, Germany (all datasets except for 14-3-3σ/CRAFpS259/Compound 1) or at the Diamond Light Source (DLS) beamline Io3, Oxfordshire, United Kingdom (14-3-3σ/CRAFpS259/Compound **1**).

Automatic processing was done by DESY or DLS using XDS9 for data indexing and integration Initial processed data was then scaled using AIMLESS and Molrep was used for limited molecular replacement using PDB ID's 4JC3 and 3IQU as template. Presence of co-crystallized ligands was verified by visual inspection of the Fo-Fc and 2Fo-Fc electron density maps in Coot. If electron density corresponding to the co-crystallized ligand was present, its structure and restrains were generated using eLBOW before final model rebuilding and refinement was done using phenix.refine and Coot. See Table S6 and S7 for data collection and refinement statistics. The structures were submitted to the PDB with IDs 8AFN, 8AV0, 8ADM, 8A62, 8A65, 8A68, 8A6H, 8A6F.

Author Information

Corresponding Author

michelle.arkin@ucsf.edu

l.brunsveld@tue.nl

c.ottmann@tue.nl

ORCID

Michelle R. Arkin: 0000-0002-9366-6770

Luc Brunsveld: 0000-0001-5675-511X

Christian Ottmann: 0000-0001-7315-0315

Dyana N. Kenanova: 0000-0002-0400-8961

Emira J. Visser: 0000-0002-6098-8060

Johanna M. Virta: 0000-0001-9893-5565

Eline Sijbesma: 0000-0002-4837-7574

Federica Centorrino: 0000-0002-4932-6306

Holly R. Vickery: 0000-0002-8912-9454

Mengqi Zhong: 0000-0003-0525-6999

R. Jeffrey Neitz: 0000- 0002-2247-9345

Author Contributions

D.N.K. and E.J.V. contributed equally to this work.

The manuscript was written through contributions of all authors. All authors have given approval to the final version of the manuscript.

Notes

M.R.A., L.B. and C.O. are founders of Ambagon Therapeutics. M.R.A is a director, L.B. is a member of Ambagon's scientific advisory board, C.O., E.S are employees of Ambagon.

Funding Sources

This research was funded by the ONO Pharma Foundation Breakthrough Science Initiative Award (M.A.). Netherlands Organization for Scientific Research (NWO) through Gravity program 024.001.035 and ECHO grant 711.018.003.

Acknowledgements

We thank the Renslo laboratory as well as Paul Burroughs and Joshua Ramos for the synthesis of the disulfide library; we also thank Julia Davies, Grace Pohan, and Amanda Paulson for the automated MS data processing infrastructure in the SMDC and compound data clustering. We thank Markella Konstantinidou and Priya Jaishankar for support with synthetic strategy and John Morrow for contributions in the initial stage of the 14-3-3 tethering project.

References

1. Garlick, J. M.; Mapp, A. K. Selective Modulation of Dynamic Protein Complexes. Cell Chem. Biol. 2020, 27 (8), 986–997.

2. Ivanov, A. A.; Revennaugh, B.; Rusnak, L.; Gonzalez-Pecchi, V.; Mo, X.; Johns, M. A.; Du, Y.; Cooper, L. A. D.; Moreno, C. S.; Khuri, F. R.; Fu, H. The OncoPPi Portal: An Integrative Resource to Explore and Prioritize Protein-Protein Interactions for Cancer Target Discovery. Bioinforma. Oxf. Engl. 2018, 34 (7), 1183–1191.

3. Kim, M.; Park, J.; Bouhaddou, M.; Kim, K.; Rojc, A.; Modak, M.; Soucheray, M.; McGregor, M. J.; O'Leary, P.; Wolf, D.; Stevenson, E.; Foo, T. K.; Mitchell, D.; Herrington, K. A.; Muñoz, D. P.; Tutuncuoglu, B.; Chen, K. H.; Zheng, F.; Kreisberg, J. F.; Diolaiti, M. E.; Gordan, J. D.; Coppé, J. P.; Swaney, D. L.; Xia, B.; Veer, L. van 't; Ashworth, A.; Ideker, T.; Krogan, N. J. A Protein Interaction Landscape of Breast Cancer. Science 2021, 374 (6563), abf3066.

4. Wright, M. T.; Plate, L. Revealing Functional Insights into ER Proteostasis through Proteomics and Interactomics. Exp. Cell Res. 2021, 399 (1), 112417.

5. Hu, G.; Wu, Z.; Uversky, V. N.; Kurgan, L. Functional Analysis of Human Hub Proteins and Their Interactors Involved in the Intrinsic Disorder-Enriched Interactions. Int. J. Mol. Sci. 2017, 18 (12), E2761.

6. Arkin, M. R.; Tang, Y.; Wells, J. A. Small-Molecule Inhibitors of Protein-Protein Interactions: Progressing toward the Reality. Chem. Biol. 2014, 21 (9), 1102–1114.

7. Celis, S.; Hobor, F.; James, T.; Bartlett, G. J.; Ibarra, A. A.; Shoemark, D. K.; Hegedüs, Z.; Hetherington, K.; Woolfson, D. N.; Sessions, R. B.; Edwards, T. A.; Andrews, D. M.; Nelson, A.; Wilson, A. J. Query-Guided Protein-Protein Interaction Inhibitor Discovery. Chem. Sci. 2021, 12 (13), 4753–4762.

8. Linhares, B. M.; Grembecka, J.; Cierpicki, T. Targeting Epigenetic Protein-Protein Interactions with Small Molecule Inhibitors. Future Med. Chem. 2020, 12 (14), 1305–1326.

9. Modell, A. E.; Blosser, S. L.; Arora, P. S. Systematic Targeting of Protein-Protein Interactions. Trends Pharmacol. Sci. 2016, 37 (8), 702–713.

10. Zhong, M.; Lee, G. M.; Sijbesma, E.; Ottmann, C.; Arkin, M. R. Modulating Protein-Protein Interaction Networks in Protein Homeostasis. Curr. Opin. Chem. Biol. 2019, 50, 55–65.

11. Andrei, S. A.; Sijbesma, E.; Hann, M.; Davis, J.; O'Mahony, G.; Perry, M. W. D.; Karawajczyk, A.; Eickhoff, J.; Brunsveld, L.; Doveston, R. G.; Milroy, L.G.; Ottmann, C. Stabilization of Protein-Protein Interactions in Drug Discovery. Expert Opin. Drug Discov. 2017, 12 (9), 925–940.

12. Tang, C.; Mo, X.; Niu, Q.; Wahafu, A.; Yang, X.; Qui, M.; Ivanov, A. A.; Du, Y.; Fu, H. Hypomorph Mutation Directed Small Molecule Protein-Protein Interaction Inducers to Restore Mutant SMAD4 Suppressed TGF-β Signaling. Cell Chem. Biol. 2021, 28 (5), 636-647.e5.

13. Stevers, L. M.; Sijbesma, E.; Botta, M.; MacKintosh, C.; Obsil, T.; Landrieu, I.; Cau, Y.; Wilson, A. J.; Karawajczyk, A.; Eickhoff, J.; Davis, J.; Hann, M.; O'Mahony, G.; Doveston, R. G.; Brunsveld, L.; Ottmann, C. Modulators of 14-3-3 Protein–Protein Interactions. J. Med. Chem. 2018, 61 (9), 3755–3778.

14. De Vries van Leeuwen, I. J.; da Costa Pereira, D.; Flach, K. D.; Piersma, S. R.; Haase, C.; Bier, D.; Yalcin, Z.; Michalides, R.; Feenstra, K. A.; Jiménez, C. R.; de Greef, T. F. A.; Brunsveld, L.; Ottmann, C.; Zwart, W.; de Boer, A. H. Interaction of 14-3-3 Proteins with the Estrogen Receptor Alpha F Domain Provides a Drug Target Inter-face. Proc. Natl. Acad. Sci. U. S. A. 2013, 110 (22), 8894–8899.

15. Mayor-Ruiz, C.; Bauer, S.; Brand, M.; Kozicka, Z.; Si-klos, M.; Imrichova, H.; Kaltheuner, I. H.; Hahn, E.; Seiler, K.; Koren, A.; Petzold, G.; Fellner, M.; Bock, C.; Müller, A. C.; Zuber, J.;

Geyer, M.; Thomä, N. H.; Kubicek, S.; Winter, G. E. Rational Discovery of Molecular Glue Degraders via Scalable Chemical Profiling. Nat. Chem. Biol. 2020, 16 (11), 1199–1207.

16. Chamberlain, P. P.; Cathers, B. E. Cereblon Modulators: Low Molecular Weight Inducers of Protein Degradation. Drug Discov. Today Technol. 2019, 31, 29–34.

17. Słabicki, M.; Kozicka, Z.; Petzold, G.; Li, Y.-D.; Manojkumar, M.; Bunker, R. D.; Donovan, K. A.; Siev-ers, Q. L.; Koeppel, J.; Suchyta, D.; Sperling, A. S.; Fink, E. C.; Gasser, J. A.; Wang, L. R.; Corsello, S. M.; Sellar, R. S.; Jan, M.; Gillingham, D.; Scholl, C.; Fröhling, S.; Golub, T. R.; Fischer, E. S.; Thomä, N. H.; Ebert, B. L. The CDK Inhibitor CR8 Acts as a Molecular Glue Degrader That Depletes Cyclin K. Nature 2020, 585 (7824), 293–297.

18. Hartman, A. M.; Elgaher, W. A. M.; Hertrich, N.; Andrei, S. A.; Ottmann, C.; Hirsch, A. K. H. Discovery of Small Molecule Stabilizers of 14-3-3 Protein-Protein Interactions via Dynamic Combinatorial Chemistry. ACS Med. Chem. Lett. 2020, 11 (5), 1041–1046.

19. Pfaff, S. J.; Chimenti, M. S.; Kelly, M. J. S.; Arkin, M. R. Biophysical Methods for Identifying Fragment-Based Inhibitors of Protein-Protein Interactions. In Protein-Protein Interactions: Methods and Applications; Meyerkord, C. L., Fu, H., Eds.; Methods in Molecular Biology; Springer: New York, NY, 2015; pp 587–613.

20. Erlanson, D. A.; Arndt, J. W.; Cancilla, M. T.; Cao, K.; Elling, R. A.; English, N.; Friedman, J.; Hansen, S. K.; Hession, C.; Joseph, I.; Kumaravel, G.; Lee, W.-C.; Lind, K. E.; McDowell, R. S.; Miatkowski, K.; Nguyen, C.; Nguyen, T. B.; Park, S.; Pathan, N.; Penny, D. M.; Romanowski, M. J.; Scott, D.; Silvian, L.; Simmons, R. L.; Tangonan, B. T.; Yang, W.; Sun, L. Discovery of a Potent and Highly Selective PDK1 Inhibitor via Fragment-Based Drug Discovery. Bioorg. Med. Chem. Lett. 2011, 21 (10), 3078–3083.

21. Hallenbeck, K. K.; Davies, J. L.; Merron, C.; Ogden, P.; Sijbesma, E.; Ottmann, C.; Renslo, A. R.; Wilson, C.; Arkin, M. R. A Liquid Chromatography/MassSpectrometry Method for

Screening Disulfide Tethering Fragments. SLAS Discov. Adv. Life Sci. R D 2018, 23 (2), 183–192.

22. Raimundo, B. C.; Oslob, J. D.; Braisted, A. C.; Hyde, J.; McDowell, R. S.; Randal, M.; Waal, N. D.; Wilkinson, J.; Yu, C. H.; Arkin, M. R. Integrating Fragment Assembly and Biophysical Methods in the Chemical Advancement of Small-Molecule Antagonists of IL-2: An Approach for Inhibiting Protein-Protein Interactions. J. Med. Chem. 2004, 47 (12), 3111–3130.

23. Lodge, J. M.; Rettenmaier, T. J.; Wells, J. A.; Pomerantz, W. C.; Mapp, A. K. FP Tethering: A Screening Technique to Rapidly Identify Compounds That Disrupt Protein-Protein Interactions. MedChemComm 2014, 5, 370–375.

24. Sadowsky, J. D.; Burlingame, M. A.; Wolan, D. W.; McClendon, C. L.; Jacobson, M. P.; Wells, J. A. Turning a Protein Kinase on or off from a Single Allosteric Site via Disulfide Trapping. Proc. Natl. Acad. Sci. U. S. A. 2011, 108 (15), 6056–6061.

25. Sijbesma, E.; Hallenbeck, K. K.; Leysen, S.; de Vink, P. J.; Skóra, L.; Jahnke, W.; Brunsveld, L.; Arkin, M. R.; Ottmann, C. Site-Directed Fragment-Based Screening for the Discovery of Protein–Protein Interaction Stabilizers. J. Am. Chem. Soc. 2019, 141 (8), 3524–3531.

26. Burlingame, M. A.; Tom, C. T. M. B.; Renslo, A. R. Simple One-Pot Synthesis of Disulfide Fragments for Use in Disulfide Exchange Screening. ACS Comb. Sci. 2011, 13 (3), 205–208.

27. Morrison, D. K. The 14-3-3 Proteins: Integrators of Diverse Signaling Cues That Impact Cell Fate and Cancer Development. Trends Cell Biol. 2009, 19 (1), 16–23.

28. Obsilova, V.; Obsil, T. The 14-3-3 Proteins as Important Allosteric Regulators of Protein Kinases. Int. J. Mol. Sci. 2020, 21 (22), E8824.

29. Aghazadeh, Y.; Papadopoulos, V. The Role of the 14-3-3 Protein Family in Health, Disease, and Drug Development. Drug Discov. Today 2016, 21 (2), 278–287.

30. Gardino, A. K.; Smerdon, S. J.; Yaffe, M. B. Structural Determinants of 14-3-3 Binding Specificities and Regulation of Subcellular Localization of 14-3-3-Ligand Complexes: A Comparison of the X-Ray Crystal Structures of All Human 14-3-3 Isoforms. Semin. Cancer Biol. 2006, 16 (3), 173–182.

31. Zhao, J.; Meyerkord, C. L.; Du, Y.; Khuri, F. R.; Fu, H. 14-3-3 Proteins as Potential Therapeutic Targets. Semin. Cell Dev. Biol. 2011, 22 (7), 705–712.

32. Molzan, M.; Kasper, S.; Röglin, L.; Skwarczynska, M.; Sassa, T.; Inoue, T.; Breitenbuecher, F.; Ohkanda, J.; Kato, N.; Schuler, M.; Ottmann, C. Stabilization of Physical RAF/14-3-3 Interaction by Cotylenin A as Treatment Strategy for RAS Mutant Cancers. ACS Chem. Biol. 2013, 8 (9),1869–1875.

33. Bank, R. P. D. RCSB PDB: Homepage. https://www.rcsb.org/ (accessed 2022-06-21).

34. Liau, N. P. D.; Wendorff, T. J.; Quinn, J. G.; Steffek, M.; Phung, W.; Liu, P.; Tang, J.; Irudayanathan, F. J.; Izadi, S.; Shaw, A. S.; Malek, S.; Hymowitz, S. G.; Sudhamsu, J. Negative Regulation of RAF Kinase Activity by ATP Is Overcome by 14-3-3 Induced Dimerization. Nat. Struct. Mol. Biol. 2020, 27 (2), 134–141.

35. Ballone, A.; Lau, R. A.; Zweipfenning, F. P. A.; Ottmann, C. A New Soaking Procedure for X-Ray Crystallographic Structural Determination of Protein-Peptide Complexes. Acta Crystallogr. Sect. F Struct. Biol. Com-mun. 2020, 76 (Pt 10), 501–507.

36. Saha, M.; Carriere, A.; Cheerathodi, M.; Zhang, X.; La-voie, G.; Rush, J.; Roux, P. P.; Ballif, B. A. RSK Phosphorylates SOS1 Creating 14-3-3 Docking Sites and Negatively Regulating MAPK Activation. Biochem. J. 2012, 447 (1), 159–166.

37. Saline, M.; Badertscher, L.; Wolter, M.; Lau, R.; Gunnarsson, A.; Jacso, T.; Norris, T.; Ottmann, C.; Snijder, A. AMPK and AKT Protein Kinases Hierarchically Phosphorylate the N-Terminus

of the FOXO1 Transcription Factor, Modulating Interactions with 14-3-3 Proteins. J. Biol. Chem. 2019, 294 (35), 13106–13116.

38. Centorrino, F.; Ballone, A.; Wolter, M.; Ottmann, C. Biophysical and Structural Insight into the USP8/14-3-3 Interaction. FEBS Lett. 2018, 592 (7), 1211–1220.

39. Molzan, M.; Schumacher, B.; Ottmann, C.; Baljuls, A.; Polzien, L.; Weyand, M.; Thiel, P.; Rose, R.; Rose, M.; Kuhenne, P.; Kaiser, M.; Rapp, U. R.; Kuhlmann, J.; Ottmann, C. Impaired Binding of 14-3-3 to CRAF in Noonan Syndrome Suggests New Approaches in Diseases with Increased Ras Signaling. Mol. Cell. Biol. 2010, 30 (19), 4698–4711.

40. Falcicchio, M.; Ward, J. A.; Chothia, S. Y.; Basran, J.; Mohindra, A.; Macip, S.; Roversi, P.; Doveston, R. G. Cooperative Stabilisation of 14-3-3σ Protein–Protein In-teractions via Covalent Protein Modification. Chem. Sci. 2021.

41. Molzan, M.; Ottmann, C. Synergistic Binding of the Phosphorylated S233-and S259-Binding Sites of CRAF to One 14-3-3ζ Dimer. J. Mol. Biol. 2012, 423 (4), 486–495.

42. Cossar, P. J.; Wolter, M.; van Dijck, L.; Valenti, D.; Levy, L. M.; Ottmann, C.; Brunsveld, L. Reversible Covalent Imine-Tethering for Selective Stabilization of 14-3-3 Hub Protein Interactions. J. Am. Chem. Soc. 2021, 143 (22), 8454–8464.

Chapter 3

Development of a NanoBRET assay for evaluation of 14-3-3σ molecular glues

Contributing Authors:

Holly R. Vickery[1,‡], Johanna M. Virta[1,‡], Markella Konstantinidou[1], Michelle R. Arkin[1]

[1]Department of Pharmaceutical Chemistry and Small Molecule Discovery Center, University of California, San Francisco 94158, United States.

[‡]H.R.V. and J.M.V. contributed equally to this work.

Abstract

We report the development of a 384-well formatted NanoBRET assay to characterize molecular glues of 14-3-3/client interactions in living cells. The seven isoforms of 14-3-3 are dimeric hub proteins with diverse roles including transcription factor regulation and signal transduction. 14-3-3 interacts with hundreds of client proteins to regulate their function and is therefore an ideal therapeutic target when client selectivity can be achieved. We have developed the NanoBRET system for three 14-3-3σ client proteins CRAF, TAZ, and estrogen receptor α (ERα), which represent three specific binding modes. We have measured stabilization of 14-3-3σ/client complexes by molecular glues with EC_{50} values between 100 nM and 1 μM in cells, which align with the EC_{50} values calculated by fluorescence anisotropy in vitro. Developing this NanoBRET system for the hub protein 14-3-3σ allows for a streamlined approach, bypassing multiple optimization steps in the assay development process for other 14-3-3σ clients. The NanoBRET system allows for an assessment of PPI stabilization in a more physiologically relevant, cell-based environment using full-length proteins. The method is applicable to diverse protein-protein interactions (PPIs) and offers a robust platform to explore libraries of compounds for both PPI stabilizers and inhibitors.

Introduction

Protein-Protein Interactions

Protein-protein interactions (PPIs) are crucial for various cellular processes and modulation of these interactions, by inhibition or stabilization, results in profound effects on cellular function.[1–4] Molecular glues are small molecules that stabilize the interaction between two proteins by binding cooperatively to the PPI interface.[5–7] Recent work on PPI stabilization has focused on developing molecular glues and bifunctional small molecules, called PROTACs, that link a ubiquitin ligase to a protein of interest to induce the protein's degradation.[8,9] Generally, PROTACs and molecular-glue degraders induce neomorphic interactions to degrade target proteins selectively.[6,7,9] However, an intriguing and relatively underexplored approach lies in harnessing the potential of molecular glues as non-degradative stabilizers of PPIs.[5,10] This novel perspective offers a promising approach to precisely modulate and stabilize PPIs for therapeutic interventions and for a deeper understanding of cellular processes.

Systematic technologies geared towards the identification of native PPI stabilizers[11–13] tend to be target-directed, compared to cell-based technologies for molecular glue degraders.[14–16] For instance, we have established biochemical fragment-based assays for the identification, validation, and optimization of PPI stabilizers. Our workflow employs a mass spectrometry (MS)-based site-directed disulfide tethering approach that has identified highly cooperative stabilizers for multiple 14-3-3/client complexes.[11,12,17] During chemical optimization, PPI stabilizers are evaluated using MS- and fluorescence anisotropy (FA)-based assays. These technologies measure stabilization of 14-3-3 and a peptide derived from the client protein, facilitating screening and x-ray crystallography.[11,12,18] With effective PPI stabilizers in hand, we sought a systematic approach to measure stabilization of full-length protein complexes. Ideally, such an approach would be suitable to lysate and cellular contexts. Here we describe the validation of NanoBRET assays to evaluate PPI stabilizers for the hub protein 14-3-3 bound to diverse protein partners.

The Hub Protein 14-3-3

14-3-3 modulates the function of hundreds of disease-relevant 'client' proteins through binding to linear sequences containing phosphorylated serine and threonine residues. Within the 14-3-3 family there are seven isoforms, each encoded by different genes.[19,20] Notably, these isoforms exhibit pronounced sequence similarity within the phospho-binding groove, underscoring a shared mechanism of interaction with phosphorylated regions of client proteins.[21,22] Peptides derived from the client proteins interact with the 14-3-3 binding groove via distinct conformations,[20,22,23] including: (1) turning out of the groove after a phosphoserine/phosphothreonine (pS/pT) residue, typically guided by a proline in the +2 position, (2) binding straight through the phospho-binding groove, and (3) using a truncated sequence with a pS/pT at the penultimate residue of the protein. The three clients we describe here represent these three binding modes, with CRAF representing mode 1, TAZ reflecting mode 2, and Estrogen Receptor α (ERα) binding as mode 3 (Figure 3.1A; Figure S3.2).[24–26] Figure 3.1B illustrates the 14-3-3σ/client pocket we aim to target and example molecular glues.

14-3-3 plays important biological roles in the regulation of CRAF, TAZ, and ERα. 14-3-3 is involved in both the inhibition and activation of CRAF, with CRAF pS259 acting as a regulatory switch that is only phosphorylated in the inhibited state. In the activation of CRAF, pS259 releases from 14-3-3 and can be dephosphorylated.[27–32] Stabilizing the 14-3-3σ/CRAF pS259 interaction with molecular glues could therefore represent a novel method of inhibiting the MAPK pathway in various cancers (Figure 3.1C).[32] The interaction between 14-3-3 and TAZ is a regulatory mechanism in the Hippo pathway. Phosphorylation of TAZ at S89 promotes association with 14-3-3, preventing TAZ translocation into the nucleus and activation as a transcription factor.[25,33] Stabilizing the 14-3-3σ/TAZ pS89 interaction with molecular glues would inhibit the oncogenic role of TAZ in driving cell proliferation and survival (Figure 3.1D). 14-3-3 binds to ERα at the penultimate residue pT594. Binding to 14-3-3 inhibits ERα by preventing its dimerization and DNA

binding. This interaction is crucial in the context of ER-positive breast cancer, where stabilizing the 14-3-3σ/ERα pT594 interaction may offer a potential therapeutic strategy to disrupt estrogen-driven tumorigenesis (Figure 3.1E).[26] Not only do these clients represent different binding modes, but also different subcellular locations and functions.

Distinct classes of molecular-glue stabilizers of 14-3-3/client complexes have been discovered. Fusicoccane natural products and semisynthetic analogs,[20,26,34–36] non-covalent synthetic compounds,[37,38] and lysine-reactive fragments bind in the 14-3-3 phospho-binding groove and stabilize clients to all 14-3-3 isoforms.[39,40] We have also identified disulfide fragments that bind to a cysteine residue at the periphery of the binding groove of the sigma isoform only and stabilize diverse 14-3-3σ/client complexes.[11,12] Structure-guided optimization towards 14-3-3/ERα stabilizers yielded cysteine-reactive molecules with EC_{50} values in the low μM range in biochemical assays and the ability to stabilize the complex by 120-fold, eg, *app*K_D = 2 μM to 18 nM (Figure S3.1).[18] We and our colleagues have also developed 14-3-3σ-specific stabilizers for CRAF and TAZ phosphopeptides. These three chemical series require cell-based validation of their ability to act as molecular glues for 14-3-3σ and full-length proteins.

NanoBRET Assay

NanoLuciferase bioluminescence resonance energy transfer (NanoBRET) assays are widely adopted methods for measuring PPI and protein/small-molecule interactions in live cells.[30,41–44] This innovative approach utilizes fusion proteins to quantify energy transfer, a process contingent upon the proximity between the tagged proteins of interest. NanoBRET assays have been effectively harnessed to measure PPI inhibition in cells and to measure formation of ubiquitin ligase/target complexes for PROTACs, showcasing their utility in probing the effects of modulating PPIs.[41,45,46] However, to our knowledge, NanoBRET systems have not been used to measure PPI stabilization in the presence of molecular glues. We selected NanoBRET over related technologies such as cell-based fluorescence resonance energy transfer (FRET) or NanoLuc

Binary Technology (NanoBiT) due to its improved sensitivity and geometric flexibility, respectively.[42,45,47,48]

Here we report a 384-well plate-based cellular NanoBRET method for the evaluation of 14-3-3σ/client molecular glues. The optimized assay allows for a statistically robust (Z' = 0.7-0.95) increase in the BRET signal of 14-3-3σ/client interactions in the presence of small-molecule stabilizers. This 14-3-3σ/client stabilization NanoBRET methodology can be universally applied to characterize stabilizers for other PPIs, employing a similarly efficient and systematic approach.

Materials & Methods

Construct design and cloning

14-3-3σ and client proteins CRAF, TAZ, and ERα were cloned into the Promega NanoBRET vectors (Promega N1811) using Gibson Assembly (NEB E2611) with a GSSG linker between the protein and the tag. 17 residues were deleted from the C-terminus of 14-3-3σ to reduce dynamics of C-terminal tags; therefore, all 14-3-3σ constructs contain residues 1-231. NES-TAZ and NES-ERα constructs contain an engineered nuclear export signal (NES) on the N-terminus with a GSSG linker before the NanoLuc tag.

Compounds

CRAF-01-05 were synthesized in house and will be disclosed in due course. TAZ-01-03 were identified in a high-throughput screening campaign; the structures have not been disclosed (Ambagon Therapeutics). ERα-01 and ERα-02 were published as compounds 85 and 181, respectively.[18] Fusicoccin-A was purchased from Enzo Life Sciences (BML-EI334-0001) and XMU-MP-1 was purchased from MedChemExpress (HY-100526).

Cell lines

HEK293T cells were purchased from ATCC (CRL-3216) and used as recommended. To avoid signal inhibition by endogenous, unlabeled proteins, we selected HEK293T cells because they express minimal to no 14-3-3σ, TAZ, and ERα. HEK293T cells also have an inactive MAPK pathway, suggesting that transfected CRAF would be phosphorylated at S259.

NanoBRET

NanoBRET assays were performed as described by Promega. Four constructs (two for ERα) were generated for each client protein to test in combination with four constructs of 14-3-3σ. Combination tests were performed at a 1:10 ratio of NanoLuc:HaloTag; ratios of 1:1, 1:10, 1:100, and 1:1000 were then tested with selected combinations. Plasmids were transfected using jetOPTIMUS transfection reagent following the manufacturer's protocol and cells were plated in white, flat bottom TC-treated 384-well microplates (Corning 3570) after transfection in Gibco FluoroBrite DMEM with 4% fetal bovine serum (FBS; Sigma-Aldrich). ERα experiments were conducted with 4% charcoal dextran stripped FBS (Corning 35-072-CF). Each experiment was performed in triplicate and included no-acceptor controls and samples with the HaloTag NanoBRET 618 Ligand. Plates were read on an EnVision XCite 2105 plate reader at 618 nm (HaloTag) and 460nm (NanoLuc) (Filters: M647 CWL=647nm BW=75nm; M460 CWL=460nm BW=80nm Mirror: LUM/D585).

Fluorescence Anisotropy Measurements

ERα FA measurements were performed as previously described.[18] For CRAF and TAZ, peptides were purchased from Elim Biopharmaceuticals, Inc (CRAF: QRSTpSTPNVH; TAZ: RSHpSSPASLQ).

For CRAF, fluorescein-labeled peptides (5-FAM), full-length 14-3-3σ protein, the compounds (50 mM stock solution in DMSO) were diluted in buffer (10 mM HEPES, pH 7.5, 150

mM NaCl, 0.1% Tween20, 1 mg/mL Bovine Serum Albumin (BSA; Sigma-Aldrich). Final DMSO in the assay was always 1%. Dilution series of 14-3-3 proteins or compounds were made in black, flat-bottom 384-microwell plates (Greiner Bio-one 784900) in a final sample volume of 10 µL in triplicate. For compound titrations the initial 50 mM compound stock solutions in DMSO were diluted to 20mM in a 384-well master plate, followed by a serial 2-fold dilution. Then, 500 nL of the dilution series were transferred in the assay plates. A master mix containing 10 nM fluorescein-labeled peptide and 5 µM full-length 14-3-3σ (concentration at EC_{20} value of the protein-peptide complex) in buffer (10 mM HEPES, pH 7.5, 150 mM NaCl, 0.1% Tween20, 1 mg/mL BSA) was dispensed on the assay plates. The final volume per well was 10µL, with final top concentration of compounds dose response series at 1mM. Each compound was measured in triplicate, in two independent experiments. Fluorescence anisotropy measurements were performed directly and after overnight incubation at room temperature. Protein titrations were made by titrating 14-3-3σ in a 2-fold dilution series (starting at 250 µM) to a mix of fluorescein-labeled peptide (10 nM) and DMSO or compound (100 µM). Fluorescence anisotropy measurements were performed after overnight incubation at room temperature. Fluorescence anisotropy values were measured using a Molecular Devices ID5 plate reader (filter set λ_{ex}: 485 ± 20 nm, λ_{em}: 535 ± 25 nm; integration time: 50 ms; settle time: 0 ms; shake 5sec, medium, read height 3.00 mm, G factor = 1. Data reported are at endpoint. EC_{50} and apparent K_D values were obtained from fitting the data with a four-parameter logistic model (4PL) in GraphPad Prism. Data was obtained and averaged based on two independent experiments.

TAZ FA experiments were done as described for CRAF with the following exceptions: final sample volume was 25 µL using 384-well plates (Corning 3575), final peptide concentration was 100 nM 5-FAM-TAZ, and final full-length 14-3-3σ protein concentration was 300 nM in the compound titration. Measurements were taken at 1 hour and 24 hours for compound titration and protein titration, respectively.

Procedure

We have developed a NanoBRET assay to test small molecule molecular glues of 14-3-3σ/client PPIs (Figure 3.2A). To test new PPIs, eight NanoLuc/HaloTag-fused protein constructs were cloned, and all eight combinations were tested. After selecting the desired combination, four ratios of NanoLuc:HaloTag plasmid were used to determine the optimal transfection ratio before testing compounds to measure their effects on PPI stabilization (Figure 3.2B).

Construct design

14-3-3σ and client proteins were cloned into NanoLuc and HaloTag vectors with N- or C-terminal tags. The constructs were named based on the placement of the tag, with "HaloTag-14-3-3σ" denoting N-terminal placement of the tag, and "14-3-3σ-HaloTag" denoting C-terminal placement. Because the C-terminus of ERα is crucial for binding to 14-3-3, ERα was only cloned with N-terminal tags. A nuclear export signal (NES; LPPLERLTL) was inserted at the N-terminus of TAZ and ERα for the "NES-client" constructs.[49] The DNA binding domain (185-250) was truncated out of ERα to make the "ΔDBD-ERα" construct.

Assay Setup

Generally, we followed the manufacturer's protocol.[41,50] In short, plasmids were transfected in HEK293T cells in bulk for 48 hours. Ratios of NanoLuc:HaloTag plasmids were transfected by keeping the amount of HaloTag plasmid constant and decreasing the amount of NanoLuc plasmid. For example, a 1:10 transfection ratio could include 1 μg of HaloTag plasmid plus 0.1 μg of NanoLuc plasmid. The decrease in the amount of NanoLuc plasmid transfected is reflected in the amount of protein expressed as measured by western blot (Figure S3.3A). Cells were trypsinized and counted before adjusting the cell density to 250,000 cells/mL and adding HaloTag ligand (1 μL ligand/1 mL of media). A no-HaloTag-ligand control was also made wherein DMSO was added instead of ligand at the same % v/v (1 μL/1 mL). 30 μL of the cell/HaloTag

ligand or DMSO mixture was added to each well in a 384-well assay plate. Compound (or DMSO) was diluted in media to 4x the final concentration. Then, 10 µL of this 4x compound stock was added to corresponding wells. All samples had the same final percent DMSO of less than 0.5%. After 24 hours, NanoLuc substrate was added, and assay plates were read to measure luminescence in the NanoLuc and HaloTag channels (Figure 3.2C).

An alternative approach can be used to measure NanoBRET in lysate using the detergent digitonin. This approach can be used if the compounds are not cell permeable or are cytotoxic at the desired concentration range. Digitonin permeabilizes the outer membrane to release cytosolic proteins into the media (Figure S3.3B). As exemplified for CRAF, we added digitonin at 200 µg/mL after seeding cells and before dosing with compound.

Data Analysis

The following formulas were used to calculate the raw milliBRET units (mBU), mean corrected mBU, and fold change. Data was then analyzed and visualized in GraphPad Prism to obtain EC_{50} values by fitting the data with a 4PL model.

$$\frac{acceptor\ emission\ value\ (618nm)}{donor\ emission\ value\ (460nm)} * 1{,}000 = mBU$$

$$mean\ mBU_{experimental} - mean\ mBU_{no\ HaloTag\ ligand\ control} = mean\ corrected\ mBU$$

$$\frac{mBU_{experimental}}{mBU_{DMSO\ control}} = fold\ change$$

Results

CRAF/14-3-3σ NanoBRET

To measure cysteine-targeting stabilizers of the 14-3-3σ/CRAF pS259 interaction, eight constructs were cloned for 14-3-3σ/CRAF: HaloTag-14-3-3σ, 14-3-3σ-HaloTag, NanoLuc-14-3-3σ, 14-3-3σ-NanoLuc, HaloTag-CRAF, CRAF-HaloTag, NanoLuc-CRAF, and CRAF-NanoLuc. With these constructs, eight combinations were tested at a 1:10 NanoLuc:HaloTag transfection ratio (Figure 3.3A). Combinations where the NanoLuc was fused to 14-3-3σ and the HaloTag fused to CRAF resulted in low BRET signal. Two combinations, NanoLuc-CRAF/14-3-3σ-HaloTag and CRAF-NanoLuc/14-3-3σ-HaloTag (Z' = 0.91 and 0.92, respectively), were selected for ratio testing. CRAF-NanoLuc/14-3-3σ-HaloTag gave higher signal and was chosen to move forward with. In these ratio tests, 1:10 and 1:100 CRAF-NanoLuc:14-3-3σ-HaloTag gave the highest signals (Z' = 0.90, Z' = 0.95, respectively; Figure 3.3B). Ratios of 1:1 and 1:1,000 were excluded due to low signal and high background, respectively.

When using NanoBRET to identify molecular glues, careful selection of a combination and ratio is essential to ensure that the protein complex is not completely formed, such that it maintains sensitivity to stabilization by small molecules. Thus, we evaluated both 1:10 and 1:100 in the presence of stabilizers. 1:10 resulted in higher fold-stabilization with molecular glues than 1:100 (Figure S3.4A); thus, we proceeded with this condition.

We tested three compounds, initially identified as molecular glues through MS and FA assays, along with one negative control, in the CRAF/14-3-3σ NanoBRET system. The negative control was structurally related to the stabilizers but inactive in the FA assay. The molecular glues exhibited up to 1.6-fold increase in NanoBRET signal, and EC_{50} values in the sub-μM to low-μM range (Figure 3.3C). The fold increase in signal and the Z' values were similar between the NanoBRET and FA assays, suggesting similar sensitivity. These compounds were dependent on

the presence of C38 in 14-3-3σ, as mutation of this residue rendered the compounds ineffective in stabilizing the interaction (Figure S3.4B).

In comparing the EC_{50} values obtained from FA and NanoBRET, it is noteworthy that FA was performed in vitro with a fully phosphorylated CRAF pS259 peptide with the 14-3-3σ concentration kept at its EC_{20}, while NanoBRET was performed in cells with the full-length CRAF that may not have been fully phosphorylated. Moreover, the degree of phosphorylation of CRAF may increase over the time of compound incubation, since increased 14-3-3 binding protects clients from dephosphorylation. These factors make it difficult to quantitatively compare EC_{50} values from the biochemical and cell-based binding assays. Nevertheless, the trends in EC_{50} values track between NanoBRET and FA, with the negative control CRAF-01 exhibiting a non-stabilizing effect. In contrast, CRAF-02 emerged as the most potent stabilizer with an EC_{50} value of 0.18 μM and the highest maximum signal. CRAF-03 had a similar EC_{50} value of 0.20 μM, but a lower maximum signal. CRAF-04 demonstrated a comparatively diminished stabilizing capacity with an EC_{50} value of 1.1 μM, making it the weakest of the three molecular glues (Table 1). The difference in signal maximum was reproducible and consistent with the FA data (Figure S3.1A-E). The calculated EC_{50} values from the NanoBRET assay for CRAF-02 and CRAF-03 were lower than those calculated from FA assays (Table 1), but the rank order was maintained.

Using the procedure described above, we introduced the detergent digitonin into the assay to permeabilize the cell membrane, releasing the NanoBRET pair into the media. In the cellular NanoBRET assay, CRAF stabilizers were tested up to 10 μM based on their cytotoxicity in HEK293T (data not shown). To compare the lysate and cell-based assays, we measured CRAF-05 activity in the CRAF/14-3-3σ NanoBRET with four doses, from 1 – 250 μM in lysate and 1 – 10 μM in cells. The results in both assays were similar, with CRAF-05 showing significant stabilization even at 1 μM. The lower signal ratio at the maximum concentrations (1.3- vs 1.5-fold)

led us to use the cell-based assay going forward (Figure S3.4C). Thus, PPI stabilization can be measured either in cells or in lysates using the same transfection ratio and assay formats.

TAZ/14-3-3σ NanoBRET

The following four constructs were cloned to test both donor and acceptor tags on the N- or C-terminus of TAZ: HaloTag-TAZ, TAZ-HaloTag, NanoLuc-TAZ, and TAZ-NanoLuc. To aid in developing the 14-3-3σ/TAZ NanoBRET system, we used an MST1/2 inhibitor, XMU-MP-1 ("XMU"), at 60 μM to prevent phosphorylation of TAZ, which in turn inhibited the 14-3-3σ/TAZ interaction (Figure 3.1D). After testing all eight NanoBRET combinations of 14-3-3σ and TAZ, we chose to move forward with NanoLuc-TAZ/14-3-3σ-HaloTag because it produced the largest BRET signal (24 mBU) with the most significant difference between untreated and XMU treated samples (fold change = 1.4, Z' = 0.84; Figure 3.4A). NanoLuc:HaloTag ratios were then evaluated, and 1:10 gave the largest fold-change between untreated and XMU treated samples (fold-change = 1.4, Z' = 0.90; Figure 3.4B).

14-3-3σ controls trafficking of TAZ between the cytoplasm and the nucleus, so we evaluated whether manipulating NanoLuc-TAZ subcellular localization would alter the BRET signal. We engineered a nuclear export signal (NES) into the N-terminus of the TAZ construct before the NanoLuc tag. With this NES-NanoLuc-TAZ (NES-TAZ) construct, the basal NanoBRET signal increased 3.1-fold (Figure 3.4C). While the raw mBU signal varied between biological replicates, perhaps due to transfection efficiency, the BRET signal was consistently larger with the NES construct.

We compared the 14-3-3σ/TAZ complex formation with C38-reactive molecular glues, TAZ-02 and TAZ-03, along with an inactive compound, TAZ-01 (Figure S3.5). The NES-TAZ construct led to increased mBU values but decreased the fold-change compared to NanoLuc-TAZ itself. For instance, TAZ-02 increased the BRET signal by 4.2-fold and 2.2-fold with NanoLuc-TAZ and NES-TAZ, respectively (Figure 3.4C). Nevertheless, the compound dose-responses

yielded similar EC_{50} values with both TAZ constructs. The negative control TAZ-01 had no effect on the BRET signal, while TAZ-02 had an EC_{50} of 810 nM; TAZ-03 did not reach a plateau, with an estimated EC_{50} of 120 nM (Figure 3.4D). In FA assays, TAZ-02 and TAZ-03 performed similarly to each other with EC_{50} values of 1.2 μM and 1.6 μM, respectively (Figure S3.1F-I; Table 3.1). Thus, the TAZ/14-3-3σ NanoBRET assays confirmed the stabilizing effects of these molecular glues.

ERα/14-3-3σ NanoBRET

ERα binds 14-3-3σ at its penultimate residue, pT594. Therefore, only N-terminal tag constructs were developed for ERα to avoid interference with 14-3-3σ binding. ERα combination and ratio tests were performed in the presence of a natural product stabilizer, Fusicoccin-A (FC-A) at 30 μM. Similar to CRAF and TAZ, little to no signal was measured for the combinations in which 14-3-3σ was tagged with NanoLuc. The NanoLuc-ERα plus 14-3-3σ-HaloTag combination gave the largest signal and fold stabilization for the positive control FC-A (Z' = 0.79, Figure 3.5A). In the ratio test, 1:10 was the only combination where there was a measurable difference between DMSO and FC-A (Z' = 0.96, Figure 3.5B). Therefore, this ratio was selected to advance to the subsequent testing phase for new 14-3-3σ specific, cysteine-reactive molecular glues (Figure S3.6A). The most potent molecular glue, ERα-02, resulted in 2.5-fold stabilization with an EC_{50} of 2.4 μM (Figure 3.5C). In FA dose-responses, ERα-02 had a similar EC_{50} value of 1.0 μM when tested with the ERα peptide (Figure S3.1J,K).[18] The inactive compound, ERα-01, had no effect in NanoBRET or FA dose response assays (Figure 3.5C, Table 3.1). FC-A resulted in low fold stabilization (Figure 3.5A,B) likely because binding of the NanoBRET pair was diluted by binding to other 14-3-3 isoforms and clients. Because HEK293T cells did not contain endogenous 14-3-3σ, the sigma-specific stabilizer, ERα-02, was highly effective at binding to the transfected 14-3-3σ.

Since ERα is also a transcription factor, a significant fraction could be localized in the nucleus, resulting in a low NanoBRET signal. We therefore engineered two cytoplasmic constructs containing an NES at the N-terminus (“NES-ERα”) or removing the DNA-binding domain (aa 185-250; "ΔDBD-ERα”). While both methods increased the BRET signal, from 5-10 to 10-15 mBU, the stabilizer dose response effects were diminished (Figure 3.5D). Although these methods of increasing the NanoBRET signal did not improve the 14-3-3σ/ERα NanoBRET assay for ERα-02, they are useful techniques to apply when troubleshooting low NanoBRET signal for other PPI NanoBRET systems, as seen with TAZ.

A benefit of developing the ERα/14-3-3σ NanoBRET assay in HEK293T cells was the low endogenous expression of both proteins. We extended these experiments to an ER-positive breast cancer cell line, MCF7, where both ERα and 14-3-3σ were expressed, and MDA-MB-231, an ER-negative breast cancer cell line, where only 14-3-3σ was endogenously expressed. Comparing the ERα/14-3-3σ NanoBRET assay in these three cell lines, HEK293T cells had the largest signal window with minimal background (Figure S3.6B-D). Thus, using a cell line that does not endogenously express the proteins of interest ensured that the tagged proteins were not outcompeted by endogenous proteins.

Discussion

14-3-3σ NanoBRET Summary and Workflow

In developing analogous NanoBRET assays for three 14-3-3σ/client complexes, we learned that the HaloTag acceptor was always preferred on 14-3-3σ and that varying the subcellular localization of the client protein sometimes improved the BRET signal, depending on the biology of the complex (Table 2). Traditional NanoBRET assay development conventionally involves a four-step workflow: (1) generating eight constructs of 14-3-3σ and the client tagged

with NanoLuc or HaloTag, (2) testing eight combinations, (3) evaluating four ratios of the best combination, and (4) subsequently testing molecular glues (Figure 3.2B). Leveraging the insights gained from our results across 14-3-3σ/client systems, we propose a streamlined workflow that condenses the NanoBRET assay design for 14-3-3σ/client interactions into three efficient steps: (1) constructing two client constructs (or one depending on client binding restrictions, e.g. ERα), (2) test two combinations, and (3) evaluate molecular glues (Figure 3.6). This simplified workflow promises expedited discovery of 14-3-3σ/client molecular-glue stabilizers, offering a potentially impactful resource for diverse therapeutic applications.

Assay Throughput

NanoBRET assays to discover and characterize molecular glues can be set up in a low-, medium-, or high-throughput format depending on materials and instruments employed. Generally, we have run approximately 200-2,000 samples at a time. Because optimizing the transfection ratio is necessary to detect PPI stabilizers, the NanoBRET assay requires a transient transfection. This manual step reduces throughput and precision; in particular, raw mBU values can vary between experiments. Nevertheless, with automation for cell seeding and compound dosing, the NanoBRET assay for PPI stabilizers can be performed in a high-throughput manner.

Conclusions

We describe the development of a NanoBRET assay designed to characterize molecular-glue stabilizers of 14-3-3σ/client PPIs. Building from the published NanoBRET protocol,[50] we have identified multiple factors that required careful evaluation. Specific to PPI stabilizers, it is critical to select a combination of protein constructs and transfection ratio that leads to a measurable but incomplete formation of the PPI, such that the assay can detect an increase in BRET signal. Additional general considerations include optimizing the cell permeability and colocalization of the protein partners. For example, digitonin releases cytoplasmic proteins into the media, allowing for

higher compound concentrations and effectively transforming the assay into a lysate assay. Furthermore, adding a nuclear export signal increased mBU values for the transcription factor/14-3-3σ complexes, suggesting that localization motifs should be considered if the BRET signal is low. Lastly, choice of cell line should account for the endogenous expression levels of the proteins of interest. With these considerations, our NanoBRET results closely mirror the sensitivity of FA and the NanoBRET EC_{50} values were consistent with the FA EC_{50} values measured for diverse molecular glues. Thus, NanoBRET is a valuable tool to characterize stabilizers targeting 14-3-3σ/client interactions. Notably, the distinct advantage of NanoBRET is the physiological relevance of the assay, as it is performed in a cellular environment with full-length proteins.

This comprehensive method can be efficiently adapted and streamlined for the exploration of other 14-3-3σ client proteins. Moreover, the systematic approach can be readily applied to other hub protein systems and to discover novel molecular glues. As research in this domain progresses, the integration of NanoBRET assays for PPI stabilization could significantly broaden the repertoire of techniques available for studying PPIs and their implications in cellular processes.

Figures

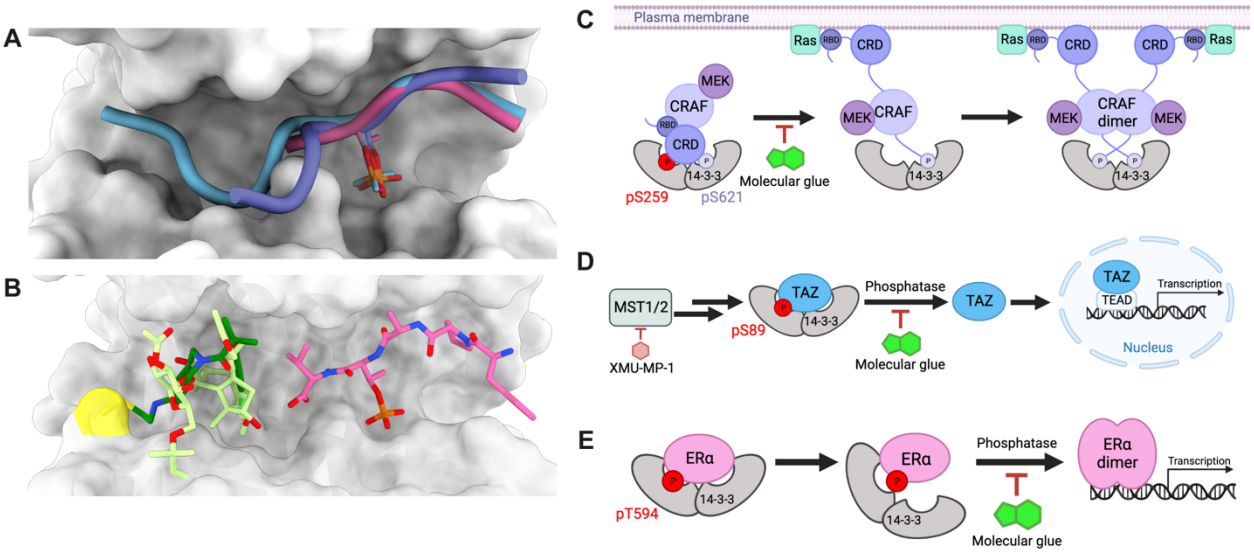

Figure 3.1: 14-3-3σ/client binding and regulatory mechanisms
A) Crystal structure overlay of 14-3-3σ (grey) bound to CRAF (purple), ERα (pink), and TAZ (blue) peptides illustrating the three different binding modes. pS/T residues are shown to illustrate the overlap in this position of the peptide. PDBs: CRAF 4IHL, ERα 4JDD, TAZ 3MHR. **B)** Visualization of the molecular glue binding pocket within the 14-3-3σ phospho-binding groove. Both the fragment stabilizer (dark green) and Fusicoccin-A (light green) bind in the 14-3-3σ phospho-binding groove proximal to the ERα peptide (pink). 14-3-3σ C38 is highlighted in yellow. PDB 8AFN with Fusicoccin-A overlaid from PDB 4JDD. **C)** Proposed 14-3-3/CRAF mechanism. 14-3-3 binding to CRAF pS259 (red) maintains the inhibited state of CRAF. 14-3-3σ/CRAF pS259 molecular glues would prevent the opening and subsequent activation of CRAF. **D)** 14-3-3 regulation of TAZ in the Hippo signaling pathway. MST1/2 activity leads to the phosphorylation of TAZ at pS89 (red). In the nucleus, TAZ binds TEAD transcription factors and activates transcription. 14-3-3σ/TAZ pS89 molecular glues would localize TAZ in the cytoplasm, impeding its role as a transcription factor. **E)** 14-3-3 regulation of ERα. 14-3-3 binds ERα at pT594 (red) to prevent ERα dimerization and binding to DNA. 14-3-3σ/ERα pT594 molecular glues would prevent ERα dissociation and activation.

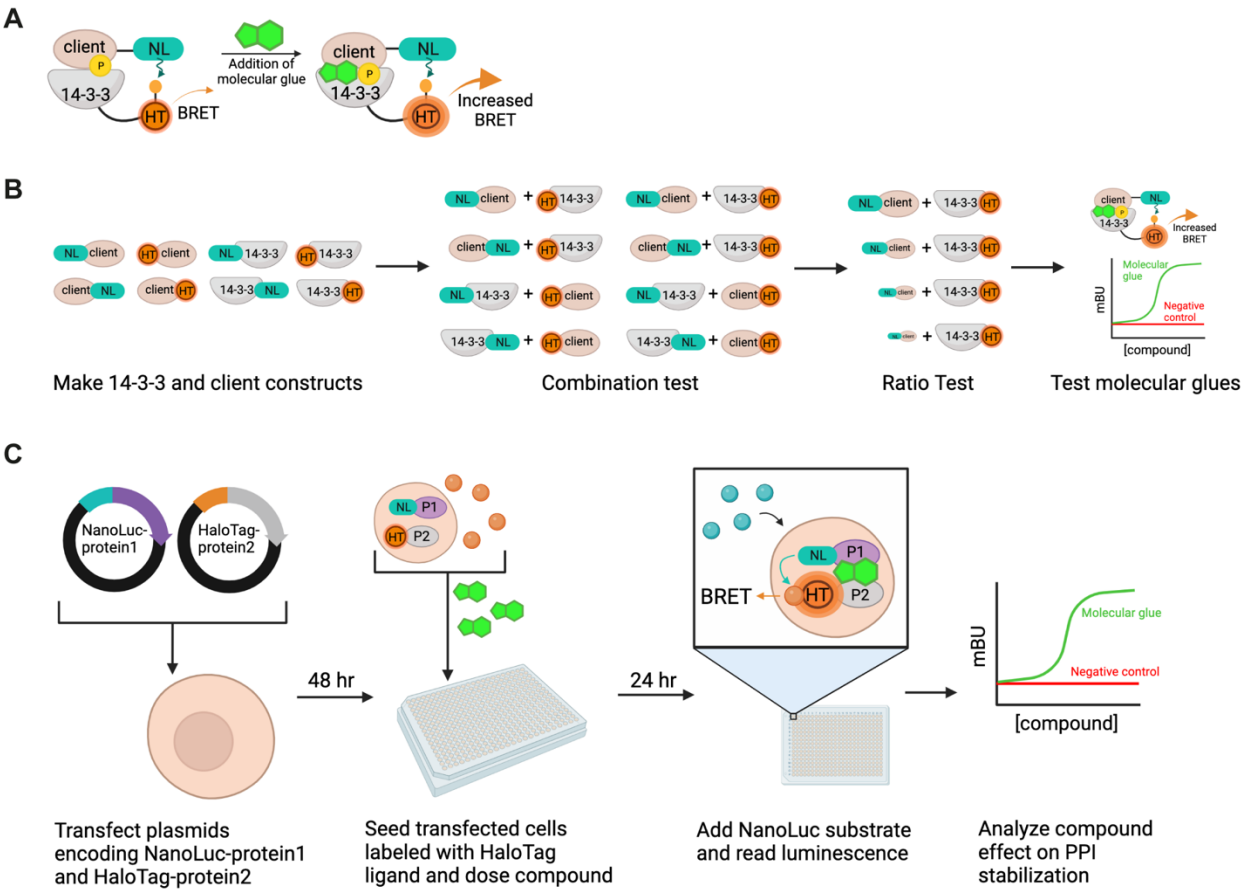

Figure 3.2: NanoBRET assay overview

A) Schematic representation of the 14-3-3/client NanoBRET assay, where one protein is tagged with NanoLuc (NL) and the other with HaloTag (HT). Addition of molecular glues is expected to increase the BRET signal. **B)** Steps to set up a NanoBRET assay for a new PPI. **C)** Procedure to set up NanoBRET assay.

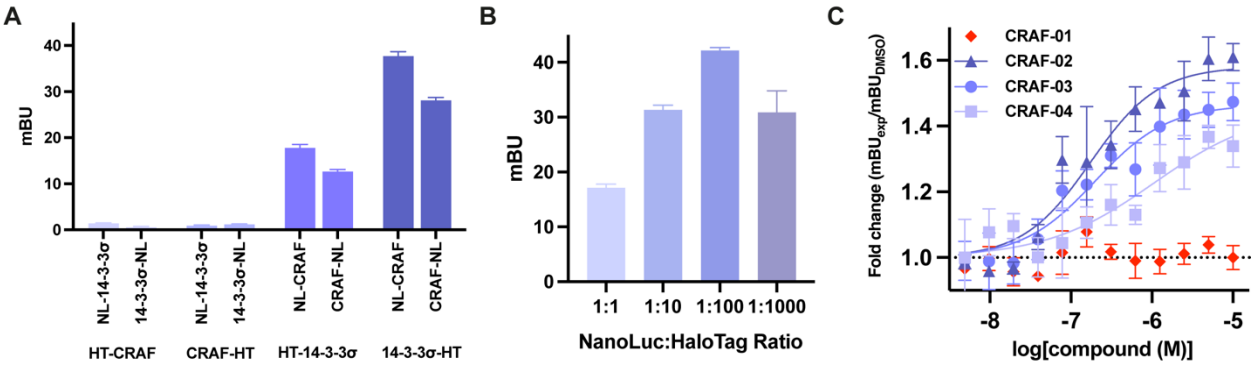

Figure 3.3: NanoBRET results for CRAF/14-3-3σ

A) Combination test (n = 3). 14-3-3σ with a C-terminal HaloTag and CRAF with an N- or C-terminal NanoLuc tag resulted in the highest signal. **B)** CRAF-NanoLuc/14-3-3σ-HaloTag ratio test (n = 3). **C)** CRAF-NanoLuc/14-3-3σ-HaloTag NanoBRET data with 4 compounds, three stabilizers (CRAF-02-04) and one negative control (CRAF-01) (n = 3). Data shown in C are representative of 5 biological replicates.

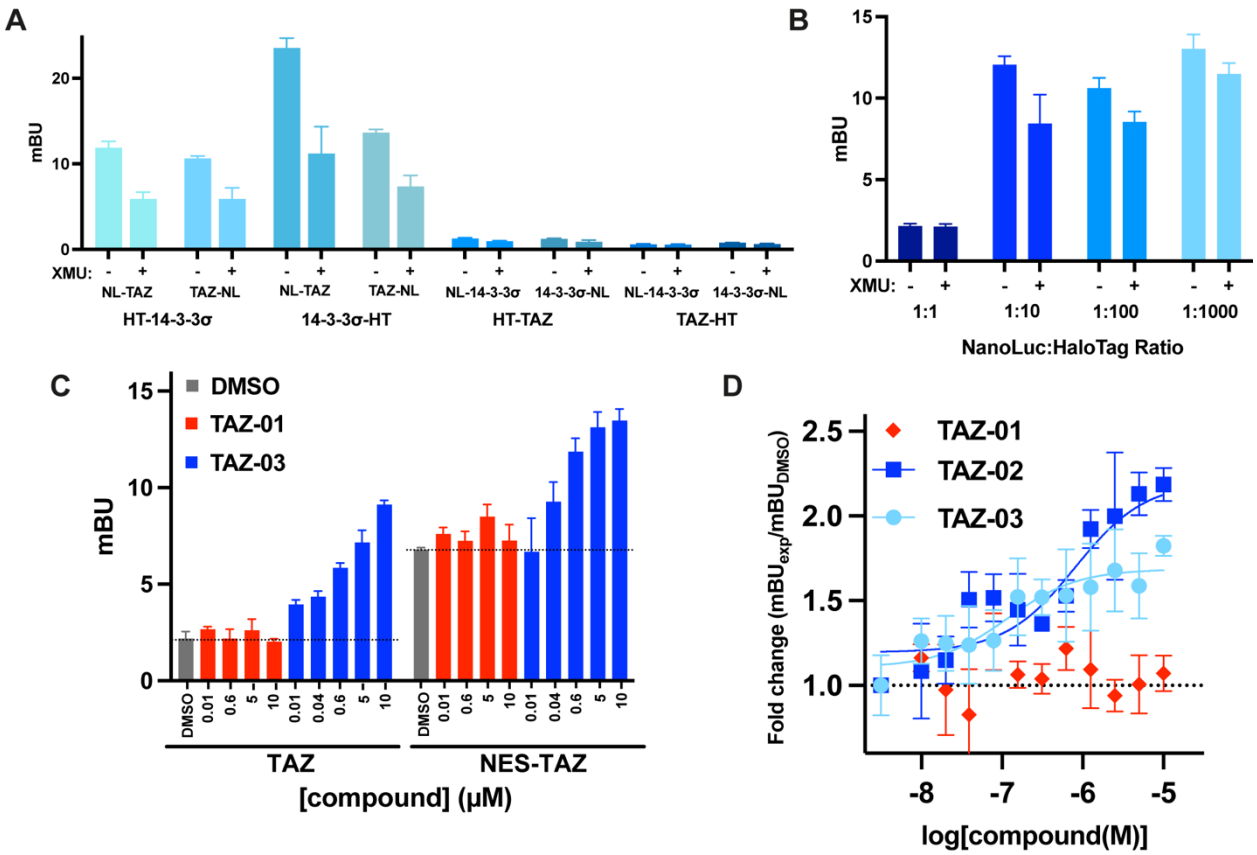

Figure 3.4: NanoBRET results for TAZ/14-3-3σ
A) Combination test comparing untreated and XMU (60 μM) treated samples (n = 3). NanoLuc-TAZ/14-3-3σ-HaloTag gave the highest signal and largest fold change with XMU. **B)** NanoLuc-TAZ/14-3-3σ-HaloTag ratio test (n = 3). **C)** Comparison of TAZ and NES-TAZ constructs with one inactive compound (TAZ-01) and one stabilizer (TAZ-02) (n = 3). A subset of tested compound concentrations is shown. **D)** NES-TAZ/14-3-3σ NanoBRET results with two TAZ/14-3-3σ stabilizers (TAZ-02 and TAZ-03) and TAZ-01 with all data points in the dilution series shown (n = 3). Data shown in C and D are representative of 3 biological replicates.

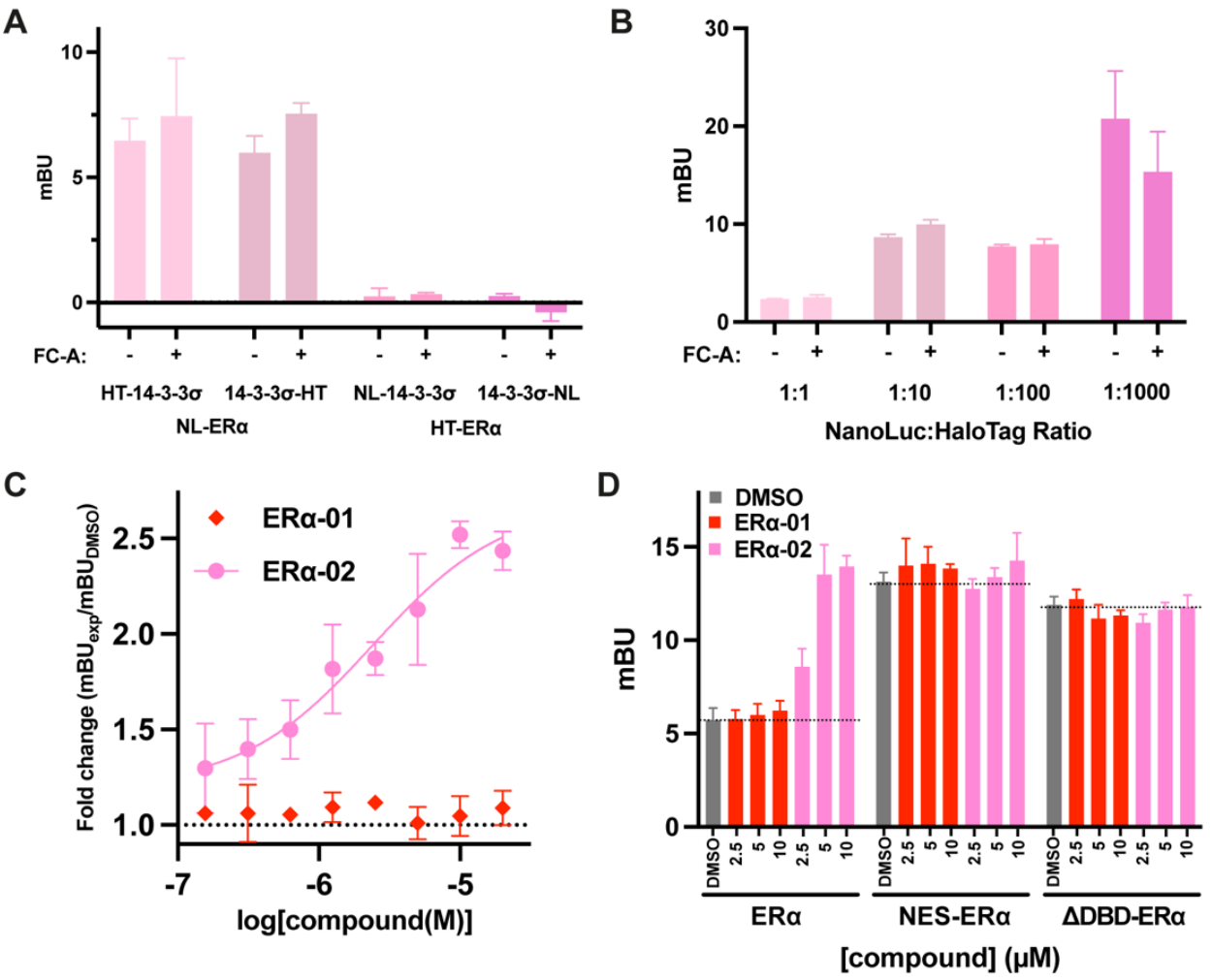

Figure 3.5: NanoBRET results for ERα/14-3-3σ

A) Combination test comparing untreated and FC-A (30 μM) treated samples (n = 3). NanoLuc-ERα/14-3-3σ-HaloTag gave the only significant difference with DMSO vs FC-A treatment. **B)** NanoLuc-ERα/14-3-3σ-HaloTag ratio test (n = 3). **C)** ERα/14-3-3σ NanoBRET results with one molecular-glue stabilizer (ERα-02) and one inactive compound (ERα-01) (n = 3). **D)** Comparison of different ERα constructs with ERα-01 and ERα-02 (n = 3). Data shown in C and D are representative of 3 biological replicates.

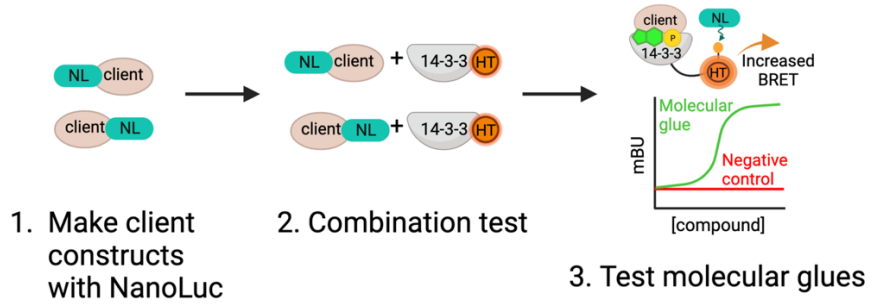

Figure 3.6: Simplified NanoBRET workflow for identification of 14-3-3σ/client molecular glues

Tables

Table 3.1: EC_{50} values for 14-3-3σ/client NanoBRET and FA

NanoBRET Complex	Compound	NanoBRET EC_{50} (μM)	FA EC_{50} (μM)
CRAF-NanoLuc/14-3-3σ-HaloTag	**CRAF-01**	>10	>150
	CRAF-02	0.18	1.0
	CRAF-03	0.20	1.2
	CRAF-04	1.1	1.2
NES-NanoLuc-TAZ/14-3-3σ-HaloTag	**TAZ-01**	>20	>150
	TAZ-02	0.81	1.2
	TAZ-03	0.12 (est.)	1.6
NanoLuc-ERα/14-3-3σ-HaloTag	**ERα-01**	>20	>150
	ERα-02	2.4	1.0

Table 3.2: Tag placement for 14-3-3σ/CRAF, TAZ, and ERα NanoBRET assays

14-3-3σ client	NanoLuc	HaloTag
CRAF	CRAF (C-terminus)	14-3-3σ (C-terminus)
TAZ	TAZ (N-terminus)	14-3-3σ (C-terminus)
ERα	ERα (N-terminus)	14-3-3σ (C-terminus)

Supplementary Figures

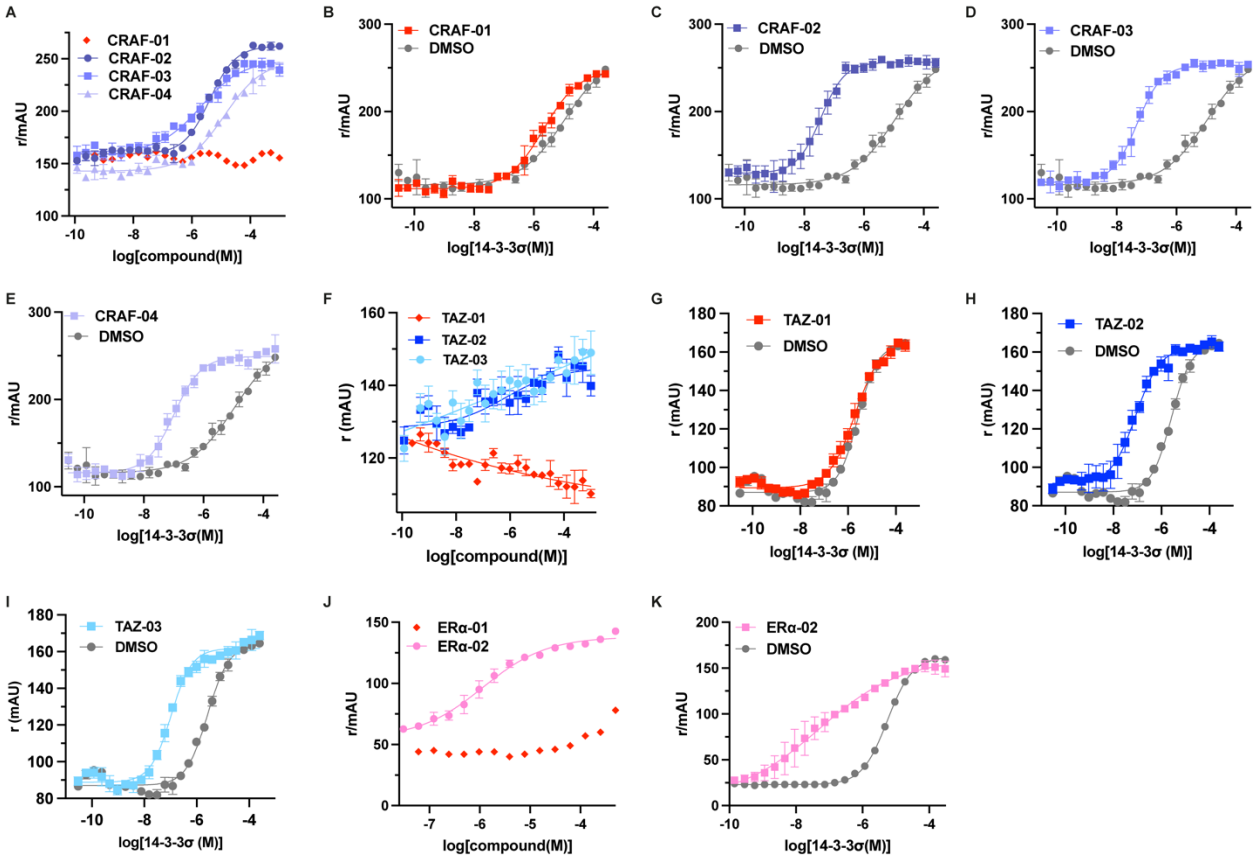

Figure S3.1: CRAF, TAZ, and ERα compound and protein titrations
CRAF pS259, TAZ pS89, and ERα pT594 peptide FA compound and protein titrations. **A)** CRAF-01-04 compound titrations. **B)** CRAF-01 protein titration. **C)** CRAF-02 protein titration. **D)** CRAF-03 protein titration. **E)** CRAF-04 protein titration. **F)** TAZ-01-03 compound titrations. **G)** TAZ-01 protein titration. **H)** TAZ-02 protein titration. **I)** TAZ-03 protein titration. **J)** ERα-01 and ERα-02 compound titrations. **K)** ERα-02 protein titration. All experiments n = 3.

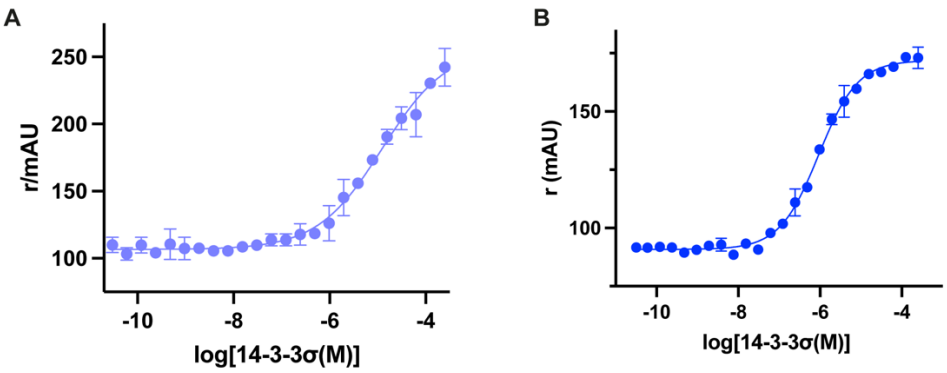

Figure S3.2: 14-3-3/client peptide affinities
A) CRAF pS259 peptide FA K_D assay (n = 3). **B)** TAZ pS89 peptide FA K_D assay (n = 3).

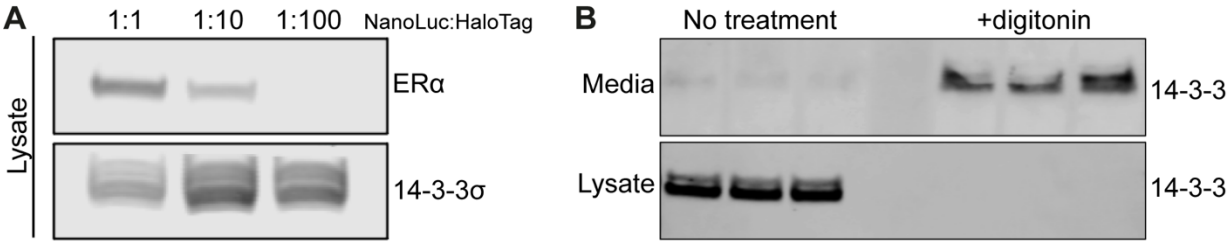

Figure S3.3: Protein expression and effects of detergent
A) NanoLuc:HaloTag plasmid transfection ratios reflected in protein expression in HEK293T cells. **B)** Western blot for 14-3-3 without and with digitonin treatment (n=3). Cytosolic proteins are released into the media when treated when cells are treated with digitonin.

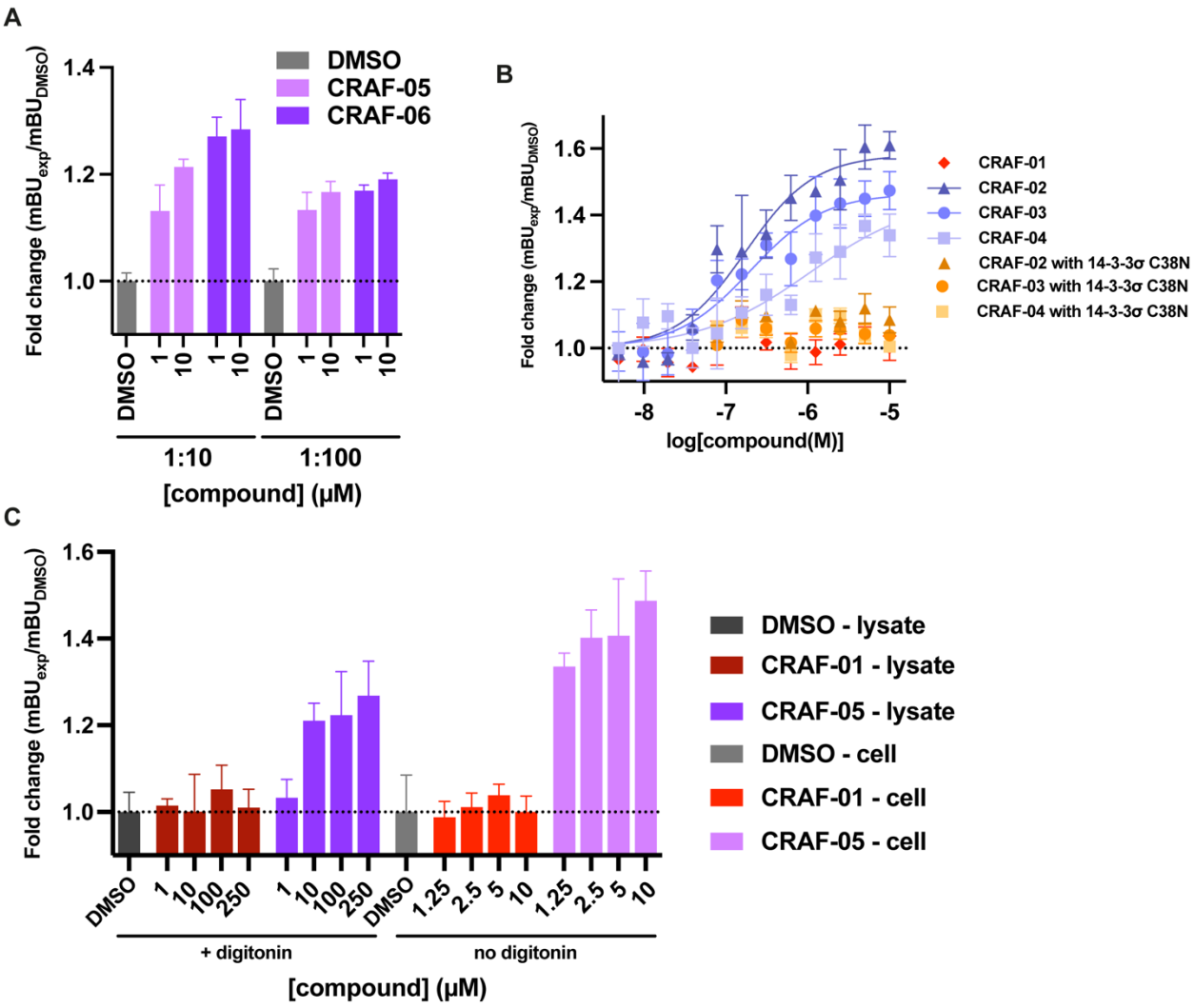

Figure S3.4: CRAF/14-3-3σ NanoBRET optimization
A) CRAF/14-3-3σ 1:10 and 1:100 ratio comparison (n = 3). 1:10 resulted in a larger fold increase. **B)** 14-3-3σ WT vs 14-3-3σ C38N NanoBRET. Stabilizers were dependent on the presence of C38 (n = 3). **C)** Comparison of lysate and in cell NanoBRET assays (n = 3). Both showed stabilization with CRAF-05.

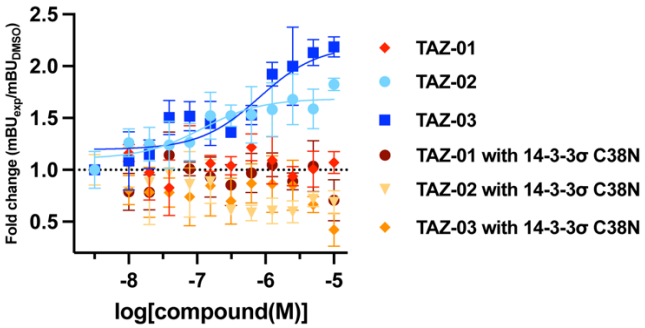

Figure S3.5: TAZ NanoBRET with 14-3-3σ C38N
Compounds bind to C38 (n=3).

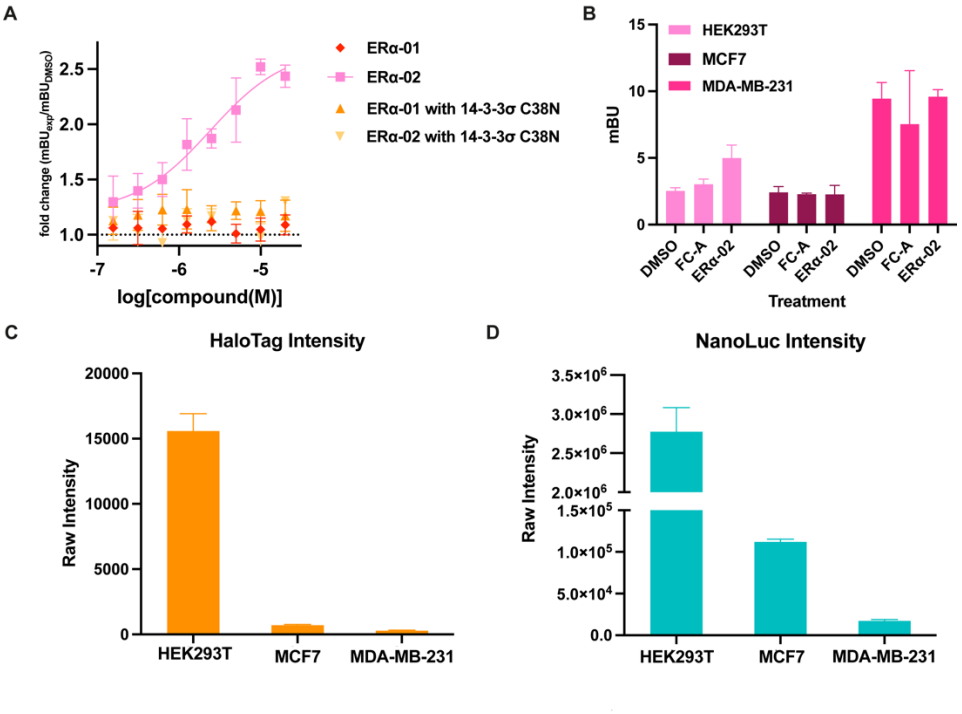

Figure S3.6: ERα/14-3-3σ NanoBRET optimization
A) ERα NanoBRET with 14-3-3σ C38N (n = 3). Compounds are dependent on C38. **B)** ERα/14-3-3σ NanoBRET cell line comparison with FC-A (30 μM) and ERα-02 (10 μM) treatment (n = 3). HEK293T showed a measurable stabilization with ERα-02. **C)** Raw HaloTag luminescence intensity in HEK293T, MCF7, and MDA-MB-231 (n = 3). **D)** Raw NanoLuc luminescence intensity in HEK293T, MCF7, and MDA-MB-231 (n = 3).

Author Contributions

H.R.V. and J.M.V. contributed equally to this work. The manuscript was written through contributions of all authors. All authors have given approval to the final version of the manuscript.

Funding

This research was funded by the National Institutes of Health grant GM147696.

Declaration of Conflicting Interests

The authors declare the following competing financial interest: M.R.A. is a co-founder and director of Ambagon Therapeutics.

Acknowledgements

The authors would like to thank Ambagon Therapeutics for providing 14-3-3σ/TAZ stabilizers. We also thank Dr. Luc Brunsveld and Dr. Christian Ottmann for collaborative discussion. We would like to thank Dr. Ziwen Jiang for assay support, Dr. Andrew J Ambrose for useful discussion, and Dr. Jezrael Lafuente Revalde and Zain Alam for instrument training. We also thank Sean Woods for assay support and discussion.

References

1. Arkin, M. R., Tang, Y. & Wells, J. A. Small-Molecule Inhibitors of Protein-Protein Interactions: Progressing toward the Reality. *Chem. Biol.* **21**, 1102–1114 (2014).

2. Ran, X. & Gestwicki, J. E. Inhibitors of Protein-Protein Interactions (PPIs): An Analysis of Scaffold Choices and Buried Surface Area. *Curr. Opin. Chem. Biol.* **44**, 75–86 (2018).

3. Andrei, S. A. *et al.* Stabilization of protein-protein interactions in drug discovery. *Expert Opin. Drug Discov.* **12**, 925–940 (2017).

4. Garlick, J. M. & Mapp, A. K. Selective Modulation of Dynamic Protein Complexes. *Cell Chem. Biol.* **27**, 986–997 (2020).

5. Schreiber, S. L. The Rise of Molecular Glues. *Cell* **184**, 3–9 (2021).

6. Dong, G., Ding, Y., He, S. & Sheng, C. Molecular Glues for Targeted Protein Degradation: From Serendipity to Rational Discovery. *J. Med. Chem.* **64**, 10606–10620 (2021).

7. Sasso, J. M. *et al.* Molecular Glues: The Adhesive Connecting Targeted Protein Degradation to the Clinic. *Biochemistry* **62**, 601–623 (2023).

8. Békés, M., Langley, D. R. & Crews, C. M. PROTAC targeted protein degraders: the past is prologue. *Nat. Rev. Drug Discov.* **21**, 181–200 (2022).

9. Chamberlain, P. P. & Hamann, L. G. Development of targeted protein degradation therapeutics. *Nat. Chem. Biol.* **15**, 937–944 (2019).

10. Soini, L., Leysen, S., Davis, J. & Ottmann, C. Molecular glues to stabilise protein-protein interactions. *Curr. Opin. Chem. Biol.* **69**, 102169 (2022).

11. Kenanova, D. N. *et al.* A Systematic Approach to the Discovery of Protein–Protein Interaction Stabilizers. *ACS Cent. Sci.* **9**, 937–946 (2023).

12. Sijbesma, E. *et al.* Site-Directed Fragment-Based Screening for the Discovery of Protein–Protein Interaction Stabilizers. *J. Am. Chem. Soc.* **141**, 3524–3531 (2019).

13. Sijbesma, E. *et al.* Structure-based evolution of a promiscuous inhibitor to a selective stabilizer of protein–protein interactions. *Nat. Commun.* **11**, 3954 (2020).

14. Toriki, E. S. *et al.* Rational Chemical Design of Molecular Glue Degraders. *ACS Cent. Sci.* **9**, 915–926 (2023).

15. King, E. A. *et al.* Chemoproteomics-enabled discovery of a covalent molecular glue degrader targeting NF-κB. *Cell Chem. Biol.* **30**, 394-402.e9 (2023).

16. Mayor-Ruiz, C. *et al.* Rational discovery of molecular glue degraders via scalable chemical profiling. *Nat. Chem. Biol.* **16**, 1199–1207 (2020).

17. Hallenbeck, K. K. *et al.* A Liquid Chromatography/Mass Spectrometry Method for Screening Disulfide Tethering Fragments. *SLAS Discov. Adv. Sci. Drug Discov.* **23**, 183–192 (2018).

18. Konstantinidou, M. *et al.* Structure-Based Optimization of Covalent, Small-Molecule Stabilizers of the 14-3-3σ/ERα Protein–Protein Interaction from Nonselective Fragments. *J. Am. Chem. Soc.* **145**, 20328–20343 (2023).

19. Obsilova, V. & Obsil, T. The 14-3-3 Proteins as Important Allosteric Regulators of Protein Kinases. *Int. J. Mol. Sci.* **21**, 8824 (2020).

20. Stevers, L. M. *et al.* Modulators of 14-3-3 Protein–Protein Interactions. *J. Med. Chem.* **61**, 3755–3778 (2018).

21. Obsil, T. & Obsilova, V. Structural basis of 14-3-3 protein functions. *Semin. Cell Dev. Biol.* **22**, 663–672 (2011).

22. Pennington, K. L., Chan, T. Y., Torres, M. P. & Andersen, J. L. The dynamic and stress-adaptive signaling hub of 14-3-3: emerging mechanisms of regulation and context-dependent protein–protein interactions. *Oncogene* **37**, 5587–5604 (2018).

23. Manschwetus, J. T. *et al.* Binding of the Human 14-3-3 Isoforms to Distinct Sites in the Leucine-Rich Repeat Kinase 2. *Front. Neurosci.* **14**, (2020).

24. Molzan, M. *et al.* Impaired Binding of 14-3-3 to CRAF in Noonan Syndrome Suggests New Approaches in Diseases with Increased Ras Signaling. *Mol. Cell. Biol.* **30**, 4698–4711 (2010).

25. Sijbesma, E. *et al.* Identification of Two Secondary Ligand Binding Sites in 14-3-3 Proteins Using Fragment Screening. *Biochemistry* **56**, 3972–3982 (2017).

26. De Vries-van Leeuwen, I. J. *et al.* Interaction of 14-3-3 proteins with the estrogen receptor alpha F domain provides a drug target interface. *Proc. Natl. Acad. Sci. U. S. A.* **110**, 8894–8899 (2013).

27. Lavoie, H. & Therrien, M. Regulation of RAF protein kinases in ERK signalling. *Nat. Rev. Mol. Cell Biol.* **16**, 281–298 (2015).

28. Park, E. *et al.* Architecture of autoinhibited and active BRAF–MEK1–14-3-3 complexes. *Nature* **575**, 545–550 (2019).

29. Kondo, Y. *et al.* Cryo-EM structure of a dimeric B-Raf:14-3-3 complex reveals asymmetry in the active sites of B-Raf kinases. *Science* **366**, 109–115 (2019).

30. Martinez Fiesco, J. A., Durrant, D. E., Morrison, D. K. & Zhang, P. Structural insights into the BRAF monomer-to-dimer transition mediated by RAS binding. *Nat. Commun.* **13**, 486 (2022).

31. Sun, Q. & Wang, W. Structures of BRAF–MEK1–14-3-3 sheds light on drug discovery. *Signal Transduct. Target. Ther.* **4**, 1–2 (2019).

32. Park, E. *et al.* Cryo-EM structure of a RAS/RAF recruitment complex. *Nat. Commun.* **14**, 4580 (2023).

33. Freeman, A. K. & Morrison, D. K. 14-3-3 Proteins: Diverse Functions in Cell Proliferation and Cancer Progression. *Semin. Cell Dev. Biol.* **22**, 681–687 (2011).

34. Molzan, M. *et al.* Stabilization of Physical RAF/14-3-3 Interaction by Cotylenin A as Treatment Strategy for RAS Mutant Cancers. *ACS Chem. Biol.* **8**, 1869–1875 (2013).

35. Ballone, A., Centorrino, F. & Ottmann, C. 14-3-3: A Case Study in PPI Modulation. *Molecules* **23**, 1386 (2018).

36. Wolter, M. *et al.* Selectivity via Cooperativity: Preferential Stabilization of the p65/14-3-3 Interaction with Semisynthetic Natural Products. *J. Am. Chem. Soc.* **142**, 11772–11783 (2020).

37. Richter, A., Rose, R., Hedberg, C., Waldmann, H. & Ottmann, C. An Optimised Small-Molecule Stabiliser of the 14-3-3–PMA2 Protein–Protein Interaction. *Chem. – Eur. J.* **18**, 6520–6527 (2012).

38. Visser, E. J. *et al.* From Tethered to Freestanding Stabilizers of 14-3-3 Protein-Protein Interactions through Fragment Linking. *Angew. Chem. Int. Ed Engl.* **62**, e202308004 (2023).

39. Wolter, M. *et al.* Fragment-Based Stabilizers of Protein–Protein Interactions through Imine-Based Tethering. *Angew. Chem. Int. Ed.* **59**, 21520–21524 (2020).

40. Cossar, P. J. *et al.* Reversible Covalent Imine-Tethering for Selective Stabilization of 14-3-3 Hub Protein Interactions. *J Am Chem Soc* **143**, 8454–8464 (2021).

41. Machleidt, T. *et al.* NanoBRET—A Novel BRET Platform for the Analysis of Protein–Protein Interactions. *ACS Chem. Biol.* **10**, 1797–1804 (2015).

42. Dale, N. C., Johnstone, E. K. M., White, C. W. & Pfleger, K. D. G. NanoBRET: The Bright Future of Proximity-Based Assays. *Front. Bioeng. Biotechnol.* **7**, (2019).

43. Robers, M. B. *et al.* Target engagement and drug residence time can be observed in living cells with BRET. *Nat. Commun.* **6**, 10091 (2015).

44. Cho, E. J. & Dalby, K. N. Luminescence Energy Transfer–Based Screening and Target Engagement Approaches for Chemical Biology and Drug Discovery. *SLAS Discov.* **26**, 984–994 (2021).

45. Wade, M., Méndez, J., Coussens, N. P., Arkin, M. R. & Glicksman, M. A. Inhibition of Protein-Protein Interactions: Cell-Based Assays. in *Assay Guidance Manual* (eds. Markossian, S. et al.) (Eli Lilly & Company and the National Center for Advancing Translational Sciences, 2004).

46. Jiang, Z. *et al.* Adaptor-Specific Antibody Fragment Inhibitors for the Intracellular Modulation of p97 (VCP) Protein–Protein Interactions. *J. Am. Chem. Soc.* **144**, 13218–13225 (2022).

47. Massoud, T. F. & Paulmurugan, R. Chapter 47 - Molecular Imaging of Protein–Protein Interactions and Protein Folding. in *Molecular Imaging (Second Edition)* (eds. Ross, B. D. & Gambhir, S. S.) 897–928 (Academic Press, 2021). doi:10.1016/B978-0-12-816386-3.00071-5.

48. Nadel, C. M., Ran, X. & Gestwicki, J. E. Luminescence complementation assay for measurement of binding to protein C-termini in live cells. *Anal. Biochem.* **611**, 113947 (2020).

49. Xu, D., Farmer, A., Collett, G., Grishin, N. V. & Chook, Y. M. Sequence and structural analyses of nuclear export signals in the NESdb database. *Mol. Biol. Cell* **23**, 3677–3693 (2012).

50. NanoBRET™ Protein:Protein Interaction System Protocol. https://www.promega.com/resources/protocols/technical-manuals/101/nanobret-protein-protein-interaction-system-technical-manual/.

Chapter 4

Small molecule stabilization of the 14-3-3σ/CRAF complex inhibits the MAPK pathway

Contributing Authors:

Holly R. Vickery[1,‡], Markella Konstantinidou[1,‡], Johanna M. Virta[1], Marloes A.M. Pennings[2], Maxime C.M. van den Oetelaar[2], R. Jeffrey Neitz[1], Christian Ottmann[2], Luc Brunsveld[2], and Michelle R. Arkin[1]

[1]Department of Pharmaceutical Chemistry and Small Molecule Discovery Center, University of California, San Francisco 94158, United States.

[2]Laboratory of Chemical Biology, Department of Biomedical Engineering and Institute for Complex Molecular Systems (ICMS), Eindhoven University of Technology, 5600 MB Eindhoven, The Netherlands

[‡]H.R.V. and M.K. contributed equally to this work.

Abstract

The hub protein 14-3-3 interacts with hundreds of client proteins and has diverse roles including transcription factor regulation and signal transduction. The kinase CRAF is regulated in two ways by 14-3-3: (1) interaction of 14-3-3 with phospho-Ser259 (pS259) CRAF inhibits CRAF by restraining the kinase and cysteine rich domains and (2) interaction of 14-3-3 with pS621 CRAF activates CRAF by promoting formation of the active dimer. We aim to stabilize the 14-3-3/CRAF pS259 interaction with small molecules to inhibit CRAF kinase activity and therefore inhibit MAPK pathway signaling. We have performed a mass spectrometry-based site-directed disulfide tethering screen to identify stabilizers of the 14-3-3/CRAF pS259 interaction. The screen identified five stabilizers of the 14-3-3/CRAF pS259 interaction which were selective for CRAF pS259 over four other 14-3-3/client interactions and showed no stabilization of the activating pS621 CRAF/14-3-3 interaction. Top 14-3-3/CRAF pS259 stabilizers identified in the disulfide tethering screen were non-selective for CRAF over other 14-3-3 clients. These fragments were computationally merged with another 14-3-3/client stabilizer to gain selectivity and potency for CRAF. This designed scaffold was modified based on binding and stabilization through mass spectrometry, fluorescence anisotropy, and X-ray crystallography. Optimized stabilizers have EC_{50} values of 0.3 – 5 μM and stabilize the complex over 200-fold by fluorescence anisotropy. These stabilizers show up to 1.6-fold stabilization of the 14-3-3/CRAF interaction in cells through a NanoBRET assay. The stabilizers also inhibit CRAF kinase activity by reducing NRAS/CRAF interaction and CRAF/CRAF dimerization up to 75% and 50%, respectively, indicating that they act as molecular glues of the 14-3-3/CRAF inhibited complex. 14-3-3/CRAF inhibitors also lead to up to 60% reduction in phospho-ERK, indicating inhibition of the MAPK pathway. This work has revealed how we can use small molecule-mediated modulation of PPIs as a novel method to inhibit the MAPK pathway and will be used to study the MAPK pathway in various disease states.

Introduction

The MAPK signaling pathway controls multiple cellular processes, including cell proliferation, differentiation, and survival.[1] Signaling is initiated with the binding of epidermal growth factor (EGF) to epidermal growth factor receptor (EGFR), which generates binding sites for adaptor proteins, like GRB2, to recruit the GEF SOS to the plasma membrane. SOS interacts with RAS, a small GTPase, which acts as a molecular switch and cycles between the inactive GDP-bound state to the active GTP state. GTP-RAS activates the first kinase of the pathway, RAF, via a complex, multistep process.[2–4] Upon translocation to the membrane, Ras activates the serine/threonine kinase function of RAF, which then phosphorylates and thus activates MEK, which ultimately phosphorylates ERK (Figure 4.1A). Once activated, ERK phosphorylates cytoplasmic and nuclear substrates, which are involved in numerous cellular functions.[5]

The simplified, linear representation of the pathway does not take into account the underlying dynamics and regulation of protein-protein interactions (PPIs) in the pathway. Especially for RAF, its regulation and kinase activity are controlled on different levels by phosphorylation, conformation, dimerization, and binding to 14-3-3 proteins. The kinase activity of RAF is suppressed when RAF is kept in a closed conformation and in that state, 14-3-3 proteins play a central role.[6,7] 14-3-3 proteins are adaptor proteins that recognize phospho-serine or phospho-threonine (pS/pT) sites on client proteins.[8,9] Two different hypotheses have been reported for the role of 14-3-3 in the regulation of RAF; 14-3-3, acting as a dimer, binds to two distinct sites in a single RAF molecule,[10] or 14-3-3 dimerizes different RAF molecules by connecting their kinase domains.[11,12] The three RAF isoforms (A-, B-, and CRAF) have highly conserved amino acid sequences and consist of three main domains: the conserved region 1 (CR1) domain on the N-terminus containing the RAS binding domain (RBD) and the cysteine-rich domain (CRD), CR2 which includes phosphorylation sites, and the C-terminus with the kinase catalytic domain (CAD). The 14-3-3 binding sites are located in the conserved regions on either

side of the kinase catalytic domain. The two 14-3-3 binding sites have opposite functions on the regulation of the pathway: regulatory roles for those located on CR2 (ARAF pS214, BRAF pS365, CRAF pS259), and structural roles for those located on the CR3 domain (ARAF p582, BRAF pS729, CRAF pS621) (Figure 4.1B).

In addition to a plethora of crystallographic studies, cryo-EM structures have recently begun to elucidate the underlying dynamics and provide structural insights, especially for PPI complexes involving BRAF, 14-3-3, and MEK.[13–15] Although only one cryo-EM structure of a 14-3-3/CRAF complex has been reported, CRAF activation is hypothesized to proceed in a similar manner as BRAF.[16,17] This hypothesis is supported by a recent single-molecule FRET (smFRET) study, which focused on the dynamics of CRAF and 14-3-3 binding in live cells.[18] Mutations at the 14-3-3 recognition sites, including CRAF phosphorylation sites pS259 and pS621, and the CRD region significantly affected the FRET distribution, indicating the importance of the 14-3-3/CRAF interaction in the regulation of RAF. In analogy to BRAF, the model for CRAF activation includes the transition from a monomeric, closed or autoinhibited state to the dimeric, open, active conformation. In the proposed model (Figure 4.1C), CRAF is maintained in the autoinhibited monomer state via interactions of the pS259 and pS621 with the 14-3-3 dimer. The pS259 regulatory phosphorylation site (corresponding to the BRAF pS365 site) and the pS621 structural phosphorylation site (corresponding to the BRAF pS729 site) are bound on the amphipathic grove of the 14-3-3 dimer. Upon pathway activation, CRAF is recruited to the plasma membrane and interacts with RAS via the RBD domain. This is followed by the release of the CRD domain from the autoinhibited complex and its interaction with RAS and the membrane. This exposes the CRAF pS259 site to dephosphorylation by the SHOC2-PP1 complex.[19,20] Dephosphorylation of the regulatory pS259 site allows the formation of an open monomer, which leads to the formation of the active dimer via the dimerization of RAF catalytic domains. This dimer can form either as a homodimer or a heterodimer, with each RAF structural phosphorylation site bound to a single 14-

3-3 monomer. In the BRAF cryo-EM structures, the active dimer is reported as a BRAF homodimer, however, CRAF preferentially forms heterodimers with BRAF, which increases the likelihood of heterodimerization between monomeric BRAF and monomeric CRAF bound to MEK.[12,21,22] CRAF and ARAF heterodimers have also been reported in KRAS-driven cancers.[23]

Aberrant activation due to mutations on the components of the MAPK pathway commonly occurs in different types of human cancers, thus the pathway is one of the most studied pathways in oncology. RAS mutations occur in 30% of human cancers.[24] BRAF is the most commonly mutated RAF isoform, with missense mutations occurring in 7-10% of human cancers.[25] CRAF gene fusions that promote RAS-independent CRAF dimerization are less common, but can occur in low-grade pediatric gliomas and pancreatic cancer.[26] ARAF S214C and CRAF P261A mutations were identified in lung adenocarcinoma and non-small cell lung cancer, respectively.[27,28,29] Upregulated ERK signaling, due to germline and somatic gain-of-function mutations in the proteins of the MAPK pathway, is also associated with a family of developmental disorders, commonly referred to as RASopathies.[30]

Due to the frequency of BRAF oncogenic mutations, the development of BRAF inhibitors has been the focus of extensive drug discovery campaigns.[31,32] A significant challenge, especially for first generation BRAF inhibitors has been the phenomenon of “paradoxical activation”. Although BRAF inhibitors seemed to suppress RAF activity and ERK signaling in cells expressing BRAF V600E, in cells expressing wild-type BRAF, most inhibitors caused an undesired increase in RAF activity and ERK signaling.[33,34] An early report in 2005 showed that BRAF can activate CRAF through a mechanism involving 14-3-3 mediated heterooligomerization and CRAF transphosphorylation.[11] The BRAF/CRAF heterodimers were reported as part of the physiological activation process and their presence was enhanced by 14-3-3.[12] Recently, it was shown that CRAF dimerization with ARAF is involved in KRAS driven tumor growth and the RAF dimerization

process is one of the mechanisms linked to RAF inhibitor resistance in cancer therapy.[23,33,35] Currently, the common belief is that the BRAF/CRAF heterodimer is the primary species involved both in native signaling and paradoxical activation. Consequently, direct CRAF inhibitors are also expected to be impacted by paradoxical activation.[36] Interestingly, an AMPK inhibitor (AMPKi) was able to block the paradoxical activation in Ras-mutated cancer cells by blocking the phosphorylation of CRAF S621.[37]

Here, taking into account that CRAF is considered the key isoform involved in the RAF inhibitor-induced paradoxical activation and as an alternative approach to direct RAF inhibition, we are focusing on disrupting the transition of the autoinhibited CRAF monomer to the active dimer by stabilizing the autoinhibited monomer 14-3-3/CRAF pS259 complex using molecular glues. The feasibility of this approach is supported by the fact that a complex natural product, Cotylenin-A (CN-A), is a known stabilizer of the 14-3-3/CRAF interaction.[38] CN-A binds exclusively near the CRAF pS259 regulatory site, which contains a threonine in the +1 position (Figure 4.1D), but not near the structural pS621 site, which has a +1 glutamic acid. In RAS mutant cancer models, CN-A was inactive as single agent, however, co-treatment with an anti-EGFR antibody synergistically suppressed tumor growth.[38]

In our recent work, we successfully developed covalent, irreversible 14-3-3σ/ERα stabilizers starting from hits identified in a MS-based site-directed disulfide tethering screening.[39] The 14-3-3σ/ERα stabilizers, although tested for potential CRAF pS259 stabilization, lacked specific interactions with the +1 Thr of CRAF pS259, and thus lacked molecular recognition and were mostly inactive for the 14-3-3σ/CRAF pS259 complex. Here, we used a computational fragment-merging approach and combined the previously identified chloroacetamide piperidine moiety (analog 1074202) with fragments bearing a sulfonyl group (TC-521), which were originally developed as lysine-targeting 14-3-3/p65 stabilizers (Figure 4.1E,F).[40] The sulfonyl-containing

fragments showed two different conformations in the crystal structures, in close proximity to the phosphorylated residue. By merging the two fragment moieties, our aim was to maintain the covalent bond with the native cysteine of 14-3-3σ and at the same time use the sulfonyl group as a flexible handle for potential polar interactions with the CRAF pS259 peptide. The most potent 14-3-3σ/CRAF molecular glues resulted in increased levels of the regulatory phosphorylation, CRAF pS259, and stabilization of the PPI in cells. These stabilizers also decreased CRAF activation and signaling through the MAPK pathway as measured by a decrease in phospho-ERK (pERK).

Results and Discussion

Chemical Optimization

The chemical modifications on the designed scaffold were divided into five groups (Figure 4.1F). Modifications (I) and (II), in close proximity to CRAF, included the investigation of appropriate linkage of the two merged fragments and substitutions on the aryl ring. Modification (III) focused on the replacement of the generic, promiscuous piperidine ring with spirocycles with varying ring sizes and orientations. Modification (IV) involved the replacement of the chloroacetamide warhead with halogenated analogs. The last modification was the combination of the most potent elements of (II) and (III) and aimed at the exploration of synergistic effects.

In analogy to our previous work, two orthogonal assays were used for screening (Figure S4.1D). Briefly, the MS assay was used to monitor the formation of the irreversible covalent bond with the native cysteine (C38) in the periphery of the binding groove on 14-3-3σ. Dose responses as compound titrations were performed in the absence and presence of the CRAF pS259 phospho-peptide (pp), to distinguish between neutral binders and stabilizers. Full-length BRAF

cryo-EM structures allowed for the direct comparison with crystal structures of 14-3-3/RAF peptide complexes (Figure S4.1A-C). The high degree of conformational overlap between the sequence derived from the full-length client protein and the phospho-peptides justifies the use of the peptide in screening and follow-up assays. The experiment was performed as a time-course, with measurements every 8 hours, after an 1h incubation. All the compounds were also screened against the 14-3-3σ/ERα protein-peptide interaction to rule out undesired stabilization. None of the compounds showed any effect on ERα (data not shown). Additionally, the compounds were tested in an FA assay in the presence of FAM-labeled CRAF pS259 peptide. For stabilizers, a significant increase in anisotropy was observed in the overnight measurement. The full dose-response data for all compounds are available in the supporting information. The dose-response data from both assays were also visually compared in the form of bar graphs. For the MS data, the bar graphs represented the % bound at 1 μM compound concentration and 100 nM 14-3-3σ (10:1 ratio) in the absence or presence of peptide. For FA experiments, the EC_{50} values from the overnight measurement were calculated and plotted as bar graphs showing the positive log EC_{50} value (pEC_{50}). Compounds acting as stabilizers were expected to show an increase in both types of bar graphs.

For the development of the designed scaffold, the first key modification (I) focused on the appropriate linkage of the two merged fragments (Figure 4.2). Chemically, the two fragments could be merged with the reaction of an appropriately modified piperidine with various sulfonyl chlorides. The sulfonyl chloride moiety could be either attached via a methylene group to the aryl ring and or directly attached to the aryl ring without the methylene. In the first case, the compounds would be more similar to compound 1074202 regarding their size, whereas in the second case the compounds would be smaller and more similar to the TC521 fragment. Seven compounds were synthesized to test both linkages with small modifications on the aryl ring (no substitution, -F or -Cl substitution). In both the MS and FA assays, compounds with the methylene linker were

inactive (**6**-**9**) (Figure 4.2A,B). Interestingly, compounds without the methylene, showed stabilization of the 14-3-3σ/CRAF pS259 interaction. Compound **10** (no substitution on the aryl ring) was a very weak stabilizer, but compounds with halogen substituents showed significant improvement. In the MS assay, analogs **11** (p-F) and **12** (p-Cl) showed binding in the presence of the CRAF pS259 peptide and very low binding in the apo screening (no peptide) (Table S4.1, Figure S4.2, S4.3). In the FA assay, in compound titrations the EC_{50} values were 17 ± 3 μM for **11** and 3 ± 1 μM for **12** (Figure S4.4, Table S4.2). The two compounds were further validated as 14-3-3σ/CRAF pS259 stabilizers in FA protein titrations at 100 μM compound concentration. 14-3-3σ was titrated into 10 nM FAM-labeled CRAF pS259 peptide in the presence of DMSO or saturating concentration of the compounds. Compounds **11** and **12** showed *app*K_D of 400 nM (4-fold stabilization) and 190 nM (22-fold stabilization), respectively (Figure S4.5, Table S4.2). Two more analogs bearing the p-Cl substitution were synthesized. Compound **13** had a longer 3C-linker of the chloroacetamide warhead. Remarkably, this modification made the compound inactive. Compound **14** had a pyridine ring, instead of a benzyl ring. This modification also reduced the potency. For further SAR development, the 1C-linker was kept constant, and modifications focused on aryl ring substitutions.

Aryl ring modifications (II) focused on substitutions in o-, m- and p-positions either with electron-withdrawing or electron-donating groups (Figure 4.2A,B, Figure S4.2, S4.3, S4.4, Table S4.1, S4.2). The aryl substituents, being in close proximity to CRAF, were expected to be involved in the formation of specific interactions and, as a result, have a direct effect on binding and cooperativity. Regarding SAR, moving the -F substituent from the p- position to o- (**15**) or m- (**16**) reduced the potency. Larger and strongly electron withdrawing groups, like the -CF_3 group were not tolerated in the m-position (**17**), indicating potential steric hindrance. In the p-position the -CF_3 analog (**18**) showed moderate stabilization (FA EC_{50} = 17 ± 1 μM, *app*K_D = 280 nM, 15-fold stabilization, Figure S4.4, S4.5). The slightly larger -OCF_3 analog (**19**) seemed more potent in the

MS assay than the FA assay (FA EC_{50} = 13 ± 3 μM, *app*K_D = 213 nM, 14-fold stabilization), however both compounds were weaker in the FA assay, compared to the p-Cl analog **(12).** Introducing a p-cyano group (**20**) significantly reduced the activity (FA EC_{50} > 150 μM). One more analog with an electron-withdrawing group was synthesized, bearing a p-formyl substituent **(21)**, thus containing two covalent warheads that could simultaneously interact with C38 and K122 of 14-3-3σ. This analog was weak in the MS assay and lacked selectivity with the CRAF pS259 and ERα peptides (Figure S4.2, S4.3, Table S4.1, S4.2, ERα data not shown). In the FA assays, although the EC_{50} with CRAF pS259 appeared to be low (5 ± 1.0 μM, Figure S4.4), the protein titration assay resulted in an *app*K_D of 480 nM and the compound showed only 9-fold stabilization (Figure S4.5). The above observations support the hypothesis that the increased apo binding due to the double warheads decreased the cooperativity.

A crystal structure was solved for analog **12** (p-Cl) in complex with 14-3-3σ and CRAF pS259 and showed that the compound was bound in an unusual, upward conformation at the 14-3-3σ/CRAF pS259 peptide interface (Figure 4.2C). The chloroacetamide moiety of **12** bound covalently to C38 of 14-3-3σ, and two hydrogen bonds were formed between the carbonyl group and R41, and one between the -NH of the amide and the backbone carbonyl of C38, at 2.7 Å, 3.0 Å, and 3.3 Å respectively. Importantly, the sulfonyl group of **12** interacted with K122 of 14-3-3σ via a charged-assisted hydrogen bond and with T260 (+1 position) of CRAF via a hydrogen bond (3.2 Å and 3.4 Å, respectively). The p-Cl group of **12** is positioned in a small pocket at the top of the 14-3-3σ binding groove, in which p-Cl forms halogen bonds with D215 (4.1 Å and 3.8 Å), L218 (3.8 Å), and I219 (3.9 Å) of 14-3-3σ. Furthermore, a halogen bond between p-Cl and V263 of CRAF (3.8 Å) increased the stabilization of the complex. Besides the interactions of **12**, N42 of 14-3-3σ directly interacts with the backbone of CRAF by two hydrogen bonds (both 3.0 Å) (Figure 4.2D). The overlay of the binary 14-3-3/CRAF crystal structure with the ternary complex with analog **12** reveals a significant conformational change in helix 9 of 14-3-3σ, in a downward

position closer to the compound. This movement of helix 9 clamps the stabilizer inside the 14-3-3σ binding groove and causes conformational changes of D215, L218, and I219 that provide the formation of halogen bonds with **12** (Figure 4.2E). Crystallization of analog **21** in complex with 14-3-3σ/CRAF revealed the formation of two covalent bonds via the chloroacetamide and p-formyl of **21** with C38 and K122 of 14-3-3σ, respectively (Figure 4.2F). However, no interactions were observed with CRAF T260. Therefore, the conformation of the stabilizer flipped in the 14-3-3σ binding pocket, which abolished the interactions that were observed with **12**. In addition, helix 9 of 14-3-3σ did not move upon binding of analog **21** (Figure 4.2G).

For further SAR development, two bigger halogens were introduced, p-Br (**22**) and p-I (**23**) to further investigate the effect of potential halogen bonds. In the MS assay, both analogs showed significantly faster kinetics than the p-Cl analog (**12**) and in the time courses 100% bound was reached in the first hour measurement in moderate micromolar compound concentrations. The time course graphs didn't show large shifts over time, indicating that the compounds were able to rapidly adopt a favorable and stable conformation (Figure S4.2, S4.3, Table S4.1). The p-I analog (**23**) showed almost no binding to the apo protein, thus acting as a potent molecular glue for the 14-3-3σ/CRAF pS259 complex. For the p-Br analog (**22**), less than 25% binding was observed in the apo screening in the overnight measurement, indicating that this compound was also highly cooperative. In the FA assay, both compounds were very active with EC_{50} values in the low micromolar to nanomolar range (1 ± 0.5 μM for **22**, 1 ± 0.5 μM for **23**, Figure S4.4, Table S4.2). In protein titrations, the *app*K_D of 14-3-3σ/CRAF pS259 complex was 8427 nM and decreased to 47 nM in the presence of **22** and 30 nM in the presence of **23**. Thus, compounds **22** and **23** stabilized the 14-3-3σ/CRAF pS259 complex by 179- and 280-fold, respectively (Figure S4.5, Table S4.2). Crystal structures were solved for both compounds **22** and **23** (Figure 4.2H). Interestingly, the structure of analog **23** binding at the 14-3-3σ/CRAF interface revealed the presence of a water network that connects the pS259 and T260 of CRAF with K122 of 14-3-3σ,

the sulfonyl of **23**, all the way along the backbone and N262 of CRAF towards N42 of 14-3-3σ (Figure 4.2H). This water network was not observed for the binary 14-3-3σ/CRAF structure, or in the presence of analogs **12** and **22**, which might explain the high stabilization factor of **23**. Notably, the distance between the sulfonyl group and the +1 T260 is longer for **23** (4.1 Å) compared to **12** (3.4 Å), therefore the direct hydrogen bond in presence of analog **12** can be compensated with the water-mediated hydrogen bonds in presence of **23**. Structural overlays of 14-3-3σ and CRAF showed conformational changes of residues N262, V263, and H264 of CRAF and N42 of 14-3-3σ upon binding of **23** compared to **12** and **22**. The movement of these residues could be assigned to the substitution of a larger halogen and/or the presence of the water network.

Electron donating groups, including p-methyl (**24**) and p-methoxy (**25**) were also investigated, but were less tolerated than the p-Cl analog (**12**). The piperonal moiety (**26**), which could potentially form hydrogen bonds with the +1 Thr of the peptide was not tolerated, probably due to steric hindrance (Figure S4.2, S4.3, S4.4, S4.5, Table S4.1, S4.2).

Taking into account the observed favorable interactions between the compounds and the CRAF residues in close proximity to them, we investigated additional potential interactions by synthesizing double and triple halogen-substituted aryl analogs (Figure 4.3, Figure S4.6, S4.7, S4.8). The two analogs containing a p-F substituent and an additional fluorine in o- (**27**) or m-position (**28**) were both weak in the MS assay. In the FA assay, compound **27** with the additional o-fluoro-group was significantly weaker compared to **28** where the fluoro-group was in m-position (FA EC_{50} > 150 μM and EC_{50} = 88 ± 2 μM, respectively, Figure S4.8, Table S4.1). Notably, both compounds were less potent than compound **11** that had only the p-F substitution (FA EC_{50} = 17 ± 3 μM). Two more analogs were synthesized: **29** (m-F, p-Cl) and **30** (m-Cl, p-F). **29** was significantly more potent than **30** in both assays. Although low FA EC_{50} values were observed for both compounds (1 ± 0.5 μM for **29** and 12 ± 2 μM for **30**), the shape of the curves and the

reached maximum differed significantly in the biophysical assays (Figure S4.7, S4.8). In protein titrations, **29** showed an *app*K_D of 100 nM (84-fold stabilization), whereas **30** only 780 nM (4-fold stabilization) (Figure S4.5, Table S4.2). Additionally, analog **29** bearing the m-F group was more potent in protein titrations compared to **12**, which was non-substituted (*app*K_D of 100 nM for 29 and 190 nM for 12, Figure S4.5, Table S4.2).

A crystal structure was solved for **29**/14-3-3σ/CRAF pS259 and elucidated the underlying cause for the differences (Figure 4.3C). The compound adopted an upward conformation, similar to compound **12** (p-Cl analog), and similar interactions were observed. In contrast to **12**, additional water-mediated hydrogen bonds between the sulfonyl of **29**, K122 of 14-3-3σ, and T260 and pS259 of CRAF connect all three components in the complex. However, this water network was smaller compared to the structure with analog **23** (Figure 4.2H). Importantly, the m-fluoro-substituent was oriented towards 14-3-3σ and formed an additional halogen bond with I219 at 2.4 Å. The binding mode of **29** supported the observations from the screening assays, which showed steric hindrance from the o-position and the tolerance of only the small, fluoro group in the m-position. Consequently, in compound **30**, where the larger chloro-substituent was in the m-position, steric hindrance would occur. This observation translated in both screening assays, as lower maximum. Similar graphs were obtained for **31**, with the bulky CF_3-group in m-position and a Cl-group in p-position. On the other hand, a fluoro-substitution in m-position was well-tolerated for analogs **32** (p-CF_3) and **33** (p-OMe). The electron withdrawing CF_3-group in **32** was more potent than the electron-donating methoxy group in **33** (FA EC_{50}= 4 ± 1 μM and *app*K_D 140 nM for **32** and EC_{50}= 9 ± 1 μM and *app*K_D 230 nM for **33**, Figure S4.5, S4.8, Table S4.2). A crystal structure was solved for **32**/14-3-3σ/CRAF pS259 showing a similar conformation of analog **32** compared to **29**, including the halogen bond of m-F with I219. The p-CF_3 group, although able to bind in a similar manner as the other p-halogen-containing analogs, was involved in weaker halogen bonds, which resulted in weaker stabilization compared to **29**. Strikingly, replacing the

aryl ring with aliphatic rings containing F-substituents led to completely inactive compounds (**34**, **35**).

Due to the consistent importance of halogen bonds in the stabilization of the 14-3-3σ/CRAF interaction, an exhaustive fluorine scanning was performed for p-Br analogs (Figure 4.3, Figure S4.6, S4.7, S4.8). In agreement with previous observations, the o-F analog was weaker than the m-F (**36** and **37**, respectively). Analog **37** showed fast kinetics in the MS assay and was highly potent in the FA assay (EC_{50}= 5 ± 1 μM, *app*K_D 92 nM, 92-fold stabilization, Figure S4.5, Table S4.2). For the triple substituted analogs, the two ortho-analogs (2,3-difluoro **38**, 2,5-difluoro **39**) were weaker in the MS assay and the observed maximum was lower in the FA assay. For the 3,5-difluoro analog (**40**), the shape of the MS and FA graphs also indicated steric hindrance, correlating with the lower reached maximum. All of these observations were in good agreement with the *app*K_D values in protein titrations (**36**: 240 nM, **37**: 92 nM, **38**: 218 nM, **39**: 420 nM, **40**: 320 nM) (Figure S4.5, Table S4.2). A crystal structure of compound **37** was solved in complex with 14-3-3σ/CRAF pS259 (Figure 4.3D). Similar conformations and interactions were observed for **37** compared to analog **29**. The larger halogen p-Br of **37** compared to p-Cl of **29** could form more optimal halogen bonds with D215, L218, and I219 of 14-3-3σ. An overlay of double halogen-substituted aryl analogs, **29**, **32**, and **37**, with the single halogen-substituted analog, **22**, showed a similar orientation of the compounds. The m-F interacted with I219 and the backbone of D215 of 14-3-3σ with halogen bonds. In addition, the presence of the m-F seemed to slightly affect the conformation of the linker and piperidine ring (Figure 4.3E). The compounds showed comparable *app*K_D in protein titrations (Figure S4.5, Table S4.2), despite the observed differences in the halogen bonds.

The next modification (III) focused on the piperidine position, while maintaining the m-F, p-Br aryl ring substitution (Figure 4.4, Figure S4.9, S4.10, S4.11, Table S4.1, S4.2). The

introduction of a methyl group on the piperidine ring on a short 0C-chloroacetamide warhead (**43**) made the compound almost inactive. The methyl group was tolerated on the 1C-warhead (**46**), but the compound was less active compared to **37** that lacked the methyl group (EC_{50} = 11 ± 1 μM, *app*K_D 170 nM for **46** and EC_{50} = 5 ± 1 μM, *app*K_D 92 nM for **37**) (Figure S4.12, Table S4.2). To further investigate this position, the piperidine ring was replaced with a series of bicyclic or spiro amines. Compound **49** was tolerated (FA EC_{50}= 47 ± 4 μM) but was less active than the linear analog **37**. Analog **52**, with two additional fluoro-substituents on the same ring system was even weaker (FA EC_{50} =94 ± 9 μM) and displayed increased apo binding in the MS assay. The addition of an extra bond on the spiro-ring system (**55**) made this longer compound inactive. All the above point to the limited available space at the rim of the 14-3-3σ/CRAF pS259 interface. Different bicyclic ring systems were incorporated in compounds **58**, **61** and **64**, aiming to alter the orientation of the warhead. However, these compounds showed increased apo binding, which translated in the FA assay as weaker stabilization. Apo binding was reduced for the spirocycles bearing an oxygen atom in the rings (**67**, **70**). The 6-membered ring in **70** was more potent in the FA assay compared to the 5-membered analog **67** (FA EC_{50} = 2 ± 1 μM, *app*K_D 58 nM for **70**, EC_{50} = 14 ± 1 μM, *app*K_D 250 nM for **67**). Replacement of the piperidine position with an aryl ring made the compound inactive (**73**)**.** For the most active analog of this group, compound **70**, a crystal structure was solved in complex with 14-3-3σ/CRAF pS259 (Figure 4.4C). Notably, the key interactions between the compound and 14-3-3σ/CRAF are maintained, including its halogen bonds with 14-3-3σ and V263 of CRAF and hydrogen bonds between the sulfonyl group, K122 of 14-3-3σ, and T260 of CRAF. Compared to the piperidine analog **37**, the water network that is present on the interface of 14-3-3σ/CRAF/**70** is extended, resulting in more hydrogen bonds with the CRAF peptide, potentially stabilizing its conformation. Also, an additional hydrogen bond was formed between the oxygen of the spirocycle with N42. Therefore, the water-mediated hydrogen bonding network is further elongated starting from CRAF pS259 along the backbone and CRAF N262, 14-3-3σ N42, towards the spiro ring of **70** (Figure 4.4D). Furthermore, the orientation of

the compound was slightly tilted compared to the linear, piperidine analog **37**, which was possibly necessary to form the additional hydrogen bond with 14-3-3σ N42 (Figure 4.4E).

Regarding warhead modifications (IV), two variations of the chloroacetamide electrophile were tested on the weak analog **52**. Introducing warheads with two chlorine atoms (**74**) or with a fluoro-acrylamide (**75**) made the compounds completely inactive in both assays. A plausible hypothesis is that the bigger warheads were unable to access the 14-3-3σ C38 due to steric hindrance.

Warhead replacements were not pursued further. Instead, we focused on combining the most potent structural features of modifications (II) and (III). The last chemical modification (V) focused on combinations between different spirocycles and aryl rings bearing the p-Br or p-I groups or the double m-F,p-CF_3 or m-F,p-Br substitutions (Figure 5, Figure S4.13, Table S4.1, S4.2). For analogs with the same oxygen spirocycle as **70**, three aryl ring combinations were tested p-Br (**78**), p-I (**79**) and m-F,p-CF_3 (**80**). The p-Br analog (**78**) showed slightly reduced apo binding and was highly potent in the FA assay (FA EC_{50} = 2 ± 1 μM, *app*K_D 40 nM for **78**, EC_{50} = 2 ± 1 μM, *app*K_D 58 nM for **70**) (Figure S4.12, Table S4.1, S4.2). The iodine analog **79**, although slightly less active in the MS assay (potentially due to worse solubility compared to the bromo-analog), showed similar stabilization in the FA assay (FA EC_{50} = 2 ± 1 μM, *app*K_D 35 nM for **79**). The double substituted analog (**80,** m-F,p-CF_3) appeared significantly weaker in both the MS and FA assays (FA EC_{50} = 9 ± 2 μM, *app*K_D 420 nM for **80**), due to the lack of the specific halogen bond originating from the para position in the previous analogs. The observed worse solubility in the MS assay for those analogs, led to the design of analog **83**, which contains a similar spirocycle as **82**, but lacks the oxygen. The potential loss of the hydrogen bond with N42 in this case did not seem to affect the MS assay or the FA compound titrations significantly (EC_{50} = 5 ± 2 μM for **83**). However, analog **83** appeared slightly weaker in FA protein titrations compared to **70** (*app*K_D 102

nM for **83**, *app*K_D 58 nM for **70**). Lastly, a smaller bicyclic ring system was introduced (two 5-membered rings, without oxygen) and led to a significant improvement in the case of **86**. The -*S* analog reacted rapidly in the MS assay and in the FA assay and showed high stabilization (FA EC_{50} = 1 ± 1 µM, *app*K_D 28 nM, 300-fold stabilization). The -*R* analog (**89**) was weaker in the MS assay with increased apo binding but was inactive in the FA compound and protein titrations (Figure S4.12, S4.13, Table S4.1, S4.2). Crystal structures were solved for analogs **78**, **79**, **80**, **83** and **86**, supporting the observed SAR (Figure 4.5C-G). The binding mode of analog **78** at the 14-3-3σ/CRAF interface showed similar interactions as for analog **70**. The piperidine analog of **78**, compound **22**, did not show any water-mediated hydrogen bonds, while **78** caused the presence of a large hydrogen bond network (Figure 4.5C). This water network is likely not induced by the oxygen in the spiro ring, as analog **83** and **86** without this oxygen showed a similar water network (Figure 4.5D). The overlay of analogs **70** and **83** reveals that the presence of the oxygen caused the slight shift of the spiro ring towards N42 of 14-3-3σ, resulting in increased stabilization (Figure 4.5E). Interestingly, analog **86** with two 5-membered rings, induced a similar shift of the stabilizer towards CRAF as **70**, without the oxygen present in the spiro ring (Figure 4.5F,G). The 5-membered rings of **86** have an increased ring strain compared to the 6-membered rings of the other analogs, thereby potentially decreasing the entropic penalty of binding.

After establishing the SAR for the 14-3-3σ/CRAF pS259 molecular glues in the biochemical assays, we selected eleven analogs for further evaluation (Figure 4.6A); first we tested their selectivity over all the regulatory and structural sites of ARAF, BRAF and CRAF, and then we tested their activity in cell assays. Compound **8**, which lacked activity in the CRAF pS259 assays, was used as a negative control.

The compounds were tested in an MS assay for potential selectivity over the other regulatory sites, using the acetylated ARAF pS214 and BRAF pS365 phospho-peptides at 2xK_D

(Figure 4.6B, Figure S4.14, S4.15, Table S4.3). Regarding, the sequences surrounding the regulatory phosphorylation sites, the ARAF pS214 site has the same sequence as the CRAF pS259 site (+1 to +5 amino acids: TPNVH). The BRAF pS365 site varies only in the +1 residue, which is an alanine instead of a threonine (APNVH). Despite the same +1 to +5 sequences for ARAF pS214 and CRAF pS259, different selectivity profiles were observed in the MS assay. Overall, analogs containing the promiscuous piperidine moiety (**22**, **23**, **29**, **32**, **37**) showed increased binding in the presence of the ARAF pS214 peptide (comparable or slightly higher than with the CRAF pS259 peptide). Remarkably, analogs containing spiro-rings (**70**, **78**, **79**, **80**, **83**, **86**) instead of the piperidine showed very low binding in the presence of ARAF pS214, in contrast to the CRAF pS259 data (Figure 4.6B, Figure S4.14). A plausible explanation lies in the plasticity of the peptides, which could adopt different conformations in solution. The piperidine position seemed to have a greater contribution compared to the substituents on the aryl ring, suggesting that the conformation of the peptides in solution varied. For the BRAF pS365 site, which lacked the +1 threonine, all compounds showed low binding (Figure 4.6B, Figure S4.15), which did not exceed the apo binding, observed in the absence of the peptides. The +1 alanine residue in BRAF pS365 site lacks the ability to form a hydrogen bond with the compounds, thus specific molecular recognition is highly unlikely. In other words, the observed hydrogen bond between the compounds and the +1 Thr in CRAF pS259 was driving the selectivity over the BRAF pS365 site, where the +1 residue was small and hydrophobic.

Moreover, the compounds were tested in FA protein titrations with 10nM of each peptide. For the ARAF pS214 site, similar SAR was observed as in the MS assay (Figure 4.6C, Figure S4.16, Table S4.4); analogs with the piperidine moiety (**22**, **23**, **29**, **32**, **37**) showed significant stabilization of the 14-3-3σ/ARAF pS214 complex. The greatest effect was observed for compounds **22** (p-Br) and **23** (p-I), which contained the larger halogens in p-position (*app*K_D of 12 nM, 337-fold and 15 nM 270-fold stabilization, respectively). The spiro-analogs **78** (p-Br) and **79**

(p-I) showed significantly weaker stabilization (*app*K_D of 250 nM, 16-fold and 270 nM 15-fold stabilization respectively), indicating that the presence of the spiro-ring had a greater impact that the halogens in the p-position. For the BRAF pS365 site, all the compounds showed low affinity (fold stabilization 4-15-fold, Figure 4.6C, Figure S4.17, Table S4.4). The weak stabilization effect was associated with the residues in positions +2 to +5 (PNVH), which were common in all the regulatory sites.

For the structural sites (ARAF pS582, BRAF pS729, CRAF pS621), the sequences of the +1 to +4 amino acids were conserved (EPSL). The +1 glutamic acid engaged in an ionic bond with K122 (published CRAF pS621 structure, PDB: 4IEA). In agreement with a previous report for the natural product CN-A,[38] none of the compounds showed stabilization for the ARAF pS582, BRAF pS729 and CRAF pS621 sites (Figure S4.18, S4.19, S4.20). The explanation for this lack of stabilization was obvious in the crystal structures of the binding site. In addition to the ionic bond between the +1 glutamic acid and 14-3-3σ K122, the presence of the sulfonyl group would lead to an unfavorable electrostatic interaction with the glutamic acid, due to partial negative charges on both substituents. The expected lack of stabilization was confirmed by compound and protein titrations. Overall, the tested compounds showed preferential stabilization for the CRAF pS259 site, with significant *app*K_D shifts starting from 10 μM in the affinity measurement to low nanomolar.

14-3-3σ/CRAF binding in cells

The ten most active compounds in the biochemical assays with 14-3-3σ/CRAF pS259 were further validated in cell assays (Figure 4.6A). Compound **8** served as the negative control. Binding of full-length 14-3-3σ/CRAF was measured in cells using a NanoBRET assay (Figure 4.7A).[41] In this assay, CRAF is tagged with NanoLuciferase and 14-3-3σ is tagged with HaloTag. The interaction was measured in the absence and presence of stabilizer, with the expectation that

a molecular glue would increase the BRET signal, indicating an enhanced interaction. The NanoBRET assay resulted in a range of fold stabilization by each molecular glue with up to 1.6-fold stabilization and EC_{50} values ranged from 0.1-2 μM (Figure 4.7B, Figure S4.21D). Compound **23** resulted in the highest fold stabilization at 1.61-fold, followed by **22** at 1.47-fold. Compounds **22** and **23** were also among the most potent stabilizers, with EC_{50} values of 0.20 μM and 0.18 μM, respectively. Binding of full-length 14-3-3σ/CRAF was further validated through co-immunoprecipitation (co-IP). NRAS Q61L, FLAG-CRAF, and HA-14-3-3σ were transfected and IP was performed with anti-flag beads. We measured up to a 3-fold increase in 14-3-3σ pulled down with FLAG-CRAF normalized to FLAG band intensity (Figure 4.7C). The increase in 14-3-3σ pulled down is dependent on transfecting FLAG-CRAF (Figure S4.21A).

One function of 14-3-3 is that it can protect phosphorylated residues on its client proteins from dephosphorylation. The top 10 stabilizers plus compound **8** were evaluated for their effect at protecting CRAF pS259 from dephosphorylation by western blot. We measured up to 3.15-fold increase in CRAF pS259 levels with **23** (Figure 4.7D). The two different compound scaffolds represented by the top 10 compounds generally had different efficacy in cells. **22**, **23**, **29**, **32**, and **37** resulted in a larger fold increase in CRAF pS259 protection (1.91-3.15), whereas **70**, **78**, **79**, **83**, and **86** resulted in a lower fold increase (1-2.28). We could also measure an increase in endogenous CRAF pS259 levels in KRAS G12C cancer cells, where compound **23** showed a 1.5-fold increase in CRAF pS259 levels relative to total CRAF (Figure S4.21B). The stabilizers showed minimal increase in phosphorylation of the regulatory phosphorylation site ARAF pS214 (Figure S4.21C). **23** resulted in only 1.5-fold increase in ARAF pS214 levels and 3.15-fold increase in CRAF pS259 levels.

In addition to measuring 14-3-3σ/CRAF binding, we developed NanoBRET assays to quantify 14-3-3σ/ARAF and 14-3-3σ/BRAF binding to determine compound selectivity in cells. The top 10 stabilizers show various amounts of selectivity between the three RAFs (Figure S4.21D-F). Figure 4.7E shows how compound **22** affects the binding of 14-3-3σ with the three

RAFs to identify stabilizer selectivity with full-length proteins in cells. **22** shows an increase in BRET signal with all three RAFs, but the calculated EC_{50} values indicate that **22** is slightly selective for 14-3-3σ/CRAF over ARAF and BRAF, with EC_{50} values of 0.2 μM (CRAF), 4.7 μM (ARAF), and 0.7 μM (BRAF). Conversely, treatment with compound **70** only results in stabilization of the 14-3-3σ/CRAF complex, not 14-3-3σ/ARAF or 14-3-3σ/BRAF (Figure 4.7F). Additionally, both **23** and **70** require 14-3-3σ Cys38 to stabilize the 14-3-3σ/CRAF PPI, as mutation of this residue results in no stabilization (Figure 4.7E,F).

Stabilizer effects on CRAF activity

To analyze the mechanism of these 14-3-3σ/CRAF pS259 molecular glues, we have developed NanoBRET assays to measure the interactions between NRAS and CRAF as well as CRAF and CRAF to identify the effect of 14-3-3σ/CRAF stabilization on NRAS/CRAF interaction and CRAF dimerization. We expect to see a decrease in both NRAS/CRAF NanoBRET and CRAF/CRAF NanoBRET with addition of stabilizer since we are stabilizing the autoinhibited monomer complex where CRAF is a monomer and not expected to interact with Ras. The NRAS/CRAF and CRAF/CRAF NanoBRET were performed with NRAS Q61L to activate the MAPK pathway. Small molecule stabilization of 14-3-3σ/CRAF resulted in up to 75% reduction in NRAS Q61L/CRAF interaction with **22** (Figure 4.8A). Treatment with compound **23** resulted in a 52% decrease in NRAS Q61L/CRAF interaction. As expected, compound **8** did not alter NRAS Q61L/CRAF binding. CRAF/CRAF NanoBRET showed up to a 43% decrease in CRAF dimer formation with **22** and a 47% decrease in CRAF dimer formation with compound **23** in the presence of NRAS Q61L (Figure 4.8B). The decrease in both NRAS Q61L/CRAF and CRAF/CRAF NanoBRET indicates that the stabilizers are gluing the 14-3-3σ/CRAF autoinhibited monomer complex and shifting the equilibrium of the 14-3-3σ/CRAF mechanism away from the active form of CRAF.

To further analyze the effects of 14-3-3σ/CRAF stabilizers on the MAPK pathway, we measured the level of pERK. ERK is the final kinase in the MAPK signaling pathway and

phosphorylates many transcription factors to regulate gene expression. Inhibiting CRAF kinase activity is expected to decrease signaling through the MAPK pathway and, therefore, decrease levels of pERK. In CRAF dependent KRAS G12D cancer cells, treatment with pan-RAF inhibitors LY3009120 and Naporafenib resulted in 93% and 80% decrease in pERK, respectively. Treatment with 14-3-3σ/CRAF pS259 stabilizer **22** decreased pERK levels by 47% and compound **23** resulted in 60% decrease in pERK levels. This decrease in pERK levels normalized to total ERK indicates that the 14-3-3σ/CRAF stabilizers are effectively inhibiting CRAF kinase activity and, therefore, MAPK pathway signaling.

Conclusions

14-3-3σ/CRAF pS259 stabilization with small molecule molecular glues is a novel method to inhibit the MAPK pathway in cancer. Our stabilizers covalently bind 14-3-3σ C38 and make various interactions with CRAF T260-V263 and water networks. Stabilization of the 14-3-3σ/CRAF pS259 peptide complex was measured with these molecular glues, which showed selectivity for CRAF pS259 over ARAF pS214, BRAF pS365, ARAF pS582, BRAF pS729, CRAF pS621, and other 14-3-3σ client proteins, such as ERα. These stabilizers have been used to dissect the mechanism of CRAF activation and resulted in reduced NRAS/CRAF interaction and CRAF dimerization. 14-3-3σ/CRAF pS259 stabilizers ultimately lead to inhibition of CRAF kinase activity and decreased signaling through the MAPK pathway. These compounds can serve as invaluable tools for advancing our understanding of RAF biology, while also holding promise for optimization as potential therapeutics for RAS mutant cancers.

Figures

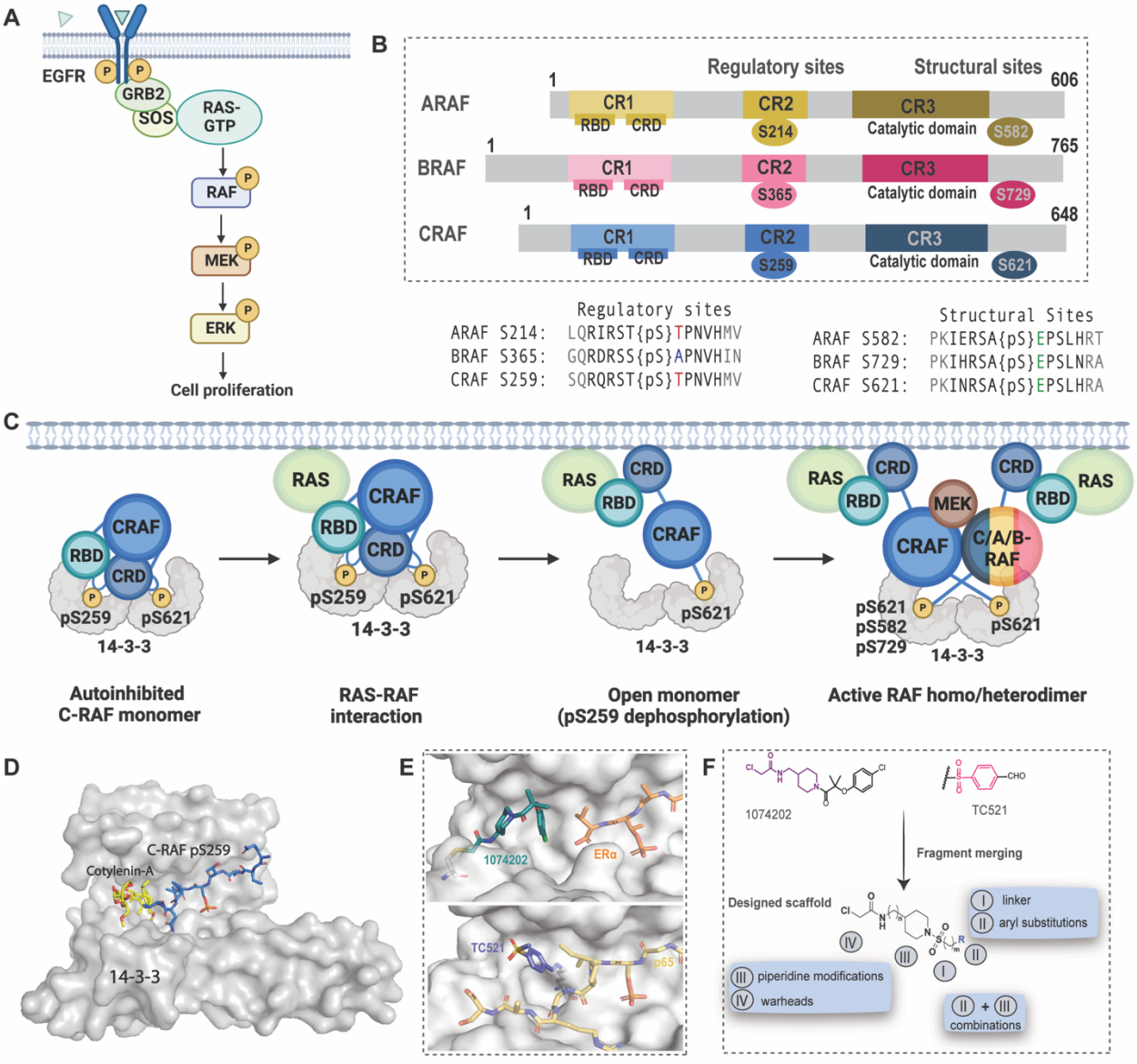

Figure 4.1: 14-3-3 regulation of RAF kinases
A) MAPK pathway schematic. **B)** Regulatory and structural phosphorylation sites on A-, B-, and CRAF. Sequences for phosphorylation sites with differences and similarities in +1 residues highlighted. **C)** Proposed mechanism of monomer to dimer transition for CRAF, based on 14-3-3/BRAF and 14-3-3/CRAF cryo-EM structures. **D)** Crystal structure of CN-A bound to the 14-3-3ζ/CRAF pS259 complex. PDB 4IHL. **E)** Top: Crystal structure of 1074202/14-3-3σ/ERα (PDB 8AWG). Bottom: Crystal structure of fragment TC521/14-3-3σ/p65 (PDB 6YOW). **F)** Fragment merging general scaffold for 14-3-3σ/CRAF pS259 stabilizers.

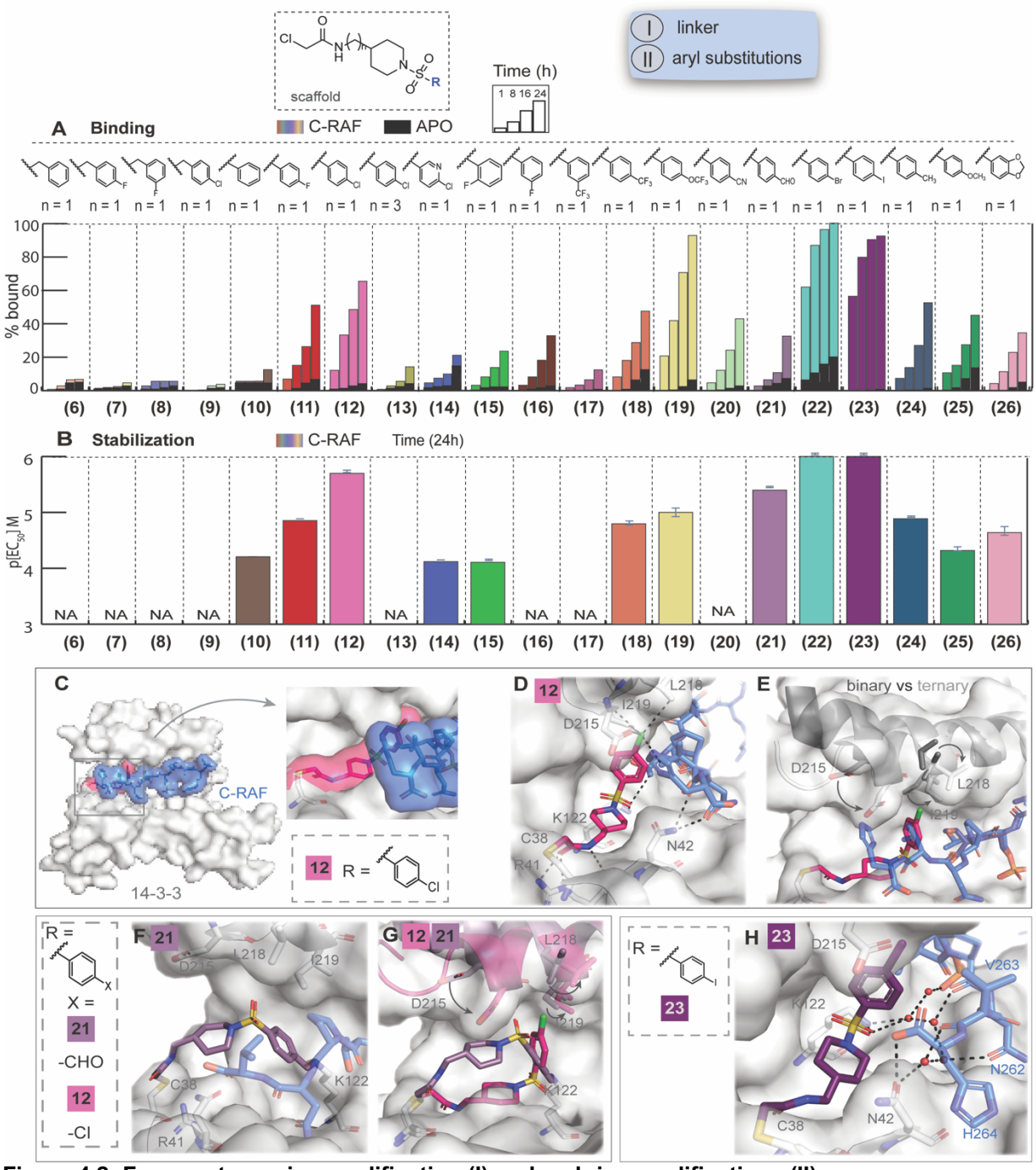

Figure 4.2: Fragment merging modification (I) and aryl ring modifications (II)
A) MS bar graphs at 1 µM compound, 100 nM 14-3-3σ (10:1 ratio). CRAF pS259 data are shown in different colors, apo data (in the absence of peptide) are shown in black. For each compound, time course experiments were performed with measurements at 1h, 8h, 16h and 24h. **B)** Bar graphs of FA compound titration pEC_{50} values after overnight incubation. CRAF pS259 data are shown with different colors. **C)** Crystal structure of 14-3-3σ (grey), CRAF pS259 peptide (blue), and **12** (pink). **D)** Interactions of **12** at the 14-3-3σ/CRAF pS259 interface. **E)** Movement of helix 9 of 14-3-3σ comparing the binary (dark grey) with ternary (light grey) 14-3-3σ/CRAF/**12** structures. **F)** Crystal structure of 14-3-3σ (grey), CRAF pS259 (blue), and **21** (purple). **G)** Overlay of analogs **12** (pink) and **21** (purple). **H)** Interactions of **23** (dark purple) at the 14-3-3σ/CRAF interface are shown in black dashes and water molecules as red dots.

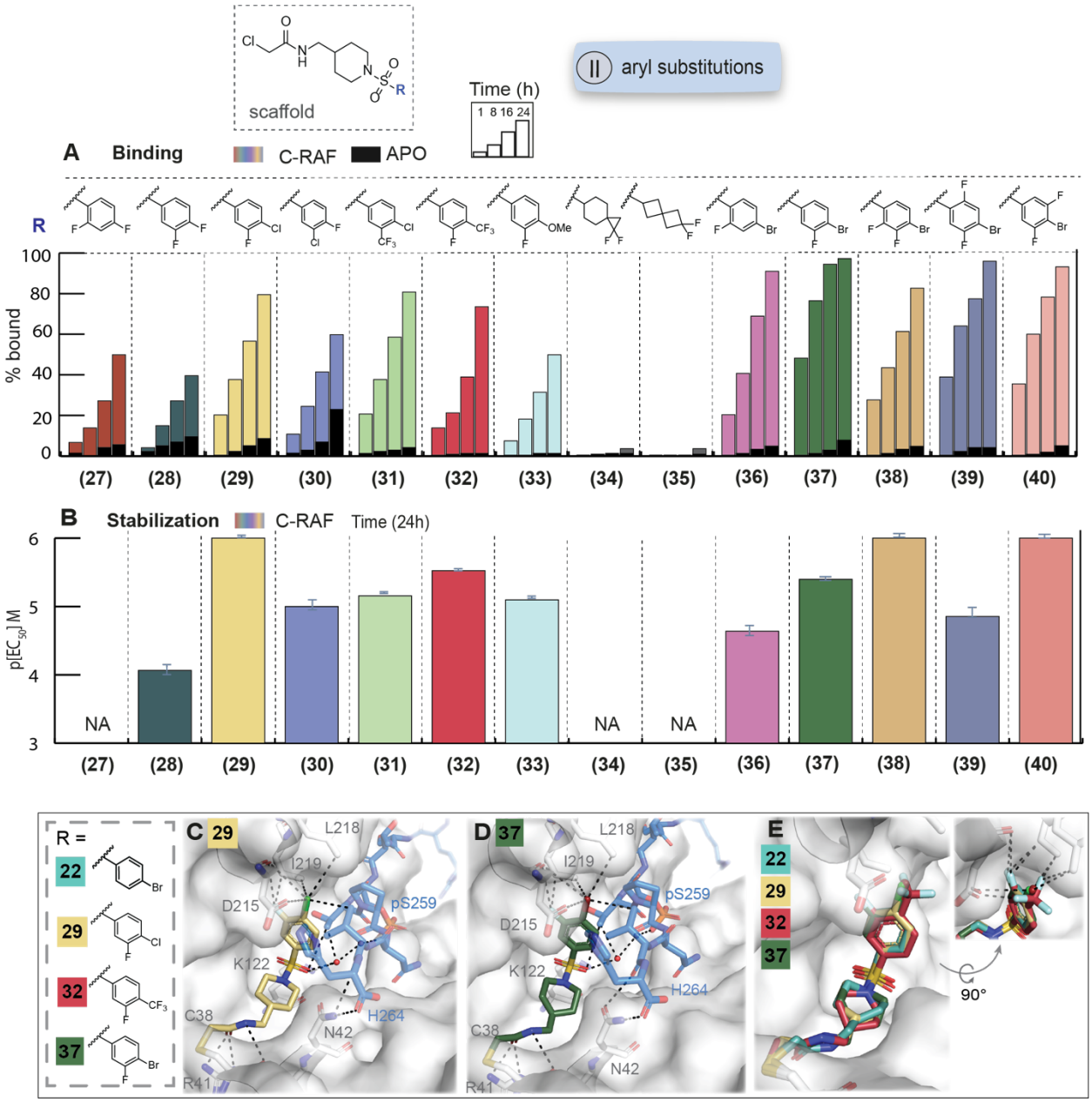

Figure 4.3: Poly-substitutions on the aryl ring and aliphatic analogs

A) MS bar graphs at 1 µM compound, 100 nM 14-3-3σ (10:1 ratio). CRAF pS259 data are shown in different colors, apo data (in the absence of peptide) are shown in black. For each compound, time course experiments were performed with measurements at 1h, 8h, 16h and 24h. **B)** Bar graphs of FA compound titration pEC_{50} values after overnight incubation. CRAF pS259 data are shown with different colors. Interactions of analog **29** (yellow) **(C)** and analog **37** (green) **(D)** at the 14-3-3σ (grey)/CRAF pS259 (blue) interface. **E)** Structural overlay of analogs **22** (cyan), **29** (yellow), **32** (red), **37** (green).

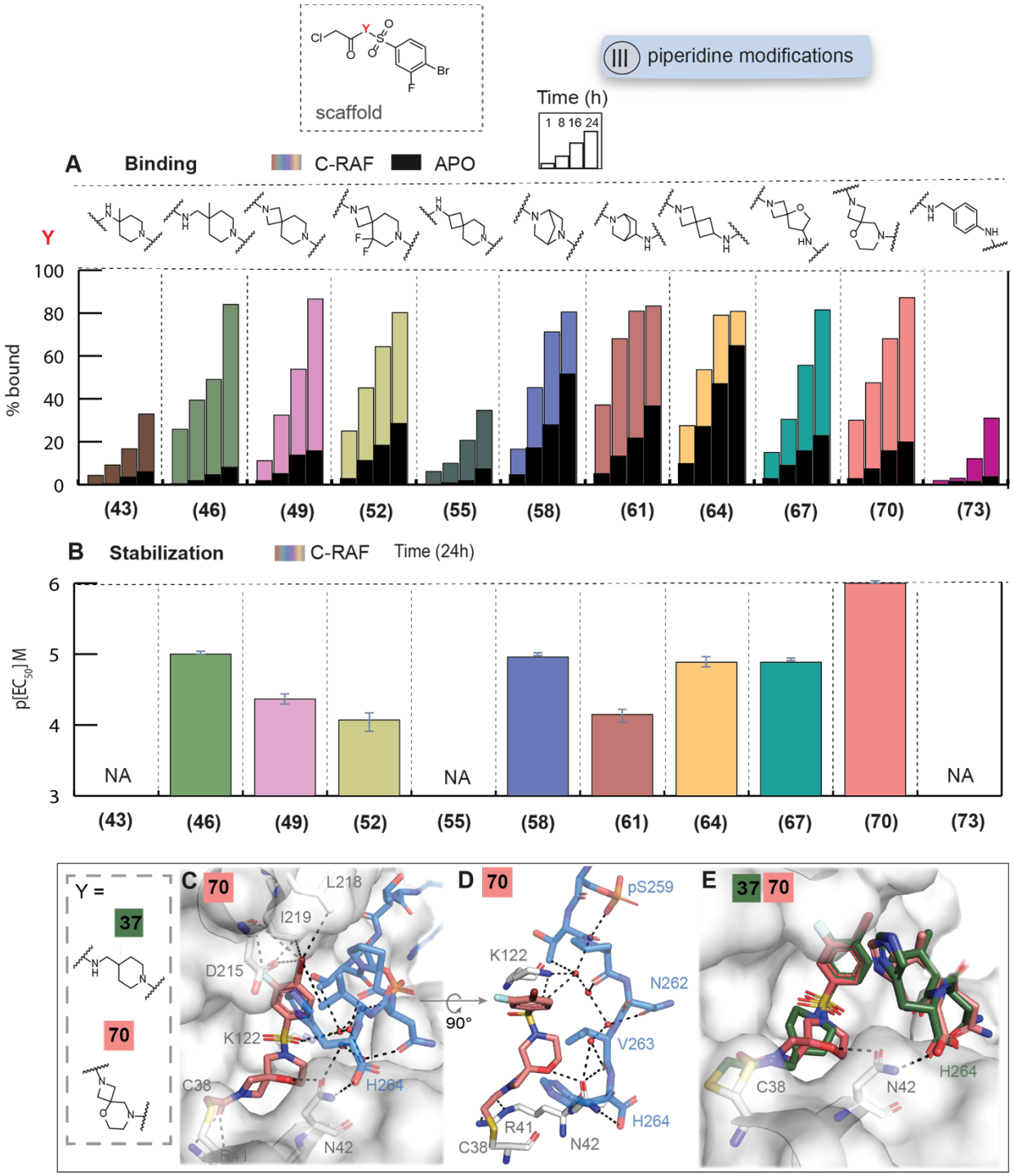

Figure 4.4: Piperidine replacements (III)

A) MS bar graphs at 1 µM compound, 100 nM 14-3-3σ (10:1 ratio). CRAF pS259 data are shown in different colors, apo data (in the absence of peptide) are shown in black. For each compound, time course experiments were performed with measurements at 1h, 8h, 16h and 24h. **B)** Bar graphs of FA compound titration pEC_{50} values after overnight incubation. CRAF pS259 data are shown with different colors. **C)** Interactions of **70** (salmon) at the 14-3-3σ (grey) / CRAF pS259 (blue) interface. **D)** Hydrogen bond network between 14-3-3σ residues (white), CRAF pS259 (blue), and **70**, mediated by water. **E)** Structural overlay of analogs **37** (green) and **70** (salmon).

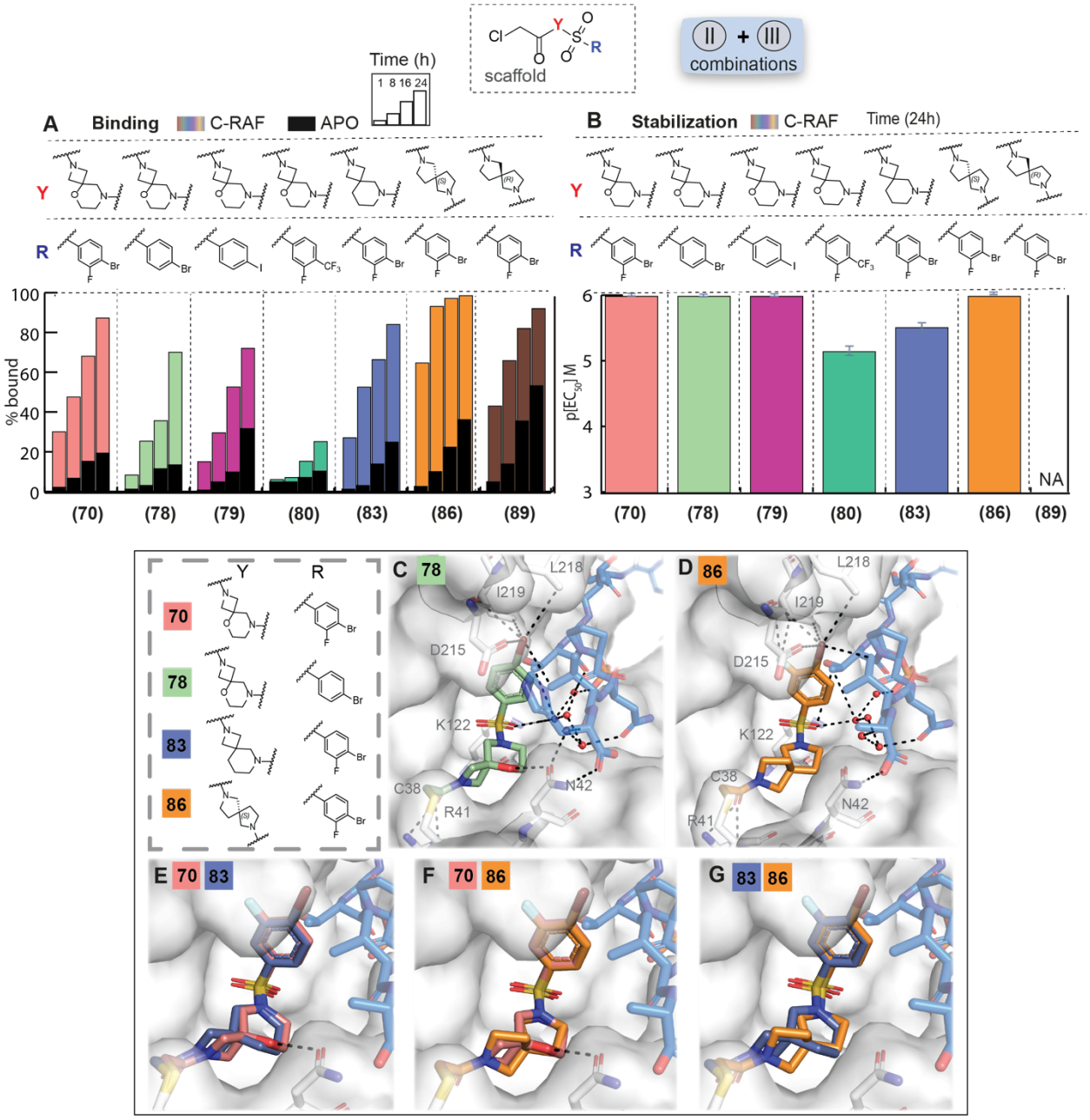

Figure 4.5: Combinations of spirocycles and aryl ring modifications (V)
A) MS bar graphs at 1 μM compound, 100 nM 14-3-3σ (10:1 ratio). CRAF pS259 data are shown in different colors, apo data (in the absence of peptide) are shown in black. For each compound, time course experiments were performed with measurements at 1h, 8h, 16h and 24h. **B)** Bar graphs of FA compound titration pEC_{50} values after overnight incubation. CRAF pS259 data are shown with different colors. Interactions of **78** (light green) **(C)** and **86** (orange) **(D)** at the 14-3-3σ (grey) / CRAF pS259 (blue) interface. Structural overlays of analogs **70** (salmon) and **83** (blue) **(E)**, **70** (salmon) and **86** (orange) **(F)**, and **83** (blue) and **86** (orange) **(G)**.

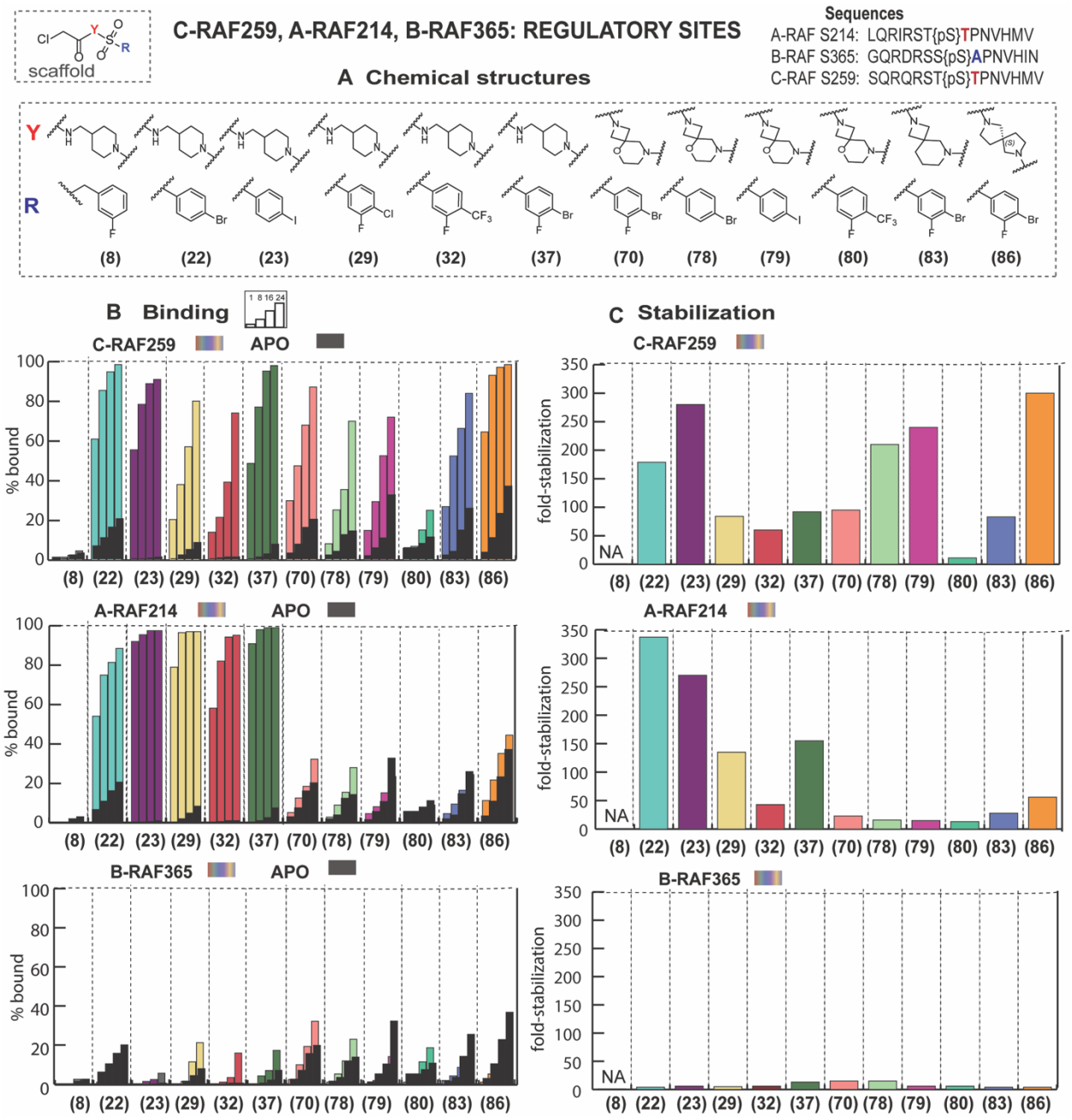

Figure 4.6: Stabilizer selectivity with A-, B-, and CRAF

A) Chemical structures of compounds tested in biochemical assays for all regulatory RAF sites. **B)** MS bar graphs at 1 µM compound, 100 nM 14-3-3σ (10:1 ratio), CRAF pS259 data (top left), ARAF pS214 (middle left), BRAF pS365 (bottom left). For each compound apo bar graphs are shown in black. Time course experiments were performed with measurements at 1h, 8h, 16h and 24h. **C)** Fold-stabilization observed in FA protein titrations after overnight incubation in the presence of 100 µM compound, 10 nM CRAF pS259 (top right), ARAF pS214 (middle right), BRAF pS365 (bottom right). Data are shown in SI (Table S4.4 for the MS, S4.5 for the FA).

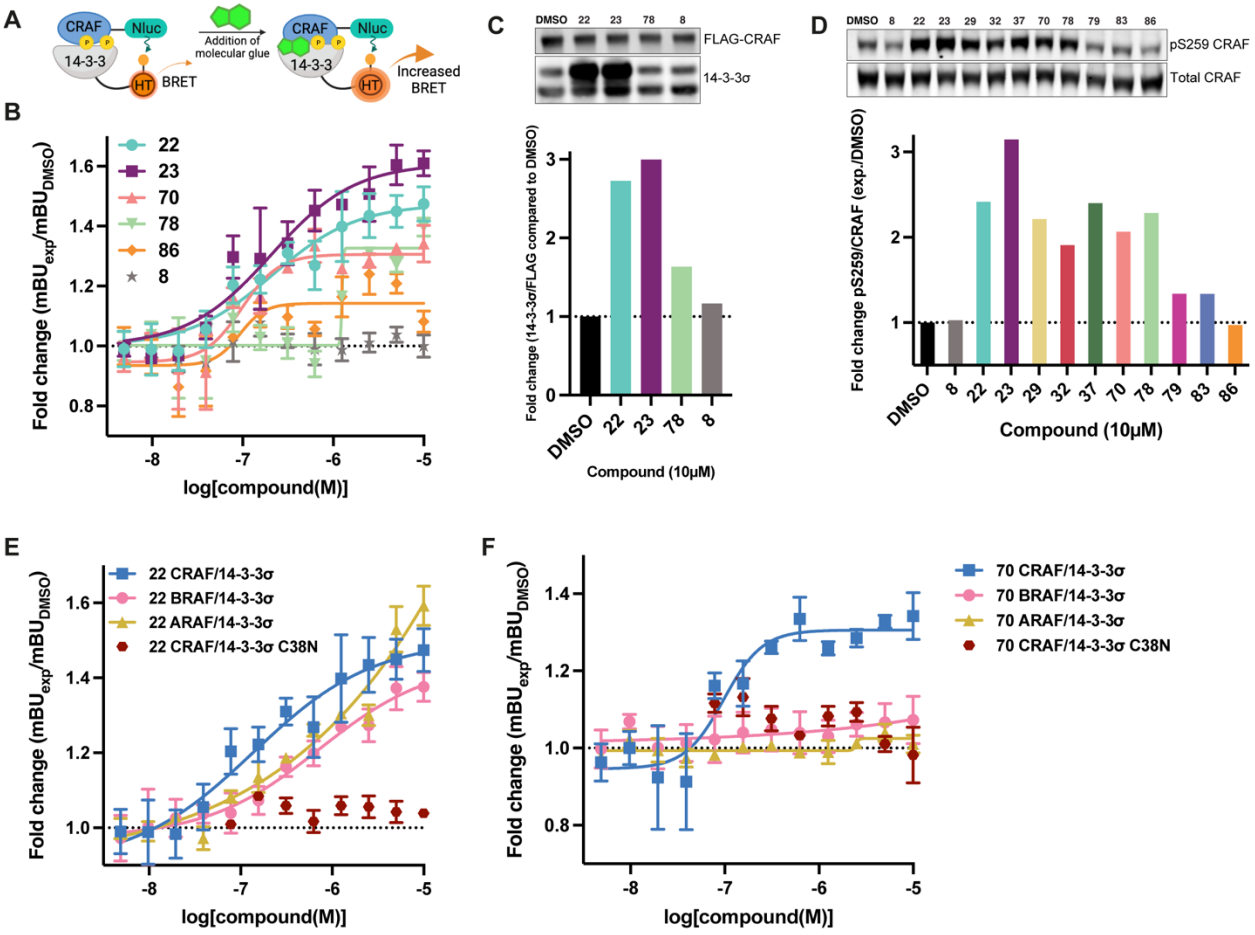

Figure 4.7: Results of top stabilizers on 14-3-3σ/RAF binding in cells

A) Schematic of NanoBRET assay. CRAF is tagged with NanoLuc and 14-3-3σ is tagged with HaloTag. Molecular glues are expected to increase in the BRET signal. **B)** NanoBRET results for 14-3-3σ/CRAF with 5 of the top stabilizers plus an inactive compound **8**. Stabilizers resulted in various levels of stabilization and EC_{50} values between 100 nM – 1 μM. **C)** Co-IP pulling down on FLAG-CRAF and measuring the amount of 14-3-3σ bound. **23** resulted in 3-fold increase in 14-3-3σ/CRAF interaction. **D)** Protection of pS259 CRAF with treatment of stabilizer. **23** resulted in over 3-fold increase in CRAF pS259 levels normalized to total CRAF. **E)** Comparison of 14-3-3σ/A-, B-, and CRAF NanoBRET to measure selectivity of compound **22** between the RAFs. **22** stabilizes 14-3-3σ/CRAF the most but is non-selective. Stabilization requires 14-3-3σ C38. **F)** Comparison of 14-3-3σ/A-, B-, and CRAF NanoBRET to measure selectivity of compound **70** between the RAFs. **70** is selective for CRAF over A- and BRAF. Stabilization requires 14-3-3σ C38.

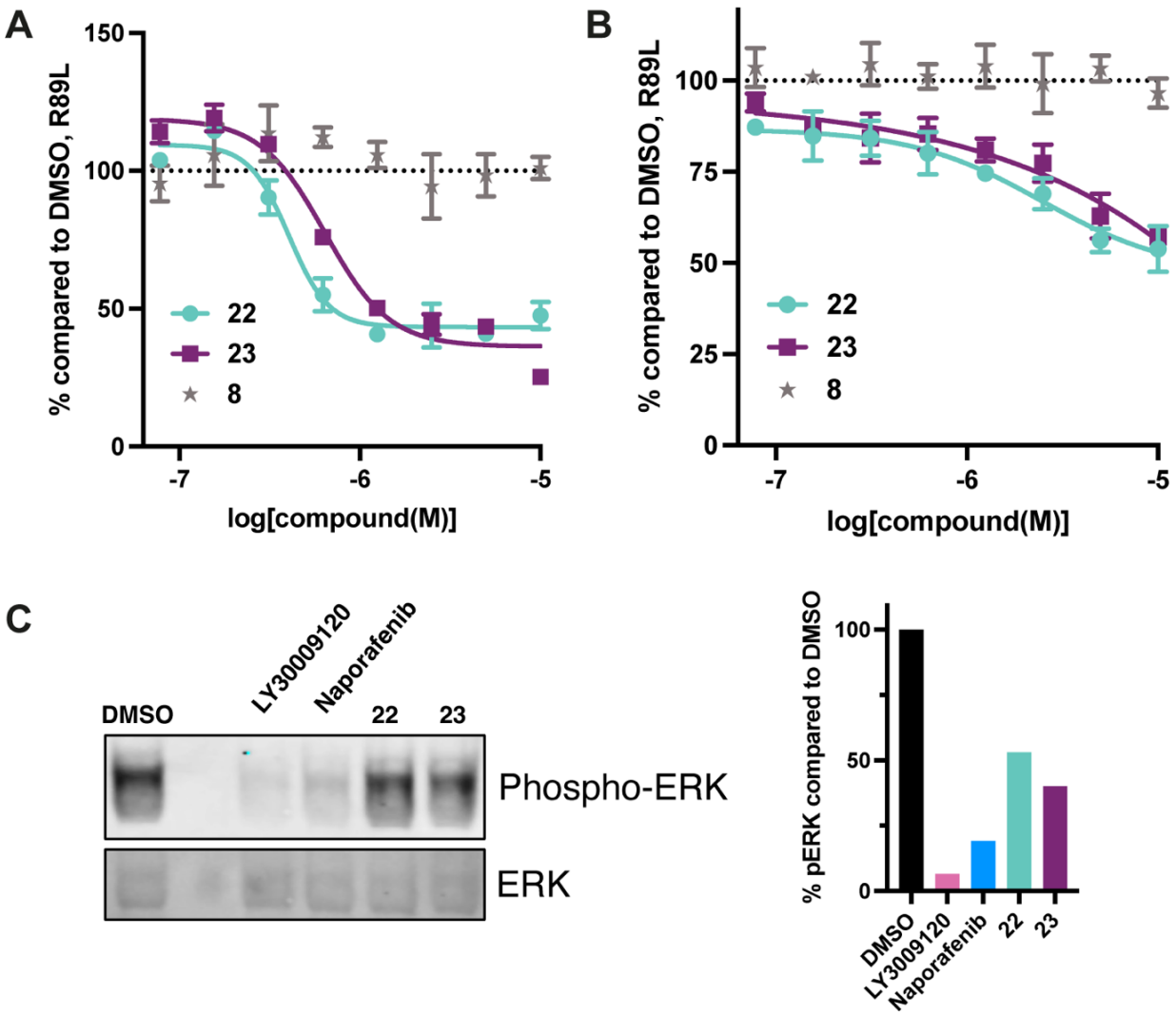

Figure 4.8: Results of top stabilizers on CRAF activity in cells
A) NRAS Q61L/CRAF NanoBRET. **23** results in up to 75% reduction in NRAS Q61L/CRAF interaction. **B)** CRAF/CRAF NanoBRET. **22** results in 50% reduction in CRAF dimerization. **C)** pERK levels after treatment. Commercial RAF inhibitors result in up to 90% reduction in pERK and **23** results in 60% reduction in pERK levels compared to total ERK.

Supplementary Figures

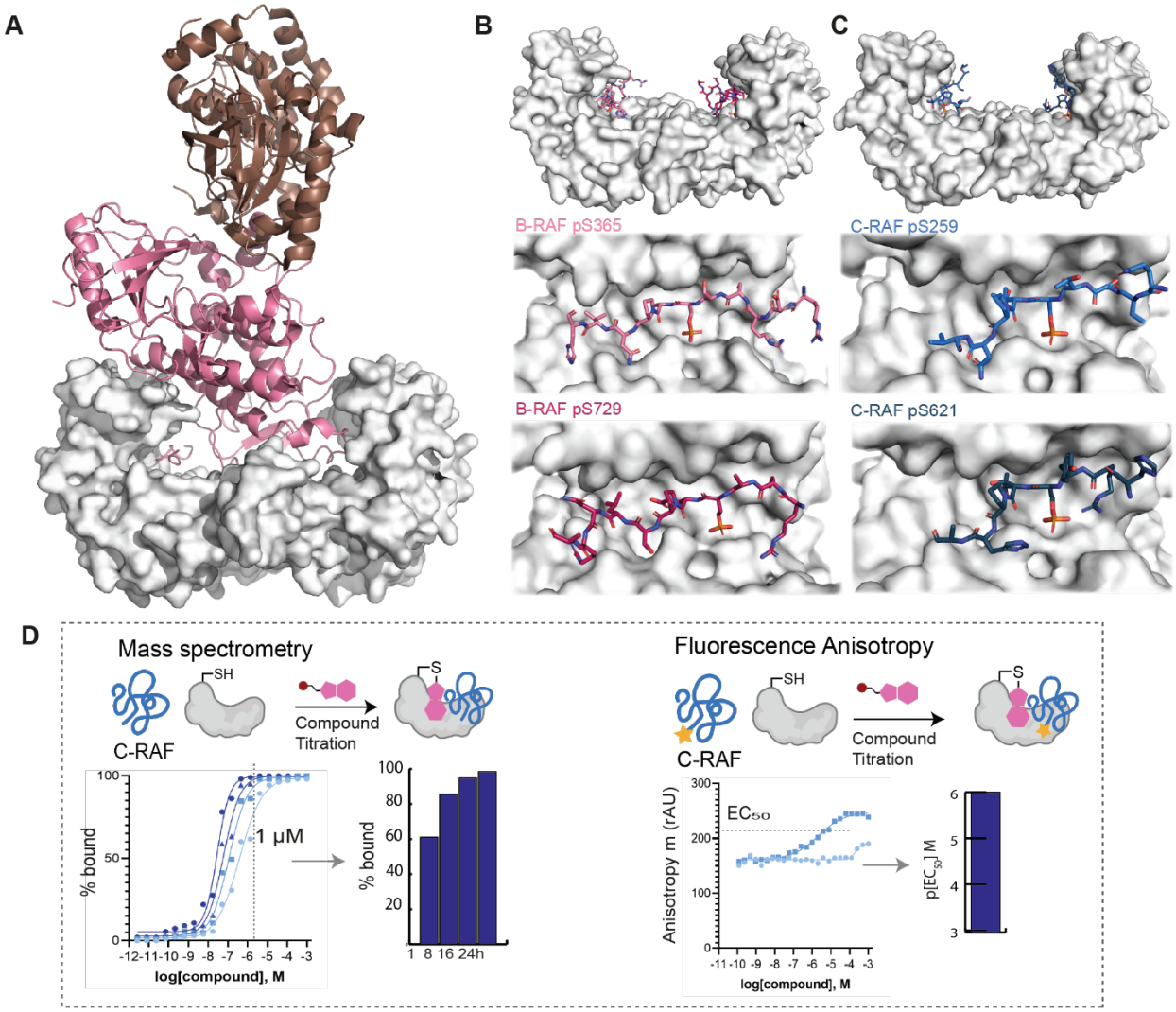

Figure S4.1: 14-3-3/RAF binding and assay overview

Comparison of 14-3-3/full length client structure with 14-3-3/phosphopeptides. **A)** Cryo-EM structure of 14-3-3ζ (dark grey cartoon) bound to full-length BRAF (red cartoon) and MEK (gold cartoon), PDB 6NYB. **B)** Close-up view of BRAF pS365 regulatory site (left monomer, pink sticks) and BRAF pS729 structural site (right monomer, red sticks) bound to 14-3-3ζ (dark grey cartoon), PDB 6NYB. **C)** Left monomer: 14-3-3ζ (grey cartoon) bound to CRAF pS259 phosphopeptide (blue sticks), PDB 4IHL. Right monomer: 14-3-3σ (grey cartoon) bound to CRAF pS621 phosphopeptide (dark blue sticks), PDB 4IEA. **D)** Overview of assays. Mass spectrometry time-course experiments were performed at 1h, 8h, 16h and 24h in the presence of CRAF pS259 phosphopeptide. Bar graphs were used to represent % bound at 1 µM compound concentration (10:1 [protein]:[compound] ratio). Fluorescence anisotropy compound titrations were performed in the presence of FAM-labeled CRAF pS259 phosphopeptide. EC_{50} values were calculated from the overnight measurement. pEC_{50} bar graphs represent the positive log EC_{50} value.

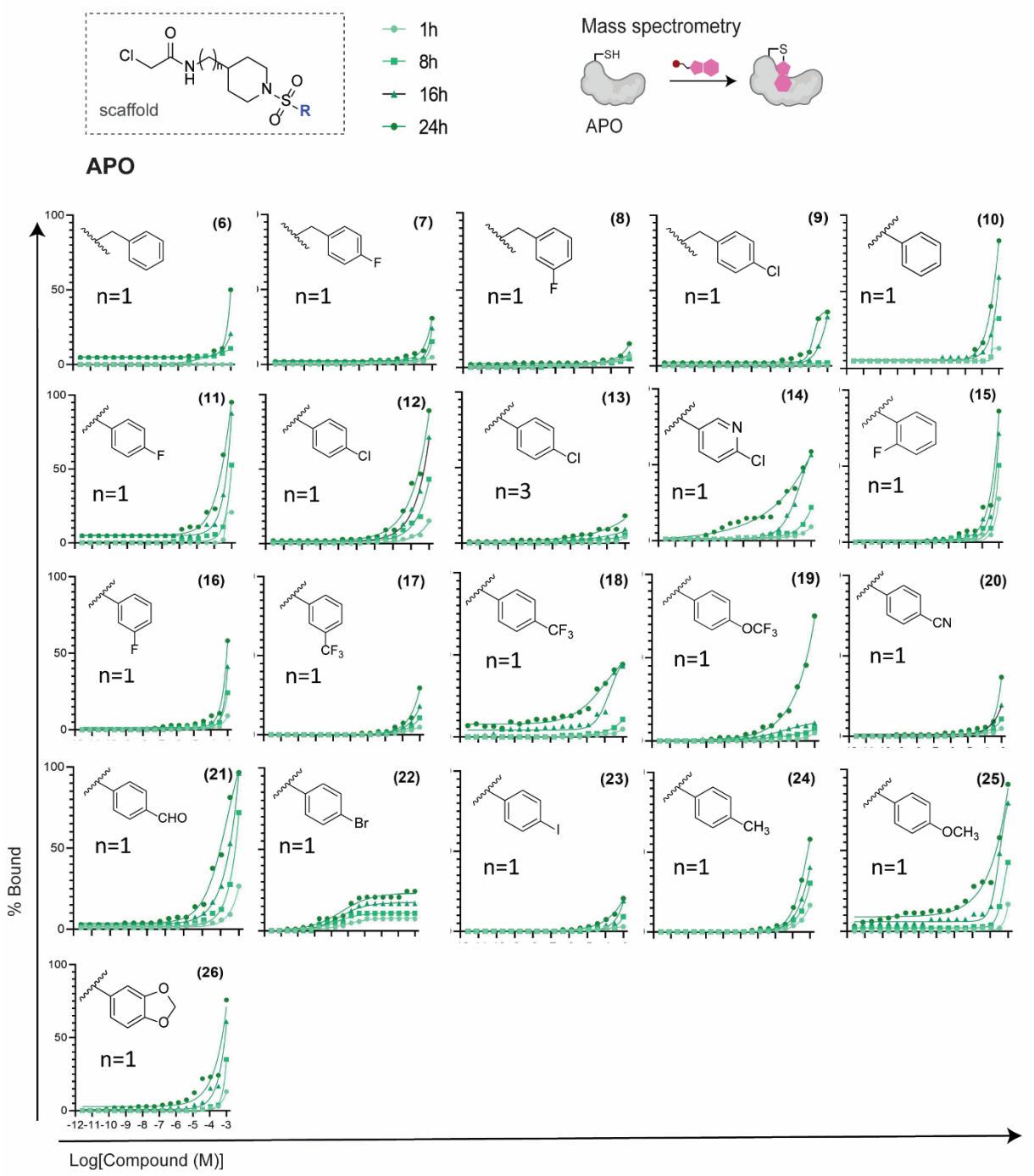

Figure S4.2: MSDR (apo) for compounds discussed in Figure 4.2

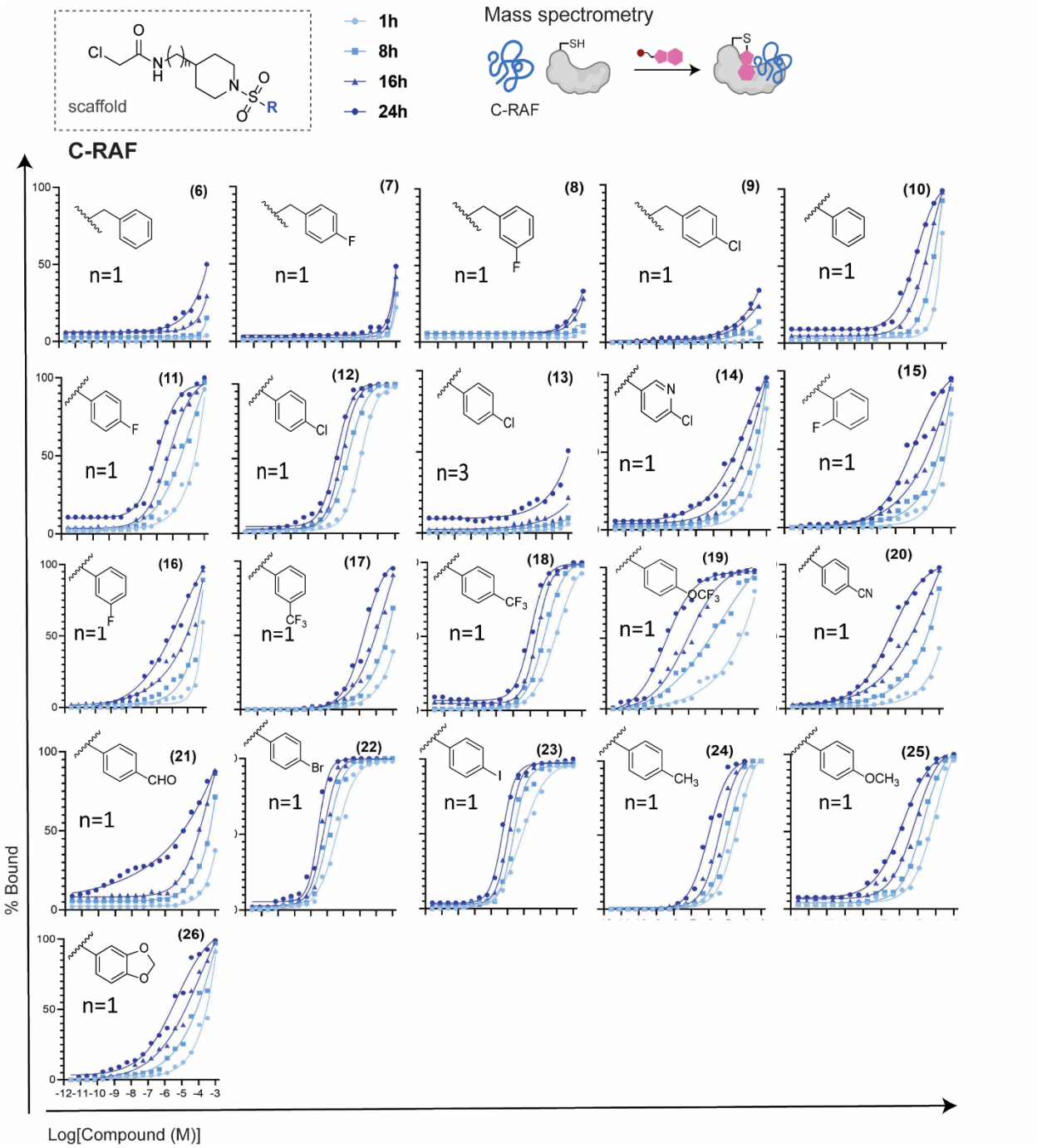

Figure S4.3: MSDR (CRAF pS259) for compounds discussed in Figure 4.2

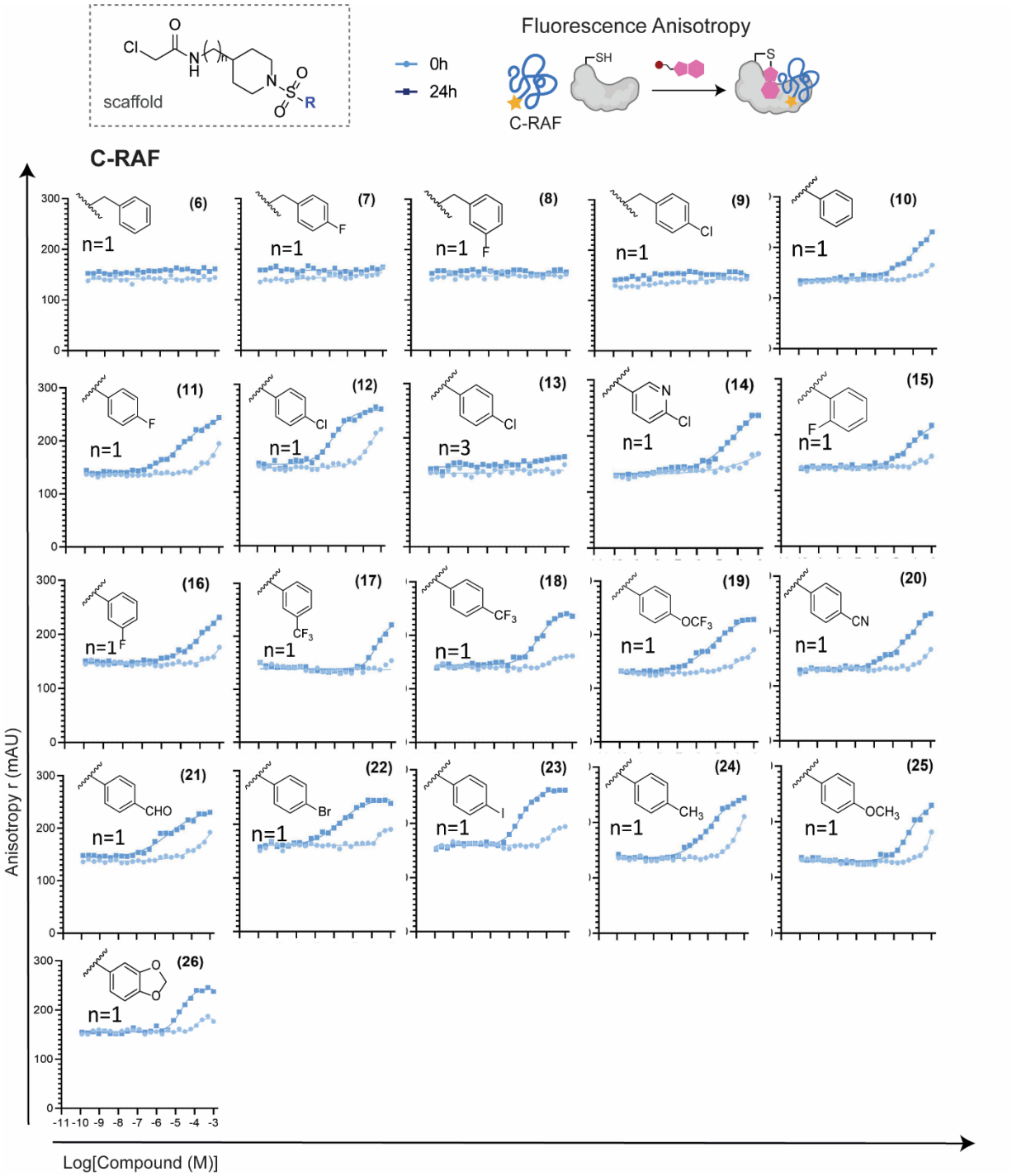

Figure S4.4: FADR with CRAF pS259 for compounds discussed in Figure 4.2

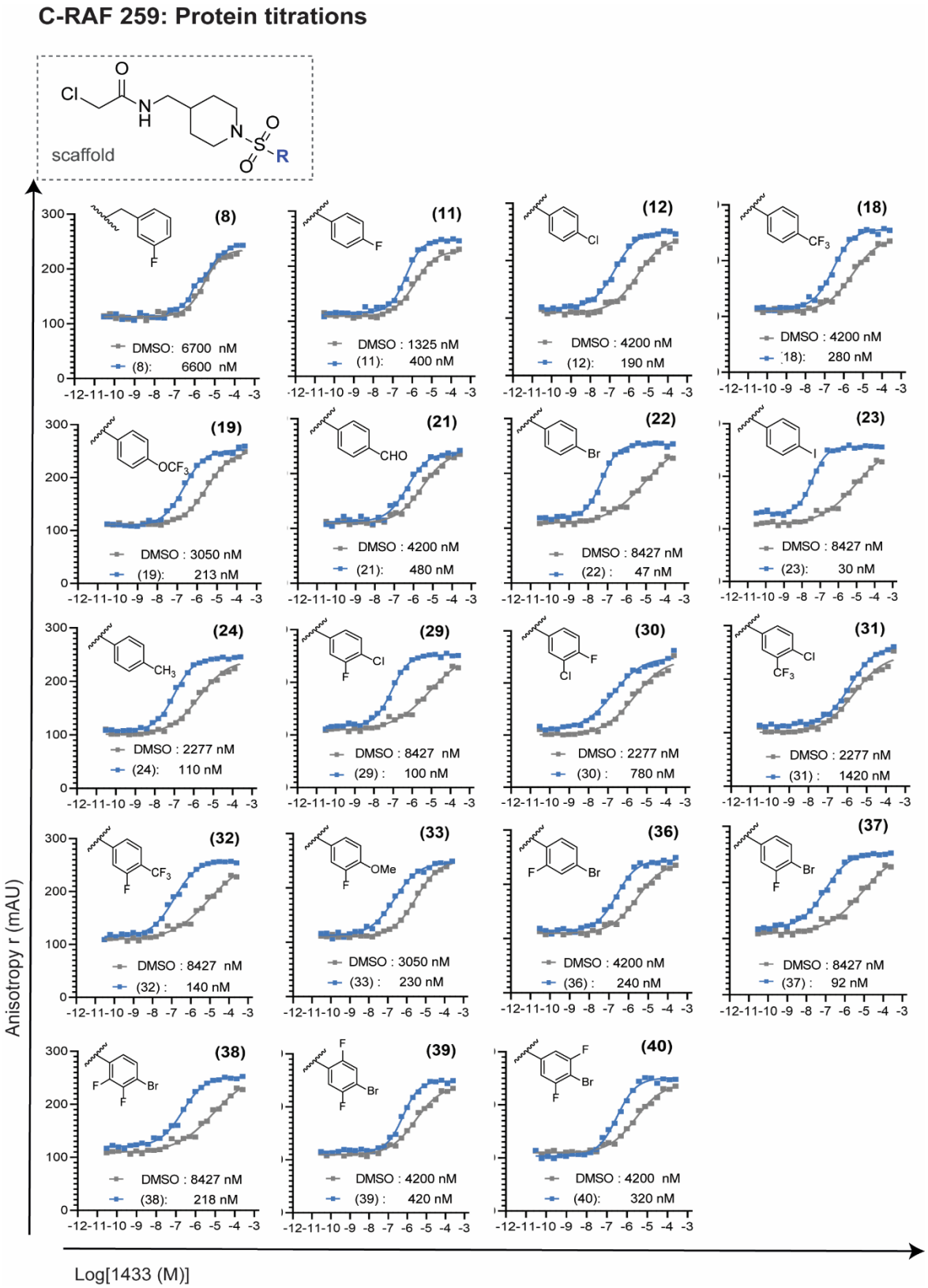

Figure S4.5: FA protein titrations with CRAF pS259 with compounds 8-40
Measured K_D values are indicated in the legend.

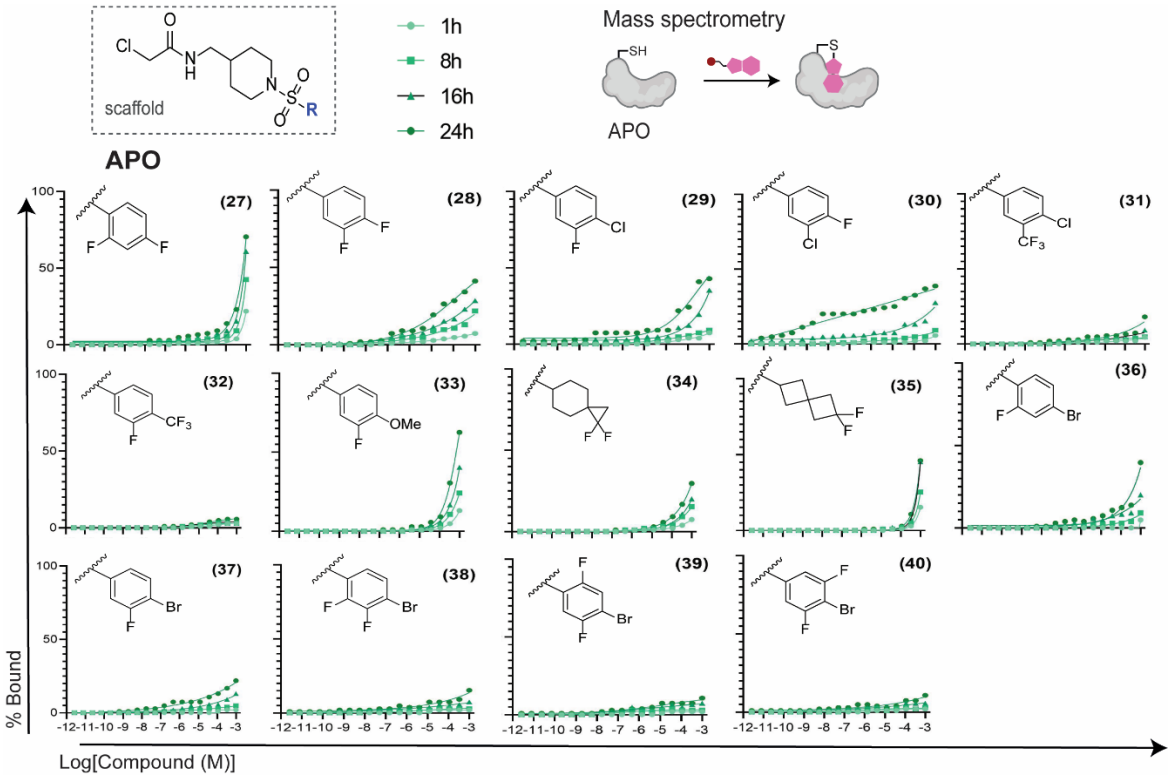

Figure S4.6: MSDR curves (apo) for compounds discussed in Figure 4.3

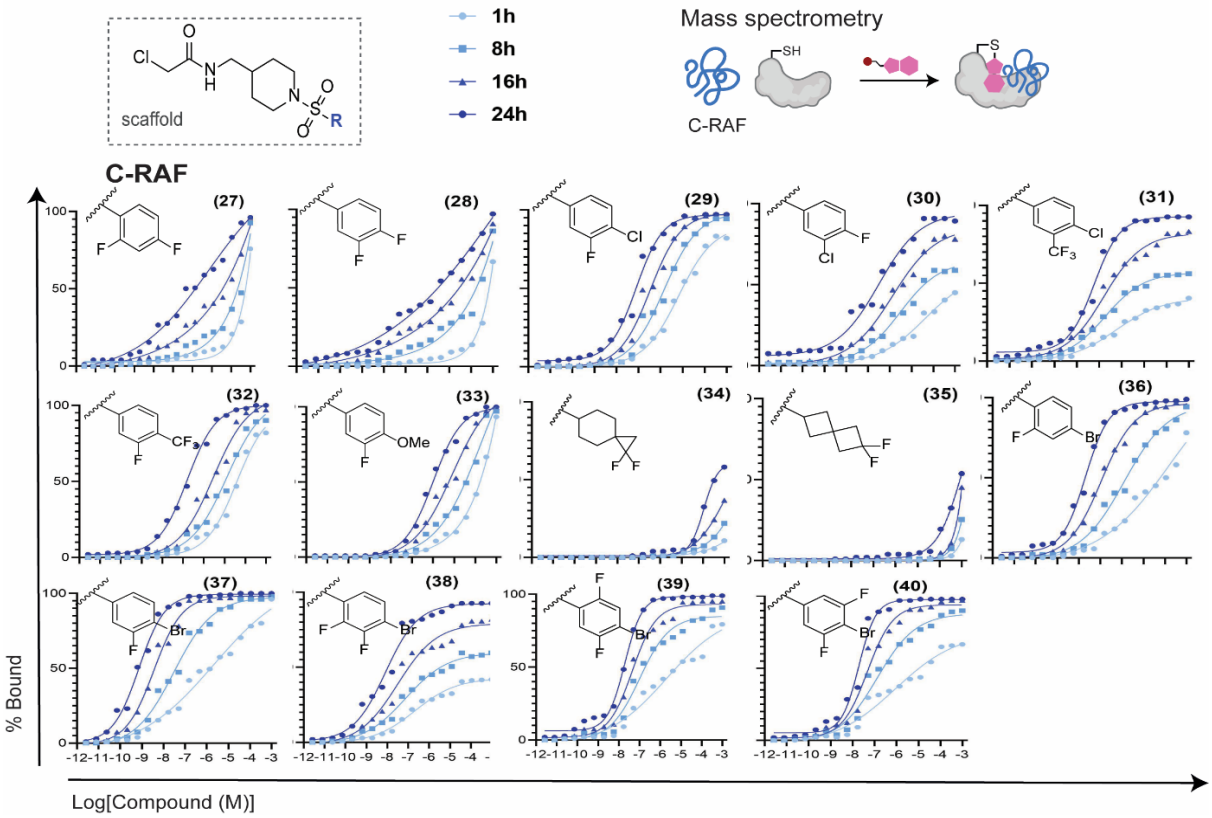

Figure S4.7: MSDR (CRAF pS259) for compounds discussed in Figure 4.3

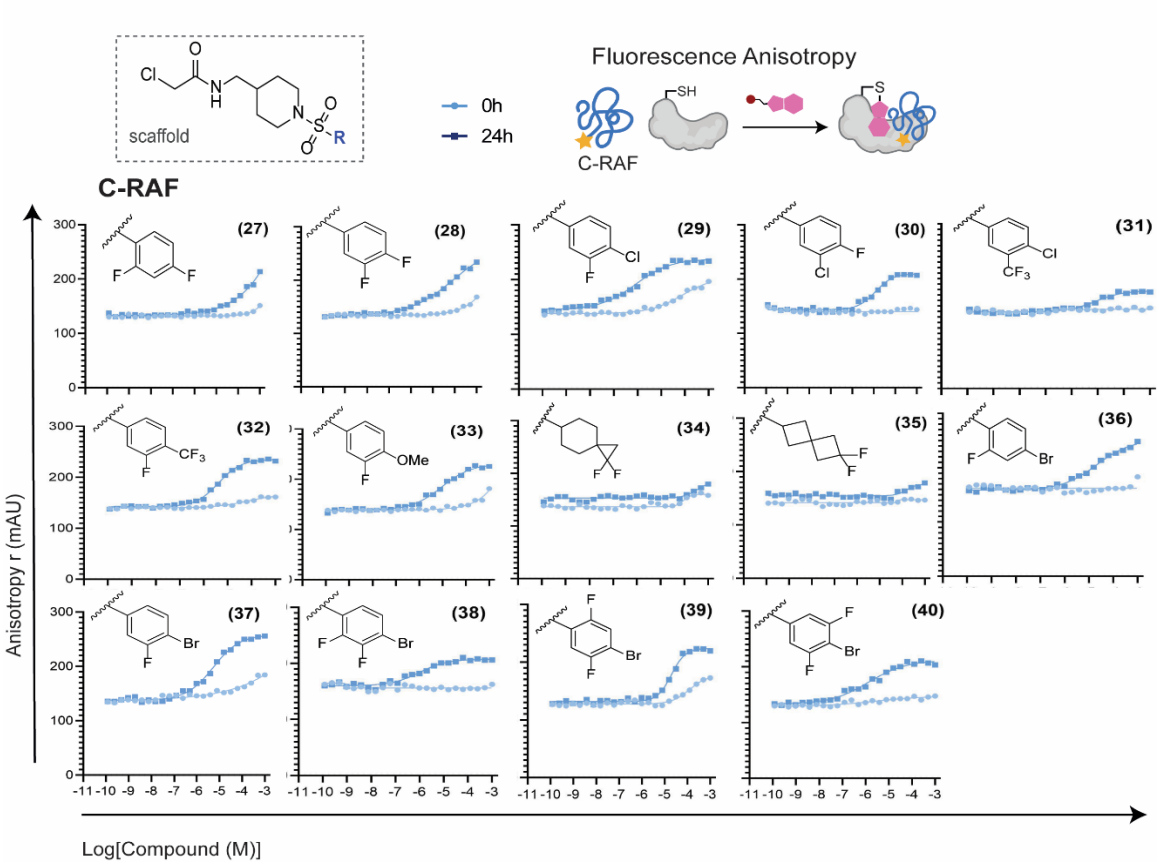

Figure S4.8: FADR with CRAF pS259 for compounds discussed in Figure 4.3

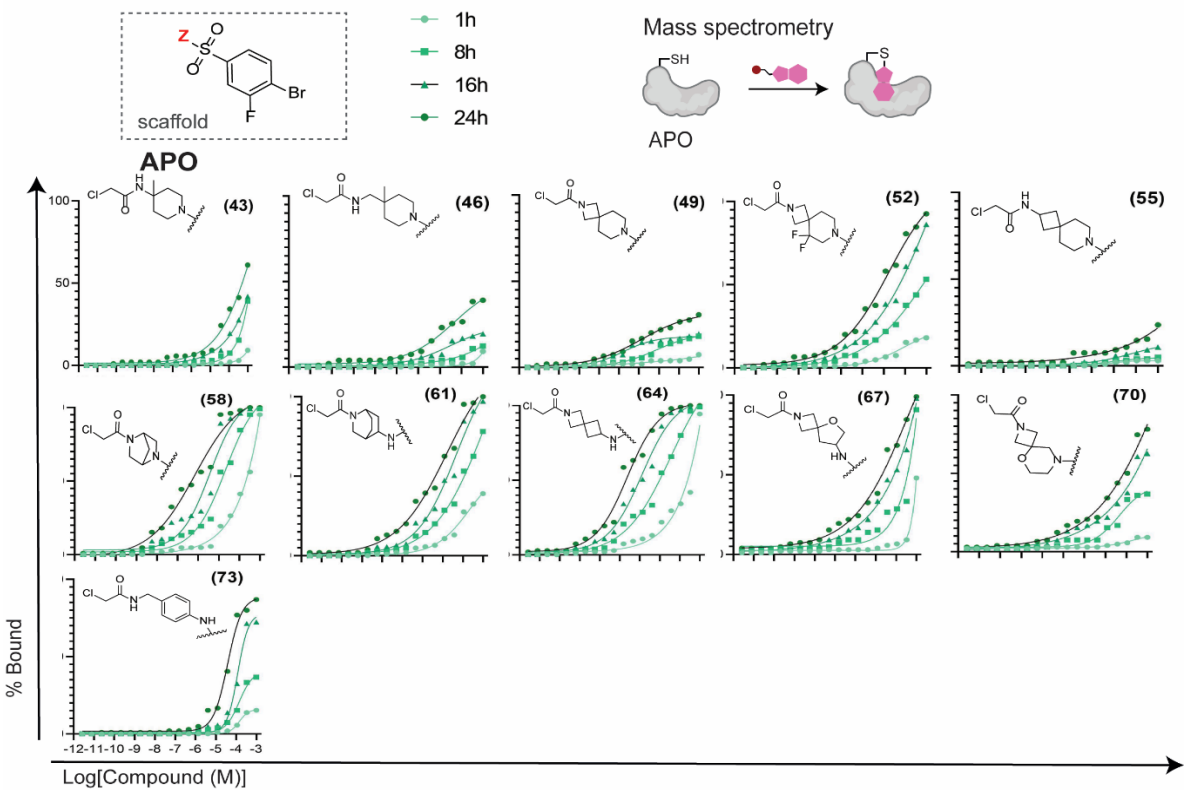

Figure S4.9: MSDR (apo) for compounds discussed in Figure 4.4

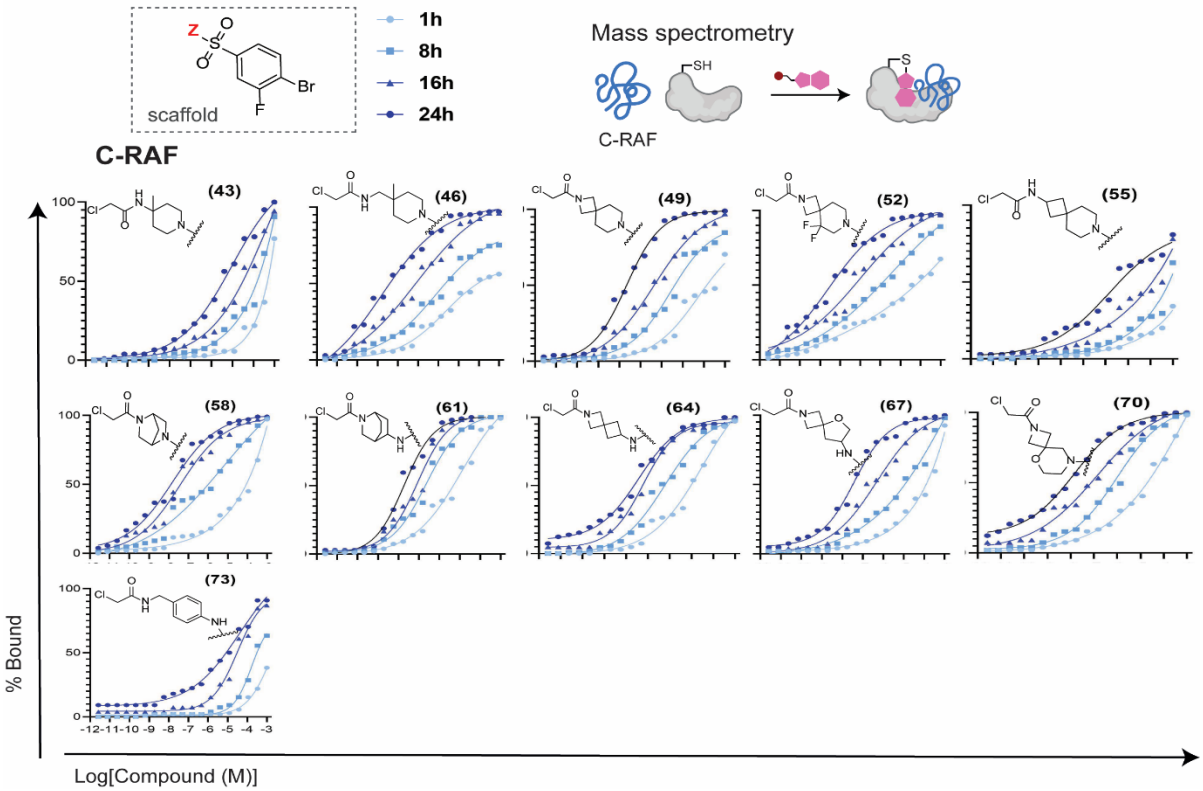

Figure S4.10: MSDR (CRAF pS259) for compounds discussed in Figure 4.4

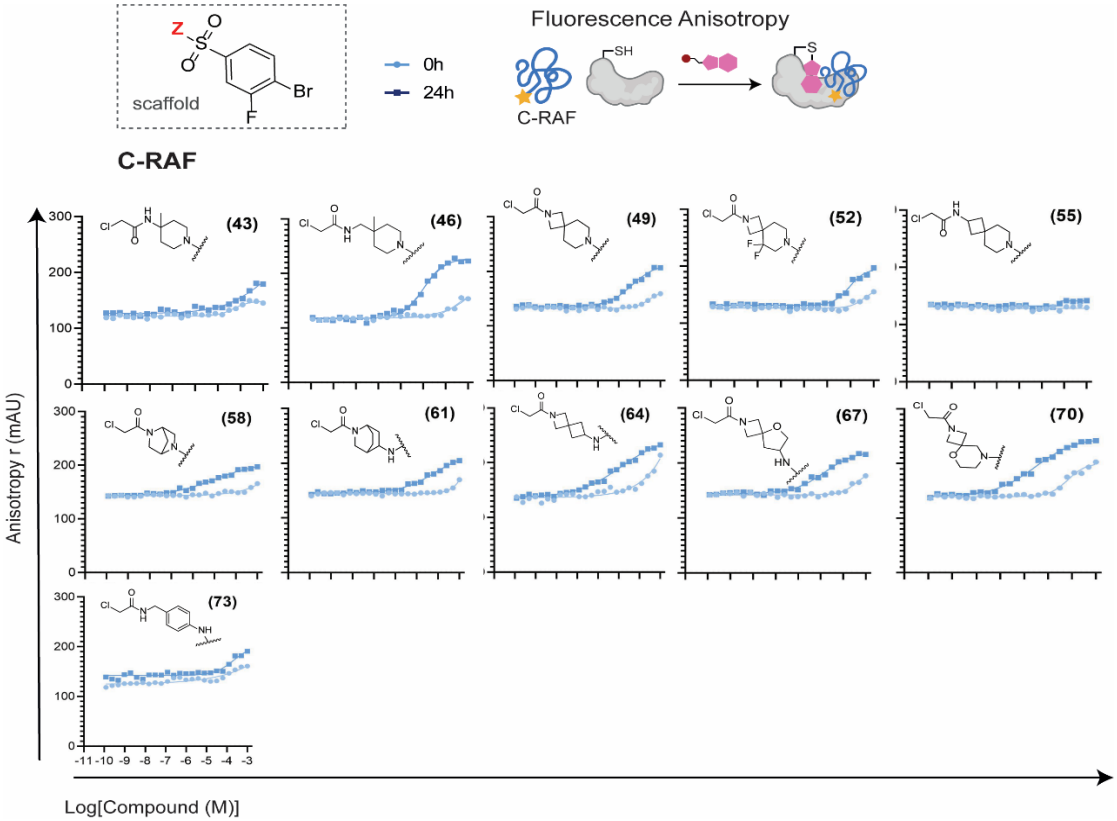

Figure S4.11: FADR with CRAF pS259 for compounds discussed in Figure 4.4

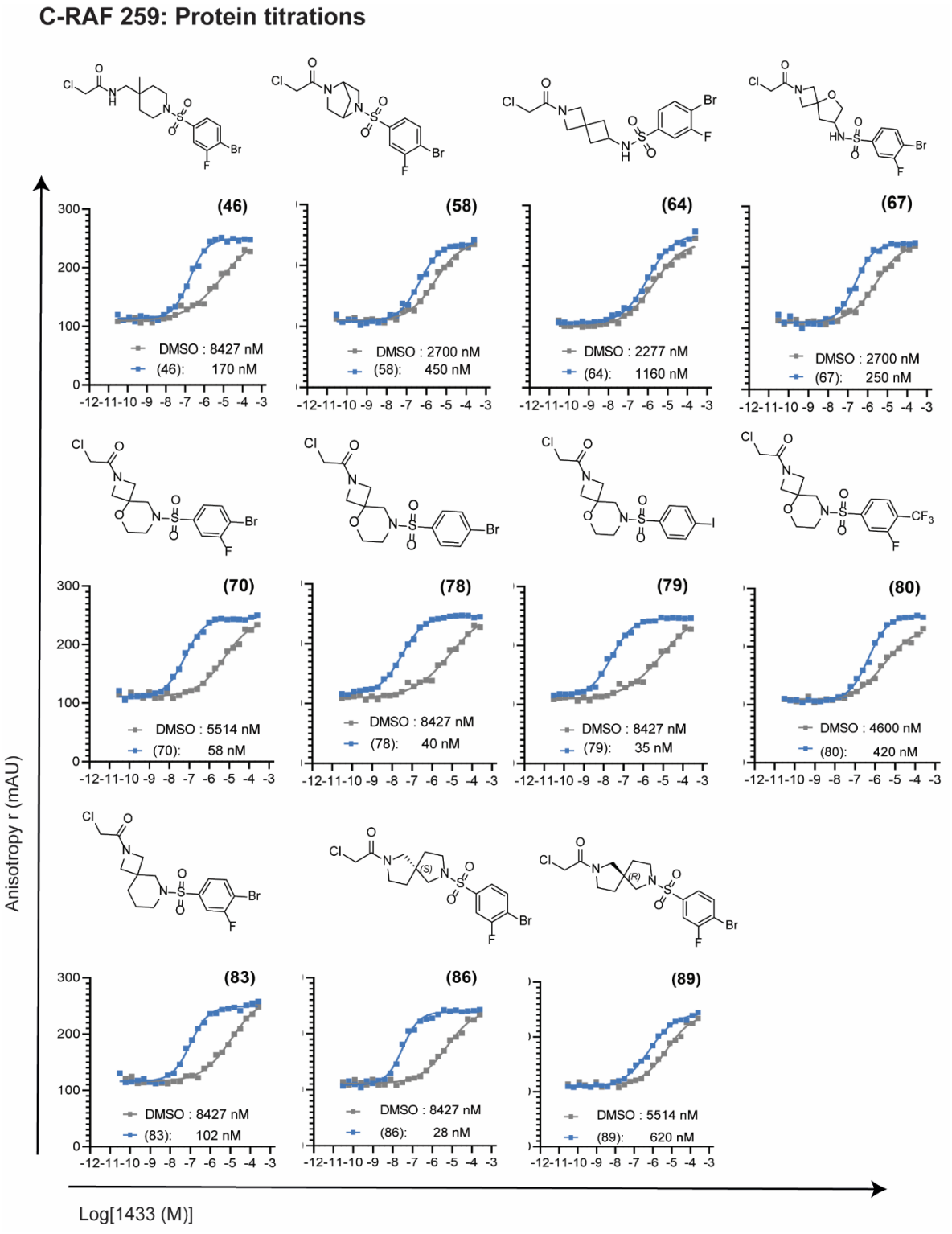

Figure S4.12: FA protein titrations with CRAF pS259 with compounds 46-89

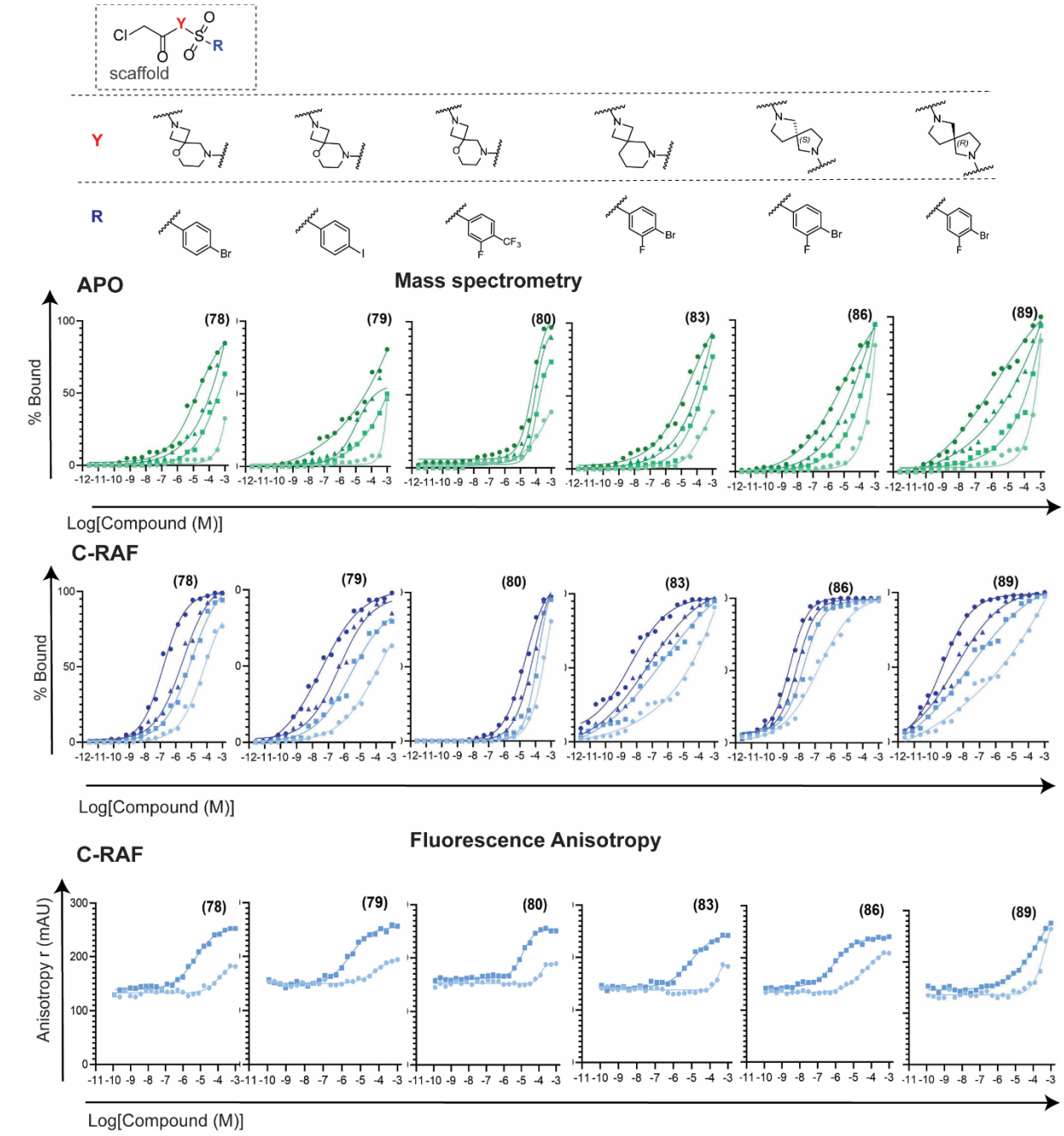

Figure S4.13: MSDR (apo, CRAF pS259) and FADR for compounds in Figure 4.5

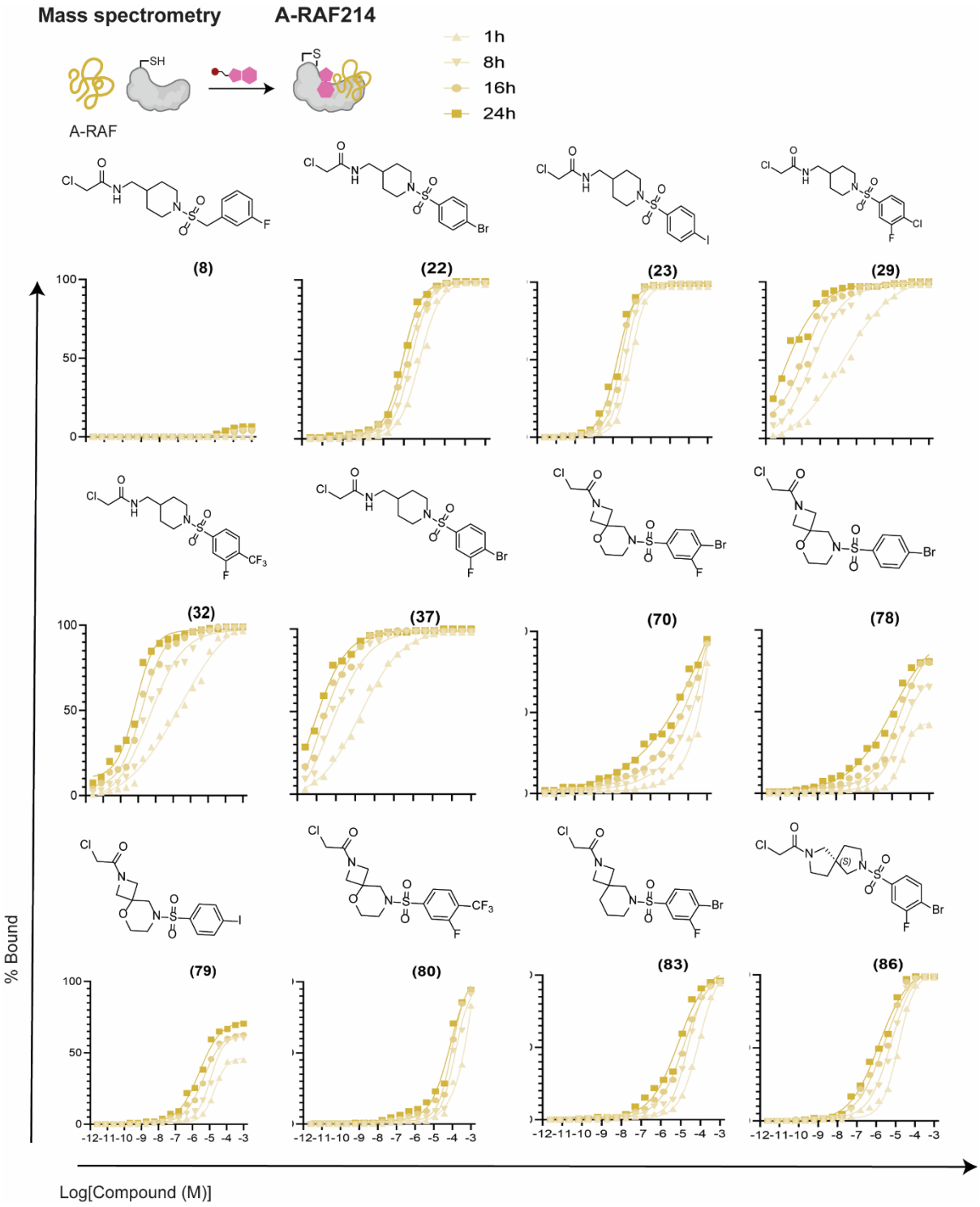

Figure S4.14: MSDR (ARAF pS214) for compounds in Figure 4.5

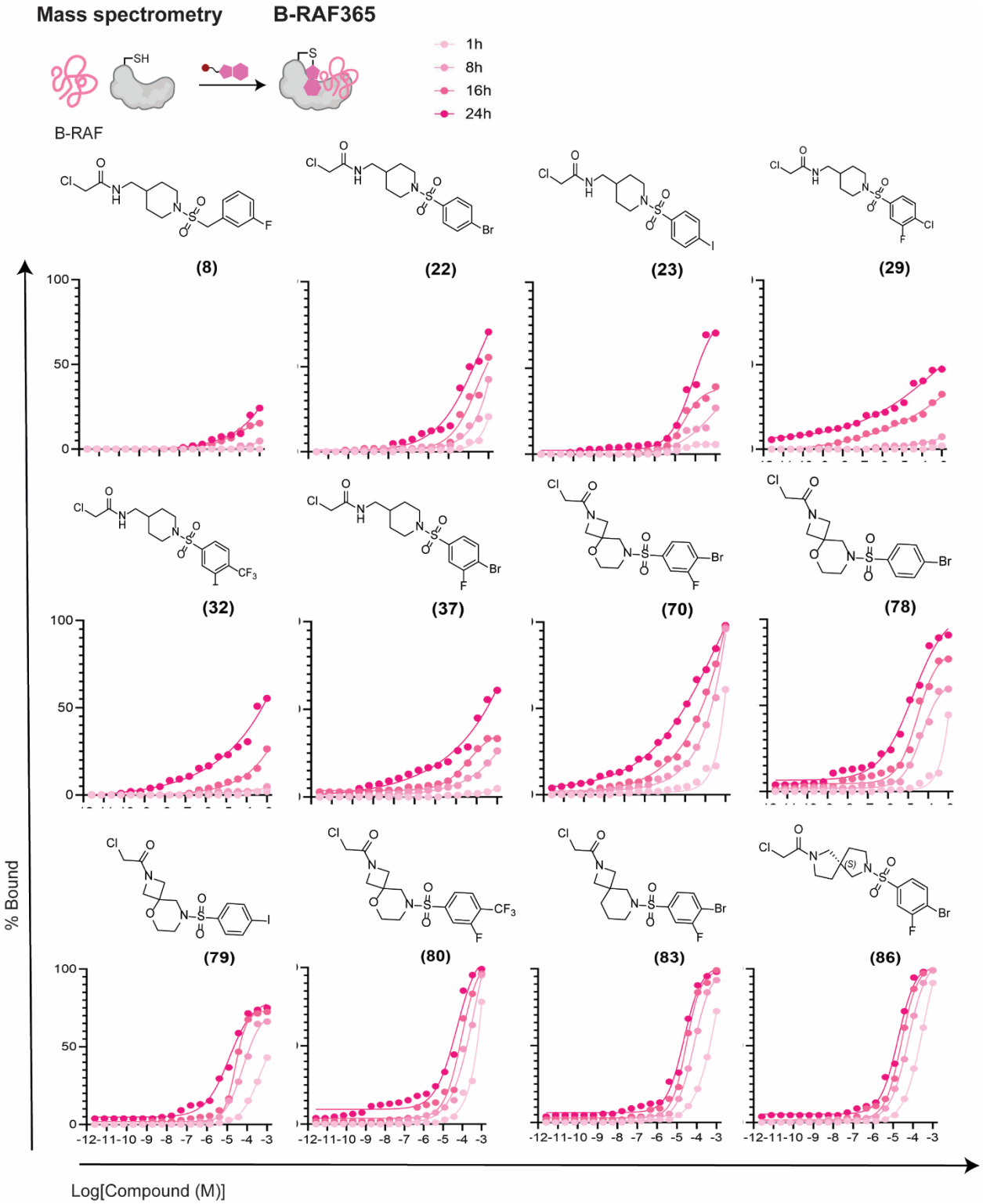

Figure S4.15: MSDR (BRAF pS365) for compounds in Figure 4.5

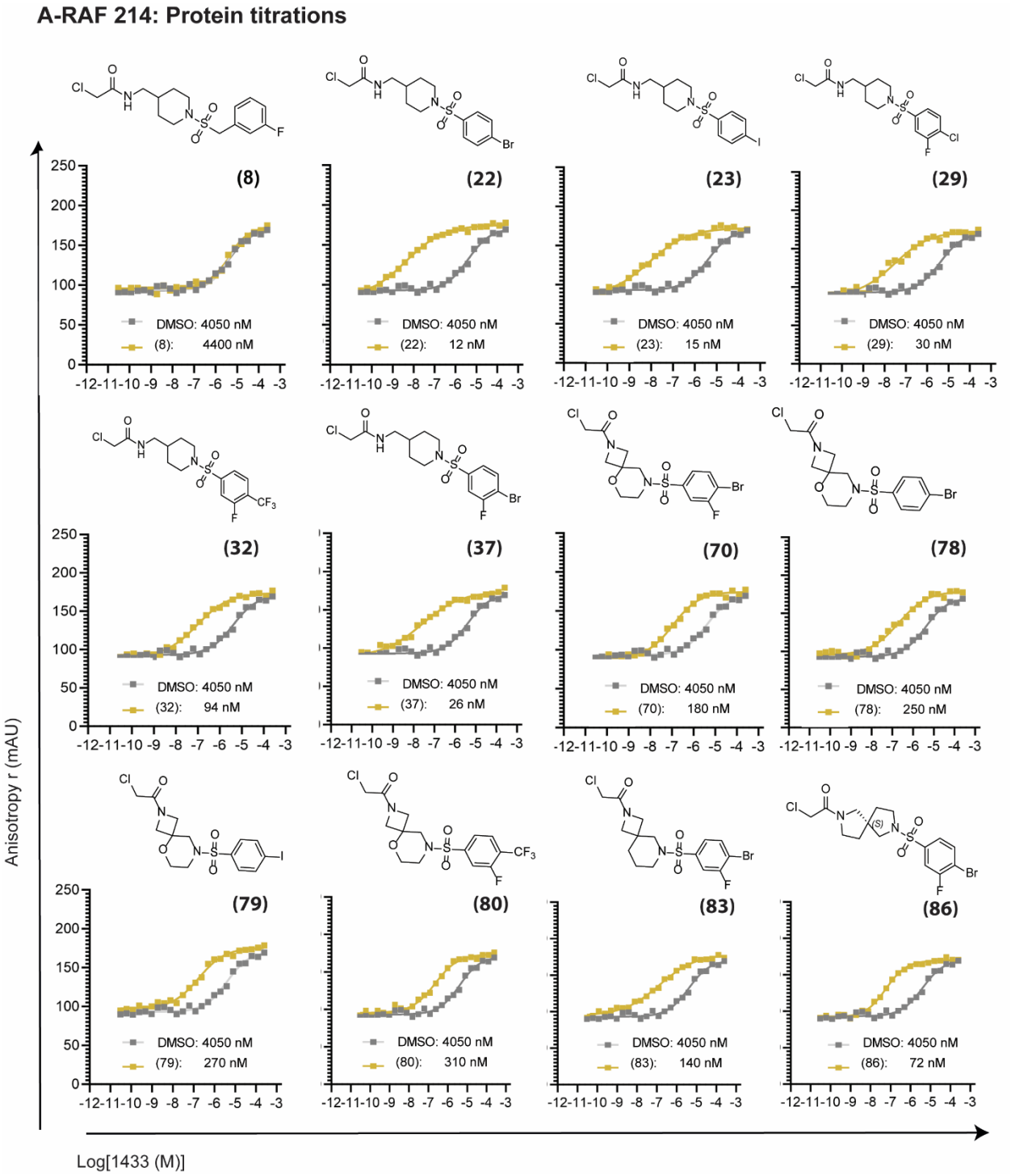

Figure S4.16: FA protein titrations (ARAF pS214) with top stabilizers

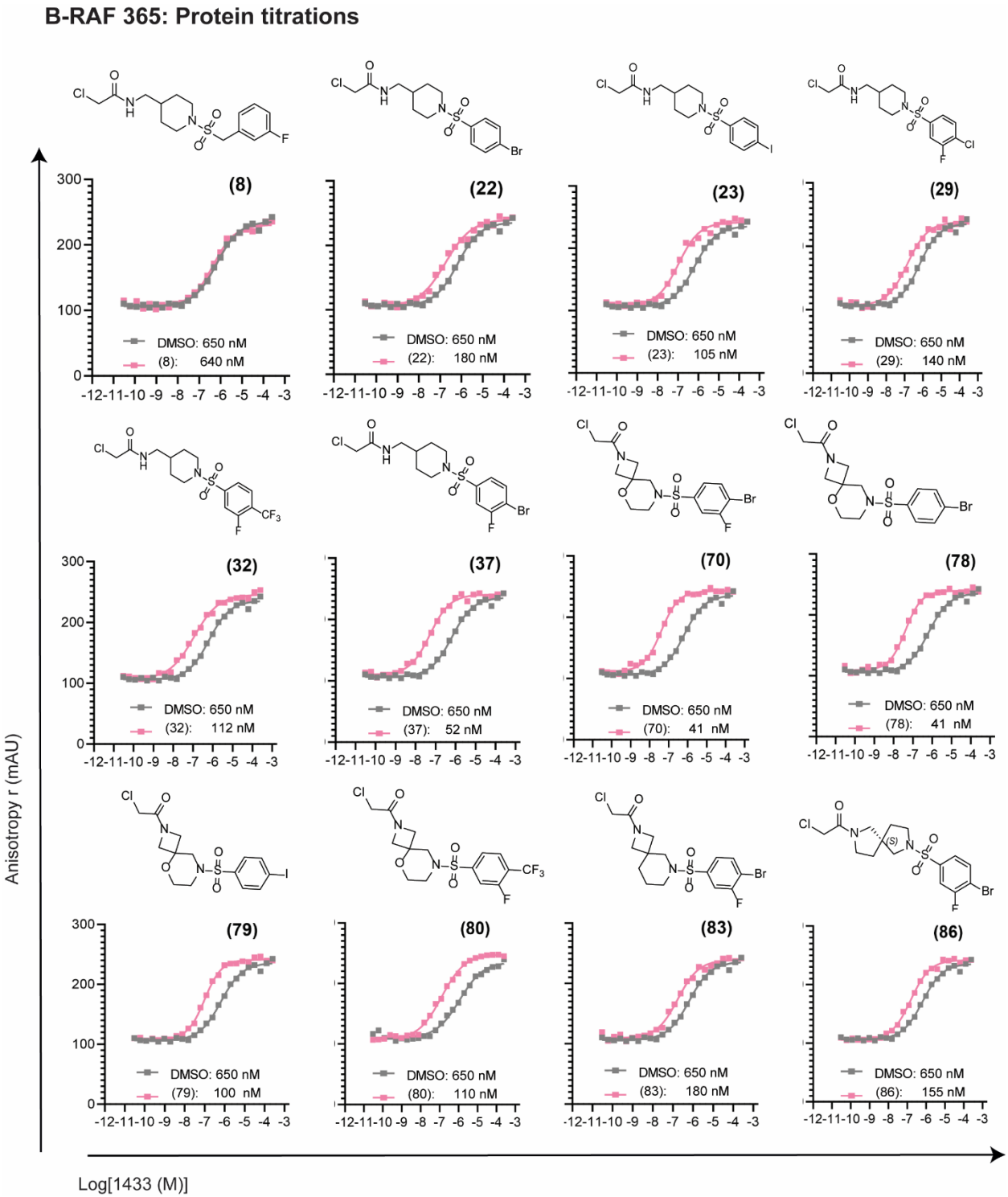

Figure S4.17: FA protein titrations (BRAF pS365) with top stabilizers

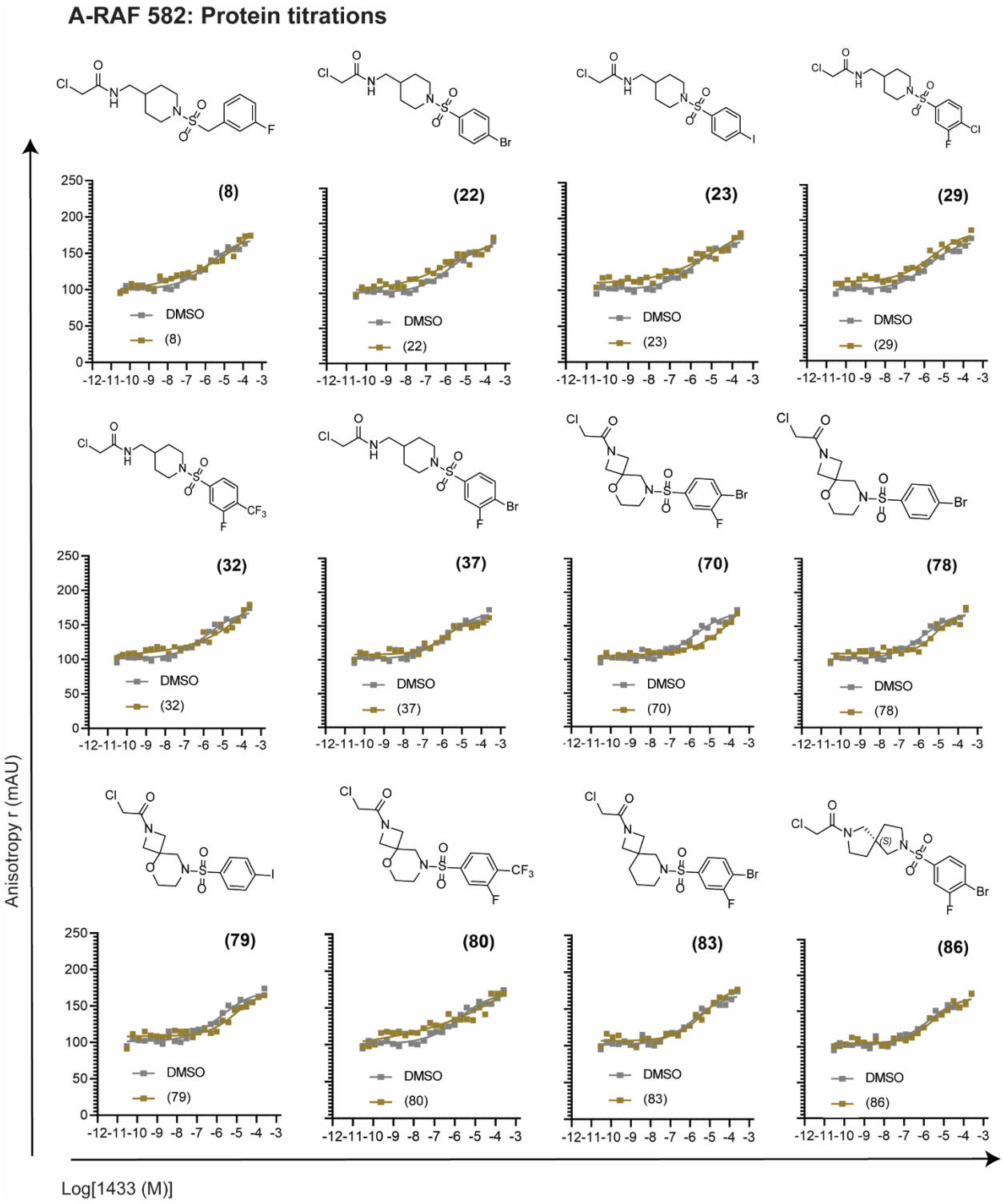

Figure S4.18: FA protein titrations (ARAF pS582) with top stabilizers

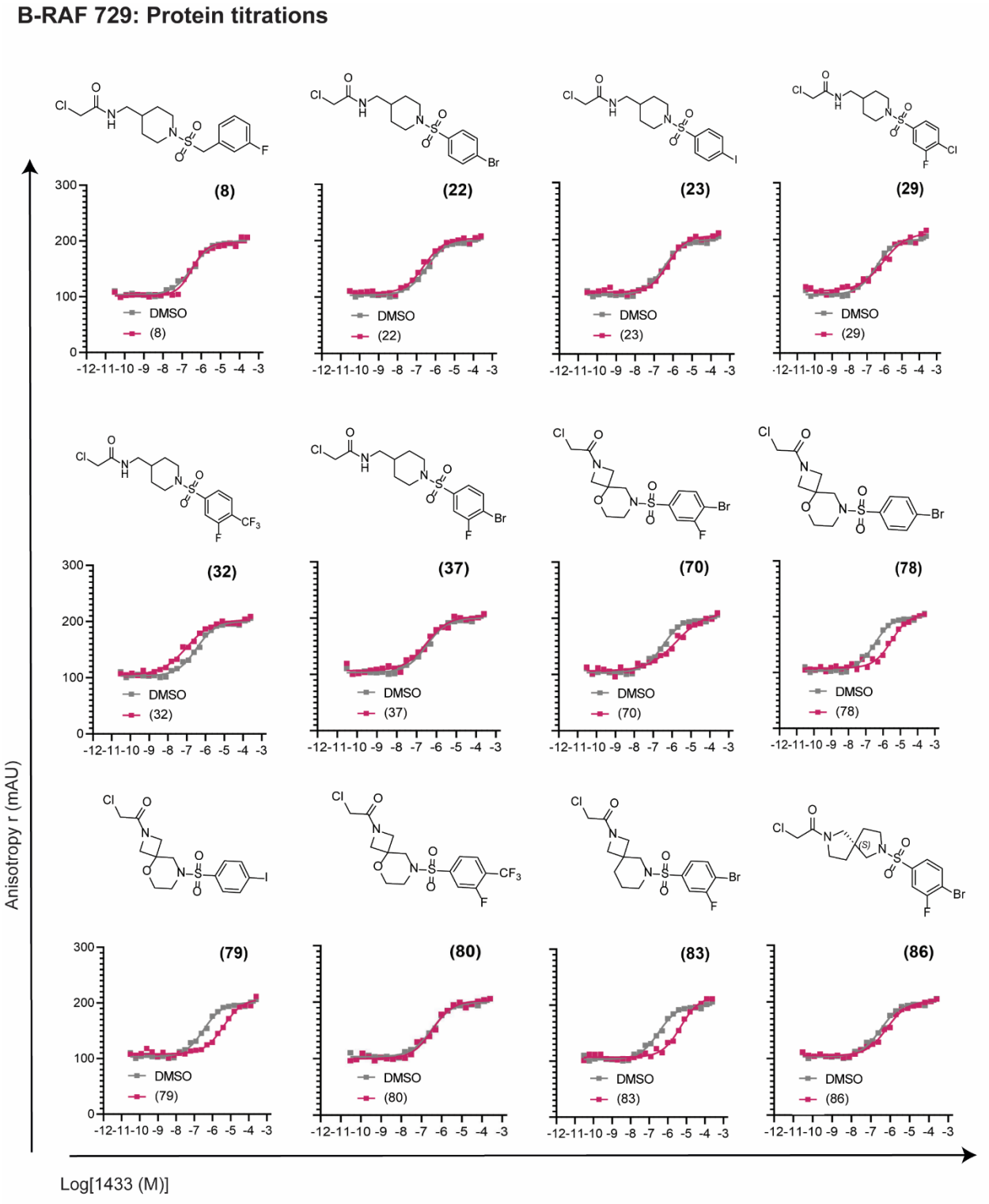

Figure S4.19: FA protein titrations (BRAF pS729) with top stabilizers

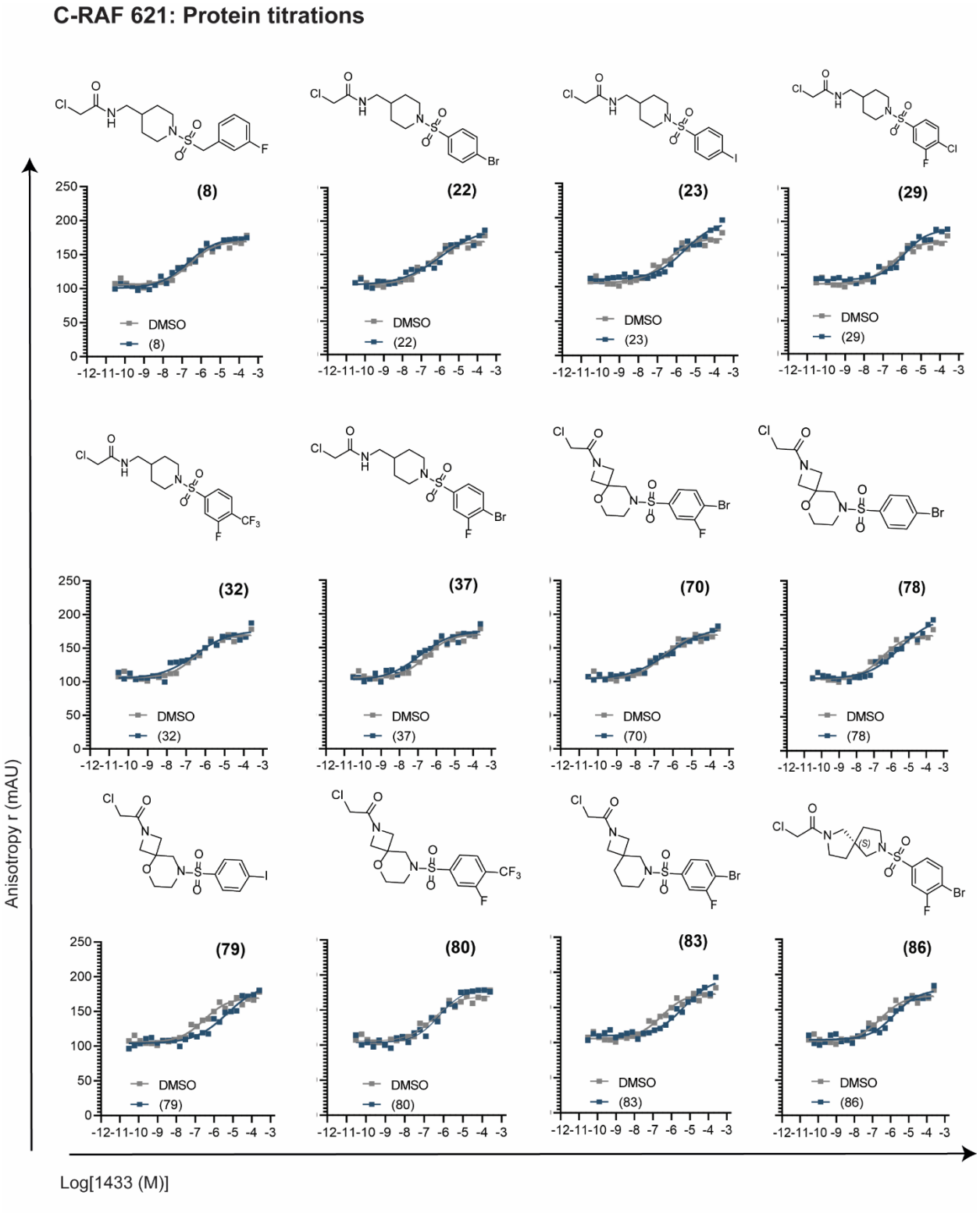

Figure S4.20: FA protein titrations (CRAF pS621) with top stabilizers

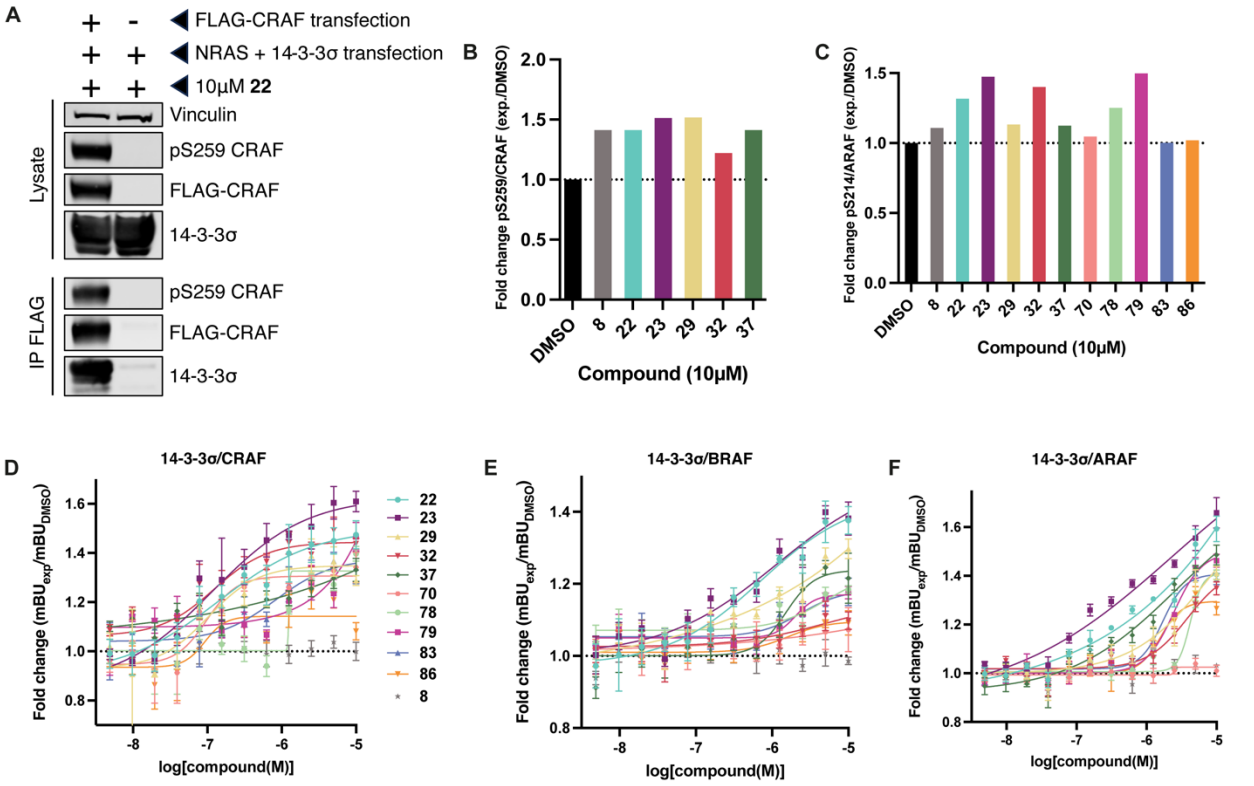

Figure S4.21: Cellular results of top stabilizers

A) Co-IP results with and without FLAG-CRAF transfection. **B)** Endogenous CRAF pS259 levels in MIA PaCa-2 cells after compound treatment. **C)** ARAF pS214 levels after compound treatment. **D)** NanoBRET results for 14-3-3σ/CRAF with top 10 stabilizers and an inactive compound. **E)** NanoBRET results for 14-3-3σ/BRAF with top 10 stabilizers and an inactive compound. **F)** NanoBRET results for 14-3-3σ/ARAF with top 10 stabilizers and an inactive compound.

Supplementary Tables

Table S4.1: MS time course results for apo and CRAF pS259

Percentage (%) bound of compound (1 μM) to 14-3-3σ (100 nM) measured by mass spectrometry in the absence of peptide (apo) or with CRAF pS259 peptide (18 μM) after 1, 8, 16 and 24 hours.

		APO				CRAF pS259			
Compound	**SMDC ID**	**1h**	**8h**	**16h**	**24h**	**1h**	**8h**	**16h**	**24h**
(6)	**1075353**	0	1	4.7	4.7	0.9	2.9	6.5	7
(7)	**1075476**	1	1.9	1.9	2.9	1.5	1.5	2.5	4.7
(8)	**1075477**	0	0	1.9	2.9	2.9	5.6	5.6	5.6
(9)	**1075352**	0	0	1.5	1.9	0	0.5	2.9	3.2
(10)	**1076407**	4.7	4.7	4.7	4.7	4.7	5.6	5.7	13
(11)	**1076408**	0	1.5	4.7	6.9	6.9	15	26	50.3
(12)	**1075475**	1	1.5	2.9	4.3	12.1	32.8	47.8	64.4
(13)	**1076390**	0	1.5	2.5	4.3	0.9	2.9	5.6	14.1
(14)	**1076413**	1.9	2.5	3	15	4.7	7.4	9.9	20.9
(15)	**1083849**	0.5	1.9	2.4	2.4	3.3	8.2	13.7	23.3
(16)	**1083843**	0	1	1.9	2.9	3.3	8.2	18	32.4
(17)	**1083844**	0	0	0.5	0.9	1.9	3.4	6.5	12.3
(18)	**1076412**	0	0.9	6.5	12.7	8.2	17.9	28.4	46.8
(19)	**1083842**	0	0.5	2.5	6.5	20.5	41.3	69.5	91.3
(20)	**1083841**	0	0.5	1.5	2.9	4.7	12.1	23.9	42.3
(21)	**1075354**	1,5	2.9	4.4	7.4	2.9	6.5	10.7	32.2
(22)	**1083853**	6.5	10.7	16	20.3	61	85.5	94.8	98.5
(23)	**1083848**	0	0	0.5	0.9	55.6	78.5	88.9	91
(24)	**1083852**	0	0.5	0.5	1.5	7.3	13.7	26.7	51.8
(25)	**1076411**	0.5	1.9	7.4	13.8	10.6	15	27.1	44.4
(26)	**1124380**	0	0	1.9	5.2	4.3	11.3	22.6	34.1
(27)	**1083846**	1	2,5	3.8	5.2	6.9	14.1	27.5	50.3
(28)	**1083845**	1.9	4.7	6.5	9.1	4.3	15.2	27.5	40
(29)	**1076409**	0	1.9	4.7	8.2	20.5	38.1	57.1	80.1
(30)	**1076410**	1	2.5	6.5	22.5	11	24.8	41.8	60.3
(31)	**1083850**	0.9	1.9	2.5	3.8	21	38.1	59.1	81.4
(32)	**1083854**	0	0.5	0.9	0.9	14.1	21.6	39.3	74.1
(33)	**1083847**	0	0	0.9	0.9	7.7	18.5	31.8	50.3
(34)	**1083851**	0	0.5	0.9	0.9	0.5	0.9	0.9	3.8
(35)	**1083855**	0	0	0	0.5	0	0	0	3.8
(36)	**1083916**	0	0.9	2.9	4.5	20.6	41.1	69.5	91.7
(37)	**1083917**	0	0.9	2.5	7.4	48.7	77.1	95.2	98
(38)	**1083918**	0	0.9	2.9	4.4	28	43.9	61.9	83.3
(39)	**1083919**	0	1.9	3.8	3.8	39.3	64.6	78.1	96.7
(40)	**1083920**	0	0.5	1.5	4.7	35.9	60.5	78.9	93.9
(43)	**1124381**	0	0.5	3.5	6.1	4.3	9.1	16.7	32.9
(46)	**1124382**	0.5	1.9	4.7	8.2	25.8	39.4	49	84
(49)	**1084346**	1.9	5.2	13.8	15.9	11.1	32.4	53.8	86.6
(52)	**1084353**	2.9	11.3	18.5	28.6	25	45.1	64.3	80.2
(55)	**1084347**	0	0.9	1.9	7.4	6.1	9.9	20.6	34.6
(58)	**1084348**	4.7	17.3	28	51.8	16.5	45.2	71.2	80.5
(61)	**1084349**	5.2	13.3	21.8	36.8	37.1	68	80.9	83.3
(64)	**1084350**	9.9	27.2	47.2	65	27.5	53.6	79	80.8
(67)	**1084351**	2.9	9.1	15.9	23	15	30.4	55.6	81.5
(70)	**1084352**	2.9	7.4	15.9	20	30	47.5	68	87.2
(73)	**1084354**	0	1.5	1.5	3.8	1.9	2.9	12.1	31
(74)	**1084757**	0	0	0	0	0	0	0	4.7
(75)	**1084758**	0	0	0	0	0	0	0	2.9
(78)	**1124378**	1.9	3.8	12.2	14.1	8.3	25.3	35.6	70
(79)	**1124379**	1.5	5.6	10.6	32.4	15	29.5	52.6	72
(80)	**1124898**	5.6	5.6	7.8	11	6	7	15.2	25.1

		APO				CRAF pS259			
Compound	**SMDC ID**	**1h**	**8h**	**16h**	**24h**	**1h**	**8h**	**16h**	**24h**
(83)	**1124383**	1.9	3.8	14.5	25.6	27	52.5	66.3	84
(86)	**1124384**	3.3	10.7	23	36.8	64.6	93.1	97.1	98.5
(89)	**1124385**	5.6	14.5	36.2	53.9	43	65.8	82	92

Table S4.2: FA results with CRAF pS259

EC_{50} values derived from FA compound titrations in the presence of 10 nM of CRAF pS259-FAM labeled peptide and 5 µM 14-3-3σ. Protein titrations with CRAF pS259-FAM for compounds with EC_{50} < 20 µM (10 nM of CRAF pS259-FAM, 100 µM compound, 250 µM 14-3-3σ starting concentration, 2-fold dilution). EC_{50} and *app*K_D values refer to overnight measurements.

		Compound titrations	Protein titrations		
Compound	**SMDC ID**	**EC_{50} value CRAF pS259 (µM)**	***app*K_D (nM) (100 µM compound)**	**K_D with DMSO reference**	**X Fold stabilization (100 µM compound)**
(6)	**1075353**	>1000	NA	NA	NA
(7)	**1075476**	>1000	NA	NA	NA
(8)	**1075477**	>1000	6600 nM	6700 nM	1
(9)	**1075352**	>1000	NA	NA	NA
(10)	**1076407**	66 ± 4 µM	NA	NA	NA
(11)	**1076408**	17 ± 3 µM	400 nM	1325 nM	4
(12)	**1075475**	3 ± 1 µM	190 nM	4200 nM	22
(13)	**1076390**	>1000	NA	NA	NA
(14)	**1076413**	82 ± 6 µM	NA	NA	NA
(15)	**1083849**	87 ± 9 µM	NA	NA	NA
(16)	**1083843**	> 150	NA	NA	NA
(17)	**1083844**	> 150	NA	NA	NA
(18)	**1076412**	17 ± 1 µM	280 nM	4200 nM	15
(19)	**1083842**	13 ± 3 µM	213 nM	3050 nM	14
(20)	**1083841**	>150	NA	NA	NA
(21)	**1075354**	5 ± 1.0 µM	480 nM	4200 nM	9
(22)	**1083853**	1 ± 0.5 µM	47 nM	8427 nM	179
(23)	**1083848**	1 ± 0.5 µM	30 nM	8427 nM	280
(24)	**1083852**	14 ± 1 µM	110 nM	2277 nM	21
(25)	**1076411**	57 ± 9 µM	NA	NA	NA
(26)	**1124380**	26 ± 3 µM	NA	NA	NA
(27)	**1083846**	>150 µM	NA	NA	NA
(28)	**1083845**	88 ± 2 µM	NA	NA	NA
(29)	**1076409**	1 ± 0.5 µM	100 nM	8427 nM	84
(30)	**1076410**	12 ± 2 µM	780 nM	2277 nM	3
(31)	**1083850**	8 ± 1 µM	1420 nM	2277 nM	2
(32)	**1083854**	4 ± 1 µM	140 nM	8427 nM	60
(33)	**1083847**	9 ± 1 µM	230 nM	3050 nM	13
(34)	**1083851**	> 1000	NA	NA	NA
(35)	**1083855**	> 1000	NA	NA	NA
(36)	**1083916**	25 ± 2 µM	240 nM	4200 nM	18
(37)	**1083917**	5 ± 1 µM	92 nM	8427 nM	92
(38)	**1083918**	2 ± 1 µM	218 nM	8427 nM	39
(39)	**1083919**	17 ± 3 µM	420 nM	4200 nM	7
(40)	**1083920**	2 ± 1 µM	320 nM	4200 nM	13
(43)	**1124381**	> 1000	NA	NA	NA
(46)	**1124382**	11 ± 1 µM	170 nM	8427 nM	49
(49)	**1084346**	47 ± 4 µM	NA	NA	NA
(52)	**1084353**	94 ± 9 µM	NA	NA	NA
(55)	**1084347**	> 1000	NA	NA	NA
(58)	**1084348**	12 ± 1 µM	450 nM	2700 nM	6
(61)	**1084349**	78 ± 7 µM	NA	NA	NA
(64)	**1084350**	15 ± 2 µM	1160 nM	2277 nM	2
(67)	**1084351**	14 ± 1 µM	250 nM	2700 nM	11
(70)	**1084352**	2 ± 1 µM	58 nM	5514 nM	95
(73)	**1084354**	> 1000	NA	NA	NA

		Compound titrations	Protein titrations		
Compound	**SMDC ID**	**EC_{50} value CRAF pS259 (µM)**	***app*K_D (nM) (100 µM compound)**	**K_D with DMSO reference**	**X Fold stabilization (100 µM compound)**
(74)	**1084757**	> 1000	NA	NA	NA
(75)	**1084758**	> 1000	NA	NA	NA
(78)	**1124378**	2 ± 1 µM	40 nM	8427 nM	210
(79)	**1124379**	2 ± 1 µM	35 nM	8427 nM	240
(80)	**1124898**	9 ± 2 µM	420 nM	4600 nM	11
(83)	**1124383**	5 ± 2 µM	102 nM	8427 nM	83
(86)	**1124384**	1 ± 1 µM	28 nM	8427 nM	300
(89)	**1124385**	> 250	620 nM	5514 nM	9

Table S4.3: MS time course results for regulatory phosphorylation sites
Percentage (%) bound of compound (1 µM) to 14-3-3σ (100 nM) measured by mass spectrometry in the presence of CRAF pS259 peptide (18 µM) or ARAF pS214 peptide (16 µM) or BRAF pS365 peptide (5 µM) after 1, 8, 16 and 24 hours.

		CRAF pS259				ARAF pS214				BRAF pS365			
No.	**SMDC ID**	**1h**	**8h**	**16h**	**24h**	**1h**	**8h**	**16h**	**24h**	**1h**	**8h**	**16h**	**24h**
(8)	**1075477**	0	0	1.9	2.9	0	0	0	0	0	0	2.5	2.5
(22)	**1083853**	61	85.5	94.8	98.5	54.1	75	81.4	88.5	1	1.9	1.9	11.6
(23)	**1083848**	55.6	78.5	88.9	91	92	95.5	97.5	97.5	0	1.4	2.4	5.6
(29)	**1076409**	20.5	38.1	57.1	80.1	79	96.5	97	97	0	1.4	11.4	21.2
(32)	**1083854**	14.1	21.6	39.3	74.1	58.2	82.1	94.3	95.2	0	1	3.4	15.9
(37)	**1083917**	48.7	77.1	95.2	98	90.9	98	99	99	0	4.2	7	17.3
(70)	**1084352**	30	47.5	68	87.2	5.2	12.6	18.5	32.3	2.4	9.9	19.3	32.2
(78)	**1124378**	8.3	25.3	35.6	70	2.9	9	15.5	28	1	5.2	11.9	23
(79)	**1124379**	15	29.5	52.6	72	4.7	8.2	15.2	23.5	0	1.9	5.1	14.1
(80)	**1124898**	6	7	15.2	25.1	1.9	3.8	6.5	9	1	4.7	11.4	18.6
(83)	**1124383**	27	52.5	66.3	84	4.7	9.5	16.5	24.5	1.9	4.2	8.6	12.6
(86)	**1124384**	64.6	93.1	97.1	98.5	11.3	21.7	35.2	44.5	1	5.2	9.9	11.8

Table S4.4: FA protein titrations with regulatory phosphorylation sites
Protein titrations in the presence of 10 nM FAM-labeled peptides: ARAF pS214, BRAF pS365 or CRAF pS259, 100 µM compound, 250 µM 14-3-3σ starting concentration, 2-fold dilution. *app*K_D values refer to overnight measurements.

		ARAF pS214		BRAF pS365		CRAF pS259		
No.	**SMDC ID.**	***app*K_D**	**X fold stab.**	***app*K_D**	**X fold stab.**	***app*K_D**	***app*K_D DMSO**	**X fold stab.**
(8)	**1075477**	4400 nM	1	640 nM	1	6600 nM	6700 nM	1
(22)	**1083853**	12 nM	337	180 nM	4	47 nM	8427 nM	179
(23)	**1083848**	15 nM	270	105 nM	6	30 nM	8427 nM	280
(29)	**1076409**	30 nM	135	140 nM	5	100 nM	8427 nM	84
(32)	**1083854**	94 nM	43	112 nM	6	140 nM	8427 nM	60
(37)	**1083917**	26 nM	155	52 nM	13	92 nM	8427 nM	92
(70)	**1084352**	180 nM	23	41 nM	15	58 nM	5514 nM	95
(78)	**1124378**	250 nM	16	41 nM	15	40 nM	8427 nM	210
(79)	**1124379**	270 nM	15	100 nM	6	35 nM	8427 nM	240
(80)	**1124898**	310 nM	13	110 nM	6	420 nM	4600 nM	11
(83)	**1124383**	140 nM	28	180 nM	4	102 nM	8427 nM	83
(86)	**1124384**	72 nM	56	155 nM	4	28 nM	8427 nM	300
	DMSO	4050 nM	-	650 nM	**-**	**-**	**-**	**-**

Materials and Methods

Protein expression and purification

The 14-3-3 σ isoform (full-length for mass spectrometry and fluorescence anisotropy assays, ΔC for crystallography) with an N-terminal His6 tag was expressed in Rosetta™ 2(DE3)pLysS competent E. coli (Novagen) from a pPROEX HTb expression vector. After transformation following manufacturer's instructions, single colonies were picked to inoculate 30 mL precultures (LB), which were added to 1.5 L terrific broth (TB) medium after overnight growth at 37°C, 250 rpm. Expression was induced upon reaching OD_{600} 1.9−2.1 by adding 400 μM IPTG. After overnight expression at 30°C, 150 rpm, cells were harvested by centrifugation at 6,500 rpm, resuspended in lysis buffer (50 mM HEPES pH 7.5, 500 mM NaCl, 20 mM imidazole, 10% glycerol, 1 mM TCEP), and lysed by sonication. The His6-tagged protein was purified by Ni-affinity chromatography (Ni-NTA Agarose, Invitrogen) (Wash buffer 50 mM HEPES pH 7.5, 500 mM NaCl, 20 mM imidazole, 1 mM TCEP; Elution buffer 50 mM HEPES pH 7.5, 500 mM NaCl, 500 mM imidazole, 1 mM TCEP) and analyzed for purity by SDS-PAGE and Q-Tof LC/MS. The protein was buffer exchanged (Storage buffer 25 mM HEPES pH 7.5, 150 mM NaCl, 1 mM TCEP) and concentrated to ~16 mg/mL and aliquots flash-frozen for storage at −80°C. The ΔC variant was truncated at the C-terminus after T231 to enhance crystallization and after the first Ni-affinity chromatography column, the construct was treated with TEV protease to cleave off the His6 tag during dialysis (25 mM HEPES, pH 7.5, 200 mM NaCl, 5% glycerol, 10 mM $MgCl_2$, 250 μM TCEP) overnight at 4 °C. The flow-through of a second Ni-affinity column was subjected to a final purification step by size exclusion chromatography (Superdex 75 pg 16/60 size exclusion column (GE Life Science) (SEC buffer: 25 mM HEPES pH 7.5, 100 mM NaCl, 10 mM $MgCl_2$, 250 μM TCEP). The protein was concentrated to ~60 mg/mL, analyzed for purity by SDS-PAGE and Q-Tof LC/MS and aliquots flash-frozen for storage at -80 °C.

Peptide sequences

Peptides for mass spectrometry assays were purchased from Elim Biopharmaceuticals, Inc. (Hayward, CA). Peptides for X-ray crystallography were purchased from GenScript Biotech Corp. Fluorescein-labeled (5-FAM) peptides for fluorescence anisotropy assays were purchased from Elim Biopharmaceuticals, Inc. (Hayward, CA) or GenScript Biotech Corp. K_D values of the fluorescently labeled peptides for 14-3-3σ are shown in the following graphs.

Acetylated peptides	**Sequences for mass spectrometry**	**Sequences for crystallography**
A-RAF pS214-pp	*Ac*-LQRIRST{pS}TPNVHMV-*CONH$_2$*	*Ac*- RIRST(pS)TPNVHM -*CONH$_2$*
B-RAF pS365-pp	*Ac*-DRSS{pS}APNVH -*CONH$_2$*	*Ac*- RDRSS(pS)APNVHI -*CONH$_2$*
C-RAF pS259-pp	*Ac*-RQRST{pS}TPNVH-*CONH$_2$*	*Ac*-QRST(pS)TPNVH -*CONH$_2$* *Ac*- RQRST(pS)TPNVHM-*CONH$_2$*
5-FAM peptides	**Sequences for fluorescence anisotropy**	
A-RAF pS214-pp	*5-FAM*-LQRIRST{pS}TPNVHMV-*CONH$_2$*	
B-RAF pS365-pp	*5-FAM*-DRSS{pS}APNVH-*CONH$_2$*	
C-RAF pS259-pp	*5-FAM*-QRST{pS}TPNVH-*CONH$_2$*	
A-RAF pS582-pp	*5-FAM*-PKIERSA{pS}EPSLHRT-*CONH$_2$*	
B-RAF pS729-pp	*5-FAM*-PKIHRSA{pS}EPSLNRA-*CONH$_2$*	
C-RAF pS621-pp	*5-FAM*-PKINRSA{pS}EPSLHRA-*NH$_2$*	

LC-MS dose response assays

Mass spectrometry dose response assays were performed on a Waters Acquity UPLC/ Xevo G2-XS Q-Tof mass spectrometer. A Waters UPLC Protein BEH-C4 Column (300 Å, 1.7 µm, 2.1 mm x 50 mm) was used to desalt the samples prior to application on the mass spectrometer. For 19-point MS dose responses, 50 mM compound stocks in DMSO were serially diluted in 3-fold increment in a master plate, then 1000 nL of the compounds were transferred in the assay plates. Master mixes containing 100 nM full-length wild type 14-3-3σ in the absence or presence of either 18 µM C-RAF259 or 16 µM A-RAF214 or 5 µM B-RAF365 were then dispensed into 384 well

plates (Greiner Bio-One, catalog number 784201). Assay buffer was TRIS (10 mM, pH 8.0) and final volume per well was 50 µL, with final top concentration of compounds dose response series at 1 mM. The reaction mixtures were incubated for 1h at rt before subjected to MS. Four measurements (1h, 8h, 16h, 24h) were performed for time-course experiments. The injection volume for each sample was 6 µl. 24 µL of sample were needed for the time-course experiments, so the total volume in the assay plate was adjusted to 50 µL, to account for the dead volume in the injections. Data collection and automated processing followed a custom workflow, as previously described. z Plots were created using GraphPad Prism with the log(agonist) vs. response (variable slope, four parameters) fitting model.

Fluorescence anisotropy measurements

Fluorescein-labeled peptides (5-FAM), 14-3-3σ full-length protein, the compounds (50 mM stock solution in DMSO) were diluted in buffer (10 mM HEPES, pH 7.5, 150 mM NaCl, 0.1% Tween20, 1 mg/mL Bovine Serum Albumin (BSA; Sigma-Aldrich). Final DMSO in the assay was always 1%. Dilution series of 14-3-3σ proteins or compounds were made in black, round-bottom 384-microwell plates (Greiner Bio-one 784900) in a final sample volume of 10 µL in triplicates.

For **compound titrations** the initial 50 mM compound stock solutions in DMSO were diluted to 20mM in a 384-well master plate, followed by a serial 2-fold dilution. Then, 500 nL of the dilution series were transferred in the assay plates. A master mix containing 10 nM fluorescein-labeled C-RAF-pS259 peptide and 5 µM full length 14-3-3σ (concentration at EC_{20} value of the protein-peptide complex) in buffer (10 mM HEPES, pH 7.5, 150 mM NaCl, 0.1% Tween20, 1 mg/mL BSA) was dispensed on the assay plates. The final volume per well was 10µL, with final top concentration of compounds dose response series at 1mM. Each compound was measured in triplicates, in two independent experiments. Fluorescence anisotropy measurements were

performed directly and after overnight incubation at room temperature. The high protein concentration used in this assay limits the sensitivity for potent compounds (EC_{50} < 1μM).

Protein titrations were made by titrating 14-3-3σ in a 2-fold dilution series (starting at 250 μM) to a mix of fluorescein-labeled peptide (10 nM) and DMSO or compound (100 μM). Fluorescence anisotropy measurements were performed after overnight incubation at room temperature. Protein titrations were more sensitive than compound titrations for highly potent compounds and the *app*K_D values obtained were not limited by the protein concentration used.

Fluorescence anisotropy values were measured using a Molecular Devices ID5 plate reader (filter set λ_{ex}: 485 ± 20 nm, λ_{em}: 535 ± 25 nm; integration time: 50 ms; settle time: 0 ms; shake 5sec, medium, read height 3.00 mm, G factor = 1. Data reported are at endpoint. EC_{50} and apparent K_D values were obtained from fitting the data with a four-parameter logistic model (4PL) in GraphPad Prism 7 for Windows. Data was obtained and averaged based on two independent experiments.

X-ray crystallography data collection and refinement

The 14-3-3σΔC protein, Ac-CRAF/BRAF/ARAF and compounds (50 mM stock in DMSO) were dissolved in complexation buffer (25 mM HEPES pH=7.5, 2 mM $MgCl_2$ and 100 μM TCEP) and mixed in a 1:2:3 or 1:3:5 molecular stoichiometry (protein : peptide : compound) with a final protein concentration of 11 or 12 mg/mL The complex was set-up for sitting-drop crystallization after overnight incubation at 4 °C, in a custom crystallization liquor (0.05 M HEPES (pH 7.1, 7.3, 7.5, 7.7), 0.19 M $CaCl_2$ 24-29% PEG400, and 5% (v/v) glycerol). Crystals grew within 10-14 days at 4 °C. Crystals were fished and flash-cooled in liquid nitrogen. X-ray diffraction (XRD) data were collected at the European Synchrotron Radiation Facility (ESRF Grenoble, France, beamline ID23-1, ID30A-3/MASSIF-3, or ID23-2). Initial data processing was performed at ESRF using

autoPROC after which pre-processed data was taken towards further scaling steps, molecular replacement, and refinement.

Data was processed using CCP4i2 suite (version 8.0.003). After indexing and integrating the data, scaling was done using AIMLESS. The data was phased with MolRep, using 3IQU as template. The presence of co-crystallized ligands was verified by visual inspection of the Fo-Fc and 2Fo-Fc electron density maps in COOT (version 0.9.6). If electron density corresponding to the co-crystallized ligand was present, its structure and restrains were generated using AceDRG. After building in the ligand, model rebuilding and refinements was performed using REFMAC5. The PDB REDO server (pdb-redo.edu) or phenix.refine form Phenix software suite (version 1.19.2-4158) was used to complete the model building and refinement. The images were created using the PyMOL Molecular Graphics System (Schrödinger LLC, version 4.6.0).

NanoBRET

NanoBRET assays were performed as previously described in Chapter 3. Briefly, eight constructs were generated, and combination and ratio tests were performed in HEK293T cells. The table blow describes the constructs used and additional transfections for each NanoBRET experiment.

NanoBRET assay	NanoLuc	HaloTag	Additional Transfections
14-3-3σ/CRAF	CRAF-NanoLuc	14-3-3σ-HaloTag	
14-3-3σ/ARAF	ARAF-NanoLuc	14-3-3σ-HaloTag	
14-3-3σ/BRAF	BRAF-NanoLuc	14-3-3σ-HaloTag	
NRAS/CRAF	CRAF-NanoLuc	HaloTag-NRAS Q61L	14-3-3σ
CRAF/CRAF	CRAF-NanoLuc	HaloTag-CRAF	NRAS Q61L, 14-3-3σ

Cell culture and western blots

HEK293T and MIA PaCa-2 cells were grown in DMEM, high glucose (Gibco) with 10% Fetal Bovine Serum (FBS) and PANC0813 cells were grown in RPMI 1640 medium (Gibco) with 15%

FBS plus insulin. All compound treatments were for 24 hours. Anti-CRAF pS259 (Invitrogen 44-502), anti-CRAF (BD Biosciences 610152), anti-phospho-ERK (Cell Signaling Technology 4370S), anti-ERK (Santa Cruz Biotechnology sc-514302), anti-Vinculin (Cell Signaling Technology 13901S), anti-FLAG (Cell Signaling Technology 8146S), and anti-14-3-3σ (Invitrogen SD2070) antibodies were used to detect protein. All were used at a 1:1,000 dilution except anti-Vinculin, which was used at 1:2,000. Western blots were imaged on a LI-COR imaging system and analyzed using Image Studio.

Co-immunoprecipitation

HEK293T cells were dosed with compound for 24 hours before lysis (Triton X-100). Clarified lysate was incubated with Pierce anti-FLAG magnetic beads (Thermo Fisher A36797) following the manufacturers protocol. Lysate and IP samples were analyzed using antibodies described above.

Docking

Computational design for SAR optimization and docking was performed with SeeSAR version 11.2.0; BioSolveIT GmbH, Sankt Augustin, Germany, 2022, www.biosolveit.de/SeeSAR

Software versions

Prism (10.2.0)

Illustrator (22.1 (64-bit))

Biorender (64-bit)

Pymol (4.6.0)

CCP4i2 (8.0.003)

COOT (0.9.8.1)

Phenix (1.19.2-4158)

Image Studio (5.2.5)

References

1. Dhillon, A. S., Hagan, S., Rath, O. & Kolch, W. MAP kinase signalling pathways in cancer. *Oncogene* **26**, 3279–3290 (2007).

2. Van Aelst, L., Barr, M., Marcus, S., Polverino, A. & Wigler, M. Complex formation between RAS and RAF and other protein kinases. *Proc. Natl. Acad. Sci.* **90**, 6213–6217 (1993).

3. Moodie, S. A., Willumsen, B. M., Weber, M. J. & Wolfman, A. Complexes of Ras·GTP with Raf-1 and Mitogen-Activated Protein Kinase Kinase. *Science* **260**, 1658–1661 (1993).

4. Stokoe, D., Macdonald, S. G., Cadwallader, K., Symons, M. & Hancock, J. F. Activation of Raf as a Result of Recruitment to the Plasma Membrane. *Science* **264**, 1463–1467 (1994).

5. Roberts, P. J. & Der, C. J. Targeting the Raf-MEK-ERK mitogen-activated protein kinase cascade for the treatment of cancer. *Oncogene* **26**, 3291–3310 (2007).

6. Cutler, R. E., Stephens, R. M., Saracino, M. R. & Morrison, D. K. Autoregulation of the Raf-1 serine/threonine kinase. *Proc. Natl. Acad. Sci.* **95**, 9214–9219 (1998).

7. Chong, H. & Guan, K.-L. Regulation of Raf through Phosphorylation and N Terminus-C Terminus Interaction. *J. Biol. Chem.* **278**, 36269–36276 (2003).

8. Aitken, A. 14-3-3 proteins: a historic overview. *Semin. Cancer Biol.* **16**, 162–172 (2006).

9. Sluchanko, N. N. Reading the phosphorylation code: binding of the 14-3-3 protein to multivalent client phosphoproteins. *Biochem. J.* **477**, 1219–1225 (2020).

10. Tzivion, G., Luo, Z. & Avruch, J. A dimeric 14-3-3 protein is an essential cofactor for Raf kinase activity. *Nature* **394**, 88 (1998).

11. Garnett, M. J., Rana, S., Paterson, H., Barford, D. & Marais, R. Wild-Type and Mutant B-RAF Activate C-RAF through Distinct Mechanisms Involving Heterodimerization. *Mol. Cell* **20**, 963–969 (2005).

12. Rushworth, L. K., Hindley, A. D., O'Neill, E. & Kolch, W. Regulation and Role of Raf-1/B-Raf Heterodimerization. *Mol. Cell. Biol.* **26**, 2262–2272 (2006).

13. Kondo, Y. *et al.* Cryo-EM structure of a dimeric B-Raf:14-3-3 complex reveals asymmetry in the active sites of B-Raf kinases. *Science* **366**, 109–115 (2019).

14. Martinez Fiesco, J. A., Durrant, D. E., Morrison, D. K. & Zhang, P. Structural insights into the BRAF monomer-to-dimer transition mediated by RAS binding. *Nat. Commun.* **13**, 486 (2022).

15. Park, E. *et al.* Architecture of autoinhibited and active BRAF-MEK1-14-3-3 complexes. *Nature* **575**, 545–550 (2019).

16. García-Alonso, S. *et al.* Structure of the RAF1-HSP90-CDC37 complex reveals the basis of RAF1 regulation. *Mol. Cell* **82**, 3438-3452.e8 (2022).

17. Dedden, D. *et al.* Cryo-EM Structures of CRAF2/14-3-32 and CRAF2/14-3-32/MEK12 Complexes. *J. Mol. Biol.* **436**, 168483 (2024).

18. Okamoto, K. & Sako, Y. Two Closed Conformations of CRAF Require the 14-3-3 Binding Motifs and Cysteine-Rich Domain to be Intact in Live Cells. *J. Mol. Biol.* **435**, 167989 (2023).

19. Liau, N. P. D. *et al.* Structural basis for SHOC2 modulation of RAS signalling. *Nature* **609**, 400–407 (2022).

20. Young, L. C. *et al.* SHOC2-MRAS-PP1 complex positively regulates RAF activity and contributes to Noonan syndrome pathogenesis. *Proc. Natl. Acad. Sci. U. S. A.* **115**, E10576–E10585 (2018).

21. Tran, T. H. *et al.* KRAS interaction with RAF1 RAS-binding domain and cysteine-rich domain provides insights into RAS-mediated RAF activation. *Nat. Commun.* **12**, 1176 (2021).

22. Hu, J. *et al.* Allosteric Activation of Functionally Asymmetric RAF Kinase Dimers. *Cell* **154**, 1036–1046 (2013).

23. Venkatanarayan, A. *et al.* CRAF dimerization with ARAF regulates KRAS-driven tumor growth. *Cell Rep.* **38**, 110351 (2022).

24. Fernandez-Medarde, A. & Santos, E. Ras in Cancer and Developmental Diseases. *Genes Cancer* **2**, 344–358 (2011).

25. Davies, H. *et al.* Mutations of the BRAF gene in human cancer. *Nature* **417**, 949–954 (2002).

26. Jain, P. *et al.* CRAF gene fusions in pediatric low-grade gliomas define a distinct drug response based on dimerization profiles. *Oncogene* **36**, 6348–6358 (2017).

27. Imielinski, M. *et al.* Oncogenic and sorafenib-sensitive ARAF mutations in lung adenocarcinoma. *J. Clin. Invest.* **124**, 1582–1586 (2014).

28. Noeparast, A. *et al.* CRAF mutations in lung cancer can be oncogenic and predict sensitivity to combined type II RAF and MEK inhibition. *Oncogene* **38**, 5933–5941 (2019).

29. Ullah, R., Yin, Q., Snell, A. H. & Wan, L. RAF-MEK-ERK pathway in cancer evolution and treatment. *Semin. Cancer Biol.* **85**, 123–154 (2022).

30. Kim, Y. E. & Baek, S. T. Neurodevelopmental Aspects of RASopathies. *Mol. Cells* **42**, 441–447 (2019).

31. Zhang, W. BRAF inhibitors: the current and the future. *Curr. Opin. Pharmacol.* **23**, 68–73 (2015).

32. Wang, P.-F., Qiu, H.-Y. & Zhu, H.-L. A patent review of BRAF inhibitors: 2013-2018. *Expert Opin. Ther. Pat.* **29**, 595–603 (2019).

33. Poulikakos, P. I., Zhang, C., Bollag, G., Shokat, K. M. & Rosen, N. RAF inhibitors transactivate RAF dimers and ERK signalling in cells with wild-type BRAF. *Nature* **464**, 427–430 (2010).

34. Hatzivassiliou, G. *et al.* RAF inhibitors prime wild-type RAF to activate the MAPK pathway and enhance growth. *Nature* **464**, 431–435 (2010).

35. Heidorn, S. J. *et al.* Kinase-Dead BRAF and Oncogenic RAS Cooperate to Drive Tumor Progression through CRAF. *Cell* **140**, 209–221 (2010).

36. Morgan, C. W., Dale, I. L., Thomas, A. P., Hunt, J. & Chin, J. W. Selective CRAF Inhibition Elicits Transactivation. *J. Am. Chem. Soc.* **143**, 4600–4606 (2021).

37. Yuan, J. *et al.* The AMPK inhibitor overcomes the paradoxical effect of RAF inhibitors through blocking phospho–Ser-621 in the C terminus of CRAF. *J. Biol. Chem.* **293**, 14276–14284 (2018).

38. Molzan, M. *et al.* Stabilization of physical RAF/14-3-3 interaction by cotylenin A as treatment strategy for RAS mutant cancers. *ACS Chem. Biol.* **8**, 1869–1875 (2013).

39. Konstantinidou, M. *et al.* Structure-Based Optimization of Covalent, Small-Molecule Stabilizers of the 14-3-3σ/ERα Protein–Protein Interaction from Nonselective Fragments. *J. Am. Chem. Soc.* **145**, 20328–20343 (2023).

40. Wolter, M. *et al.* An Exploration of Chemical Properties Required for Cooperative Stabilization of the 14-3-3 Interaction with NF-κB—Utilizing a Reversible Covalent Tethering Approach. *J. Med. Chem.* **64**, 8423–8436 (2021).

41. Vickery, H. R., Virta, J. M., Konstantinidou, M. & Arkin, M. R. Development of a NanoBRET assay for evaluation of 14-3-3σ molecular glues. 2023.12.31.573792 Preprint at https://doi.org/10.1101/2023.12.31.573792 (2024).

Chapter 5

Expansion of the disulfide tethering technology to a new class of hub proteins

Contributing Authors:

Holly R. Vickery[1] and Johanna M. Virta[1]

[1]Department of Pharmaceutical Chemistry and Small Molecule Discovery Center, University of California, San Francisco 94158, United States.

Abstract

The field of drug discovery has seen a recent surge of interest in PPI stabilization. Notably, the Arkin and Brunsveld Labs have pioneered the development of PPI stabilizers targeting numerous 14-3-3/client interactions, effectively modulating client protein function in disease contexts. In our endeavor to broaden systematic approaches for PPI stabilizer discovery, we have harnessed mass spectrometry-based disulfide tethering screening technology to explore a novel class of hub proteins, WD-40 domain containing proteins. These hub proteins, which have similar properties to 14-3-3/client interactions, represent a promising avenue for intervention. Modulation of novel hub protein/client interactions could be therapeutically beneficial in many diseases such as cancer. By employing the tethering approach with this new class of hub proteins, we have successfully identified stabilizers and inhibitors for their protein/peptide interactions. This pioneering work demonstrates the potential expansion of tethering technology for accelerated discovery of PPI modulators across diverse hub protein systems.

Introduction

Having successfully employed the mass spectrometry-based site-directed disulfide tethering screen to discover stabilizers targeting several 14-3-3σ/client interactions,[1–4] we aimed to expand the application of this methodology to explore a new hub protein system. As outlined in Chapter 2, this screening approach evaluates the covalent binding of disulfide fragments to a protein of interest, both in the presence and absence of a client protein, thus enabling the identification of PPI stabilizers and inhibitors. In our pursuit of identifying a new hub protein system for comprehensive investigation, we sought proteins demonstrating broad client binding, harboring potential small molecule binding sites proximal to the protein/client interface, and bearing relevance to disease pathogenesis. We chose to explore WD-40 domain-containing proteins, specifically the hub protein Kelch-like ECH-associated protein 1 (Keap1).[5,6] Keap1 interacts with a client protein Nrf2, which plays a pivotal role in response to oxidative stress. Additionally, Keap1 forms part of an E3 ubiquitin ligase complex, which tightly regulates the degradation and activity of Nrf2. In response to oxidative stress, sensor cysteine residues on Keap1 lead to the release of Nrf2, allowing Nrf2 to translocate to the nucleus and promote transcription of antioxidant response element genes (Figure 5.1A). In the context of cancer, Nrf2 activity can contribute to cancer cell survival and progression.[6–10] Systematically screening a diverse library of disulfide-containing fragments to identify stabilizers of the Keap1/Nrf2 interaction would lead to the inhibition and degradation of Nrf2, potentially leading to cancer cell death.

Through systematic screening of a library of disulfide-containing fragments, our aim was to identify stabilizers targeting the Keap1/Nrf2 interaction, with the ultimate goal of inhibiting and degrading Nrf2, thereby potentially inducing cancer cell death. This approach holds immense promise as a strategic approach for modulating critical PPI networks implicated in cancer pathogenesis. Furthermore, by expanding the repertoire of PPI modulators identified through this innovative technology, we envision pioneering advancements in therapeutic intervention

strategies not only in the context of cancer, but also in various other disease settings, thereby expanding outlooks for the development of targeted therapies with enhanced efficacy and selectivity.

Results and Discussion

Keap1/Nrf2 binding

Keap1 binds two distinct domains of Nrf2. The “ETGE” domain has high affinity and the “DLG” domain has lower affinity. It is unknown whether stabilizing the Nrf2 ETGE or Nrf2 DLG region would lead to a larger biological effect, so both domains were explored. Both Nrf2 ETGE and DLG motifs bind along a pocket at the top of Keap1 (Figure 5.1B). Keap1 has a WT cysteine residue proximal to the Nrf2 binding pocket, which we used for tethering. The affinity of peptides representing the Nrf2 ETGE and DLG motifs to Keap1 was measured by FA using Keap1^{C489S} to mutate the most reactive cysteine in the protein that is not the cysteine of interest.[9] The Nrf2 ETGE peptide bound to Keap1^{C489S} with a K_D of 28 nM (Figure 5.1C), while the Nrf2 DLG peptide bound to Keap1^{C489S} with a K_D of 0.48 μM (Figure 5.1D).

Disulfide Tethering Screens

The tethering screen was performed with Keap1^{C489S} alone (apo), Keap1^{C489S} plus Nrf2 ETGE peptide, and Keap1^{C489S} plus Nrf2 DLG peptide. In comparing apo screens and screens with peptide, both Nrf2 ETGE and DLG peptides resulted in 16 stabilizing hits each, a 0.8% hit rate (Figure 5.2A,B). The top fragment stabilizer for Keap1^{C489S}/Nrf2 ETGE bound 98.2% in the presence of Nrf2 ETGE and 4.3% in the absence (Figure 5.2A). The top fragment stabilizer for Keap1^{C489S}/Nrf2 DLG bound 92.2% in the presence of Nrf2 DLG and 12.7% in the absence (Figure 5.2B). The Nrf2 ETGE region occupies less of the Keap1 binding pocket, allowing more space for

fragment binding. Thus, larger fragments were identified as Keap1^{C489S}/Nrf2 ETGE stabilizers and smaller fragments were identified as Keap1^{C489S}/Nrf2 DLG stabilizers. We used covalent docking to visualize how the top stabilizing hit from Keap1^{C489S}/Nrf2 ETGE screen binds to the crystal structure of the complex. The stabilizer appears to make interactions with both Keap1^{C489S} and Nrf2 ETGE in the pocket between the Keap1 cysteine and Nrf2 ETGE (Figure 5.2C).

The tethering screen was also performed with an additional Keap1 mutant that had its target cysteine residue mutated to an alanine, Keap1^{C434A,C489S}. The goal of this tethering screen was to identify if the fragment hits were binding to the cysteine of interest or to another cysteine on Keap1. This tethering screen resulted in low percent labeling overall, with the average labeling around 10%, indicating that identified fragment stabilizers for the Keap1^{C489S}/Nrf2 ETGE and Keap1^{C489S}/Nrf2 DLG screens are likely causing a stabilization effect by binding to the cysteine of interest (Figure 5.2D).

We then pursued an Nrf2 mutation commonly found in cancers, Nrf2 ETGE^{D77V}, which lies just outside the ETGE binding motif (residues 79-82). This mutation decreases the affinity between the Nrf2 ETGE region to Keap1, leading to the stability and activation of Nrf2 in cancer. This specific mutation has been associated with an increased risk of developing various cancers, including lung cancer. Keap1 binds to the Nrf2 ETGE^{D77V} peptide with a K_D of 1.8 μM, a 64-fold loss in binding affinity (Figure 5.2E). We performed a disulfide tethering screen with Keap1 bound to the Nrf2 ETGE^{D77V} peptide and identified ~20 stabilizers of the interaction (Figure 5.2F). This screen was performed with more stringent conditions (higher concentration of β-mercaptoethanol) to selectively identify potent binders.

Conclusions

In conclusion, the use of the MS-based site-directed disulfide tethering screen has proven instrumental in our pursuit of discovering stabilizers for diverse PPIs, particularly within the intricate realm of hub protein / client interactions. Through the expansion of this innovative technology to explore a novel hub protein system, exemplified by the investigation of the Keap1/Nrf2 PPI, we have established a foundation for pioneering advancements in therapeutic intervention strategies, particularly in the context of cancer. The strategic identification of stabilizers targeting the Keap1/Nrf2 interaction holds immense promise in disrupting key pathways implicated in cancer cell survival and progression. This work expands the application of the tethering screen methodology to systematically identify PPI modulators relevant to a spectrum of diseases.

Figures

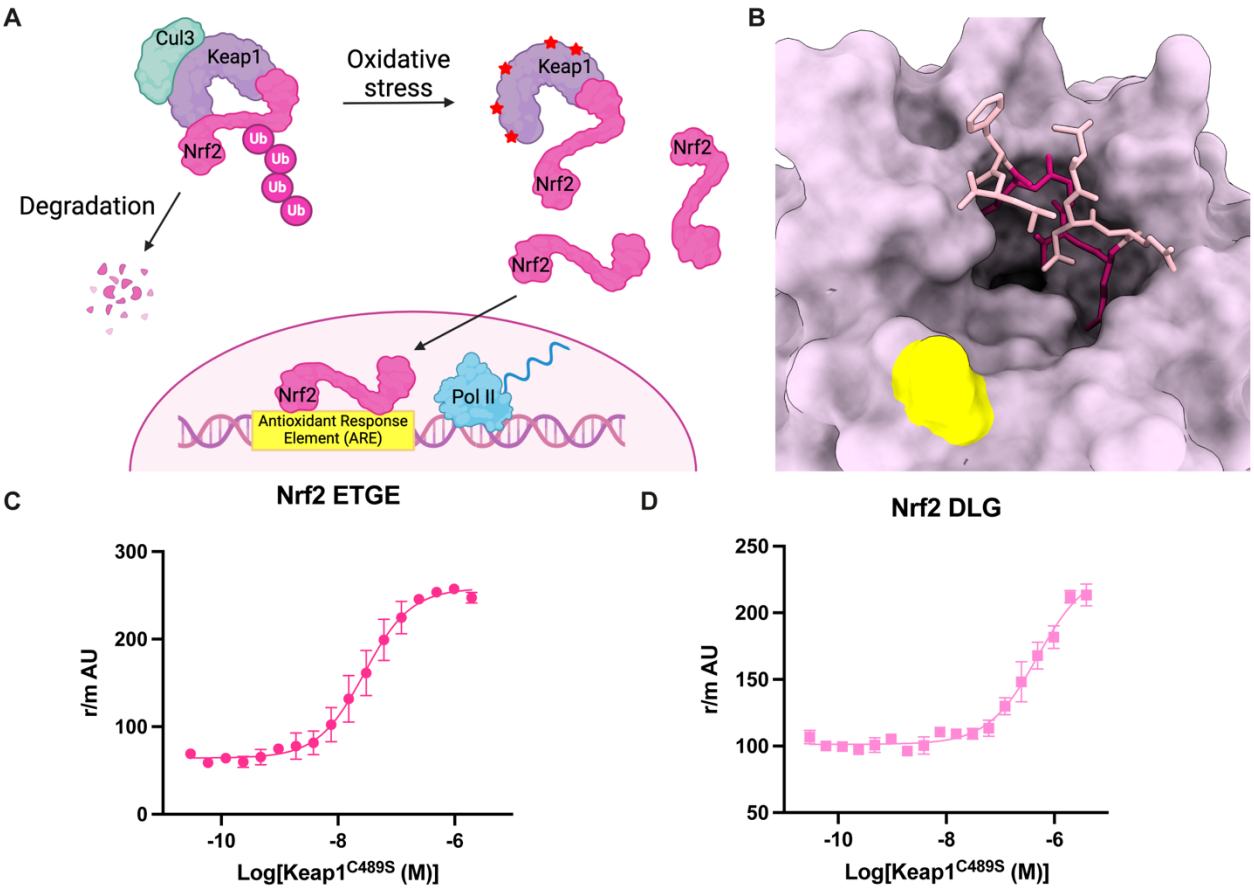

Figure 5.1: Keap1/Nrf2 regulation and binding
A) Keap1 regulation of Nrf2 degradation and activity. **B)** Crystal structure of Keap1 (purple) bound to Nrf2 ETGE peptide (pink). ETGE residues are dark pink and other residues are light pink. Position of cysteine for tethering on Keap1 is highlighted in yellow. PDB 5WFV. **C)** FA binding of Keap1^{C489S} to Nrf2 ETGE. K_D = 28 nM. **D)** FA binding of Keap1^{C489S} to Nrf2 DLG. K_D = 480 nM.

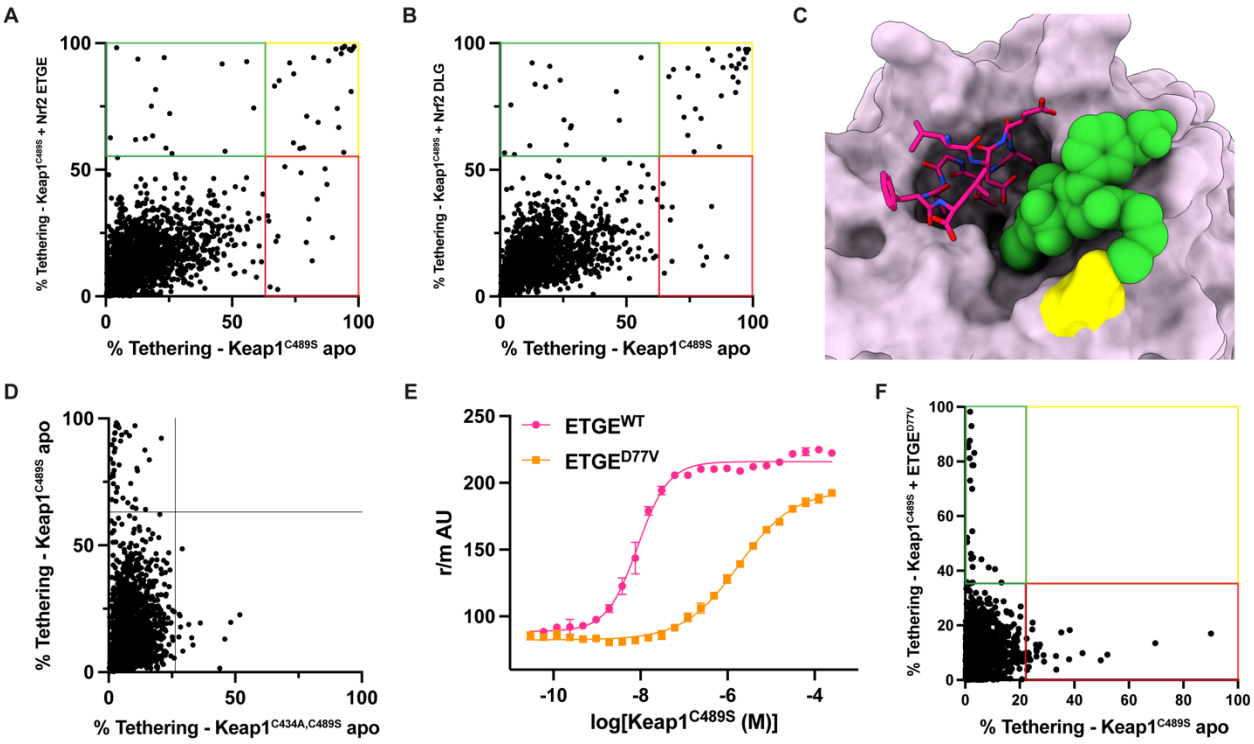

Figure 5.2: Keap1/Nrf2 tethering screen results

A) Keap1^{C489S} apo vs Keap1^{C489S} + Nrf2 ETGE tethering results. Stabilizers are highlighted in the green quadrant, neutral binders in yellow, and inhibitors in red. **B)** Keap1^{C489S} apo vs Keap1^{C489S} + Nrf2 DLG tethering results. Stabilizers are highlighted in the green quadrant, neutral binders in yellow, and inhibitors in red. **C)** Covalent docking of top stabilizing hit (green) from tethering screen to Keap1^{C489S} (purple, yellow) / Nrf2 ETGE (pink) complex. **D)** Comparison of apo tethering screens for Keap1^{C489S} and Keap1^{C434A,C489S} mutant. **E)** FA binding of Keap1^{C489S} to Nrf2 ETGE and ETGE^{D77V}. K_D for ETGE^{D77V} = 1.8 μM.

Materials and Methods

Fluorescence Anisotropy

FA assays were performed as previous described in Chapters 2-4.[3,11] Briefly, FAM-labeled Protein B peptide at 100 nM was added to full-length Protein A and allowed to incubate for 30 minutes before reading.

Peptides

Nrf2 motif	Peptide sequence
ETGE	LDE**ETGE**FLP
DLG	MDLIDILWRQDI**DLG**VSREVFDFSQRQKDYELEKQ
$ETGE^{D77V}$	LVE**ETGE**FLP

Disulfide Tethering Screen and Data Processing

Tethering screens were performed as described in Chapter 2.[3] Briefly, 100 nM full-length Protein A, 2x K_D of Protein B peptide (3.6x K_D for Protein B^{high} to reach 100 nM), and 125 μM β-mercaptoethanol were added to disulfide fragments, which were at a final concentration of 200 μM. The reactions were incubated at room temperature for 3 hours before measurement by LC/MS. Data processing followed a custom workflow, as previously described.[1–3] Keap1/Nrf2 $ETGE^{D77V}$ screen and Keap1 apo comparison were performed at 500 μM βME.

Docking

Covalent docking was performed using Glide by Schrödinger.

Acknowledgements

The authors would like to thank Elissa Fink for performing molecular docking analysis.

References

1. Hallenbeck, K. K. *et al.* A Liquid Chromatography/Mass Spectrometry Method for Screening Disulfide Tethering Fragments. *SLAS Discov. Adv. Sci. Drug Discov.* **23**, 183–192 (2018).

2. Sijbesma, E. *et al.* Site-Directed Fragment-Based Screening for the Discovery of Protein-Protein Interaction Stabilizers. *J. Am. Chem. Soc.* **141**, 3524–3531 (2019).

3. Kenanova, D. N. *et al.* A Systematic Approach to the Discovery of Protein–Protein Interaction Stabilizers. *ACS Cent. Sci.* (2023) doi:10.1021/acscentsci.2c01449.

4. Konstantinidou, M. *et al.* Structure-Based Optimization of Covalent, Small-Molecule Stabilizers of the 14-3-3σ/ERα Protein–Protein Interaction from Nonselective Fragments. *J. Am. Chem. Soc.* **145**, 20328–20343 (2023).

5. Schapira, M., Tyers, M., Torrent, M. & Arrowsmith, C. H. WD40 repeat domain proteins: a novel target class? *Nat. Rev. Drug Discov.* **16**, 773–786 (2017).

6. Baird, L. & Dinkova-Kostova, A. T. The cytoprotective role of the Keap1–Nrf2 pathway. *Arch. Toxicol.* **85**, 241–272 (2011).

7. Baird, L. & Yamamoto, M. The Molecular Mechanisms Regulating the KEAP1-NRF2 Pathway. *Mol. Cell. Biol.* **40**, e00099-20 (2020).

8. De Freitas Silva, M. *et al.* The Keap1/Nrf2-ARE Pathway as a Pharmacological Target for Chalcones. *Molecules* **23**, 1803 (2018).

9. Kansanen, E. *et al.* Electrophilic nitro-fatty acids activate NRF2 by a KEAP1 cysteine 151-independent mechanism. *J. Biol. Chem.* **286**, 14019–14027 (2011).

10. Ogura, T. *et al.* Keap1 is a forked-stem dimer structure with two large spheres enclosing the intervening, double glycine repeat, and C-terminal domains. *Proc. Natl. Acad. Sci. U. S. A.* **107**, 2842–2847 (2010).

11. Vickery, H. R., Virta, J. M., Konstantinidou, M. & Arkin, M. R. Development of a NanoBRET assay for evaluation of 14-3-3σ molecular glues. 2023.12.31.573792 Preprint at https://doi.org/10.1101/2023.12.31.573792 (2024).

Publishing Agreement

It is the policy of the University to encourage open access and broad distribution of all theses, dissertations, and manuscripts. The Graduate Division will facilitate the distribution of UCSF theses, dissertations, and manuscripts to the UCSF Library for open access and distribution. UCSF will make such theses, dissertations, and manuscripts accessible to the public and will take reasonable steps to preserve these works in perpetuity.

I hereby grant the non-exclusive, perpetual right to The Regents of the University of California to reproduce, publicly display, distribute, preserve, and publish copies of my thesis, dissertation, or manuscript in any form or media, now existing or later derived, including access online for teaching, research, and public service purposes.

DocuSigned by:
Holly Vickery
1FFA21F1809B462...
Author Signature

3/19/2024
Date